Synchronous generator and excitation system response to GIC

Prepared by:

Pitambar Jankee

JNKPIT001

Department of Electrical Engineering

University of Cape Town

Supervised by:

Dr.David Oyedokun

Department of Electrical Engineering

University of Cape Town

December 2020

Submitted to the Department of Electrical Engineering at the University of Cape Town in partial fulfilment of the academic requirements for a Master of Science degree in Electrical Engineering

DECLARATION

1. I know that plagiarism is wrong. Plagiarism is to use another's work and pretend that it is one's own.
2. I have used the IEEE convention for citation and referencing. Each contribution to, and quotation in, this final year project report from the work(s) of other people, has been attributed and has been cited and referenced.
3. This final year project report is my own work.
4. I have not allowed, and will not allow, anyone to copy my work with the intention of passing it off as their own work or part thereof

Name: **PITAMBAR JANKEE**

Signature: Signed by candidate **Date: 21 December 2020**

ABSTRACT

Solar cycle 25 has started catching the attention of space scientists, physicists, and power engineers. The resultant Geomagnetically Induced Currents (GIC) lead to periodic part wave saturation of transformers, harmonic pollution, increased non-active power demand and potential voltage collapse. While most power system studies have focussed on the transformer's response to GIC, there has been very little research investigating the response of synchronous generators and excitation systems to such disturbances. Moreover, conventional GIC modelling assumes a dc voltage induced in the neutral or along transmission lines, but this may not adequately represent the actual dynamic power system's response to GIC. Using a 4-bus and a multi-machine power system modelled in MATLAB Simulink, this project shows that the power system's response to low frequency GIC (acGIC) is different to the conventional dc approximation (dcGIC). In both cases, harmonic analysis was carried out. It was observed that under unbalanced system conditions, harmonics do not follow the conventional phase sequence. This means that multiples of the third harmonic no longer have a zero sequence. Such harmonics may affect the generator despite delta winding connections of generator step-up transformers (GSUs). The increased var demand due to saturating transformers was compared using an IEEE1459 meter and a General Power Theory meter. The analysis showed that conventional power theories using the term "reactive power" underestimate the increased var demand. The differences arise in the definitions of conventional reactive power and non-active power defined by IEEE1459. Hence, the burden of var on generators and var compensators can be higher than expected. Additionally, the responses of different complexities of generator models were compared. The results showed that ac equivalent sources might not represent the true dynamic power system's response to GIC. The multi-machine simulation results revealed that voltage dip below the 10 % limit, due to GIC, can be reduced by up to 8.75 % using proper excitation system models and control parameters. Moreover, it was shown that while one generator might not be able to provide enough non-active power to meet the increased demand, a group of generators pushing out var within the generator's capability limits, can help to reduce this deficiency of non-active power. This is because the total var output from the generators is higher. The findings of this study aim to raise concern on the conventionally used dc model of GIC which are not representative of a realistic GIC profile. Excitation system control appears to play a significant role in voltage drop reduction. As such, contingencies such as Geomagnetic Disturbances (GMDs) can be used to determine and tune optimal parameters of the excitation system control.

ACKNOWLEDGMENTS

The research for this dissertation was undertaken under the supervision of Dr.David Oyedokun, senior lecturer in the department of electrical engineering at the University of Cape Town. I thank Dr.David Oyedokun for the enormous amount of time he invested in me, his guidance, always providing excellent feedback and motivating me to work harder.

I also thank Em. Prof. CT Gaunt, the project leader of our GIC research group. His experience, wealth of knowledge and criticism have always challenged me in my research.

My deepest thanks go to my family, especially my Mum and Dad, for always being on my side through thick and thin.

My esteemed colleague, Dr.Hilary Chisepo, whom I have been continuously chatting with to understand some key concepts and results. I have always looked upon you as a mentor and you have been of immense help in polishing up my skills for academic research and writing.

Finally, I thank:

The department of electrical engineering for postgraduate degree funding.

A support grant from the Open Philanthropy Project to carry out this research.

Opti-Num and MathWorks support for addressing my queries on MATLAB Simulink.

Mr.Vithuran Vilvarajah and Mr.Ismail Rkioui, field application engineers at OPAL-RT for answering my questions on the real time simulator.

And last but not the least, Mrs.Prema Jankee for her digilent proofreading of this dissertation.

TABLE OF CONTENTS

LIST OF FIGURES

LIST OF TABLES

NOMENCLATURE

GMD	Geomagnetic Disturbance
GIC	Geomagnetically Induced Currents
ACEQ	ac equivalent voltage source
EXS	Excitation System
dcGIC	dc model of GIC
acGIC	ac model of GIC
V_t	terminal voltage of synchronous generator
I_t	terminal current of synchronous generator
X_s	synchronous reactance
R_s	Stator winding resistance
X_{md}	mutual inductance between stator and fieldwinding along the d-axis
V_{fd}	field voltage
I_{fd}	field current
R_{fd}	field winding resistance
V_d	d-axis stator voltage
V_d	q-axis stator voltage
i_d	d-axis stator current
i_q	q-axis stator current
ψ_d	d-axis stator flux linkage
ψ_{1d}	d-axis damper circuit flux linkage
ψ_{1q}, ψ_{2q}	q-axis damper circuit flux linkage
ψ_q	q-axis stator flux linkage
ψ_0	zero-axis flux linkage
ψ_{fd}	field flux linkage
L_l	Stator leakage inductance
R_{kd}, R_{kq1}, R_{q2}	damper winding resistances
θ	power angle

1 Introduction

1.1 Background to the study

Every eleven years, there is a peak in solar activity [1]. Coronal mass ejections from solar sunspots emit large volumes of charged particles towards the Earth. This causes a change in Earth's magnetic field. According to Faraday's law of electromagnetism, a change in Earth's magnetic field will induce an electric field on the surface of the ground. This leads to currents flowing in the ground called Geomagnetically Induced Currents (GIC). The most likely consequence of a Geomagnetic disturbance (GMD) to the power grid is the increased non-active power demand and loss of voltage stability. This study looks into the dynamic voltage stability of a 4-bus power system and a 2 area multi-machine power system under GIC conditions.

From the first papers studying the effects of GIC in power systems, GIC have been modelled as dc currents due to their very low frequencies compared to the power system frequency [2][3][4][5]. It is however known that GIC are not truly dc but have very low frequencies with those of highest energy densities in the range of 0 to 50 mHz [6]. Recent work has shown the underlying GIC dynamics which should be accurately modelled to understand the true power system's dynamic response to such disturbances. This project highlights the differences between dcGIC models and low frequency acGIC models including the different responses of the power system to such disturbances.

Since the saturating transformers have always taken most of the blame for the increased non-active power demand, research has been focused on transformer problems caused by GIC. There have been very few studies investigating the response of the generator and its excitation system. The main problem associated with GIC is the increased non-active power demand. The excitation system is responsible for providing the field current necessary to produce the required stator flux. The field current controls the non-active power output of the synchronous generator. Therefore, there is a need to investigate how the excitation system performs under geomagnetic disturbances and if there are possible mitigation strategies that can be adopted by overexciting the generator within its capability limits.

The hypothesis of this study is, therefore;

"Generator excitation system control contributes to reducing the drop in network voltage linked to increasing var demand from GIC laden transformers, thereby creating a buffer for high GICs to flow without violating the grid code for minimum operating voltage."

1.1.1 Research Objectives

The research aims to;

- Explore the dynamic voltage stability of a 4-bus power system and a 2-area multi-machine power system under GIC conditions.
- Compare conventional dc models of GIC (dcGIC) to low frequency ac models of GIC (acGIC).
- Understand the response of synchronous generators and excitation systems to GIC.
- Highlight the importance of using accurate definitions of apparent power and non-active power in non-ideal conditions.

1.1.2 Research Questions

The following research questions will be used to test the validity of the hypothesis.

1. How does the power system's response to GIC differ when the GIC is modelled as conventional dc compared to low frequency ac?
2. How do synchronous generators and excitation systems respond to GIC?
3. To what extent can excitation system control be used to reduce the effects of GIC?
4. What is the correct definition of apparent power and non-active power applicable to GIC studies?

1.1.3 Scope and Limitations

- Simple models of GICs have been used with dc and ac voltage sources injected in the neutral. Detailed modelling of the GIC profile and underlying dynamics is subject to space physics and complex mathematical models.
- The study makes use of three phase five limb core type transformers. The effects of transformer core design and type are not within the scope of this voltage stability assessment.
- It was found that the three phase five limb core type transformer does not model inter-phase magnetic coupling and hence, no unbalance. The MATLAB transformer model was still used for this study to allow for use with OPAL-RT which runs on MATLAB Simulink.
- Excitation systems used in this study include the IEEE AC1A, AC4A and AC5A. This is due to software limitations in MATLAB 2019a which provides only these three models.
- Field current limiters and stator current limiters could not be modelled in this study since these models are still under development within MATLAB 2019a and the 2020a version.

- The effects of a dynamic load could not be investigated due to software limitations in MATLAB 2019a providing dynamic loads which only operate under balanced conditions. It is however understood that load dynamics are important for such voltage stability analysis.

1.2 Plan of development

The thesis is outline as follows;

- Chapter 2 provides an extensive literature review to gain knowledge of the theory required throughout the project including but not limited to Geomagnetically Induced Currents, concepts relating to voltage stability and generator excitation systems.
- Chapter 3 outlines the modelling of a 4-bus power system network to investigate the effects of dcGIC and acGIC.
- Chapter 4 discusses the modelling of the multi-machine power system model using multi-frequency acGIC
- Chapter 5 shows the design of an IEEE1459 meter and a General Power Theory meter. These two meters, together with two power measurement blocks provided by MATLAB are contrasted and a choice is made on the power meter to be used for this project.
- Chapter 6 presents the simulation protocol. The steps used to run the simulations and gather results are discussed in this Section.
- The findings of this research are discussed in chapter 7.
- Conclusions are drawn in Chapter 8 where the research questions are addressed before commenting on the implications of the research.

2 Literature Review

2.1 Geomagnetically Induced Currents

Geomagnetically Induced Currents (GIC) are a direct consequence of abnormal space weather. Active areas of the sun known as sunspots, emit solar flares which result in coronal mass ejections (CMEs). The ejection is plasma consisting mainly of protons and neutrons which travel through the heliosphere referred to as the solar wind [7]. Solar winds carry these charged particles which interact with the Earth's magnetic field. The magnetic field of Earth changes over time when it is disturbed by a solar event [1]. The interplanetary magnetic field can rapidly change from 5nT to 30nT when a CME is directed towards the earth [7]. The coupling between the magnetosphere and the ionosphere gives rise to sudden and rapid variations in the geomagnetic field on the Earth surface. This phenomenon is called a Geomagnetic storm.

Auroral currents are induced in the atmosphere due to the varying magnetic field, lighting up the sky. According to Lenz's Law of electromagnetism, an opposing current must be formed. This current is a low frequency (0 – 50mHz) [6] ac current compared to the 50/60Hz power frequency waves and is considered quasi dc. These currents are called Geomagnetically Induced Currents (GIC) and are induced in the ground.

The magnitude of the GIC depends on the intensity of the flare. The K-index, created in 1932 [1] and the A-index [8] are often used as a measure of the storm intensity. The K-index ranges from 0 to 9 with 9 being the most severe and is a 3-hour measure that is site specific. The table below shows indices provided by the United States Space Weather Prediction Center (SWPC).

Table 2.1: SWPC indices to measure solar activity - the A index and K index are used as a measure of the severity of the storm

Solar activity	A-index	K-index	Solar activity	A-index	K-index
Quiet	< 7	≤ 2	Minor	$30 < A < 50$	4, 5
Unsettled	$7 < A < 15$	≤ 3	Major	$50 < A < 100$	5,6
Active	$15 < A < 30$	4	Severe	$A > 100$	7

Geographically, it was believed that regions close to the poles were the most at risk to GMDs [8]. Power systems in mid and low latitude countries were not considered vulnerable to GIC. However, Gaunt and Coetzee [9] provided evidence showing the impact of GIC in regions remote from the auroral zones. Hutchins and Overbye [10] showed that different areas of a power system may experience different electric field magnitudes and GIC. Usually, regions where the soil is very rocky

are characterised by high resistivity. GIC seeking an easier path than the rocky soil, use the power grid transformers' neutrals as the low resistance path. GIC flow through the grounded neutrals of wye-connected transformers leading to partial wave saturation, increased harmonics, increased non-active power demand, voltage collapse and other power quality issues [1][8][11][12].

The North American Electric Reliability Corporation (NERC) reports two main risks associated with GIC in bulk power systems [4][13];

1. The potential damage to transmission system assets, primarily the power transformers.
2. The loss of reactive power support leading to the potential for a voltage collapse.

2.1.1 Effects of GIC in Power Systems

2.1.1.1 Transformer part wave saturation

GIC are responsible for partial wave saturation of transformers. As shown in Figure 2.1, the quasi-dc GIC biases the magnetic circuit of the transformer. The GIC flux adds to the magnetising flux during half of the 50 Hz cycle and subtracts from the magnetising flux during the other half, thus shifting the operating point of the transformer into saturation [4].

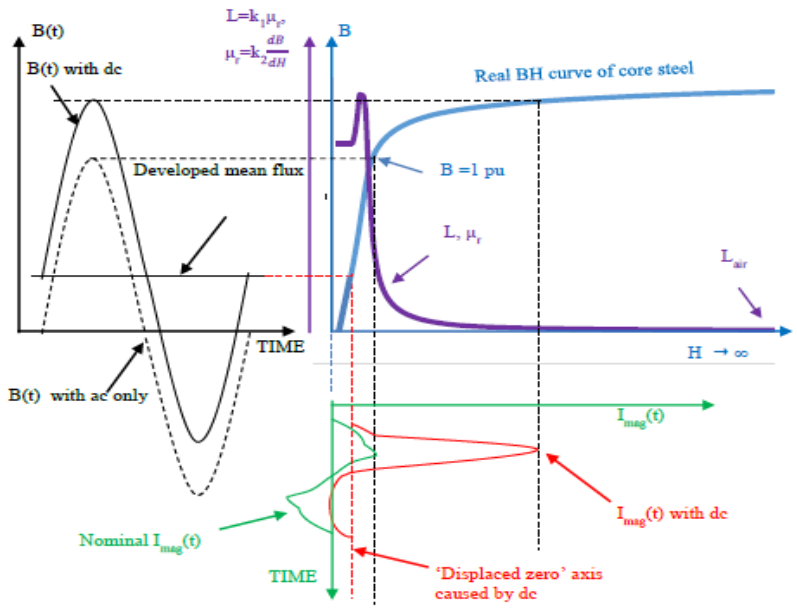

Figure 2.1: DC shift in the magnetising AC flux, drop in transformer inductance, increased magnetising current, causing transformer saturation from GIC [14]

The magnitude of the flux offset due to GIC depends on the reluctance of the dc flux path or zero-sequence path. The transformer type and design affects the flow of dc flux or the zero-sequence flux [3]. The three phase three limb (3p3L) core transformer offers a high reluctance path through the core top yoke, to the tank and returns via the bottom yoke and tank [4][12]. Hence it was often believed

that the 3p3L transformer was hard to saturate although Koen and Gaunt proved otherwise in their study of 3p3L transformers at the Grassridge station in South Africa [15]. Three phase five limb transformers (3p5L) offer a lower reluctance path through the core of the transformer which has a much higher permeability. Comparing a 5 limb and a 4 limb transformer, Price [16] showed that saturation occurs earlier in the 5 limb transformer. Hence, 3p3L transformers are identified as being more tolerant to GIC compared to the other design of transformers due to no zero sequence path for the dc current to flow [3].

2.1.1.2 Increased transformer Magnetising Current

Transformers are designed to operate in the linear region of the BH curve. The magnetising current drawn is very small, usually a fraction of a percent of the full load current [17]. GIC drive the magnetic core of transformers into higher flux densities. The permeability of the core material decreases, the hysteresis loop becomes narrower and the transformer inductance drops (See Figure 2.1). Hence, more current is allowed to flow in the magnetising branch of the transformer [18]. Asymmetrical magnetising currents with high magnitude peaks of short duration have been observed when GIC flow through transformers [19]. Field test on a 600 MVA transformer with 75 A GIC in its neutral showed a rise in magnetising current from 8 A to 294A [1]. There are old reports showing peaks in magnetising current reaching 2000 A [20].

X.Dong *et al*. [21] studied the effects of DC currents on power transformers. Harmonic analysis of the exciting current without DC bias showed the presence of odd harmonics only. As the transformer became subject to DC current, even harmonics appeared in the exciting current. The same findings were reported in the study by Hutchins and Overbye [1]. The exciting current waveform shifts according to the polarity of the dc flux and is no longer symmetrical indicating the presence of even harmonics. The same applies with GIC if they are modelled as quasi-dc. The exciting current will be distorted due to the harmonics caused from transformer saturation.

Dong and Kappenman [22] proved that the transformer type and design has an effect on the exciting current of the transformer under GIC conditions. The single-phase transformer experiences the highest exciting current followed by the three phase five limb, three phase three leg and three phase shell type.

2.1.1.1 Increased Non-active Power demand

The 2012 NERC report states;

"*The most likely worst-case system impacts from a severe GMD event and corresponding GIC flow is voltage instability caused by a significant loss of reactive power support simultaneous to a dramatic*

increase in reactive power demand. Loss of reactive power support can be caused by the unavailability of shunt compensation devices (e.g., shunt capacitor banks, SVCs) due to harmonic distortions generated by transformer half-cycle saturation [4]. "

When the core of the transformer is saturated due to GIC, the winding behaves like an air-cored inductance [3]. The large fundamental frequency magnetising current drawn by the saturating transformer lags the system voltage by 90º, thereby creating an inductive circuit which consumes positive sequence var. In field tests on a 600MVA transformer under 75A GIC conditions, a reactive power loss of 50 MVA was reported which represents 8.33% of the transformer capacity. The increased var demand leads to voltage sags if synchronous generators and SVCs are unable to cater for the high demand.

The reactive power loss by the transformer, under partial wave saturation due to GIC varies linearly with the level of GIC induced [13][3][16][10][5] and is given by;

$$Q_{loss,pu} = V_{pu} K I_{GIC,pu} \tag{2.1}$$

The value K is transformer specific and depends on the design and type [22]. An important point to be noted from the equation above is that the linear relationship between the reactive power and GIC magnitude, stems from the model of the GIC. When using dc GIC models, this linear relationship is true. However, realistic non-active power profiles under GIC conditions are highly dynamic. With more realistic GIC models such as low frequency ac currents, the non-active power profile will fluctuate with the GIC as shown in [23].

The reactive power loss can be included in the power flow to study its variations during geomagnetic disturbances with non-uniform electric field induced. This was first proposed in 1981 [24] and was later used in many research to include the GIC into the power flow of the network.

Considering a system with n buses for which m buses represent generator buses. The reactive power consumed by a load at bus i is expressed as $Q_{load,i}$. $Q_{loss,i}$ is the reactive power loss due to transformer saturation, at bus i on the HV side of the transformer. $Q_{Gen,i}$ represents the reactive power supplied by the generator. V_i, V_k are the bus voltages and θ_i, θ_k representing the voltage angle. Y_{ik} is the admittance between bus i and bus k. The admittance phasor angle is represented by α_{ik}.

At the generator bus,

$$Q_{Gen,i} - Q_{loss,i} - Q_{load,i} - \sum_{k=1}^{n} V_i V_k Y_{ik} \sin(\theta_i - \theta_k - \alpha_{ik}) = 0 \ , i = 1,2, \ldots . m \tag{2.2}$$

At the load bus

$$-Q_{loss,i} - Q_{load,i} - \sum_{k=1}^{n} V_i V_k Y_{ik} \sin(\theta_i - \theta_k - \alpha_{ik}) = 0 \ , i = m+1, \ldots . n \qquad (2.3)$$

Numerical methods are used to solve the power flow. At each iteration, the reactive power flow equation must be solved [5].

A system is said to be voltage stable if, for any bus, the increase in reactive power injection causes an increase in the bus voltage. The high demand for reactive power during GMD events leads to voltage stability issues, often leading to a voltage collapse [5] as in the Hydro Quebec blackout of 1989. The relationship between the reactive power consumption and the operating voltage of the system has been studied by many researchers using the common Q-V plot. Mkhonta *et al* [3] show the positive correlation between the absorbed reactive power and the voltage. Beyond the saturation voltage, there is a sharp increase in the gradient meaning that there is a greater demand for reactive power for the same change in voltage.

Weng *et al* [18] studied the effect of dc bias caused by GIC or HVDCs on the transformer reactive power and system voltage. They argue on the lack of mechanism analysis of the relationship between transformer, generator reactive capability limits and power system voltage under dc bias conditions. From their simulations, it was found that the reactive power increases on increasing dc injection. When the load reactive power increases, the load voltage will decrease to maintain the reactive power balance in the power flow according to static analysis. Weng *et al* noted a maximum decrease of steady state voltage of 9% when the reactive power demand is high [18].

2.1.1.1 Harmonic pollution

Harmonics are unwanted multiples of the fundamental frequency (50 Hz in South Africa) signals. When harmonics are present in a current or voltage signal, the latter is distorted. Fourier Analysis is used to find the harmonic content of current and voltage waveforms.

Voltage and current waveforms can be expressed in terms of the Fourier series;

$$v(t) = V_0 + \sum_{n=1}^{\infty} V_n \cos\ (n\omega t - \varphi_n) \qquad (2.4)$$

$$i(t) = I_0 + \sum_{n=1}^{\infty} I_n \cos\ (n\omega t - \theta_n) \qquad (2.5)$$

Harmonics are introduced by non-linear loads including transformers, due to their magnetic core and non-linear magnetic flux variation. Magnetic flux distortion and non-sinusoidal flux distribution across generator stator air gaps introduce fifth order harmonics into the power system [25].

In a transformer, the non-linear hysteresis curve causes distortion in the magnetising current with significant third order harmonic components present when operating in the linear region [12]. When operating in the non-linear region, the magnitude of odd harmonics increases and the transformer produces even harmonics. Significant harmonic distortion, unbalance and dc components are all simultaneously present when GIC flow in power systems [26]. A good harmonic analysis of power systems under GMD conditions is shown by Meliopoulos *et al.* [27].

During the March 1989 Hydro Quebec storm, voltage asymmetry (between positive and negative peaks of the voltage waveform) indicated the presence of even harmonics in transmission line currents. A direct correlation was found between GIC activity and second harmonic content in the voltage waveform [4]. Mkhonta *et al* [3] showed increased levels of Total Harmonic Distortion due to the generation of even and odd harmonics in a transformer saturating from GIC. In their analysis of the exciting current harmonics, Dong and Kappenman [22] showed that the fundamental and second harmonic currents are linear with GIC for all types of core design.

The presence of even and triplen harmonics [15] due to saturating transformers under GMD conditions causes mis-operation of relays and improper operation of breakers controlling SVCs and capacitor banks. In HVDC systems, GIC induce extra harmonics and distortion in the ac-side currents and voltages. These distortions affect the extinction angles and control schemes of inverters. Parallel resonance at the fourth and sixth harmonic frequencies also affect filters at low loading conditions. Core losses, winding losses in the transformer increase due to the extra current and harmonics and strong increase in noise levels [4][3][18][12][28] due to the asymmetric magnetising of the core occur during GIC flow. The flow of harmonic currents causes increased system losses as these harmonic currents experience higher impedances along their path in the transmission network. This is due to the skin effect whereby higher frequency components of current flow near the conductor surface. As a result, the effective area exposed of the conductor is reduced causing an increased impedance. This results in a reduced efficiency in the power transfer and hence a drop in the power factor.

2.1.1.2 Overheating of transformers

Normal leakage flux is controlled by non-magnetic shields within a transformer. The shield design is vital in controlling eddy current losses and heating [9]. Under normal conditions, flux flows through the magnetic core and the non-magnetic shields carry little flux leading to small losses. When the

transformer operates in the saturation region, the losses in some parts of the leakage flux increase causing localised heating [9]. Eddy current flow in the transformer tank and windings leading to overheating of the transformer.

The intensity of overheating depends on the saturation flux path, cooling of the transformer and loading. Overheating of the transformer leads to the breakdown of oil and paper insulation [3]. This can lead to the production of gasses. Thermal damage have been reported on transformers during the 2003 "Halloween Storm" whereby increased levels of dissolved gasses were measured in Tutuka and Matimba power stations [9].

Finite Element Modelling (FEM) methods are used to predict the hotspot temperatures. Experiments on the effects of GIC and temperature rise in transformers [3] proved that as the level of dc current is increased, the surface temperature of the transformer increases. This is due to the increased magnetising current leading to more losses and heating effects. Mkhonta *et al* [3] proved the inaccuracy of surface temperature measurements and propose that hot spot temperatures must be used instead as a measure of the heat content in transformers. Stray fluxes are blamed for the heating of transformers during GIC situations. Fig 7 of [3] shows that the windings experience the highest increase in temperature.

Price [16] analysed the effects of GIC on various transformer types and concluded that the construction and design of the transformer is important to reduce local heating. This is due to the K factor in the reactive power loss equation for different transformer types and core.

Excessive heat in the transformer leads to its degradation and reduced lifespan. Mitigation strategies need to be found to decrease these heating effects by using laminations in the transformer to reduce the eddy currents.

2.1.1.3 Impact on Generators

According to the 2012 NERC report [4], voltage imbalance and harmonic distortion caused by the saturating transformers during a GMD, can affect the generator. The primary side of generator step-up transformers are usually connected in delta. This prevents zero sequence harmonics and dc components or GIC to reach the utility side. However, increased positive and negative sequence harmonic currents can lead to generator heating due to the oscillating rotor flux [29]. The generator rotation causes the harmonics appearing on the rotor not to correspond to the stator harmonic order. Representing the harmonic number as n, for negative sequence harmonics, $n_{rotor} = n_{stator} + 1$ and $n_{rotor} = n_{stator} - 1$ for positive sequence harmonics.

Using measured harmonic data from SUNBURST, Gish *et al.* studied the rotor heating effects of GIC modelled as dc currents [29]. They found that negative sequence harmonic currents create a torque in the opposite direction of the field flux or rotor flux. Therefore, the overall useful flux produced by the generator is reduced and these conditions are worsened with imbalance that yields harmonics which do not follow the normal phase sequence. In such conditions, the second harmonic gains a positive sequence; the third and sixth harmonics both have a positive and negative sequence. The harmonic currents cause mechanical vibrations and erratic behaviour of generators mostly due to negative sequence components. A mathematical proof showing such torque pulsations, distorted armature flux and mechanical vibrations in a diesel generator is shown by Wang *et al.* [30]. Harmonic fluxes also induce currents on rotor damper bars. These currents can flow to the end-ring structures leading to concentrated ohmic heating of the rotor as illustrated in Figure 2.2. On round-rotor generators with damper circuits, the harmonic currents may flow through the bars to the end-ring structures leading to heating and rotor damage [29].

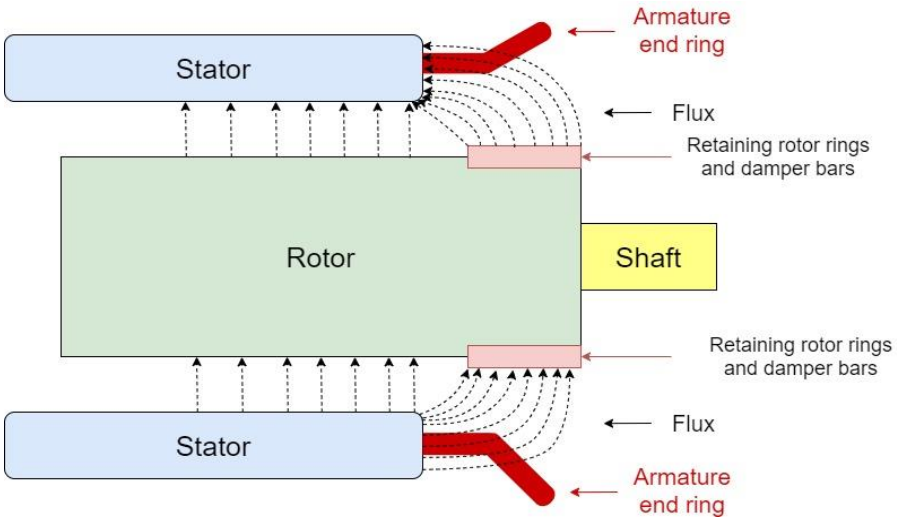

Figure 2.2: Sectional view of generator showing rotor retaining rings, damper bar placement, armature end rings and induced harmonic fluxes causing heating

Rezaei-Zare and Marti [31] use time-domain simulations to study the order and harmonic magnitudes affecting the generator. Different levels of GIC are used to show how the thermal capability limit of generators can be reached under moderate GIC levels (50 A/phase) as they generate increased levels of second, fourth and seventh harmonics. The thermal capability curve follows an inverse characteristic I^2t. The negative sequence capability of synchronous generators is proposed in IEEE Std C50.13 [32]. Rezaei-Zare and Marti point out that the IEEE Std C50.13 might underestimate the effect of even harmonics induced due to GIC activity. The authors use three single phase transformers to model a transformer bank without any considerations to system unbalance and non-conventional

harmonics. Therefore, their analysis does not cater for non-conventional harmonics observed by Gish *et al.* [29] which raises even more concerns on the current IEEE Std C50.13.

Walling *et al.* [33] show that three phase transformers exhibiting unbalance when GIC-saturated draw exciting current harmonics that do not follow conventional sequence component patterns. According to the 2012 NERC report [4], voltage imbalance and harmonic distortion caused by the saturating transformers during a GMD can affect the generator. Relays which are designed to respond to fundamental frequency unbalance may mis-operate due to the harmonic pollution.

In [34], Li and Zhang studied the effect of harmonics on a synchronous generator concluding that harmonics distort the armature voltage and current. Moreover, there is an increase in pole and armature energy loss within the generator. The fifth and seventh stator harmonic induced the sixth harmonic in the excitation current and increased the demagnetizing effect of armature reaction due to the inductive load.

Fan and Liao [35] investigated the impacts of flickers, harmonics and faults on synchronous generators. The authors also noted that the stator harmonics and rotor induced harmonics do not have the same order similar to Albertson *et al.* [36] and Gish *et al.*[29]. Moreover, the study by Fan and Liao shows the flow of damper winding current in the d and q axes due to harmonic fluxes. There is no mention of non-conventional harmonics induced due to system unbalance

Studying the impact of GIC on distributed generators, Abuhussein [37] shows an increase in generator reactive power output, decrease in generator terminal voltage and active power production when GIC is injected. The increased reactive power demand on the generators due to the saturating power transformers causes excitation system to increase their field currents beyond their limits. Without proper excitation control, generators may fail leading to a further reactive power and voltage problem. Weng *et al.* [18] highlight the need to include generator capability limits in simulations of the effects of dc bias on power transformers.

Zhang *et al.* [5] carried out a transient stability analysis of a 10k-bus synthetic electric grid exposed to GIC. The authors clearly showed the voltage transient and dip at the generator bus due to increasing levels of electric fields. A rotor angle transient of 425.7 degrees was reported due to GIC. This type of rotor angle deviation can lead to generator tripping as out of step protective relays may be activated.

2.1.2 GIC Modelling for Power System Analysis

The inclusion of GIC in the power flow was first described by Kappenman in 1981 [24]. In 1985, Lehtinen and Pirjola [38] developed the first software to model GIC. Their methods have mostly been used for space physicists and scientists. On the contrary, pioneers of the power industry focussed on

power system modelling software to model GIC [39]. Over the years, significant work has been done by many researchers in modelling realistic GIC for power system stability studies [11][13][19][10][5]. The 2012 NERC report [4] outlines the methods used in modelling GIC for power system analysis but use a dc approximation to represent the GIC. Boteler and Pirjola [40][39] show step by step methods to calculate the electric field induced from GMDs time series geomagnetic data. In the wait for the next peak in solar activity and possible geomagnetic storm, it is vital to accurately model realistic GIC profiles to allow planners and operators to design low cost mitigation strategies and operational procedures [4].

Currently, GIC are calculated using magnetic field data from observatories to calculate the induced electric field from a GMD. In power system analysis, the induced electric field magnitude has been conventionally modelled as a dc voltage in series with the transmission lines or ground. The Electric field is integrated over the length of the line and the GIC are then calculated using Ohm's law and admittance matrix.

2.1.2.1 Modelling induced electric field and voltage

According to Faraday's law of induction, the change in magnetic field induces an electric field as per the equation;

$$\nabla \times \vec{E} = -\frac{\partial \vec{B}}{\partial t} \tag{2.6}$$

E is the induced electric field on the Earth surface in V/m.

B is the magnetic field in Tesla (T).

$\frac{\partial \vec{B}}{\partial t}$ is the partial derivative acting on the B-field which represents the rate of change of the geomagnetic field.

Two methods have been proposed to represent the electric field in the power system. They can be represented as dc voltage sources in the ground, in series with the substation grounding resistance or as dc voltages expressed in terms of their Norton Equivalent, on transmission lines [13]. Only the transmission line approach can be used to represent non-uniform electric fields. Boteler and Pirjola [40] clearly identify the mathematical oddity in that uniform fields are not realistic since they do not go from 0 to infinity. Non-uniform electric fields including the angle between the electric field and transmission line are clearly better represented in power system software as quasi-dc voltages in series with the transmission line. Slow varying magnetic fields with small $\frac{\partial \vec{B}}{\partial t}$ result in an induced voltage

in the millihertz range which has favoured the modelling of the induced voltage as dc [4]. If instead, a low ac voltage source is used, the electric field angular variations can be modelled by changing the angle of the ac voltage source connected in series with the transmission line. In EMTDC software [41], dc voltage sources can be connected to the transmission lines. Some EMTP software [40] do not allow such connections.

The dc voltages induced in the transmission lines can be calculated using:

$$V_{dc} = \oint_{\mathcal{L}} \vec{E} \cdot d\vec{l} \tag{2.7}$$

$\vec{E}$ is the geoelectric field. $d\vec{l}$ is the incremental distance along the transmission line $\mathcal{L}$ path. According to the 2012 NERC report [4], it is assumed that the Electric field at the height of the transmission line is the same as the electric field on the surface of the Earth. If a constant electric field is assumed along the whole length of the transmission line, then only the end points of the transmission line are required. $d\vec{l}$ will then be equal to $\vec{\mathcal{L}}$. These distances can be calculated from transmission line length data or using the geographical coordinates of the end points.

Another method proposed in [4] computes the distance in the x and y directions independently. Then the dot product is expressed as follows;

$$\vec{E} \cdot d\vec{l} = E_x L_x + E_y L_y \tag{2.8}$$

E_x, L_x are the northward electric field and distance respectively.

E_y, L_y are the eastward electric field and distance respectively.

Knowing the latitude and longitude of the substations connected via the transmission lines, the values of L_x and L_y can be calculated as follows;

$$L_x = 111.2\ x\ \Delta lat \tag{2.9}$$

Δlat is the difference between the latitudes of the two substations.

$$L_y = 111.2\ x\ \Delta long\ x \sin(90 - \alpha) \tag{2.10}$$

$\Delta long$ is the difference between the longitudes of the two substations. The longitudinal separation of the end points assumes a spherical earth. To get more accurate values, precise Earth models are required [42] representing the curvature of the Earth.

$$\alpha = \frac{lat_{substation1} + lat_{substation2}}{2} \quad (2.11)$$

In the benchmark GMD event described by the NERC , the reference peak geomagnetic field amplitude E_{peak} was 8 V/km [19]. To accommodate for different geographical locations, a scaling factor is used on the value of E_{peak}.

$$E_{peak} = 8\ x\ \alpha_{sc}\ x\ \beta_{sc} \quad (2.12)$$

α_{sc} accounts for the geomagnetic latitude and is given by;

$$\alpha_{sc} = 0.001\ x\ e^{(0.115\ x\ lat)} \quad (2.13)$$

lat is the geomagnetic latitude in degrees.

β_{sc} accounts for the earth conductivity. Arbitrary values of 0.12 to 0.98 are used in [19] across high resistivity areas (areas of high igneous rock content).

2.1.2.2 Power system network modelling

The second step in calculating GIC is to derive an equivalent dc model of the network with the resistances of the generators, transformer windings and loads included. An example is shown in Figure 2.3. Only the dc winding resistances of transformers are modelled ignoring the reactances due to the low GIC frequencies [4][39]. Common transformer winding configurations used for GIC calculations can be found in Figure A8-3 of [4]. When the dc winding resistance is not available, the resistance of grounded wye two winding transformers can be approximated from the positive sequence resistance used in the power flow. The substation grounding resistance must also be included in the equivalent circuit. A common value used for the substation grounding resistance is 0.2Ω [4][43][13]. Typical measurement data from Western Cape substations provide a range of substation grounding resistances varying from 0.1Ω to 2Ω [19].

Shunt capacitors block dc flow and therefore do not have to be modelled in the equivalent circuit. Moreover, shunt reactors are decoupled from the dc network.

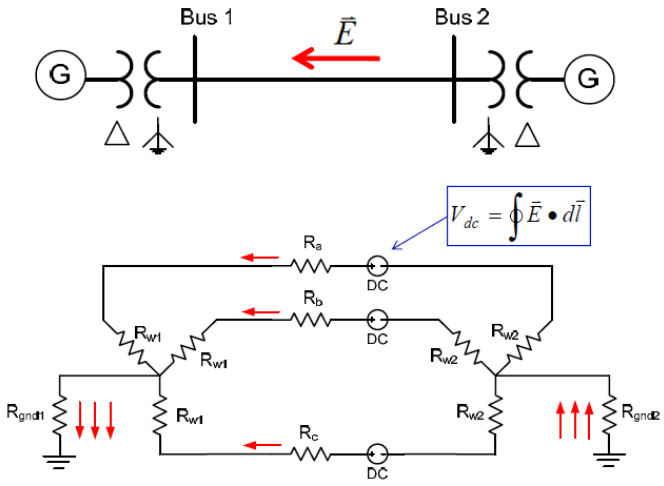

Figure 2.3: Modelling of GIC in power systems showing Geoelectric field induced from geomagnetic field variation during a GMD event and the induced dc voltage on the transmission lines [4]

The equivalent circuit is better analysed using nodal analysis. Hence, the voltage sources e, are converted into current sources j, in parallel with the transmission line admittance y_L. All resistances are converted into their admittance values. Using Kirchhoff's current law, the relationship between the nodal voltages, currents and the current sources at each node can be found. For a system of N nodes, the following equations can be developed for each node k;

$$j_k = i_k + v_k \sum_{n=1}^{N} y_{nk} - \sum_{n=1}^{N} v_n y_{nk} \tag{2.14}$$

v_k represents the voltage at node k and i_k represents the ground current at that node. Ohm's law can be applied as follows;

$$i_k = v_k y_k \tag{2.15}$$

Replacing i_k in the equation above yields;

$$j_k = v_k y_k + v_k \sum_{n=1}^{N} y_{nk} - \sum_{n=1}^{N} v_n y_{nk} \tag{2.16}$$

Two methods are proposed to calculate the GIC flowing in the network. These include the Nodal Admittance Matrix (NAM) method and the Lehtinen-Pirjola (LP) method.

Using the NAM approach, the nodal voltages are calculated as follows;

$$[V] = [Y]^{-1}[J] \tag{2.17}$$

$[J]$ represents the current injection vector calculated from the sum of all current courses at that node.

$$J_k = \sum_{n=1}^{N} j_{nk} \tag{2.18}$$

$[Y]$ is a square matrix with each element representing the power system's admittance values and has the following properties.

1. The elements of $[Y]$ are three phase values calculated from the line resistances r_L.
2. Since GIC flow in the neutral, $[Y]$ is augmented to include substation neutral buses and grounding resistance values.
3. Transmission lines with series capacitive compensation are not considered since series capacitors prevent dc current flow.
4. Transformers are modelled with their winding resistance to the substation neutral. For autotransformers, both the series and common windings are represented.

The nodal voltages in $[V]$ can then be used to calculate the currents to ground (GIC) at each node. Using the LP method to calculate the GIC yields similar results to the NAM method. Combining (2.14) and (2.15) yields;

$$[I^e] = ([1] + [Y^n][Z^e])^{-1}[J] \tag{2.19}$$

$[I^e]$ consists of GIC values at each node within the network.

$[1]$ is the identity matrix. The matrix $[Y^n]$ is calculated as follows;

$$Y_{kk}^n = \sum_{n=1}^{N} y_{nk}\,, n \neq k \tag{2.20}$$

$$Y_{kn}^n = -y_{kn} \tag{2.21}$$

$[Z^e]$ is the earthing impedance matrix. The nodal currents and voltages are related as follows;

$$v_k = \sum_{n=1}^{N} Z_{kn}^e i_n \tag{2.22}$$

$[J]$ is similar to the NAM method.

Examples on these calculations are shown in [39].

2.1.2.3 GIC dynamics

Over the years, it has been common practice to model electric fields arising from GMDs as dc voltages in series with the transmission lines or in the neutral. If magnetic field data from observatories are used to model GIC, then the standard cadence of the geomagnetic field samples become important. If a 1 sample/min measurement rate is used, then delays in GIC growth in the order of seconds are not significant [39]. However, if 1 sample/s measurement rate is used, then, with power systems operating on high X/R ratios, the power system time constants in the order of few seconds can have significant effect on the higher frequency components of GIC.

With 10 min to 1 min GIC data cadence, short term GIC dynamics were not observed. Motivations for the dc assumption gained merit due to the assumed slow GIC dynamics. With 1 s or 10 s data cadence, GIC profiles show significant dynamics with rapid transients, fast rise times in the order of seconds and magnitudes that can be positive or negative. GIC get involved in power system dynamics as additional constant current reactive loads which alter the reactive power balance of the transient stability model [5] [10].

Typical GIC profiles have also been estimated for example, in the PSE&G Salem GSU during the K9 GIC event on March 13, 1989 [44]. More recently, the IEEE Std C57.163 – 2015 [45] provided examples of GIC profiles from measured data and calculated data from magnetic field measurements. The reader is referred to Figure 11 in the standard which shows a GIC profile over a 4-minute interval. The GIC profile clearly shows the dynamic behaviour of GIC which can have both positive and negative magnitudes. Moreover, there are instances where the GIC is instantaneously zero. In [46], Figures 1, 2 show the occurrence of geomagnetic pulsations from measured GIC on 22 June 2015. Looking at such typical GIC profiles, one can clearly see that GIC have non-negligible short-term dynamics. Such dynamics need to be modelled in power system studies to show the true dynamic response of network equipment to GIC [11]. The dynamics of GIC comes into play due to the non-uniform and varying nature of the induced electric fields. The severity of the GMD is often attributed to the rise time, decay time, magnitude and duration of the geoelectric fields [10]. Smaller rise times and high magnitude GIC pose a threat to the short-term voltage stability of the power system. . Small rise time means short time for GIC to reach its amplitude which equals to a faster saturation and increased reactive power demand leading to V drop [18]. On the other hand, slow and low magnitude GIC have the least impact on power systems since the response of power system equipment are fast-acting. Overbye *et al.* [11] indicate that generator dynamic models and excitation systems are able to track fast rise in GIC since it is believed that their time constants are small enough. As mentioned

earlier, GIC can have significant dynamics on a shorter time frame within seconds, which can therefore affect the small-time constants of network equipment.

A real geomagnetic storm is characterised by a spectrum of frequencies. Oyedokun *et al.* [6] showed that GIC frequencies of highest densities (dominant GIC band) lie below 50 mHz. B_x and B_y components are the dominant magnetic field components in both hemispheres driving GIC in power systems. The rate of change of GIC is a function of the rate of change of the B-field components. Frequency and $\frac{dB}{dt}$ measurements usually taken at 1- or 10-minute intervals fail to capture short term GIC dynamics such as geomagnetic pulsations which can drive significant GICs besides sudden storm commencements, sub storms and impulsive events [46]. Pc5 and lower frequency pulsations drive significant GICs over long periods of time at mid-latitudes. Sustained pulsations are quasi-ac and cannot be represented as dc. Pc5 pulsations having a period of 150 – 600 s are 'continuous' type pulsations with durations of 10-20 minutes, commonly seen in the auroral oval. Pulsation like disturbances and large measured GIC values (120 A at node) were noted in the Kola peninsula during 28-29 June 2013. On 6-7 April 2000, Pc5 pulsations with a period between 5 to 8 minutes were identified in the Finnish power system. Pc5 pulsations during 2003 Halloween storm had periods around 255 and 295 s corresponding to 3.38 mHz to 3.92 mHz frequencies. In the Hydro-Quebec blackout of March 1989, 6 mHz Pc5 pulsations with significant amplitude were observed for about an hour. During the recovery phase of the Halloween storm, Pc5 pulsations were noted in the USA and Czech pipelines [46].

Wavelet analysis is a useful and effective tool to extract the magnitude and frequencies of GIC over different time scales. Such analysis have been used in [47] to study the energy content of GIC. Figure 4.3 from another wavelet analysis [48] showed that the rate of change of frequency is independent of the degree of change in GIC amplitude. Large fluctuations in the GIC time series corresponded to where the GIC has the greatest amplitude and were referred to burst regions. High magnitude GIC with relatively low frequencies (1-4 mHz) appear to persist for longer than high magnitude GIC with relatively larger frequencies (5-10 mHz) during such burst periods. High magnitude GIC usually associated with frequencies between 0.5 mHz to 5 mHz. Typical frequencies for burst periods in the range of 0.6 to 7 mHz.

From these recent studies, it is clear that GIC modelled as dc is no longer valid. There is a need to accurately model more representative and realistic GIC for power system impact analysis.

2.2 Voltage Stability

Power system stability refers to the ability of an electric grid to maintain an operating equilibrium under normal operating conditions and to regain an acceptable state of operating equilibrium after being subjected to a physical disturbance, with most system variables bounded so that the entire system remains intact [49] [50] [51].

The classifications of power system stability have been proposed in [49] and [50] and include;

- Physical nature of the resulting mode of instability (frequency, voltage or rotor angle)
- Size of Disturbance (Large & Small Disturbance Stability)
- Time Span of Disturbance (Long term & Short-Term stability)

In April 2020, a more recent classification of power system stability in systems with high penetration of power electronic convertors was proposed [51]. This is shown in Figure 2.4.

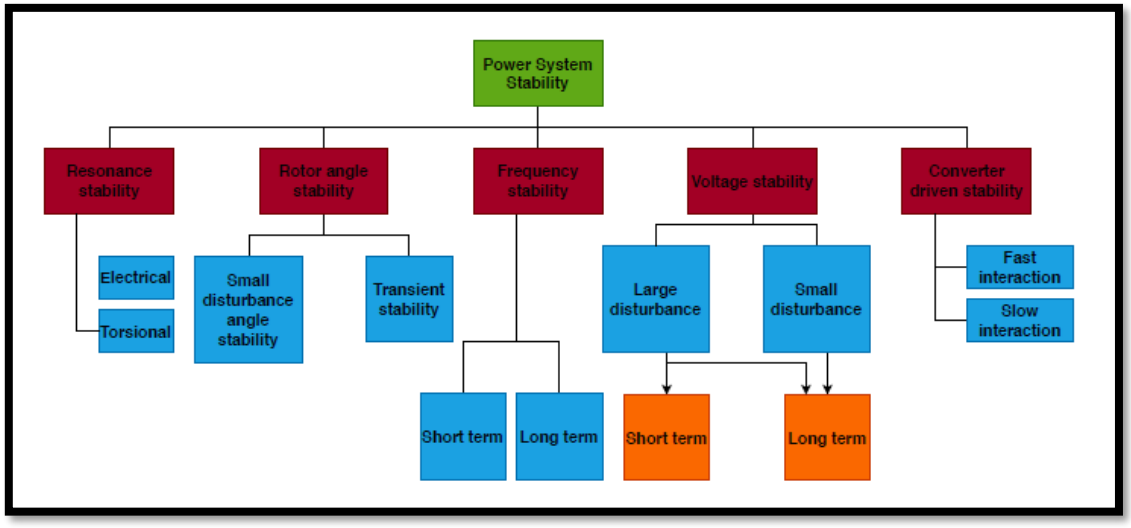

Figure 2.4: Classification of Power System Stability

More specifically, voltage stability refers to the ability of a power system to maintain steady voltages at all buses in the system after being subjected to a disturbance from a given initial operating condition. It depends on the ability to maintain or restore equilibrium between load demand and synchronous generator supply [49]. The main cause of voltage instability is the inability of the power system to meet the non-active power requirements. Synchronous generators are the main source of non-active power. Due to the increased non-active power demand, synchronous generators need to be over-excited to generate more power. If the generators reach their field current or armature current limits imposed by the capability curves, the bus voltages in the network decrease due to a lack of non-active power

According to IEEE and CIGRE [49], small disturbance voltage stability refers to the ability of the power system to maintain steady bus voltages when subject to small perturbations such as incremental changes in system load. The disturbance is considered small enough that the system dynamic equations can be linearized [49][50]. Instability can be caused by a steady increase in generator rotor angle due to lack of synchronizing torque or rotor oscillations with increasing amplitude due to lack of enough damping torque

Overbye *et al*. frame the power flow analysis under GMD conditions as a small disturbance voltage stability assessment [11]. They use PV and QV curves to show the reduction in voltage stability margins and maximum loadability limit due to GIC. Their study highlights the importance of load characteristics and sensitivity on the small disturbance voltage stability of a particular 5 bus system under GIC conditions.

To study the small signal stability, the power system must be modelled in terms of the state space matrices. The behaviour of a dynamic system such as a power system, may be described by a set of first order non-linear ordinary differential equations of the following form;

$$\dot{\boldsymbol{x}} = \boldsymbol{f}(\boldsymbol{x}, \boldsymbol{u}) \tag{2.23}$$

$$\boldsymbol{u} = \begin{bmatrix} \boldsymbol{u_1} \\ \boldsymbol{u_2} \\ \boldsymbol{\dots} \\ \boldsymbol{u_n} \end{bmatrix} \tag{2.24}$$

$$\boldsymbol{y} = \boldsymbol{g}(\boldsymbol{x}, \boldsymbol{u}) \tag{2.25}$$

$\boldsymbol{x}$ is the column vector referred to as the state vector. The elements of the state vector are the state variables of the system. Any set of linearly independent variables may be used to describe the state of a system. State variables may be physical quantities such as angle, speed, voltage.

$\boldsymbol{u}$ is another column vector representing the input to the system. These are external signals that affect the system performance.

$\boldsymbol{y}$ is a column vector representing the outputs of the system.

The equilibrium points are the points where all the derivatives are simultaneously zero. The equilibrium point must satisfy the equation $f(x_0) = 0$. A linear system has only one equilibrium state. For a non-linear system such as a power system, there may be more than one equilibrium point.

The small signal stability analysis of a system can be analysed in various degree of detail in [50] by increasing the complexity of the generator model. The base case is the classical model of a generator with the voltage behind synchronous reactance representation. The complexity of the state space model increases as the effects of field dynamics, excitation system and power stabilizers are added. These additional control loops increase the number of states in the state space representation.

In a multi-machine system, small signal stability issues may either be local or spread around the power system. Local instability involves only a small part of the power system, for example, due to rotor oscillations of a generator (local plant mode oscillations) or group of generators (inter-plant mode oscillations) close to one another. Local plant mode and inter-plant mode oscillations have frequencies between 0.7 to 2.0 Hz. Instability on a local scale can also be caused by excitation system controls, SVCs and power electronic equipment [50]. On the other hand, global stability involves a large group of generators interacting together creating inter-area oscillations. Oscillations of a group of generators in one area swing against another group of generators in a different area in the power system. Inter-area oscillations can take two forms based on the frequency.

Exciters and load characteristics have a major impact on the stability of inter-area modes. An important note from [50] reads;

"*The manner in which excitation systems affect interarea oscillations depends on the types and locations of the exciters and on the characteristics of the load*."

Large-disturbance voltage stability refers to the system's ability to maintain steady voltages following large disturbances such as system faults, loss of generation, or increased loading [49].Determination of large-disturbance voltage stability requires the examination of the nonlinear dynamic response of the power system over a period of time sufficient to capture the performance and interactions of such devices as motors, underload transformer tap changers, and generator field-current limiters [49]. Large disturbance voltage stability can be analysed using transient stability analysis and time domain simulations as shown in [11].

If voltage stability is classified in terms of the time duration of the disturbance, then short-term voltage stability and long-term voltage stability are assessed separately. Overbye *et al*. [11] frame the GIC problem at the boundary between the definitions of short term and long-term voltage stability. Short-term voltage stability involves dynamics of fast acting load components such as induction motors, electronically controlled loads, and HVDC converters [49]. The study period is in order of several seconds. The analysis of short-term voltage stability involves solutions to differential equations modelling the dynamics of the power system including load dynamics, LTC dynamics or exciter dynamics [51].

Long-term voltage stability involves slower acting equipment such as tap-changing transformers, thermostatically controlled loads, and generator current limiters [49] [51]. The study period is in order of several minutes requiring long term simulations. Instability in this case, is caused by a long-term loss of equilibrium. This could be for example due to post disturbance small signal instability or when loads try to restore their power beyond the capability of the transmission network and generation [49].

Transient stability analysis is used to assess short-term voltage stability and with appropriate additional models such as generator over excitation limiters and LTC dynamics, can be used to assess most aspects of long-term voltage stability as well [11].

Two methods have been proposed by Kundur [50] to analyse voltage stability of power systems. These include the static and dynamic analysis. Hasani *et al*. [52] compare these 2 approaches using static PV/QV curves and dynamic time domain simulations. The authors clearly show an appreciation for the dynamic approach which provides a more accurate and realistic power system performance compared to static approaches. They also highlight the effectiveness of time domain simulations to determine the chronology of events leading to voltage collapse. Contrarily, Morison *et al.* [53] are more in favour of the static approach being less computationally intensive. These two approaches are explained in the next Sections.

The static approach captures system conditions or snapshots of events, approximating stages along a time domain trajectory. Derivatives of state variables are assumed to be zero so that the power system equations reduce to purely algebraic equations. Different tools are used to assess the static voltage stability. These include PV or QV curve analysis, Load flow analysis, Lyapunov method and others.

2.2.1 Static analysis - PV and QV curves

Static analysis techniques often use P-V and Q-V curves whereby the loading is increased at a bus and the real power, reactive power and bus voltage are measured. PV curve defines two terms namely the operational margin and maximum margin. The operational margin refers to the point at which the PV curve crosses 0.9 pu voltage which represents a 10% voltage drop. The maximum margin lies at the nose point on the PV curve where a further increase in active power results in a decrease in bus voltage. With the QV curve approach, the proximity to voltage collapse can be determined. The non-active power compensation required to prevent a run-down situation can be computed from QV curve analysis. The nose point of QV curves represents the reactive power martin. When the QV curve reaches a stationary point, the stability limit is reached. The V-Q sensitivity at a bus is often used to assess the voltage stability of a system. The elements of the Jacobian matrix give the sensitivity of power with bus voltage changes.

Tigere *et al*. [54] used PV and QV curves for static voltage stability analysis of a 4 bus system under GIC conditions. A dc injection circuit with different magnitudes of dc was used to model the GIC. The active power and reactive power were measured at the load bus. PV and QV curves were generated. It was shown that the maximum power transfer is reduced when GIC flow in power systems. The authors also generated QV curves to show the positive reactive power margin which corresponds to the amount of reactive power required to maintain bus voltages at acceptable levels.

VQ curves can be superimposed with generator reactive power capability curves in order to see the generator limits usually corresponding to the lowest point on the VQ curve. As the power system operating point moves to the bottom of the VQ curve, voltage instability is approached. The amount of reactive power compensation required can be evaluated in such cases to determine operating reserves for future planning. The problem with the PV and QV curve approaches is that it does not consider all the buses in the power system. Consequently, only selected buses can be evaluated for voltage stability. Failure to study the most vulnerable buses can lead to inaccurate results. Moreover, the iterative load flow computation is time consuming and requires high computational performance if a large power system is analysed. While static voltage stability analysis provides useful information on the proximity to a collapse, such analysis do not show the power system dynamic response to GIC [55].

2.2.2 Dynamic Analysis

A power system is a highly non-linear system made up of slow acting devices and fast acting devices. The dynamics associated with these devices need to be accurately modelled to improve power system stability analysis. Dynamic voltage stability is concerned with the voltage collapse mechanism and the interaction between the different power system components leading to the continuous decline in bus voltages. The disturbance can also be of a dynamic nature whereby it fluctuates with time. This is typical of GMD dynamics as described in Section 2.1.2.3. The time constants associated with different power system equipment are also important to understand the time response of the network.

Time domain simulations are used for dynamic voltage stability analysis. At each simulation time step, the computer program solves the power system differential algebraic equations. This method of analysis is the most accurate replication of the actual dynamics pertaining to voltage instability [53]. The complexity of time domain simulations lies in the computational efforts of the CPU and the time taken for the simulations. In this regard, dynamic approaches tend to be less suitable compared to static approaches, although dynamic approaches give a better insight of the voltage collapse phenomenon. Chowdhury and Taylor [56] compare the V-Q power flow simulation and dynamic simulations for a 500kV transmission system. The authors prove that, while the QV approach can

show voltage instability, time domain dynamic simulations show the mechanism of the voltage collapse and interaction between power system components. A worthy concluding note favours the use of time domain simulations when stability depends on the switching time of excitation system control elements and load tap changer action.

Mathematically, dynamic voltage stability can be assessed by using the overall power system equations expressed as a set of first order differential equation.

$$\dot{\boldsymbol{x}} = \boldsymbol{f}(\boldsymbol{x}, \boldsymbol{V}) \tag{2.26}$$

The algebraic equations are represented as follows;

$$\boldsymbol{I}(\boldsymbol{x}, \boldsymbol{V}) = \boldsymbol{Y_N V} \tag{2.27}$$

$\boldsymbol{x}$ is a vector with states of the system. $\boldsymbol{V}$ is a vector of bus voltages. $\boldsymbol{I}$ is a vector of current injections at the buses. $\boldsymbol{Y_N}$ is the network admittance matrix.

The above equations can be solved in the time domain using Numerical integration methods and power flow analysis.

2.2.3 Voltage Collapse

Voltage collapse is a sequence of events accompanying voltage instability which lead to a blackout or abnormally low voltages in a significant part of the power system [49][50][57]. When the non-active power demand increases, for example due to additional heavy loads connected to the system or during transformer saturation by GIC, generators and var compensators must supply this additional load. If there is sufficient reserve for non-active power, then voltage stability will be maintained. However, if generators are at their limits, their terminal voltage will drop leading to a run-down situation of bus voltages and eventually a voltage collapse.

With intentional or unintentional tripping of some load, steady operation of the system at low voltages can still be maintained after transformer tap changers reach their boost limits. This in turn depends on the small signal stability of the power system.

As discussed earlier, thermostatic controls, action of motor slip adjustment, distribution voltage regulators and tap changers tend to restore the power consumed by loads after a disturbance, [49]. This increases the burden of non-active power on the HV network causing further voltage reduction. The voltage instability is further complicated due to the increased power flow through the transmission network over its limit. In this case, the surge impedance loading of the line and X/R

characteristics determine the power transfer. Extreme cases of voltage instability or sudden peak demands in non-active power cause generators to reach their field and armature time overload capability limits. A sudden change in voltage stability is observed when the excitation limit of the generators is reached. This sudden onset of instability is attributed to the change in the algebraic manifold of the dynamic system when the Q-limit is reached [57].

2.2.3.1 Prediction of voltage collapse

Monitoring of voltage levels only cannot be used as an indicator of voltage stability [58]. The proximity to voltage collapse and mechanism of voltage collapse are critical factors to be considered when predicting a collapse [50].

Bifurcation theory shows that power systems have a stable and unstable equilibrium point which lie in close proximity along the system trajectory [55][59][53][60]. If the post-disturbance equilibrium is unstable, the system can suffer from a voltage collapse. Two bifurcations have commonly been recognised as the main mechanism of voltage collapse. These include the saddle node and Hopf bifurcations. A system becomes unstable under a Saddle Node bifurcation if one of the eigenvalues of the system becomes zero. In the case of an Hopf bifurcation, a pair of complex conjugate eigenvalues cross the imaginary axis on the s plane moving in an unstable state. The state variables such as bus voltages and frequencies change continuously leading to voltage collapse. Bifurcations may also appear due to the action of fast exciters which cause induced oscillations.

There are several indices developed during the years for predicting voltage collapse.

Yang *et al*. [61] define a Voltage Deviation Index (VDI) to represent the bus voltage deviation compared to 1 pu voltage for an N-bus system. In [62], Huang *et al* test the accuracy of the L-index to determine the dynamic voltage collapse of the WSCC 9 bus system. From their results, the authors found that, for step changes in load, the L-index proved that the dynamic voltage collapse loading was less than the steady state loadability point.

In 2002, Balamourougan *et al.* [58] published a paper providing a technique for online prediction of voltage collapse. The authors derived a voltage collapse prediction index (VCPI) using only the voltage phasor at each bus in the system and the network admittance matrix. The power margin was derived by Julian *et al* [63] in year 2000 and used to track the closeness to voltage collapse using apparent power. It is defined as the power difference between the maximum apparent power and the actual power.

The voltage collapse proximity indicator (VCPI) is derived based on a 2-bus system. A set of four voltage collapse prediction indicators are developed using the power transfer limits. Chaithra *et al*.

[64][65] used the VCPI to predict a voltage collapse situation in their simulations. The authors conclude that the VCPI is the fastest and simplest way to predict the early vulnerability of voltage collapse. Moreover, both steady state and dynamic stability can be determined using VCPI.

Nizam *et al* [66] compare the different voltage stability indices including their own Power Transfer Stability Index (PTSI) to predict a voltage collapse. They conclude that the PTSI, Voltage Collapse Prediction Index (VCPI) and power margin give faster and more accurate predictions of the voltage collapse than the L-index. A commendable effort was made by Danish *et al*. [67] to compare 40 voltage stability indices based on their formulation, performance and application. The list of indexes including their calculations and references can be found in Table 1 from [67]. While most voltage stability indices agreed to one another, many indices were in total disagreement. The contradictory performances highlight the inaccuracy in predicting the voltage collapse point. Also, because of the singularity of the Jacobian at the collapse point, the load flow does not converge. Hence, system behaviour beyond the voltage collapse point cannot be predicted. Nevertheless, time domain simulations provide a clearer picture of the voltage collapse scenario. The authors recommend that the choice of voltage stability/collapse index for a particular study depends on the network topology, the desired application and overall performance.

2.3 Generator Excitation Systems

Synchronous generators are the workhorses of the grid, generating power to supply loads. The active power output of a synchronous generator is limited by its input mechanical power from a turbine or governor system. The non-active power output of the generator is controlled by the field current which is supplied by an excitation system. When power transformers partially saturate due to the flow of GIC, their non-active power demand increases. An overexcited generator can generate more non-active power to support the system voltage in such cases. Hence, excitation systems must be able to provide enough field current to cater for the increased demand. The excitation control system should be able to maintain safe operation of the generator within its capability limits and enhance the voltage stability of the power system. In this Section, the components of the excitation system are explained including their modelling for power system stability analysis. The dynamic performance of the excitation system is also discussed for its application to dynamic voltage stability analysis.

The basic function of the excitation system is to provide direct current to the synchronous machine field windings and automatically adjust the field current to maintain terminal voltage. The excitation system control elements take care of voltage control, reactive power flow control, safe operations of the generator and therefore has an impact on voltage stability.

Figure 2.5 shows a block diagram of the components within an excitation system.

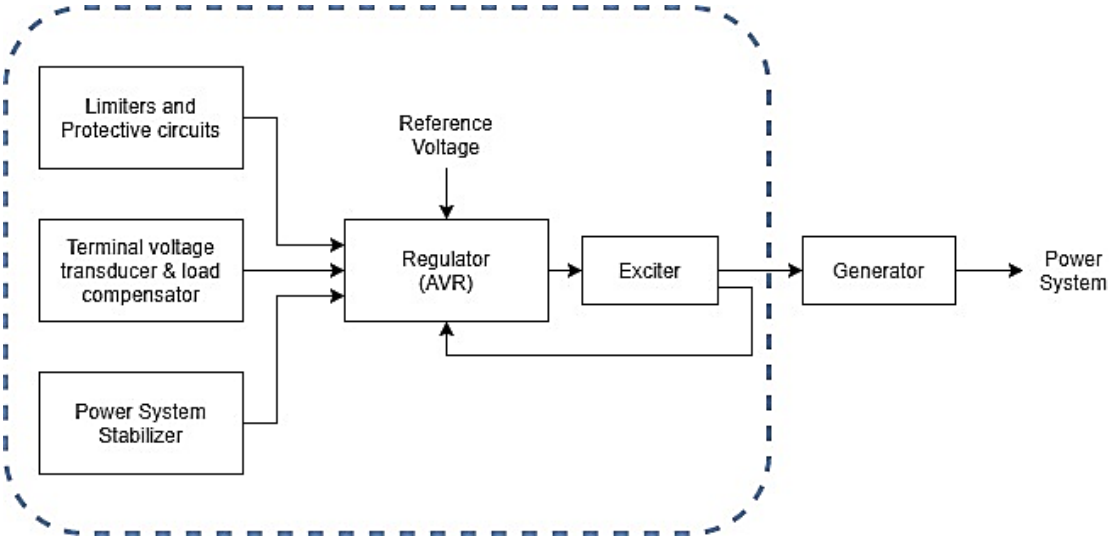

Figure 2.5: Block Diagram of Generator Excitation System

The exciter provides dc current to the field winding of the synchronous machine constituting the power stage of the excitation system. The regulator processes (Rate feedback & lead-lag compensation) and amplifies input signals to a level appropriate for controlling the exciter. The terminal voltage transducer and load compensator senses the generator terminal voltage, rectifies and filters it to a dc quantity which is compared to the desired terminal voltage. In addition, reactive power compensation may be provided if it is desired to keep the voltage constant at some point from the generator terminal (for example between the generator and generator step-up transformer). The PSS provides an additional input signal to the regulator to damp power system oscillations. Protective circuits and limiters ensure that capability limits of the exciter and field are not exceeded. The need to include these components in voltage stability studies has been outlined in many research works [10][53].

2.3.1 Types of Excitation Systems

Three types of excitation systems are defined according to IEEE Std 421.5-2016 [68];

2.3.1.1 DC Excitation System

DC excitation systems provide direct current supplied by a separate dc generator, to the rotor or field windings of the synchronous generator using slip rings. The dc generator may be self-excited or separately excited. When separately excited, the exciter field is supplied using a permanent magnet generator [50].

DC excitation systems have been superseded by ac exciters in the mid-1960s after being in use for over 40 years [50]. The issue with dc Excitation systems lies in the complexity of voltage regulators

which are made up of conventional non-continuous acting rheostatic types to more complex rotating amplifiers.

2.3.1.2 AC Excitation Systems

AC Excitation Systems use alternators and rectifiers to produce the field current needed by the synchronous generator. The ac output of the alternator is rectified using controlled or non-controlled rectifiers. These rectifiers can be rotating or stationary. The type of rectifier arrangement is often used to differentiate between different AC excitation systems. Loading effects of such exciters are significant. They do not allow the supply of negative field current with the exception of type AC4C [68].

2.3.1.3 Static Excitation Systems

Static Excitation Systems supply the excitation current directly to the field windings on the synchronous generator using slip rings. Two common types of static excitation systems used; Potential-Source controlled rectifier excitation systems or Compound-Source rectifier excitation systems. These two types of ST excitation systems differ in the way the transformers, rectifiers and generator stator windings are connected as discussed in [50] and [69].

AC and ST excitation systems are the most common ones used in today's power systems.

2.3.2 Control and Protective Functions

Figure 2.6 shows the functional block diagram for a synchronous machine excitation system including the control, limiting and protective functions to ensure safe operation of the generator. Excitation systems may include only some or all the functions depending on the requirement of the power system.

The figure also shows the interdependency between the different functional blocks of the excitation system. For example, the protection and control functions such as the Under-Excitation Limiter (UEL) and Over-Excitation Limiter (OEL) serve as inputs to the excitation control elements. Electrical parameter values such as $V.I$ and Q are fed back from the synchronous machine and power system to the excitation controllers and limiters. These protective devices use the electrical parameters to compute the output values fed to the excitation control elements.

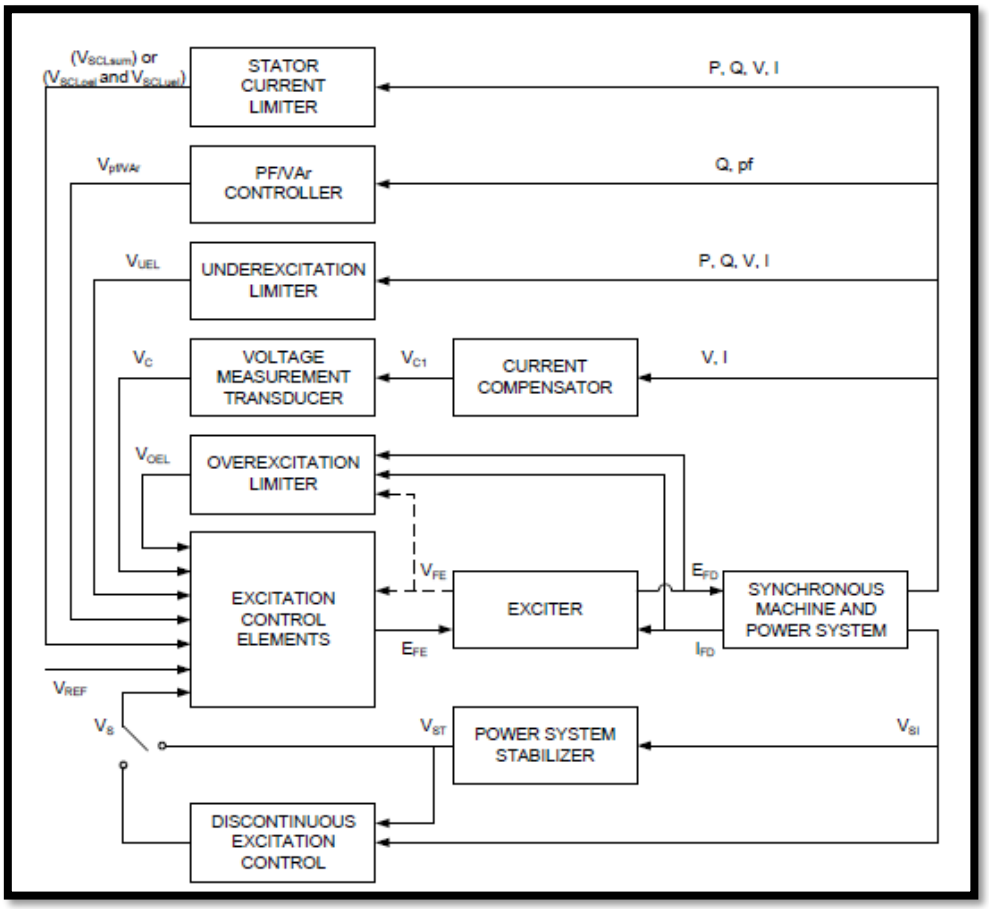

Figure 2.6: Functional Block Diagram of Synchronous machine excitation system [68]

2.3.2.1 AC/DC Regulators

The excitation control block consists of the AC and DC Regulators. The main function of the AC regulator is to maintain the generator stator voltage. The DC regulator controls the field voltage of the synchronous generator. In the event of a faulty AC regulator, the DC regulator can be manually controlled to produce a desired field voltage. Some excitation systems include automatic setpoint tracking [50] used to detect the required field voltage level and make automatic adjustments.

2.3.2.2 Stabilising circuit

Excitation control system stabilisation including series or feedback compensation is used to improve the dynamic performance of the control system. Often, elements within the excitation system have significant time delays causing an increased phase shifts between electrical signals. The impact of stabilising circuits is to reduce these phase shifts. Based on the type of excitation system, the control loop parameters can be varied to match the desired performance.

A derivative feedback compensation is shown in Figure 2.7.

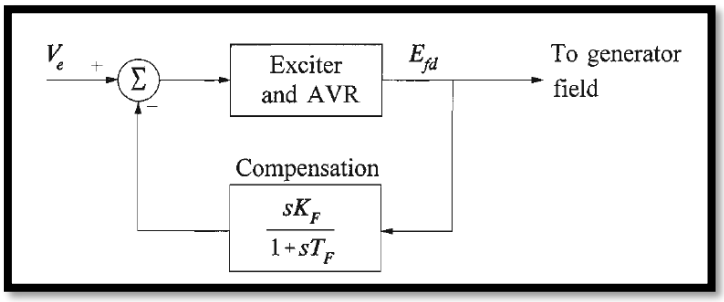

Figure 2.7: Derivative feedback compensation for excitation control systems [50]

2.3.2.3 Wind up and Non-Windup Limits

Excitation limits can be of 2 types namely;

1. Windup limit whereby the output is limited as long as the measured output exceeds the limit specified. This is the worst case scenario for the excitation limiter [57].
2. Non-Windup limit whereby output is constrained if the measured output exceeds the limit specified and the derivative of the output is greater than 0. Hence the windup limit performs one more computation to analyse the rate of change of the output. If the output increases or decreases indicated by the positive or negative derivative, then the output comes off the limit on a change of sign [57].

2.3.2.4 Terminal Voltage Sensing

The voltage across a synchronous generator terminal is sensed using a voltage transducer and usually reduced to a dc quantity [50][68]. For modelling purposes, the voltage transducer is represented by a single equivalent time constant T_R.

2.3.2.5 Power System Stabilizer (PSS)

Power system stabilizers (PSSs) use auxiliary signals to improve the dynamic performance of the power system by adding damping to system oscillations. They are used to improve the small signal stability of power systems.

2.3.2.6 Load compensator

Excitation systems offer several types of compensation including droop compensation and/or line drop compensation [68]. Synchronous machine active and reactive current compensation are the most common. Load compensation is used to control a voltage at a point within or external to the generator. Figure 2.8 shows an illustration of the load compensator within the AVR control loop.

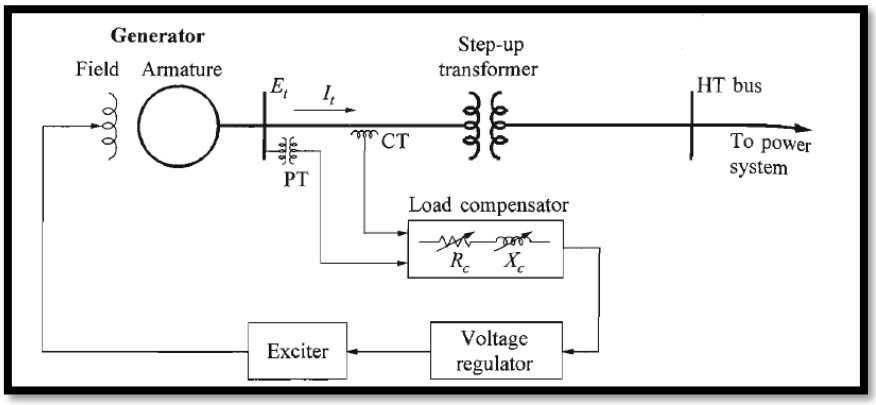

Figure 2.8: Improved AVR loop with load compensator [50]

The AVR controls the terminal voltage of the generator. The load compensator has a variable resistance and inductive reactance which simulates the impedance between the stator terminals and the point where the voltage is being regulated. The volt drop across the load compensator is then added or subtracted from the generator terminal voltage resulting in a compensated voltage fed to the AVR.

When the compensator regulates voltage at a point within the generator, the compensation is referred to as droop compensation. R_c and X_c are positive. When R_c and X_c are negative, the compensator regulates voltage at a point beyond the generator terminals. This form of compensation is called line drop compensation and is used to compensate for the voltage drop across the step up transformer [50].

2.3.2.7 Limiters

Under-excitation limiter

The Under-Excitation Limiter (UEL) is used to ensure that the generator is excited to a level where small signal stability limit and the core end-region heating limits are not exceeded. The input to the UEL can be the stator voltages and currents or the active and reactive power from the generator terminals. A reference signal is used as the limiting signal. Some UELs operate on the differential signal from the AVR. Proper coordination between the UEL and the loss of excitation relay is vital to ensure that the small signal stability limit and the core end region heating limits are respected [50].

If the inputs to the UEL are the stator voltages and currents, then the limit imposed follows a circular path as shown in the P-Q curve in Figure 2.11. On the other hand, if the inputs to the UEL are the active and reactive power, then the limit imposed follows a linear trajectory [50].

Over-excitation limiter

The role of the OEL is to prevent overheating of the generator due to excessive current in the field windings. The OEL is often referred to as the maximum excitation limiter (MXL) as in [50]. The operation of the MXL is explained in the dynamic analysis performed by Morison *et al*. [53]. When the field current exceeds the high setting of the MXL, the current is ramped down without a time delay to its continuous limit. When the field current exceeds the continuous limit but below the high setting, the current is ramped down to its continuous limit after a time delay depending on the level of field current and settings of the MXL.

Two types of time delays are used namely a fixed time delay and an inverse time delay. The fixed time limiters operate when the field current exceeds the pickup value for a fixed set time, irrespective of the degree of overexcitation. The inverse time limiters operate with the time delay matching the field thermal capability.

Stator-winding limiter

The armature windings may heat up due to excessive currents or harmonics flowing through them. The stator current limiter prevents excessive heating of the armature windings and therefore the power output of the machine is limited.

2.3.3 Generator capability curve and limits

The presence of limiters implies that the field current is bounded between defined values and so is the power output. In this Section, the relationship between generator's output power, supplied field current from the excitation system and machine reactance will be developed.

Using θ to represent the power factor angle, the per unit complex power output S, from the SM can be written as follows;

$$S = P + jQ = \widetilde{V_t} * \widetilde{I_t^*} = |V_t||I_t| \, (\cos\theta + j \sin\theta) \qquad (2.28)$$

The magnitude of the armature current is $|I_t|$. In the PQ plane, the armature current limit is represented by a circle, centred at the origin, with radius equal to the MVA rating of the machine.

The field current i_{fd} and field winding resistance R_{fd} cause heating in the rotor given by ${i_{fd}}^2 R_{fd}$ and impose another limit on the generator outputs.

With the d-axis reactance X_d equal to the q-axis reactance X_q and both equal to the synchronous reactance X_s, the equivalent circuit shown in Figure 2.9 can be used to find the relationship between the machine terminal voltage, current and the effective internal voltage E_q. E_q is the excitation voltage

due to the field current. X_s accounts for the flux produced by the stator currents (armature reaction) and R_s is the stator winding resistance. δ_i is the load angle which has a direct impact on the maximum active power transfer.

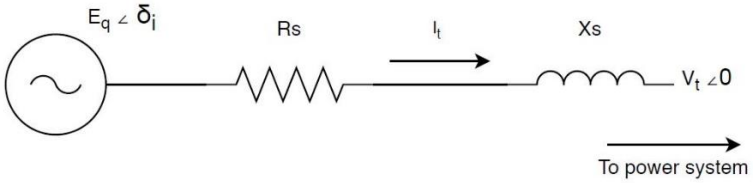

Figure 2.9: Steady state equivalent circuit of synchronous generator (saliency ignored)

$$E_q = V_q = V_t + (R_s + jX_s)I_t \tag{2.29}$$

The armature resistance R_s is usually very small and can be neglected. The corresponding phasor diagram is shown in Figure 2.10, where θ represents the power angle and X_{md} is the d-axis magnetising reactance of the synchronous generator illustrated in the IEEE1110 proposed d-axis equivalent circuit of the synchronous machine.

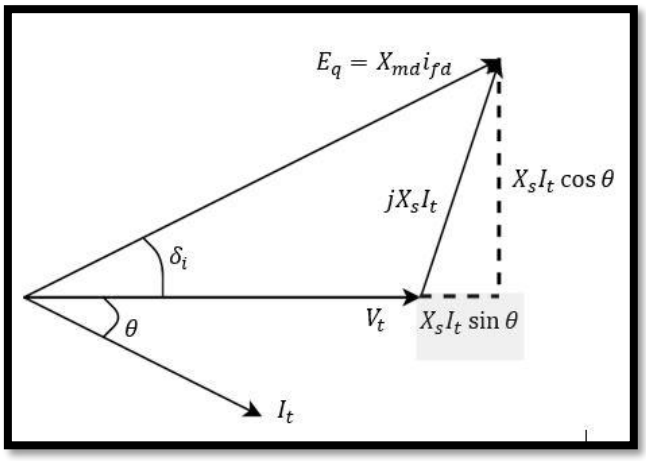

Figure 2.10: Phasor diagram of synchronous machine used for deriving power output of generator as a function of field current and machine synchronous reactance

Equating components along and perpendicular to the phasor $\widetilde{V_t}$ yields;

$$X_{md} i_{fd} \sin\delta_i = X_s I_t \cos\theta \tag{2.30}$$

$$X_{md} i_{fd} \cos\delta_i = V_t + X_s I_t \sin\theta \tag{2.31}$$

Solving for I_t gives,

$$I_t \cos\theta = \frac{X_{md} i_{fd} \sin\delta_i}{X_s} \tag{2.32}$$

$$I_t \sin\theta = \frac{X_{md} i_{fd} \cos\delta_i - V_t}{X_s} \tag{2.33}$$

Therefore, the output active and reactive power of the generator is given by;

$$P = V_t I_t \cos\theta = V_t \frac{X_{md} i_{fd} \sin\delta_i}{X_s} \tag{2.34}$$

$$Q = V_t I_t \sin\theta = V_t \left(\frac{X_{md} i_{fd} \cos\delta_i - V_t}{X_s}\right) \tag{2.35}$$

The relationship between P and Q for a given field current is a circle centred at $\frac{-V_t{}^2}{X_s}$ on the Q-axis and with $\frac{X_{md}}{X_s} i_{fd} V_t$ as the radius. From the equations above, it can be observed that both P and Q are directly proportional to i_{fd} and δ_i. It is also important to note the inverse proportionality of the synchronous machine reactance X_s and the output powers.

The restraints imposed on the generator by rotor and stator winding limiters define stable and unstable operating regions of the generator. This is commonly represented on the capability curve of the generators as shown in Figure 2.11.

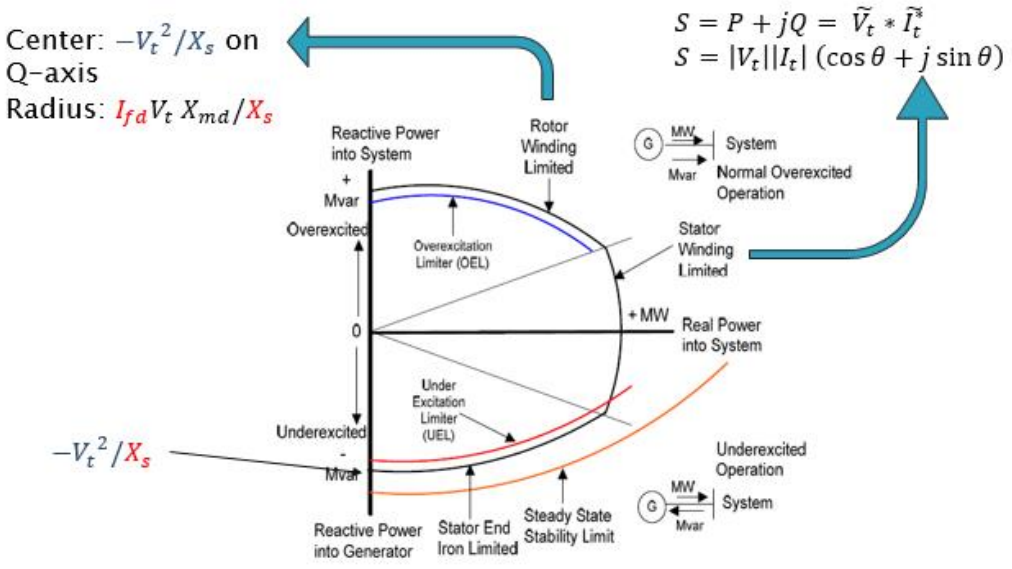

Figure 2.11: Generator power capability curve with limits imposed by excitation system control

2.3.4 Models of Excitation Systems

The importance of proper modelling of excitation systems has been highlighted by many authors studying Geomagnetic Disturbances. Since one of the goals of this project is to find the role of excitation systems in mitigating GIC, the modelling of the Excitation System (EXS) is explained in this Section.

As shown in Figure 2.12, the principal input signal to each of the excitation systems is the output V_c of the voltage transducer. At the first summing point, the signal V_c is subtracted from the reference voltage V_{ref} and the output V_S of the Power System Stabilizer (PSS). Additional signals such as the under-excitation limiter output V_{UEL} can also come into play. Under steady state, V_S is 0 [50].

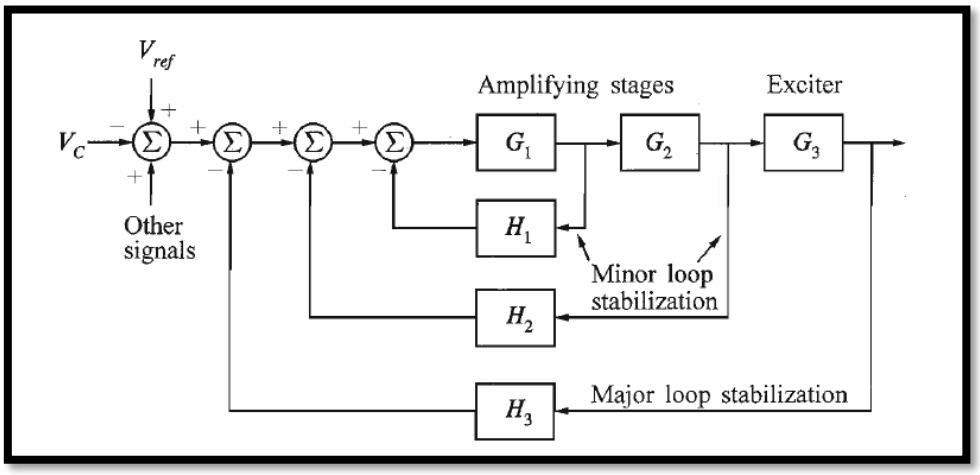

Figure 2.12: Control system in block diagram form for excitation system

In 1992, IEEE introduced standard models of excitation systems to provide a guide on their operation and modelling required for power system analysis. Modifications to the original standard for recommended practice for Excitation System models were made in two attempts and published in 2016 under the IEEE421.5-2016 Standard [68]. The document provides a summary (See tables 1,2 and 3 from [68]) of the changes and evolution in the modelling and design of the excitation systems from the original IEEE421.5 – 1992 to the IEEE421.5 – 2005 version and finally the new 2016 version of the standard. Detailed modelling of each type of Excitation System is presented and explained in terms of their application in power system stability [68].

According to the standard, the models proposed are valid for small signal stability, transient stability, short term voltage stability as defined by the IEEE/CIGRE Joint Task Force [49]. The models still need modifications for long term simulations of their dynamic performance since delayed protective and control functions are not represented in the IEEE models. The IEEE excitations systems are also compliant to IEEE Standard 1110 [70] and IEEE Standard 115 [71] which outline synchronous

generator modelling and performance. The AC excitation system models given in IEEE421.5 Standard will be discussed in the sub-section that follows. Note that the IEEE421.5 – 2016 models are very similar to the 2005 models with addition of excitation system limiters.

2.3.4.1 IEEE421.5 Standardised AC Excitation system models

2.3.4.1.1 *AC1A/AC1C excitation system*

The AC1A excitation system is shown in Figure 2.13. IEEE421.5 – 2016 uses a different name for the AC1A excitation system, calling it the AC1C instead. The latter differs from the AC1A in the fact that it includes excitation current limiters unlike the AC1A excitation system. Both AC1A and AC1C represent a brushless exciter. The dc output of the rotating rectifier is fed directly into the field winding of the generator. It uses an ac alternator which drives the non-controlled diode rectifier to produce the field voltage required by the synchronous machine. The exciter field is supplied by a pilot exciter with permanent magnet rotor. The voltage regulator controls the ac exciter field which in turn controls the field current of the main generator.

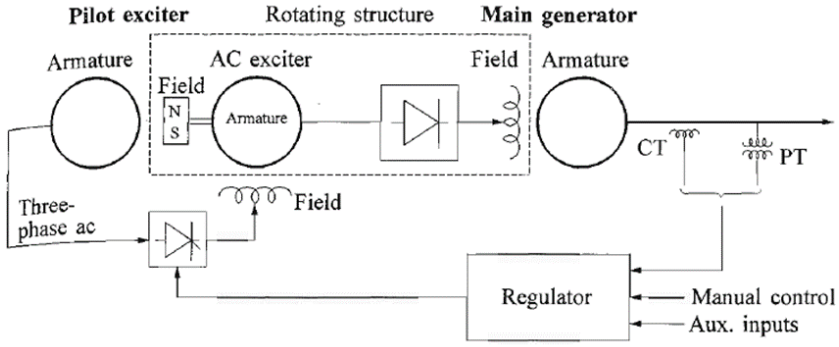

Figure 2.13: Components of AC1A excitation system

A block diagram representation of the AC1A excitation system is shown in Figure 2.14. This type of representation is usually used in Control System theory for frequency domain analysis. Using the block diagrams of the AC1A excitation system, a transfer function can be derived that relates the inputs to outputs.

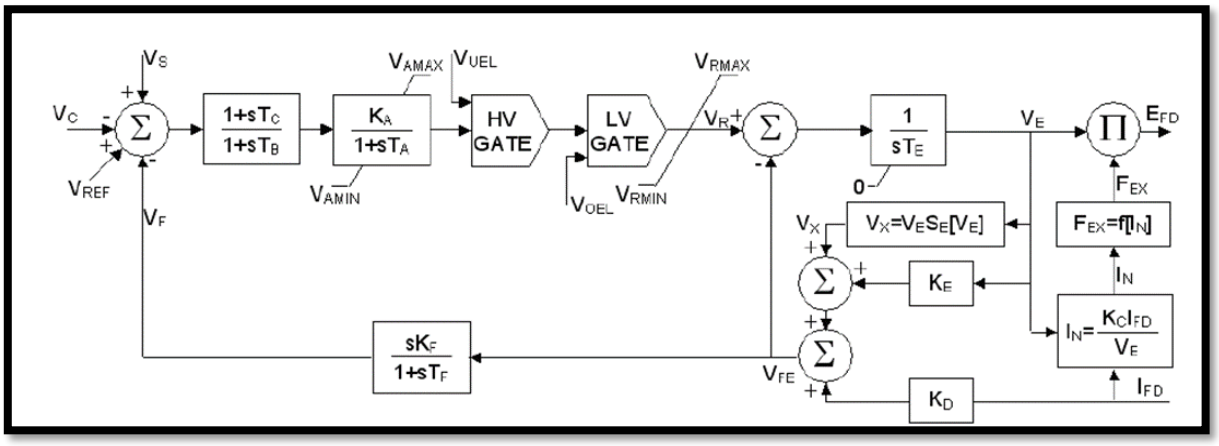

Figure 2.14: Block diagram of IEEE421.5 – 2005 AC1A excitation system

Usually, a low pass filter block $\frac{1}{1+sT_R}$ precedes the first summing junction. It represents the delay in measuring the terminal voltage V_t of the synchronous machine, with s denoting the Laplace operator and T_R representing the measurement time constant. The measured terminal voltage after compensation V_c is compared with a reference voltage V_{ref} to generate the error voltage which is applied to the voltage regulator. T_C and T_B are the time constants of the first order system representing a lead lag compensator. The voltage regulator acts as an amplifier of input signals to the exciter and has a gain K_A and time constant T_A. V_{AMAX} and V_{AMIN} are the voltage regulator internal limits. V_{UEL}, V_{OEL} represent the voltage signal from the Under-Excitation Limiter (UEL) and Over-Excitation limiter (OEL). V_{Rmax} and V_{Rmin} are the exciter field voltage limits.

The dynamics of the exciter are modelled as shown in Figure 2.15. The exciter is modelled using two gain blocks namely the exciter gain, K_E and demagnetising constant K_D. K_D is the demagnetizing factor, a function of exciter alternator reactance. It accounts for the demagnetising effect of the stator current due to lagging power factor loads. This demagnetising effect is commonly known as the armature reaction. K_C is the gain representing the rectifier loading factor proportional to the commutating reactance. The time constant for the exciter is T_e. The output is the field voltage E_{fd} which is applied to the generator field winding. The feedback loop or damping filter is used to improve the dynamic response of the exciter by reducing excessive overshoot. This feedback loop is modelled with a gain K_F and time constant T_F.

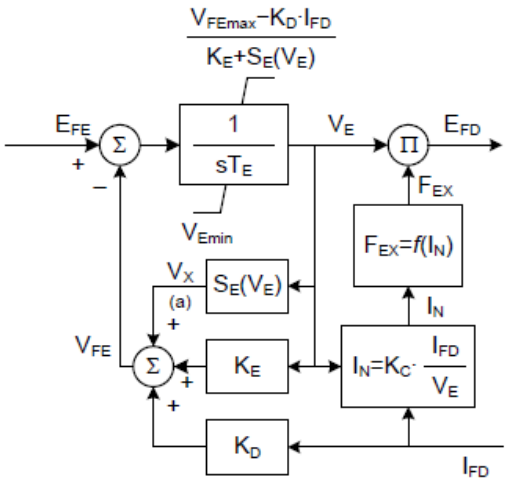

Figure 2.15: AC rotating exciter with non-controlled rectifiers

As mentioned earlier, Figure 2.14 and Figure 2.15 will be used to derive a transfer function relating inputs (V_{ref}, V_C, V_S) of the excitation system to its output which is the field voltage E_{fd}. Starting from Figure 2.15;

$$V_{FE} = K_D I_{FD} + [K_E + S_E(V_E)]V_E \tag{2.36}$$

$$E_{fd} = V_E F_{EX} \tag{2.37}$$

$$V_E = \frac{V_R - V_{FE}}{sT_E} \tag{2.38}$$

Replacing (2.38) into (2.37) gives;

$$E_{fd} = \frac{V_R - V_{FE}}{sT_E} F_{EX}, where\ F_{EX} = f(K_C \frac{I_{fd}}{V_E}) \tag{2.39}$$

Replacing expression for V_{FE} from (2.36);

$$E_{fd} = \frac{V_R - K_D I_{FD} - K_E V_E + S_E(V_E)V_E}{sT_E} F_{EX} \tag{2.40}$$

From the first summing junction in the AC1A block diagram representation, the following expressions can be derived;

$$V_R = (V_{ref} - V_C - V_F + V_S)(\frac{1 + sT_C}{1 + sT_B}) \frac{K_A}{1 + sT_A} \tag{2.41}$$

Also, the feedback loop gives the following expressions;

$$V_F = \left(\frac{sK_F}{1+sT_F}\right)V_{FE} \tag{2.42}$$

Replacing expression for V_R and V_F in the equation for E_{fd} yields;

$$E_{fd} = \frac{(V_{ref} - V_C - \left(\frac{sK_F}{1+sT_F}\right)V_{FE} + V_S)(\frac{1+sT_C}{1+sT_B})\frac{K_A}{1+sT_A} - K_D I_{FD} - K_E V_E + S_E(V_E)V_E}{sT_E} F_{EX} \tag{2.43}$$

Equation 2.43 shows the relationship between the inputs V_{ref}, V_C, V_S of the AC1A excitation system, parameters such as gain and time constant and output field voltage E_{fd}. The maximum field voltage or ceiling voltage can be calculated by using the upper limits of the non-windup and windup limiters.

2.3.4.1.2 *AC4A/AC4C excitation system*

The AC4A excitation system is shown in Figure 2.16. It represents an alternator supplied controlled rectifier excitation system. The dc output of the stationary rectifier is fed into the field winding of the generator using slip rings. The regulator directly controls the dc output voltage of the exciter by controlling the firing of the thyristors. The exciter field is supplied by self-excitation and uses an independent static voltage regulator to maintain its output voltage. The AC4A responds faster since the thyristors directly control the exciter's output. Unlike other AC exciters, the AC4A allows for negative field forcing.

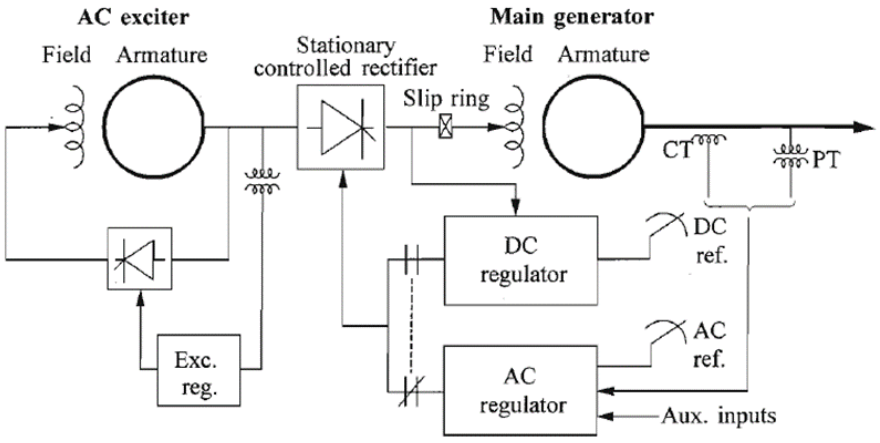

Figure 2.16: Components of AC4A excitation system

A block diagram representation of the AC4A excitation system adapted from IEEE421.5 – 2005 is shown in Figure 2.17. The summing junction is similar to the AC1A but without the feedback loop. A lead-lag network provides stabilization. The rectifier operation is limited to mode 1 region. The ac regulator automatically maintains the synchronous generator's terminal voltage at a desired value

corresponding to the reference voltage. The overall gain and time constant associated with the firing of thyristors are accounted by K_A and T_A respectively.

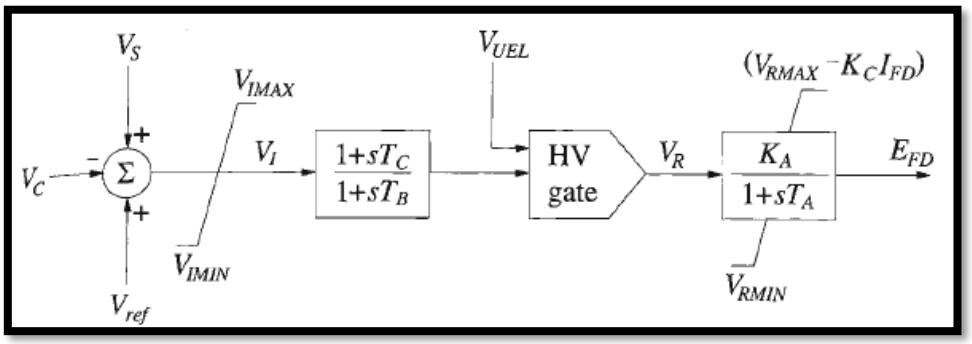

Figure 2.17: Block diagram of IEEE421.5 – 2005 AC4A excitation system

Again, the transfer function relating the inputs V_{ref}, V_C, V_S and output E_{fd} will be derived from the block diagram of the AC4A excitation system.

From the first summing junction and the load compensator block, an expression for V_R follows;

$$V_R = (V_{ref} - V_C + V_S)(\frac{1 + sT_C}{1 + sT_B}) \tag{2.44}$$

The voltage regulator block amplifies V_R to generate the field voltage E_{fd} according to;

$$E_{fd} = \frac{K_A}{1 + sT_A} V_R = \frac{K_A}{1 + sT_A} (V_{ref} - V_C + V_S)(\frac{1 + sT_C}{1 + sT_B}) \tag{2.45}$$

2.3.4.1.3 *IEEE type AC5A excitation system model*

Figure 2.18 shows the block diagram representation of the AC5A excitation system. The latter is a simplified model of the brushless excitation system. The regulator is supplied from a permanent magnet generator [72]. Unlike the AC1A and AC4A exciters, the AC5A uses loaded rather than open circuited exciter saturation data.

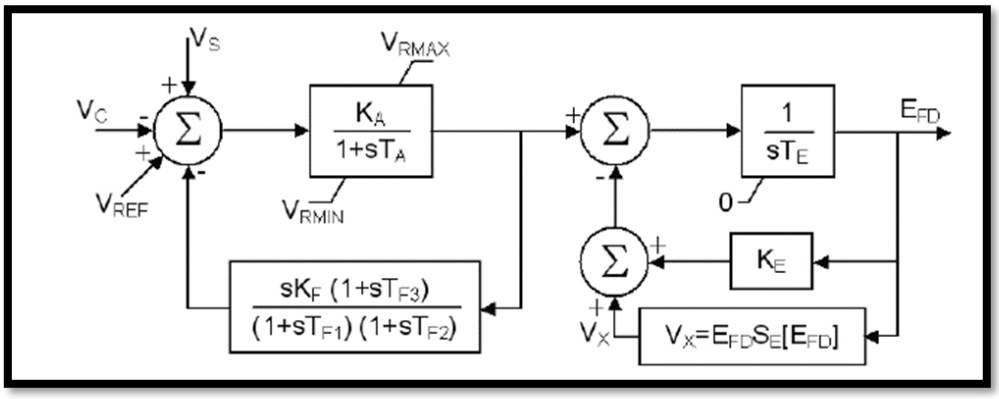

Figure 2.18: Block diagram of IEEE421.5 - 2005 AC5A excitation system

Again, the transfer function relating the inputs V_{ref}, V_C, V_S and output E_{fd} will be derived from the block diagram of the AC5A excitation system. From the first summing junction;

$$V_R = (V_{ref} - V_C - V_F + V_S)(\frac{K_A}{1 + sT_A}) \tag{2.46}$$

From the feedback loop,

$$V_F = \frac{sK_F(1 + sT_{F3})}{(1 + sT_{F1})(1 + sT_{F2})}\, V_R \tag{2.47}$$

Replacing V_F in the expression for V_R;

$$V_R = (V_{ref} - V_C - \left[\frac{sK_F(1 + sT_{F3})}{(1 + sT_{F1})(1 + sT_{F2})}\, V_R\right] + V_S)(\frac{K_A}{1 + sT_A}) \tag{2.48}$$

At the second summing junction after the voltage regulator,

$$V_R - \left[K_E E_{fd} + E_{fd} S_E(E_{fd})\right] = V_E \tag{2.49}$$

The exciter produces the field voltage using V_E

$$E_{fd} = V_E \frac{1}{sT_E} \tag{2.50}$$

Combining (2.49) and (2.50)

$$E_{fd} = V_R - \left[K_E E_{fd} + E_{fd} S_E(E_{fd})\right] \frac{1}{sT_E} \tag{2.51}$$

Replacing (2.48) into (2.51) yields;

$$E_{fd} = (V_{ref} - V_C - \left[\frac{sK_F(1+sT_{F3})}{(1+sT_{F1})(1+sT_{F2})}\, V_R\right] + V_S)(\frac{K_A}{1+sT_A}) - \left[K_E E_{fd} + E_{fd} S_E(E_{fd})\right]\frac{1}{sT_E} \quad (2.52)$$

Using the transfer functions of the different excitation systems, the relationship between synchronous generator parameters and excitation system parameters can be appreciated.

2.3.4.2 Excitation system parameters

The standard parameters applicable to most excitation systems are summarised in Table 2.2.

Table 2.2: Summary of typical excitation system parameters

EXS Block	Parameters and Signals
Rectifier	T_R
AVR	K_A, T_A
AVR Limits	V_{min}, V_{max}
Lead/Lag AVR compensator	T_1, T_2
Exciter	K_E, T_E, K_D
Reference voltage	V_{ref}
Terminal voltage	V_t
Field Voltage and Current	E_{fd}, I_{fd}
Saturation	$A, B\ where, S_E = AE_{fd}(e^{B.E_{fd}})$
Power System Stabilizer	PSS
Under-Excitation Limiter	V_{UEL}
Over-Excitation Limiter	V_{OEL}

In [73], the genetic algorithm (GA) was applied to classify parameters of the excitation system and synchronous generator into three groups; parameters effective on voltage (EOV), effective on active power output (EOP) and parameters that do not affect any of these two and are neutral (NEU). The parameters serve as inputs to the GA which computes the errors in voltage and active power. The GA then tries to minimise these errors to find the sensitivity of the parameters to the voltage, active power or non-of the two quantities. Figures 6 to 9 from [73] show the sensitivity analysis of the synchronous generator parameters including the excitation system parameters. The results of the iterative GA are summarised in Table 2.3.

Table 2.3: Classifying synchronous generator and excitation system parameters in terms of their effects on Voltage, Active Power and parameters which show no effect

	EOV	EOP	NEU
Excitation system parameters	$K_a, T_a, K_f, K_e, T_e\ A, B$	-	T_f, T_r
Synchronous Generator parameters	X_d, X_q, X'_d	$X''_d, T'_{d0}, T''_{d0},$	X''_q, T''_{q0}

From Table 2.3, it is clear that the voltage regulator gain K_a, exciter gain K_e , saturation constants and feedback control gain K_f, are effective on voltage. The outcome of the study from Zaker *et al.* [73] can be used to run a sensitivity analysis of the effect of these parameters on the voltage dip caused by GIC. In fact, a 2019 paper by Oyedokun and Scheit [74] showed how some of these parameters can have huge effect in reducing the voltage dip caused during GIC conditions. They propose a holistic approach to parameter optimization to understand which parameters have the most impact of reducing the effects of GICs.

Vournas *et al.* [75] use the concept of the Routh array and gain margin to determine excitation parameter values for which the generator dynamic stability becomes marginal. They define a stable and unstable region in the space of the dominant EXS parameters [75]. A first order excitation system is considered initially and the Routh array criterion is used to define the stable and non-stable regions. For every value of T_e, there is a maximum value K_e to operate in the stable region. The limiting value of K_e is found by applying the Routh Array criterion on the characteristic equation of the generator and exciter model. Violating the limiting value of K_e causes the roots of the characteristic equation to move to the right side of the complex plane showing oscillatory instability. Vournas *et al* also propose the concept of the gain margin to study the dynamic stability region for higher order systems such as the 4th order excitation system. For a constant voltage regulator gain K_a, values of T_a are provided. The gain margin is calculated for each time constant and a plot of the two quantities is formed. The shape of the stability is not affected by the order of the excitation system. The stability margin is however increased as the order of the EXS is raised. The findings of their study imply that there exists a stable operating point and an unstable operating point for each parameter of the excitation control system. It appears that operating close to the unstable region might cause instability of the power system if subject to a disturbance.

2.3.5 Dynamic Performance of Excitation system

Since the excitation system model is non-linear, its dynamic performance can be classified into large signal performance and small signal performance. With the generator offline, the stability of the excitation system alone can be assessed using the large signal and small signal analysis.

For large signal performance measures, the excitation system's ceiling voltage is specified as the maximum dc voltage that it can supply. Higher ceiling voltages tend to improve the transient stability of a power system. The ceiling voltage for a static excitation system is defined at the specified supply voltage and current. For rotating exciters, the ceiling voltage is found at the rated speed. The excitation system's voltage response time is the time in seconds the excitation system to attain 95% of the difference between the ceiling voltage and the rated load field voltage. An excitation system with a voltage response time of less than 0.1s is considered to show a high response and is fast acting. Usually, high initial response systems reach the ceiling voltage via the nominal response path and are therefore more efficient.

The small signal performance of the excitation system is used to analyse the response of the closed loop EXS control system when small changes to system conditions are imposed. The time response and frequency response plots serve as tools to analyse the small signal performance.

Figure 2.19 shows some indices used to describe the voltage response.

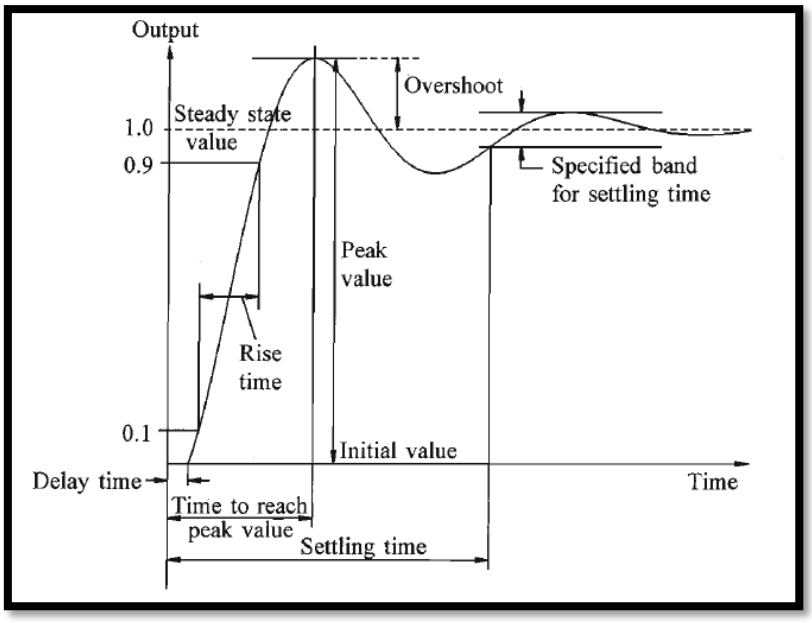

Figure 2.19: Time domain Response of closed loop system due to a unit step input used to assess the small signal stability or steady state stability [50]

The frequency domain involves the concept of the gain margin. Performance is determined from the low frequency gain, cross over frequency, phase margin and the gain margin. High values of these performance evaluation indices are associated with fast and more stable excitation system control. In the closed loop frequency response plot, the bandwidth and the peak value M_p are the two parameters of interest. A high value of M_p results in an oscillatory system with a large overshoot in the transient response.

Clearly, the dynamic performance of the excitation system depends on the nominal response plot and can be analysed in both the time domain and frequency domain.

2.3.6 Effects of Generator Excitation Systems on Voltage Stability

Generator AVRs are the primary control devices used to maintain the voltage between acceptable limits. During normal operating conditions without any faults or disturbances, the generator terminal voltage is maintained constant at a reference value (usually 1 pu). Under GIC conditions, the non-active power demand increases as discussed in Section 2.1.1.1. The high var demand on generators may exceed their field current and armature current limits. The field current is limited by the over-excitation limiter (OEL) and under-excitation limiter (UEL). As highlighted in 2.3.3, these limits define the power capability curve of the synchronous generator. With an increased non-active power demand beyond the generator capabilities, the field voltage is retained at its maximum reference value. Consequently, the generator terminal voltage can no longer be held constant and voltage stability is disturbed.

The PV curve shown in Figure 2.20 is used in [50] to show the effect of an excitation system on the voltage stability. The study was carried out by exciting the generator to its limit.

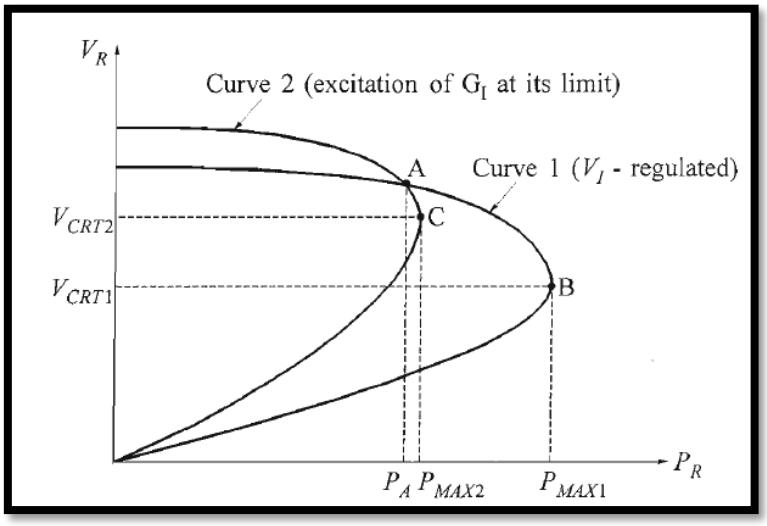

Figure 2.20: PV curve to assess the Impact of loss of voltage regulation from AVR on voltage stability [50]

The point A is more stable on Curve 1 than on Curve 2 since curve 1 provides a greater loadability limit (point B) than curve 2 (point C). The analysis shows that, if the excitation of the generator is at its limit, the loadability of the network is reduced and the critical voltage at which collapse occurs is higher than if the excitation is within limits.

Heydeman *et al*. [60] used the saddle node bifurcation and the Hopf bifurcation to assess the impact of a slow exciter and fast exciter with hard wind-up limits on the voltage profile of a power system.

From the small signal voltage stability analysis, it was found that fast exciters with hard windup limits led to sustained oscillations in the voltage due to the interaction of excitation controls at the Hopf bifurcation point. From the study, it is clear that the rate of change of the reactive power demand of the load and the dynamics of the excitation system are directly relatable to the concept of voltage collapse. When a GMD occurs, the rise time, duration and magnitude of the geoelectric field need to be considered since the reactive power demand varies with these parameters. The excitation system field dynamics has a direct impact on the reactive power output dynamics of the generator and therefore, the overall grid.

Chowdhury and Taylor [56] included models of OELs in their dynamic simulations on stability. Soft limiters were imposed instead of hard limits, possibly to counter the effect of sustained oscillations as reported by Heydeman [60]. Chowdhury discusses the different OEL models which differ in the way they ramp down the excitation field current. Some OELs instantaneously decrease the field current due to overexcitation whereas others use a ramp decrease. Some OELs also define a ramp rate as a function of the amount of overexcitation.

2.3.7 Effects of the Automatic Voltage Regulator (AVR)

Crow identified the need to include the effects of the excitation system limits and the Automatic Voltage Regulators (AVRs) in the study of power system stability [57]. Accurate modelling of excitation system components is vital in this regard. Power systems operate at different operating points, based on the loading level and system conditions. These operating points can be stable or unstable, that is, the states of the dynamic system can lie within a stable equilibrium point or an unstable equilibrium point. Bifurcation occurs when one of the states of the system changes the dynamic structure of the system. The states of the system usually move along a trajectory until equilibrium is reached. If the equilibrium is stable, the states and hence power system's response will be stable. If the equilibrium is unstable, then, the power system will be unstable. Crow uses a trajectory analysis to investigate the action of the AVR on the terminal voltage stability when the AVR reaches the voltage regulator limit following a bifurcation point. Crow's findings show that corrective actions by the AVR causes the system states to pass by an unstable equilibrium point before being attracted to the stable equilibrium point. When the system passes through the unstable equilibrium point, voltage collapse may occur. Initially, without any change in load, the state variables lie within a stable operating region and hence the power system is stable. As the load increases, the AVR tends to increase its output producing more field current to sustain the generator's terminal voltage. The state variables move along the system trajectory and tend to get attracted to a stable operating point. However, due to the AVR output reaching its limit, the dynamic system

structure changes and a bifurcation point develops in the vicinity of the stable operating point. Although the operating point is unchanged, the stability margin of this point is reduced due to the AVR limit. Hence, instead of being attracted to the stable operating point, the state variables shift into an unstable operating point [57]. Crow proves that an increase in the voltage regulator setpoint for the generator with the largest reactive power reserve, can be a solution to the problem of voltage collapse. Changing the voltage regulator setpoint causes the failed or "limited" AVR to be reactivated. Crow's findings and Vournas' findings in [75] confirm the fact that the excitation control system states are bounded by stable and unstable operating points, and that fixed parameter values need to be determined based on the stability of the power system with respect to the controllable parameters. Operating close to the unstable operating point means that the power system is more vulnerable to voltage collapse.

Zhou *et al.* [76], in a sensitivity analysis of the excitation system parameters, identified that the AVR parameters have a huge impact on the dynamic reactive power reserve. They use a sensitivity coefficient which is expressed in terms of the change in excitation parameter ΔX and the change in the area of the dynamic reactive power reserve curve in a bode plot. Some excitation system parameters are increased by 20% and the change in Q-reserve area was found. The results of the frequency domain analysis showed that the voltage regulator gain have a big impact on the Q-reserve for a static excitation system model. On the other hand, considering an ac excitation system, the most impacting parameters on the Q-reserve are the controller gain, voltage regulator gain, second controller gain, rapid rising/dropping contact and the time constant of the voltage regulator. Using a time domain analysis, it was shown that the dynamic reactive power reserve decreases when the voltage regulator time constants T1 and T2 increase. In contrast, the dynamic reactive power reserve increases when the controller gain and voltage regulator gain increase.

Rahman and Chowdhury use an extra loop added to the AVR control blocks to manage the reactive power reserve [59]. When the system voltage drops, more reactive power is injected from the generators. The authors define a bias signal used to control the AVR reference voltage. A safety function of the control scheme implemented ensures that the reactive capability limits of generators are not exceeded. The simulated system shows that the voltage drop gets corrected with the reactive power injection using the Q-reserve.

The results from [76] and [59] implies that, when there is a need for reactive power, for example under GIC conditions, the excitation system control can be used to supply the reserved reactive power while operating within the generator capability limits.

2.3.7.1 AVR with PID control

An optimally tuned excitation system improves overall system performance during transient conditions due to system faults and disturbances [77]. When induction motors start, a fast exciter helps to minimise the voltage dip. An efficient exciter provides positive damping to the oscillations in the system. The voltage overshoot is also minimised if the excitation system is well tuned. With the advent in digital technology, control loops are functions of the digital system. An AVR with PID control is explained in this Section.

The *P* term is the Proportional gain, which affects the rate of voltage rise after a step change. The *I* term represents the integral gain, which affects the generator voltage settling time after the initial voltage over-shoot. Lastly, the *D* term represents the derivative gain, which affects the percent of overshoot allowed after the system disturbances [77]. It is believed that the use of digital control will aid in improving the system response achieving fast and stable response after a major disturbance. The controller gains of the PID controller used in AVRs also improves the system response. Increasing the derivative gain, integral gain and proportional gain reduces the voltage overshoot. The increase in the proportional gain also makes the system reach the maximum post disturbance peak voltage faster. The derivative gain is the main constant in helping voltage recovery by reducing the voltage overshoot. Schaefer and Kim propose the frequency domain to analyse the voltage stability of the generator and its excitation system. Bode plots are used to analyse the gain over a range of frequencies. For good system response, the gain should be high for a wide bandwidth to improve damping. The peak value of the gain just before it decreases is an indicator of the voltage overshoot.

2.3.7.2 Effects of the Power System Stabiliser (PSS)

As mentioned earlier, the role of the PSS is to improve small signal stability by adding damping to the system oscillations. When AVRs introduce negative damping torque, the PSS should be able to produce enough positive torque to add damping.

Kundur [50] analyses the effects of PSS gain on the small signal stability of a 2 area power system. With increasing gain, the local inter machine mode frequency increases and more damping is provided by the PSS. As a result, the damping constant increases. In the case of inter-area oscillations, the PSS gain increase causes a drop in the inter-area frequency modes but increased damping. Kundur highlights the importance of determining PSS locations to improve the small signal voltage stability. Moreover, the participation factor of each generator bus can provide an estimate of where to place the PSS to minimise voltage oscillations in steady-state.

2.4 Load modelling for Voltage stability analysis

With the increasing challenge of voltage stability due to power systems operating at their limits, there is a strong interest in more accurate load models for power flow simulations. An excellent paper titled "*Load representation for dynamic performance analysis*" [78] provides good background on loads, from its definition, characterisation and representation in power systems. Load characteristics are known to have a significant impact on power system dynamics. Static load models fail to capture voltage collapse dynamics and may underestimate vulnerability of a power system to collapse [60] [78].

A load model is defined as a mathematical representation of the relationship between a bus voltage phasor and power (or current phasor) flowing into a bus load. Load models are classified as follows;

Static load model – The active and reactive powers at any instant in time are expressed as functions of the bus voltages and frequency at that same time. Usually, in large scale transient stability simulations, loads are modelled as static loads.

Dynamic load model - The active and reactive powers at any instant in time are expressed as functions of the bus voltages and frequency at past instants of time or in the present instant ("Real time").

Constant impedance load model - It is considered as a static load in which the power varies with the square of the voltage.

Constant current load model - It is considered as a static load in which the power is directly proportional to the voltage.

Constant power load model – A static load model where the power is not voltage sensitive.

ZIP load model – A polynomial load model whereby the power and voltage relationship take an exponential form of second order. The ZIP model is made up of the sum of constant impedance, constant current and constant power terms. It is difficult to model the voltage and reactive power dependency using the ZIP model [79].

Exponential load model – A static load model whereby the power and voltage relationship take an exponential equation. The aggregate load model can be expressed by adding terms to the exponential load model. However, the exponential model is often questioned for exponents less than 1 in a dynamic simulation [79].

Inter-area oscillations often result in large voltage variations. The load voltage and frequency characteristics then may have significant effect on damping oscillations and improve the small signal

stability. This marks the importance of choosing the right load model for stability analysis due to their varying dynamic behaviour.

Following the excellent study in [78], another supporting paper was presented in 1995 titled "*Standard load models for power flow and dynamic performance simulation*" [79]. The paper highlights the absence of a standard model to represent aggregate loads. The paper also makes an important note that load is voltage sensitive for the first 30 to 60 seconds following a disturbance. For time frames after a minute, implicit voltage controls such as thermostatic controls, distribution voltage regulators and tap changer action restore the load power and voltage sensitivity decreases [11] [49]. This increases the reactive power burden on the HV network causing a progressive voltage reduction and therefore voltage collapse as outlined in Section 2.2.3.

The importance of assumed static load models is pointed by Overbye *et al* [11]. In their study on the voltage stability of power systems in the presence of GIC, the researchers point out the crucial contribution of loads and their voltage sensitivity in assessing the voltage stability of power systems. Load dynamics should be included, and constant power load models should be avoided to model the impact of loads on the voltage stability more accurately. The researches go further to compare the response of three types of loads under the increased electric fields from GMDs; a constant power load, constant impedance load and a 50% constant power 50% constant impedance load are used. The load responses to a peak Electric field of 8 V/km are similar since the LTC controls the load voltage. Results show that above 8 V/km, the LTC's tap limit is reached causing a voltage decline. The constant impedance load model shows a greater loadability limit compared to the 50% constant power, 50% constant impedance load model. From the research, it is clear that constant PQ load models could under-estimate the risk of a voltage collapse under extreme GIC conditions. Similar findings have been reported by Morison *et al* [53].

Clearly, the modelling of loads has a huge effect on voltage stability. The dynamics of LTCs to control load voltage levels must be included also to show how the load restoration of dynamic voltage sensitive loads can lead to voltage collapse under GIC conditions.

2.5 3-phase power calculations using IEEE1459 Standard and GPT

When it comes to GIC studies, there is continuous debate on how to measure reactive power or non-active power. A very interesting paper [80] published in 2018 by Kirkham and White aims to raise awareness around the definition of reactive power for GIC studies. The authors clearly point out that the accuracy of results is highly dependent on the measurement theory which is operational. This means that the method used to measure reactive power or non-active power should be "fit for

purpose". This chapter will focus on developments in the definitions of apparent power and non-active power that have happened over the years.

It was in the 1900s that engineers started to understand that ac circuits behave different to dc circuits. This spiked debates around the concept of apparent and reactive power leading to the quantification of a figure of merit of power transfer, namely the power factor. Debates continued on the definition of apparent power and in 1910, the definition of vector VA and arithmetic VA were discussed. In the case of balanced systems, these two quantities give equal results. However, in the case of unbalanced systems, the arithmetic VA is larger than the vector VA.

The balanced system was easy to understand and comparable to single phase systems. However, when unbalance was introduced, apparent power definitions were inaccurate which had a consequent effect on the power factor [81]. It was in 1920 that the first true definition of the power factor was identified by W.V. Lyon. Fortescue's symmetrical component theory charmed the pillars of our profession during those times that Lyon's definition of the power factor was not taken into consideration. 7 years later, C.I. Budeanu described the first model of power in non-sinusoidal distorted waveforms. The apparent power was resolved into 3 components namely the active power, reactive power and distortion power. Budeanu's theory, supported by H. Curtis and F. Silsbee in one of the most heated AIEE meetings, was included in the American Standard Definition of Electrical Terms.

There are many problems with Budeanu's theory since the arithmetic and vector VA are incorrect in the case of non-sinusoidal waves and unbalance.

Extending Lyon's concepts, the apparent power and power factor were finally given accurate definitions as per IEEE Std 100 [82]:

- *"Apparent power is the maximum power transmitted to the load while keeping the same line losses and the same load voltage and current."*
- *"Power factor is the ratio of the actual power to the maximum power that could be transmitted while keeping the line power loss and the load voltage constant."*

The arithmetic VA and vector VA agree to the above definitions under balanced, sinusoidal three phase systems. For a balanced system with non-sinusoidal conditions and other types of imbalances, the definitions do not comply [81].

The apparent power value in the above definition assumes the line losses are finite. In a 3 phase four wire system, triplen harmonics flow in the neutral under unbalance conditions. The neutral wire needs to be included in the line losses assumed in the definition. Analysing the mathematics of [81], shows that when the load is unbalanced, the arithmetic VA and vector VA give differing power factors.

The IEEE Standard 1459 [83][84], introduced in year 2000 and revised in year 2010, provides a more accurate definition of power under the effects of unbalance and non-sinusoidal conditions. The standard favours Lyon's definition of the power factor. It includes the neutral current losses which are considerable in the determination of the power factor value via the definitions that follow.

Continuing debates on the apparent power definition look into the definition of arithmetic VA (S_A) and vector VA (S_V).

The apparent power in each phase can be expressed in terms of the phase currents and voltages or in terms of the active power and reactive power following the power triangle.

$$S_i = V_i I_i \ \ where\ i = a, b\ or\ c \tag{2.53}$$

The arithmetic VA is the sum of the apparent power in each phase.

$$S_A = S_a + S_b + S_c \tag{2.54}$$

For non-ideal conditions, the arithmetic VA does not follow the power triangle definition, nor the symmetrical component theory and therefore $S_A \neq \ P^2 + Q^2$ or $S_A \neq \ S^+ + S^- + S^0$ [81][83].

Using the arithmetic VA, the power factor can be defined.

$$PF_A = \frac{P}{S_A} \tag{2.55}$$

On the other hand, the vector VA can be expressed as follows.

$$\overrightarrow{S_V} = \vec{P} + j\vec{Q} \tag{2.56}$$

$$\overrightarrow{S_V} = \overrightarrow{P_a} + \overrightarrow{P_b} + \overrightarrow{P_c} + j(\overrightarrow{Q_a} + \overrightarrow{Q_b} + \overrightarrow{Q_c}) \tag{2.57}$$

$$S_V = |P^+ + P^- + P^0 + j(Q^+ + Q^- + Q^0)| \tag{2.58}$$

Using the vector VA, the power factor can be defined.

$$PF_V = \frac{P}{S_V} \tag{2.59}$$

Consider a three-phase system with phase resistances equal to r and the neutral wire resistance equal to r_n. The system supplies an unbalanced load. The line power loss can therefore be expressed as follows [81] [83];

$$P = r\left({I_a}^2 + {I_b}^2 + {I_c}^2\right) + r_n {I_n}^2 \tag{2.60}$$

I_a , I_b and I_c is the phase A, B and C currents respectively and I_n is the neutral current.

The optimized system with unity power factor consisting of equal load resistances represents an ideal case. In this situation, the line currents would be identical leading to;

$$P = 3r({I_e}^2) \tag{2.61}$$

The IEEE 1459 standard defines an effective current including the neutral wire resistance and is given by equation (2.62).

$$I_e = \sqrt{\frac{1}{3}({I_a}^2 + {I_b}^2 + {I_c}^2 + \rho {I_n}^2)}\,, where\ \rho = \frac{r_n}{r} \tag{2.62}$$

The effective current can also be expressed in terms of the sequence components.

$$I_e = \sqrt{[(I^+)^2 + (I^-)^2 + (1 + 3\rho)(I^0)^2]} \tag{2.63}$$

Similarly, the effective voltage is given by equation (2.64).

$$V_e = \sqrt{\frac{3\left({V_a}^2 + {V_b}^2 + {V_c}^2\right) + \xi({V_{ab}}^2 + {V_{bc}}^2 + {V_{ca}}^2)}{9(1 + \xi)}} \tag{2.64}$$

Determination of ξ follows an assumption that relates the active components of the load as an equivalent resistance connected in wye. The remaining active load is connected in delta and the power dissipated by the wye connected load or delta connected load being the same. If ξ is not known, the recommended value of ξ is 1 according to the IEEE1459. Moreover, the IEEE1459 Std notes that the ratio ξ does not have an effect on the effective voltage in most practical systems [83]. This leads to a simpler expression for the effective voltage.

$$V_e = \sqrt{\frac{3\left({V_a}^2 + {V_b}^2 + {V_c}^2\right) + ({V_{ab}}^2 + {V_{bc}}^2 + {V_{ca}}^2)}{18}} \tag{2.65}$$

Expressing V_e in terms of the sequence components yields;

$$V_e = \sqrt{(V^+)^2 + (V^-)^2 + \frac{(V^0)^2}{2}} \tag{2.66}$$

The effective apparent power is found by equation (2.67).

$$S_e = 3V_e I_e \tag{2.67}$$

The above definition of apparent power agrees to the definitions proposed by Buchholz and Goodhue [81]. The apparent power includes the losses in the neutral and the effects of unbalance.

Thus, the effective power factor can be defined.

$$PF_e = \frac{P}{S_e} \tag{2.68}$$

For a balanced system, the arithmetic VA is equal to the vector VA. Both are equal to the effective VA. In the unbalanced case, $S_V \leq S_A \leq S_e$ and $PF_e < PF_A < PF_V$.

This leads to the calculation of the unbalanced power which represents the amount of VA caused by unbalance in the system.

$$S_U = \sqrt{{S_e}^2 - (S^+)^2} \tag{2.69}$$

The unbalanced power should not be confused with voltage unbalance. It represents both the load unbalance and voltage asymmetry [83].

2.5.1 3-Phase, non-sinusoidal, unbalanced system

To cater for the most common, unfortunately less ideal system, the effective current and voltage are decomposed in terms of the fundamental effective components and non-fundamental effective components.

$${I_e}^2 = {I_{e1}}^2 + {I_{eH}}^2 \tag{2.70}$$

$${V_e}^2 = {V_{e1}}^2 + {V_{eH}}^2 \tag{2.71}$$

The subscript '1' represents the fundamental (50Hz in South Africa) effective rms current and the subscript 'H' represents the non-fundamental effective rms current.

From equation (2.62)

$$I_e = \sqrt{\frac{1}{3}({I_a}^2 + {I_b}^2 + {I_c}^2 + {I_n}^2)}, where\ \rho\ has\ been\ chosen\ as\ 1.$$

$$I_{e_1} = \sqrt{\frac{1}{3}({I_{a_1}}^2 + {I_{b_1}}^2 + {I_{c_1}}^2 + {I_{n_1}}^2)} \tag{2.72}$$

$$I_{e_H} = \sqrt{\frac{1}{3}({I_{a_H}}^2 + {I_{b_H}}^2 + {I_{c_H}}^2 + {I_{n_H}}^2)} \tag{2.73}$$

$$V_e = \sqrt{\frac{3\left({V_a}^2 + {V_b}^2 + {V_c}^2\right) + ({V_{ab}}^2 + {V_{bc}}^2 + {V_{ca}}^2)}{18}} \tag{2.74}$$

$$V_{e_1} = \sqrt{\frac{3\left({V_{a_1}}^2 + {V_{b_1}}^2 + {V_{c_1}}^2\right) + ({V_{ab_1}}^2 + {V_{bc_1}}^2 + {V_{ca_1}}^2)}{18}} \tag{2.75}$$

$$V_{e_H} = \sqrt{\frac{3\left({V_{a_H}}^2 + {V_{b_H}}^2 + {V_{c_H}}^2\right) + ({V_{ab_H}}^2 + {V_{bc_H}}^2 + {V_{ca_H}}^2)}{18}} \tag{2.76}$$

The apparent power S_e, in this case is decomposed into the fundamental (S_{e1}) and non-fundamental apparent powers (S_{eN}). Since there are 2 components of the effective current and voltage, the effective apparent power consists of 4 terms.

$${S_e}^2 = (3V_{e1}I_{e1})^2 + (3V_{e1}I_{eH})^2 + (3V_{eH}I_{e1})^2 + (3V_{eH}I_{eH})^2 \tag{2.77}$$

$$S_{e1} = 3V_{e1}I_{e1} \tag{2.78}$$

The fundamental apparent power S_{e1} can be decomposed into the positive sequence fundamental apparent power ${S_{e1}}^+$ and the remaining ${S_{U1}}^{0-}$ attributed to system unbalance (negative sequence and zero sequence components).

The load unbalance can be evaluated using the fundamental unbalanced power.

$$S_{U1}{}^{0-} = \sqrt{S_{e_1}{}^2 - (S_1{}^+)^2} \tag{2.79}$$

$S_{e1}{}^+$ can be expressed in terms of its fundamental positive sequence active power and reactive power components.

$$S_{e1}{}^+ = P_1{}^+ + Q_1{}^+ \; where \; P_1{}^+ = 3V_1{}^+ I_1{}^+ cos\,\theta_1{}^+ \; and \; Q_1{}^+ = 3V_1{}^+ I_1{}^+ sin\,\theta_1{}^+ \tag{2.80}$$

The total harmonic distortion of the non-sinusoidal, unbalanced system can be calculated using equations (2.81) and (2.82).

$$THD_{eI} = \frac{I_{eH}}{I_{e1}} \tag{2.81}$$

$$THD_{eV} = \frac{V_{eH}}{V_{e1}} \tag{2.82}$$

The non-fundamental effective apparent power S_{eN} can be expressed as;

$$S_{eN} = \sqrt{S_e{}^2 - S_{e1}{}^2} = \sqrt{D_{e1}{}^2 + D_{eV}{}^2 + S_{eH}{}^2} \tag{2.83}$$

D_{eI} is the effective current distortion power.

D_{eV} is the effective voltage distortion power.

S_{eH} is the effective harmonic apparent power.

In terms of the total harmonic distortion, S_{eN} can take other forms as shown in equation (2.84).

$$S_{eN} = \sqrt{THD_{eI}{}^2 + THD_{eV}{}^2 + (THD_{eI}THD_{eV})^2} \tag{2.84}$$

$$D_{eI} = 3V_{e1}I_{eH} = 3S_{e1}(THD_{eI}) \tag{2.85}$$

$$D_{eV} = 3V_{eH}I_{e1} = 3S_{e1}(THD_{eV}) \tag{2.86}$$

$$S_{eH} = 3V_{eH}I_{eH} = 3S_{e1}(THD_{eI})(THD_{eV}) \tag{2.87}$$

The non-fundamental apparent power S_{eN} can be used to evaluate the level of distortion in the power system.

The harmonic active power is given by (2.88).

$$P_H = \sum_{\substack{h\neq 1 \\ i=a,b,c}} V_{ih} I_{ih} \cos\theta_{ih} = P - P_1 \tag{2.88}$$

The distortion power due to harmonics is a non-active term expressed as:

$$D_{eH} = \sqrt{{S_{eH}}^2 - {P_H}^2} \tag{2.89}$$

2.5.2 General Power Theory (GPT)

The measurement and calculation of power in the presence of imbalance and distortion originating from GIC requires some careful considerations [85]. All the inefficiencies of the system need to be accounted for, in power calculations. Conventional calculations such as the IEEE Standard 1459 [83], lack clarity in their definitions of non-active power although significant efforts have been made to classify power calculations based on the system conditions.

The voltage reference used in conventional power calculations is chosen as a arbitrary reference point, usually the neutral. When there is distortion and imbalance, current flows in the neutral wire if a 4-wire system is used [26]. Hence, the inefficiencies in the neutral also need to be accounted for.

After rigorous mathematical derivations, Gaunt and Malengret came up with a general power theory which uses a single formula derived from linear algebra and vector space to calculate power under non-ideal conditions. The formula can be used in systems with any number of wires, considers losses in the neutral wire and all system inefficiencies. Unlike conventional power theories, the GPT includes the effects of distortion, unbalance and dc current components. Results have shown that the conventional approach of computing power underestimates the non-active power compared to the GPT. However, the active power is the same for both theories which is expected [26]. More recently, the GPT has been amended and considers the frequency components of currents and voltages to calculate power. The new GPT is still under development and was therefore not considered for this project.

The General Power Theory, developed by Malengret and Gaunt will be discussed for its application in GIC studies [26][85][86]. Figure 2.21 shows the three-dimensional power triangle developed in the GPT.

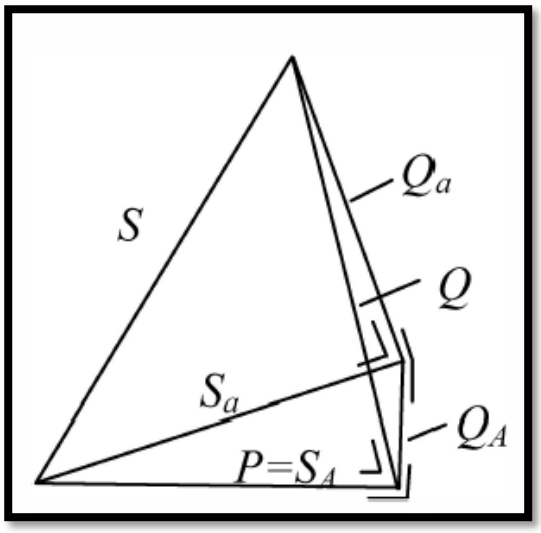

$\boldsymbol{Q}$ is the total non-active power

$\boldsymbol{S}$ is the apparent power without any compensation

$\boldsymbol{P}$ is the apparent power after compensation.

$\boldsymbol{Q_a}$ is the non-active power component that can be compensated without energy storage

$\boldsymbol{Q_A}$ is the non-active power component that needs energy storage for compensation.

$\boldsymbol{S_a}$ is the apparent power after compensation without energy storage.

$\boldsymbol{S_A}$ is the apparent power after compensation with energy storage.

Figure 2.21: Complete Power Triangle as per General Power Theory built in a Tetrahedron with the powers decomposed based on the need for compensation with or without energy storage [26]

The general procedure for finding the active and non-active power using GPT is as follows;

Using instantaneously sampled values of the currents in each phase, calculate the neutral current i_n.

$$\boldsymbol{i_n = -(i_a + i_b + i_c)} \tag{2.90}$$

The resistance-weighed square of the currents is calculated, giving the resistance weighed norm of the current.

$$\boldsymbol{\|i'\|^2 = (i_a{}^2 + i_b{}^2 + i_c{}^2 + \frac{i_n{}^2 r_4}{r})r} \tag{2.91}$$

$\boldsymbol{\|I'\|^2}$ is the average of $\boldsymbol{\|i'\|^2}$ over a whole cycle.

Next, for every sample set, a virtual, resistance-weighed reference (null point) for the voltages is calculated.

$$\boldsymbol{e_{ref} = (e_a + e_b + e_c)/(3 + \frac{r}{r_n})} \tag{2.92}$$

$$\boldsymbol{\|v'\|^2 = \left[(e_a - e_{ref})^2 + (e_b - e_{ref})^2 + (e_c - e_{ref})^2 + \frac{(0 - e_{ref})^2 r}{r_4}\right]\frac{1}{r}} \tag{2.93}$$

$\boldsymbol{\|V'\|^2}$ is the average of $\boldsymbol{\|v'\|^2}$ over a whole cycle.

Finally, the apparent power can be calculated using equation (2.94).

$$\boldsymbol{S} = \|\boldsymbol{V}'\|\|\boldsymbol{I}'\| \tag{2.94}$$

Since the real power is invariant, it can be computed from the conventional approach or derived from the products of currents and voltages measured from a common virtual reference.

The power factor is given by;

$$\boldsymbol{\lambda} = \frac{\boldsymbol{P}}{\boldsymbol{S}} \tag{2.95}$$

The total non-active power Q is calculated as follows;

$$\boldsymbol{Q^2} = \boldsymbol{S^2} - \boldsymbol{P^2} \tag{2.96}$$

2.6 Chapter summary

In Chapter 2, the GIC phenomena leading to their harmful effects on power systems was discussed. Conventional dcGIC models fail to represent realistic GIC dynamics which can vary in the order of seconds. Therefore, there is a need for more representative GIC models to understand the true dynamic response of power systems to such disturbances. Concepts related to voltage stability were highlighted in Section 2.2 including methods of analysis most suitable for GIC studies. It was shown that dynamic voltage stability analysis using time domain simulations provide more information on the mechanism of voltage collapse compared to static analysis. In Section 2.3, different configurations of excitation systems were studied including the control parameters effective on the generator's var output. Finally, the importance of load modelling and more-accurate definitions of non-active power under GIC conditions were highlighted. The literature review revealed a need for more accurate power measurements and calculations to find out with more certainty, the real var demand on generators during geomagnetic disturbances.

3 Modelling of 4-bus power system model with dc and ac GIC

One of the key challenges in GIC studies has been the lack of a test case model that can be used to validate results across different software [87]. Moreover, many power system data are confidential and power utilities do not divulge such information. However, many different power system models have been used over the years to simulate the effects of GIC. Horton *et al*. [42] developed a 20-bus network with 345 and 500 kV transmission lines as a test case for GIC studies. Realistic power grids such as the Chinese grid [88][89] and Finish 400kV grid [90] have also been modelled to predict the grid's response to GIC. Tigere *et al*. [54] and Mkhonta *et al*. [91] developed a physical 4-bus network to study the effects of GIC on transformer reactive power and temperature increases. In [18], Weng *et al*. used a similar network with a generator, two transformers and a constant power load to study the effect of dc bias on transformer reactive power and system voltage. Overbye *et al*. [13] also use a 4-bus network model with two generators and two voltage levels (345 kV and 500 kV) to study the grid's sensitivity to GIC before studying a much larger 20-bus system. Although the 4-bus models are simple, they provide conclusive results applicable to larger power systems. The response of these simpler systems to GIC can therefore be used to predict the behaviour of larger systems.

In this chapter, a preliminary 4-bus power system will be modelled in MATLAB Simulink to study the effects of GIC, represented as dc and low frequency ac currents. The 4-bus power system was used to establish preliminary relationships between network quantities and GIC before studying the response of a larger network. This 4-bus system was then augmented to a multi-machine system, discussed later in Chapter 4.

3.1 4-bus System model

The 4-bus model used for the preliminary studies on GIC is shown in Figure 3.1.

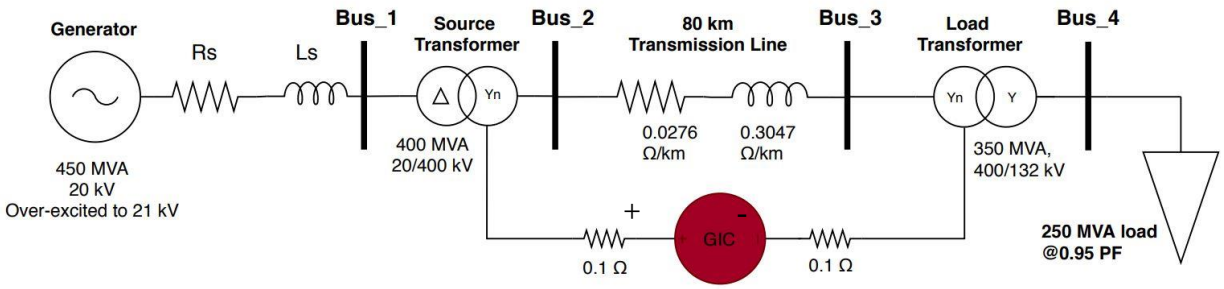

Figure 3.1: 4-bus system model used for study of dc and ac GIC

The power system is representative of a typical South African network with voltage levels chosen based on those used in South Africa. The system consists of a single generator supplying a load.

Bus 1 is the generator bus, also the slack or swing bus in the 4-bus network. The generation voltage is 20kV. However, the generator is overexcited to produce 21 kV in order to compensate for the voltage drop along the transmission path. This voltage is then stepped up to 400kV using a 400 MVA step-up transformer T12. A resistive and inductive 80 km transmission line carries the power to a 350 MVA 400/132 kV step down transformer T34. The transmission line resistance is 0.0276 Ω/km and has an XR ratio of 12.3. T34 steps down the 400kV to 132 kV used by the load. The load is modelled as a constant power load consuming 250 MVA of power at 0.95 lagging power factor.

Detailed modelling of each of the components including the mathematical models are described in Sections 3.2 to 3.5.

3.2 Generator modelling

Generators within Simscape Electrical Specialized Power System can be modelled using single phase or three phase electrical sources, or full dynamic models of synchronous machines including the turbine, governor system and excitation system.

For this GIC study, the generator was modelled using three approaches;

1. an ideal three-phase equivalent AC voltage source
2. a three-phase equivalent AC voltage source with resistive and inductive impedance.
3. a full model of a synchronous machine including the excitation system, steam turbine and governor system.

3.2.1 3-phase equivalent AC voltage source

The three-phase source block offered by MATLAB produces balanced or unbalanced three phase voltages. The three phases are wye-connected with a neutral connection that can be internally grounded or made accessible. When modelled as an ideal source (stiff voltage source), the internal impedance of the source is set to 0. This models a source with an infinite supply of power. The equivalent circuit of the ideal three phase equivalent AC voltage source is similar to Figure 3.2 but without the resistance and inductance.

If the same three phase source block is modelled as non-ideal, the internal impedance of the source is no longer 0. This in turn means that the generator needs to be over-excited so that the terminal voltage is kept at 21 kV. Hence, the internal generated voltage of the machine needs to cater for the

voltage drop across the internal impedance of the source to produce a terminal voltage of 21 kV. One phase of the 3-phase AC equivalent voltage source including RL impedance is shown in Figure 3.2.

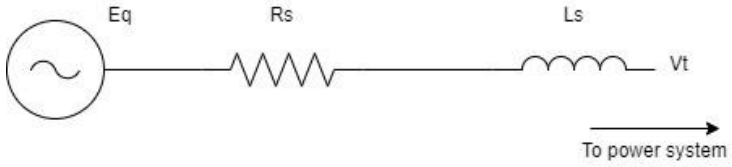

Figure 3.2: 3-phase AC equivalent source with internal impedance

E_q is the internal voltage generated which compensates for the voltage drop across the source impedance. This internal voltage is produced by field excitation and commonly referred to as the excitation voltage. R_s is the source resistance. L_s is the source inductance. V_t is the terminal voltage seen at the generator terminals.

3.2.2 Synchronous machine model

The synchronous machine block operates in a generator or motor mode depending on the sign of the input mechanical power from the turbine and governor system. If the input mechanical power is positive, the synchronous machine operates as a generator. If the mechanical power input is negative, the synchronous machine operates as a motor. In the 4-bus network, the synchronous machine operates as a generator and hence a positive mechanical power needs to be supplied to the machine. The electrical part of the machine can be analysed in the d-q axis reference frame using the equivalent circuits shown in [92]. Note that the equivalent circuit used by Matlab to represent the synchronous machine is similar to the one proposed by IEEE 1110 [70].

A detailed description of the generator including equations and state space representation can be found in [92]. The electrical part of the machine is modelled by a sixth order state space model. The mechanical part of the machine can be modelled as follows;

$$\Delta\omega(t) = \frac{1}{2H}\int_0^t T_m - T_e - K_D\Delta\omega(t)dt \tag{3.1}$$

$$\omega(t) = \Delta\omega(t) + \omega_0 \tag{3.2}$$

The speed deviation with respect to the speed of operation is represented by $\Delta\omega$, H is the inertia constant, T_m is the mechanical torque, T_e is the electromagnetic torque, K_D is the damping factor representing the effects of damper windings, $\omega(t)$ is the mechanical rotor speed and ω_0 is the speed of operation (usually 1 pu)

3.2.2.1 Synchronous machine parameters

Synchronous generators can be represented mathematically using either fundamental parameters or standard parameters. The fundamental parameters are the resistances and inductances of the stator and rotor circuits. These parameters are used to build the equivalent circuit of the synchronous generator. Determining physical synchronous machine parameters requires enhanced sudden short circuit tests, stator decrement tests and frequency response analysis [93][94][95]. In their dynamic simulations [96], Suni *et al*. use the IEEE 115 Std and IEEE 1110-2002 Std to show how the standard parameters for the synchronous generator model in MATLAB can be determined from sudden short circuit tests. The problem with fundamental parameters is that they cannot be determined directly from measured responses of the generator. Therefore, there is another representation used for synchronous generator parameters called the standard parameters. The standard parameters include the synchronous generator reactances (or inductances in pu) and time constants. The IEEE1110 – 2002 Standard [70] proposes a data translation technique that can be used to convert fundamental parameters to standard parameters and vice versa. Moeini *et al.* [93] used this technique to propose an improvement in the synchronous machine model of MATLAB Simulink by adding the Canay inductance.

In MATLAB Simulink, the synchronous generator can be represented using both fundamental and standard parameters. Since the fundamental parameters were not readily available, the synchronous generator block with standard parameters was chosen. For this research, the parameters for the standard parameters were taken from Kundur's textbook [50] and are shown below;

$X_d = 1.8$; $X'_d = 0.3$; $X''_d = 0.25$; $X_q = 1.7$; $X'_q = 0.55$; $X''_q = 0.25$; $X_l = 0.2$; $R_s = 0.0025$; $T'_{d0} = 8\ s$; $T''_{d0} = 0.03\ s$; $T'_{q0} = 0.4\ s$; $T''_{q0} = 0.05$; $H = 6.5$

3.3 Excitation system model

For this research, only AC excitation systems are used since they are the most readily used nowadays. The IEEE 421.5 Std of 2005 [69] provides standard models of AC excitation systems They are referred to as the AC1A, AC2A, AC3A, AC4A, AC5A, AC6A, AC7B and AC8B excitation systems. The MATLAB 2019a version only offers the IEEE AC1A, AC4A and AC5A excitation systems [97] and therefore these three excitation systems were used in this research initially. When the MATLAB 2020a version was released, the library was augmented and included newer models of the excitation systems as proposed in IEEE 421.5 of 2016 [68]. These newer models (AC1C, AC2C and so on) are each similar to their older equivalents except that they include inputs from field and stator current limiters. However, models of such limiters are still under development by MathWorks and therefore

could not be used in this study. It is however understood that such limiters define the operating region within the generator capability curve (See Section 2.3.3) and therefore impose a limit on the power output during GIC conditions.

The mathematical model and block diagram representation of the AC1A, AC4A and AC5A excitation systems were shown in Section 2.3.4. Parameters used to model the excitation systems were determined from the sample data of the AC1C/AC1A excitation system in Table H.8 of the IEEE 421.5 Std. To compare the excitation systems, the same gains and time constants of the AC1A excitation system were used to model the AC4A and AC5A, ensuring consistency in modelling.

3.4 Transformer model and saturation

Three phase transformers of different core types can be modelled. These include three phase transformer banks (3p-bank), three phase three limb transformers (3p3L) and three phase five limb transformers (3p5L).

The three transformer types were tested before deciding on a final transformer type to be used. Running open circuit test under balanced conditions showed that the 3p3L and 3p5L transformers do not exhibit inter-phase magnetic coupling. Under unbalanced system conditions, the 3p3L and 3p5L transformers produce unbalanced fluxes across the limbs. These preliminary modelling results were published as one of the deliverables of this dissertation [98]. For this research, only 3p5L transformers were used. To use the three- phase transformer block in MATLAB, certain parameters need to be defined. These include the power rating, voltage levels, transformer winding impedance, magnetising resistance and very importantly, the transformer magnetising curve (also referred to as saturation curve). The transformer connection type (wye or delta connected) and transformer type also needs to be specified.

3.4.1 Transformer rating, connection and type

Following the proposed 4-bus network, the transformers were rated as shown in Table 3.1.

Table 3.1: Transformer ratings, connection and type for 4-bus system model

Transformer	Power rating (MVA)	Voltage transformation (kV)	Connection	Phase shift
T12	400	20/400	Dyn11	+30
T34	350	400/132	YnY	0

3.4.2 Transformer winding impedance

The magnitude of GIC flowing in a network depends on the resistance of the network. For large power transformers, resistance values are usually small in the range of 0.04 Ω/phase to 0.4 Ω/phase [50][99][42][44]. Hence, using the transformer rating and voltage levels, the winding resistance values for T12 and T34 were chosen as shown in Table 3.2.

Table 3.2: Transformer winding resistances

Transformer	R1 (Ω)	R2 (Ω)
T12 – 400 MVA, 20/400 kV	0.04	0.1
T34 – 350 MVA. 400/132 kV	0.1	0.08

The inductance of the transformer windings determines the X/R ratio of the transformer and hence the transformer time response [100]. In the past, it has been common practice to ignore the transformer inductance in GIC studies. Delays in GIC growth due to the transformer inductances were not observed since the electric field values were measured using 1 sample/minute cadence [39]. Nowadays, HV lines are designed with low resistances owing to a high X/R ratios. These cause significant delays in GIC growth and network response time to GIC. Hence, transformer winding inductances must be carefully chosen for GIC studies.

Typical values used for transformer winding inductances are usually given in per unit and lie in the range of 0.04 pu to 0.2 pu [50][101]. The winding inductances used for T12 and T34 are given in Table 3.3. These values were carefully chosen to ensure that the transformer reactive power consumption was realistic. Note that L1 is zero because it is not possible to connect an inductive reactance to the generator terminal due to software limitations.

Table 3.3: Transformer winding inductances

Transformer	L1 (pu)	L2 (pu)
T12 – 400 MVA, 20/400 kV	0	0.06
T34 – 350 MVA. 400/132 kV	0.1	0.04

3.4.3 Shunt magnetising branch and saturation

The shunt branch of a transformer equivalent circuit includes a resistance R_m and inductance L_m. R_m accounts for the core losses within the transformer. A very high value of R_m is usually chosen to minimise core losses due to heating and eddy currents. For a 250 MVA transformer, MathWorks uses a default value of 500 pu to represent a 0.2% active power core loss at nominal voltage [102]. For both T12 and T34, the shunt branch resistance was set to the default value of 500 pu.

L_m is the magnetising inductance which is a function of the applied voltage at the primary terminals. L_m directly affects transformer saturation and reactive power consumption during GIC conditions. When the transformer operates in the linear region, the value of L_m is usually constant. In the saturation region, the inductance drops significantly [103] . The effects of L_m can be modelled using the saturation characteristic of the transformer.

Modelling a real transformer saturation curve is beyond the scope of this research due to shortage of such data provided by manufacturers. However, an approach used to model the saturation curve is discussed. It is important to consider the saturation characteristic for both the linear and non-linear regions since under GIC conditions, the transformer is expected to operate in the non-linear region.

Nowadays, power transformers are highly efficient requiring only a few amps of magnetising current (0.5 % to 2% of rated full load current) to produce the necessary flux. In their studies on the impact of dc bias on transformer reactive power, Weng *et al*. [18] make use of a 100 MVA transformer with a magnetizing current of 0.2 A when operating at nominal voltage. Field tests on a 600 MVA transformer show a normal magnetising current peaking around 6A. Under 25 A GIC/phase, the magnetising current for the 600 MVA transformer peaks at 300 A [8]. Price [16] shows a 350 A peak magnetising current for a 400 MVA transformer under 66.7 A GIC per phase. Examining Fig 8 in Price's paper shows that the magnetising current is around 10 A when there is no GIC. With 25 A GIC per phase, peaks of nearly 300 A have been shown in [44]. The same report shows over 800 A distorted magnetising current with a 100 A GIC per phase. Of course, the magnetising current will depend on the core type, shunt branch impedance and other transformer design factors. However, these values provide an idea of the expected levels of magnetising current.

Therefore, the saturation curve for T12 was designed for a peak magnetising current of 10 A required to produce the necessary flux while that of T34 requires as low as 0.8 A of magnetising current to operate. When GIC flows, depending on the dc flux the transformer should operate in the saturation region with peaks of the magnetising current over 800 A as reported in literature [8][44].

3.4.4 Transformer open circuit test

As per the design specifications mentioned earlier, the transformer magnetising curves (or saturation characteristic) for T12 and T34 were modelled. MATLAB models the saturation characteristic as a piecewise linear function. The points on the saturation curve are specified using peak values of the magnetising current and the peak flux.

Figure 3.3 show the magnetising curves for T12 and T34. There is a close match between the specified magnetisation curve and the simulated one. Note that the simulated curve is the one obtained by actually running the open circuit test at different voltages in MATLAB.

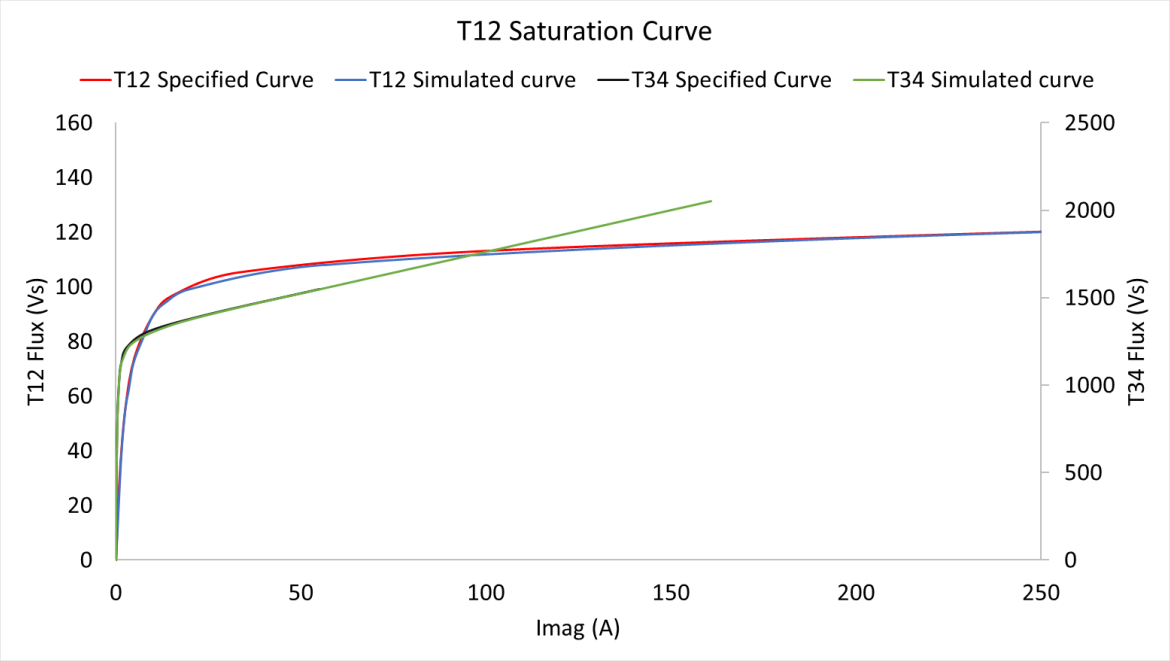

Figure 3.3: T12 and T34 Transformer magnetising curve

3.5 Transmission line and load model

The power transfer across the transmission corridor depends on the surge impedance loading (SIL) of the line which is the ratio of the line voltage squared to the characteristic impedance. The non-active power absorbed or consumed by the line depends on the SIL and operating voltage. If the line is operated below SIL, then it produces non-active power. Operating above SIL causes the line to consume non-active power, therefore increasing the demand on the power system.

The line length is important in determining the level of GIC flowing in a power system [39][104]. Transmission lines shorter than 80 km are classified as short lines and may be represented by their series resistance and inductance only (RL line model). Medium length lines lie within the range of 80

km to 200 km and are represented by the nominal π transmission line model. If the lines are longer than 200 km, the equivalent π transmission line model is usually used [50][74].

For this research, the 4-bus system is modelled with a short 80 km line using simple resistance and inductance blocks. The effect of a longer line model modelled as a π equivalent will be shown in the multi-machine system. All the phases were modelled using the same value of resistance and inductance making up a balanced transmission line. Unbalance was only introduced in the 4-bus network for harmonic analysis with an ac GIC model. The unbalance was introduced by varying the transmission line resistance and inductance, discussed in Section 6.1.2.1.

The importance of accurate load models for GIC studies was highlighted in Chapter 2.4. MATLAB Simulink library offers both single phase load blocks and three phase load blocks. Moreover, the loads can be of static nature or dynamic. The three-phase static load block was used in simulating the 4-bus network and was modelled as a constant power load. The three-phase dynamic load block could not be used because it can only simulate balanced loading conditions and accounts for only positive sequence currents. [97].

3.6 Chapter summary

In Chapter 3, the modelling of a 4-bus network for preliminary GIC impact analysis was discussed. Each individual power system component used in the simulations was investigated to see if they were suitable for the study. Section 3.1 showed the proposed 4-bus network with voltage levels typical of a South African power system. Section 3.2 showed different complexities of generators including ideal, non-ideal ac equivalent sources or full synchronous generator model with excitation system, turbine and governor. The equivalent circuit of the full generator model including standard parameters used were given. Details of different IEEE AC excitation systems used, including gains, time constants were provided in Section 3.3. Very importantly, Section 3.4 dealt with the 3p5L transformer model, its power rating, winding resistances, inductances and the saturation characteristic. Finally, the transmission line model and load models were discussed in Section 3.5. It was agreed that only static load models would be used since the dynamic load model does not cater for harmonic and unbalance. From the 4-bus base case model, a more complex but more realistic multi-machine model was modelled as discussed in the next chapter.

4 Modelling of Multi-machine power system under dynamic GIC

The 4-bus power system model helped to gain a preliminary understanding of the power system's response to both dcGIC and acGIC. However, realistic power systems consist of multiple generators supplying different areas in an interconnected system. Hence, a multi-machine power system model with 2 areas was developed in MATLAB Simulink to understand the responses of multiple generators to GIC. Chapter 4 discusses the modelling of this multi-machine system and the development of a dynamic GIC profile with multiple frequencies, amplitudes at different time instances.

While there are many benchmark interconnected systems proposed by many researchers to study the effects of GIC in power systems, there is a lack of data available for all the power system components such as transformer saturation characteristics, winding resistances and inductances, amongst others often due to data confidentiality [105]. Therefore, the multi-machine power system model used for this study has been adapted from example 12.6 (Page 813) in Kundur's textbook on power system stability and control [50]. The same model has been used in [106] for studying inter-area oscillations. Although its small size, the network mimics the response of realistic systems [107]. Figure 4.1 shows the one-line diagram of the proposed multi-machine power system including the GIC injection circuit.

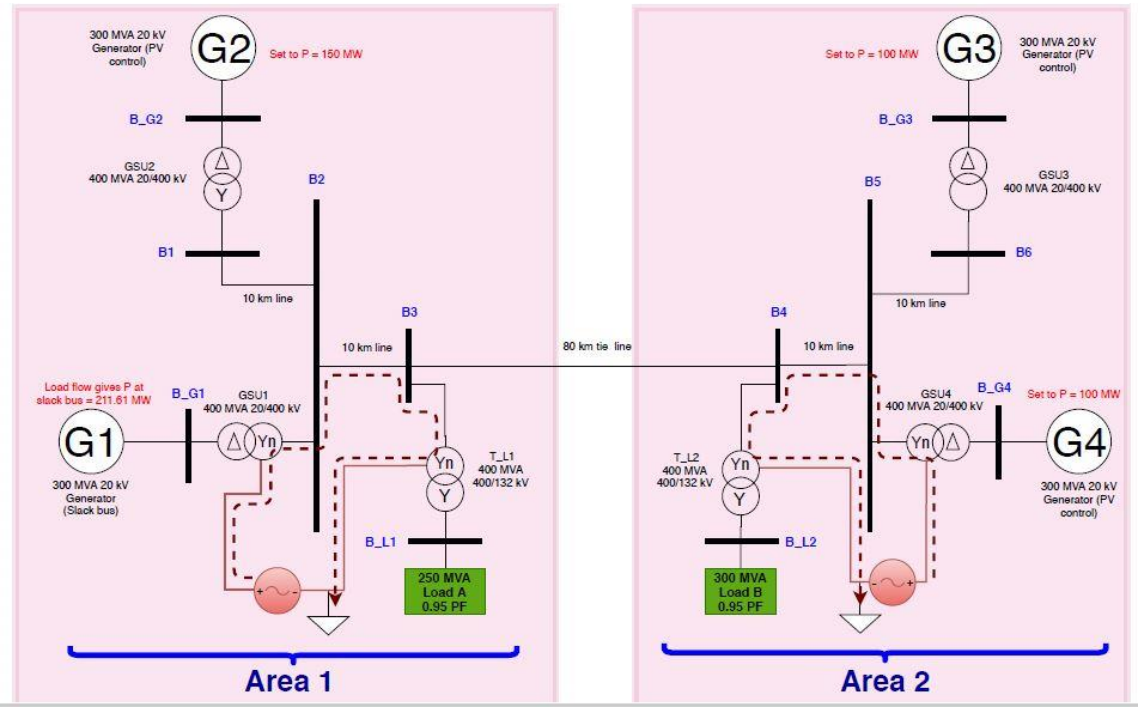

Figure 4.1: Two-area multi-machine power system model

4.1 System specifications

The power system is symmetrical and consists of two areas linked by an 80 km, 400 kV transmission line. Each area consists of two synchronous generators modelled with AC1A excitation system and turbine/governor controls. Each generator is rated at 300 MVA and the terminal voltage produced is 20 kV. The parameters used for the generators and AC1A excitation system are exactly similar to those used in the 4-bus network.

Generator G1 is the swing or slack generator. All other generators are set to run on PV control with G2 producing 150 MW of active power, G3 and G4 each pushing 100 MW of active power into the grid.

The step-up transformers (GSU1, GSU2, GSU3 and GSU4) and step-down transformers in each area are exactly similar to those used in the 4-bus network.

In the 4-bus network, the transmission line was modelled as a short line of length 80 km, represented by a resistance and inductance. Zheng *el al.* [104] conclude that for short lines, the GIC are linearly related to line length. However, it is known that, for the long lines, the GIC flowing in the line increases up to a limited value given by the ratio of the electric field and line resistance. Zheng's findings, supported by Boteler and Pirjola [108] imply that the line length is not that important for determining the level of GIC. Instead the length of the system, with interconnected lines is the most important factor to be considered. Therefore, in terms of the line model, emphasis should be made on its resistance, inductance and capacitance of the line instead its length since these parameters determine the GIC magnitude and time response.

In the multi-machine system, the response of the system with three different line lengths (80 km, 400 km and 800 km) were compared before deciding on the base case model to compare results with. Usually a short line (< 80 km) is modelled with only its resistance and inductance. As the line length increases, the capacitance of the line needs to be included. The transmission lines were therefore modelled using two different approaches; simple resistive and inductive (RL line model) blocks and an equivalent π-model of the transmission line. The resistance and inductance of both models were set exactly the same. The lines were rated at 400 kV.

The equivalent pi model requires one to define a value for the positive and zero sequence resistance, inductance and capacitance. The positive sequence resistance and inductance were matched between the RL line model and the pi-line model. The zero sequence parameters were set as MATLAB default values. To determine the line capacitance for the pi-line model, the initial load flow solution and Surge Impedance Loading (SIL) of the line were used.

Using the same per unit positive sequence resistance R_{line} and reactance X_{line} as the 4-bus model ($R_{line} = 0.0276\frac{\Omega}{km}; X_{line} = 0.340\frac{\Omega}{km}$), the capacitance ($C_{line}$) was calculated.

The characteristic impedance of the line, Z_c is given by the ratio of its impedance (z) to its admittance (y):

$$Z_c = \sqrt{\frac{z}{y}} = \sqrt{\frac{0.0276 + j0.34}{j(2\pi * 50 * C_{line})}} \tag{4.1}$$

The load flow solution showed that the line was carrying 85 MW of active power. Therefore, the SIL of the line was set to 85 MW and Z_c calculated using the SIL formula.

$$SIL = \frac{V_{rated}^2}{Z_c} \tag{4.2}$$

Therefore $Z_c = \frac{400^2}{85} = 1882\ \Omega$. Using equation (4.1), C_{line} can be calculated. The positive sequence line capacitance was set to 0.304 nF.

The results of the comparison of the line models are shown in Section 7.6.1. A final choice was made on the line model for the multi-machine system; an 80 km tie link modelled as a short line.

The load in area 1 (Load A) is rated 250 MVA 132 kV whereas the load in area 2 (Load B) is rated at 300 MVA 132 kV. Hence, G3 and G4 cannot supply load B adequately. Therefore, power is transferred by G1 and G2 from area 1 to area 2 along the 80 km tie link.

4.2 Modelling of dynamic GIC profile

To accurately determine the dynamic response of the power system to GIC, there is a need to consider the nature of the signature of GIC as discussed in Section 2.1.2.3. This signature or profile needs to accurately represent a realistic GIC event in terms of its magnitude, time duration and frequency components. Studying the effects of GIC on transformer hot spot temperatures, Girgis and Vedante [17] use a GIC profile with a base level of 100 A/phase lasting for 20 minutes followed by 2 minute duration of 400 A/phase GIC. The GIC is modelled as dc without any frequency components as in a realistic storm. Although the 400 A/phase GIC is relatively high, there are reports of large $\frac{dB}{dt}$ measurements and extreme GIC driven by superstorms with Dst index up to 3000 nT/min. Extreme storms in September 1859 and May 1921 are examples of such large disturbances which are believed to be 10 times larger than the Hydro Quebec 1989 storm [1]. Looking into peak GIC estimates for extreme GMDs, Rodger *et al.* [109] show that superstorms can have peak GIC magnitudes of above

400 A and can reach up to 2720 A on a 200 year return. Kataoka and Ngwira [110] relate such high magnitude GIC to auroral electrojet activity (AE-type) and also warn power utilities of the possibilities of high $\frac{dB}{dt}$ in the range of 6000 nT/min.

Using examples of GIC profiles in the IEEE C57.163 Std, results obtained by Heyns *et al* [46]. the wavelet analysis by Munesu *et al.* [48] and discussions on GIC dynamics (See Section 2.1.2.3) , a GIC profile with multiple frequencies and magnitudes was modelled on a time scale of 800 s as shown in Figure 4.2. Motivations for the proposed dynamic GIC profile are given in Table 4.1.

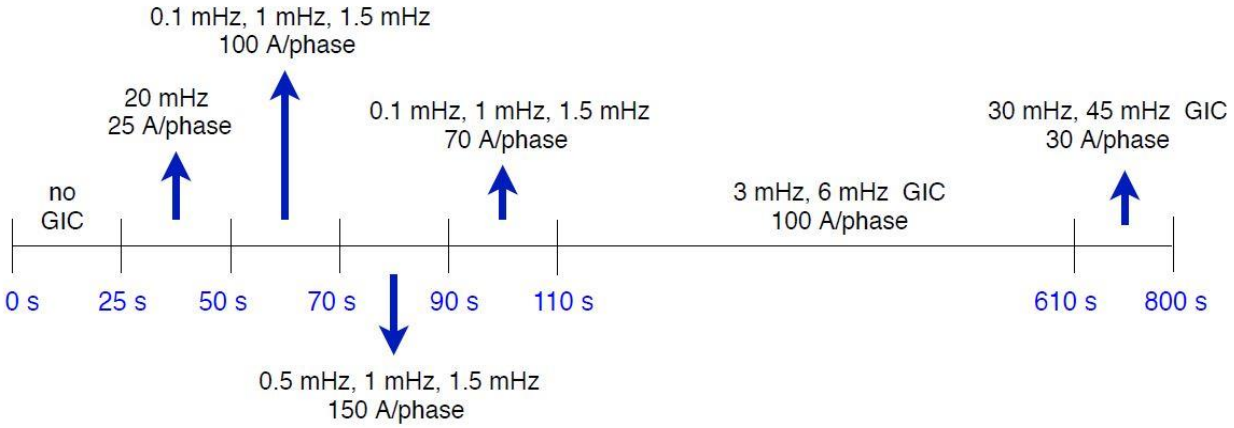

Figure 4.2: Modelling GIC profile over time scale of 800 s

Table 4.1: Modelling a GIC dynamic profile with multiple frequencies and magnitudes at different times

Time interval (s)	Motivation
0 < t < 25	No GIC condition to see steady state system conditions
25 < t < 50	Small GIC magnitudes – they usually have a range of frequencies [48]
50 < t < 70	Burst period – Fluctuations in GIC time series
70 < t < 90	High magnitude GICs which usually have low frequencies between 0.5 – 10 mHz [48]
90 < t < 110	Lower frequencies within the frequency bandwidth persist for longer times compared to higher frequencies [48]
110 < t < 610	High magnitude Pc5 pulsations with period usually from 150 – 600 s [46]
610 < t < 800	Higher frequency components with relatively small magnitudes as per CWT plots [48]

4.3 Chapter summary

Chapter 4 dealt with the modelling of a multi-machine system with 2 areas being supplied by four generators in total. Each area is supplied by two generators. The load was setup in such a way that Area 1 exports power to Area 2 along an 80 km tie link. In Section 4.2 of this chapter, a dynamic GIC profile which is more representative of a realistic GIC, was developed. This GIC signature has a range of frequencies and magnitudes over different time frames. The response of the multi-machine power system model to the dynamic GIC profile is aimed at providing a more realistic insight of the effects of GIC on power systems.

5 Power measurements and design of meters in MATLAB

As discussed in Section 2.5, an accurate definition of reactive power or non-active power is crucial to understand the effects of GIC on power systems. The importance of addressing the reactive power problem for GIC studies has been highlighted more recently by Kirkham and White [80]. Hence, Chapter 5 shows the development of power meters or measurement blocks used to measure reactive power and non-active power for this research.

5.1 MATLAB power measurement blocks

MATLAB Simulink library provides two different usable power measurement blocks. The name of these blocks lacks clarity from MathWorks. The two blocks are called:

1. **3ph instantaneous power measurement block**

This block computes the three phase instantaneous active and reactive power of a periodic set of three phase voltages and currents [111]. The computed reactive power is not accurate when harmonics are present in the three-phase voltage or current signals and when the system is unbalanced. Hence, this meter cannot be used for this research project.

2. **3ph continuous power measurement block**

MATLAB Simulink offers another meter that computes the real and reactive power of each frequency component specified in the symmetrical sequence. This block can be used with sinusoidal and non-sinusoidal systems with harmonics [112]. Hence, this meter is more suited for GIC research since it is possible to extract the active and reactive power components of each harmonic.

The apparent power is calculated by this measurement block using equation (5.1).

$$S_k = P_k + Q_k = \frac{3}{2}\left(V_k e^{j\theta_{V_k}}\right)\left(\overline{I_k e^{j\theta_{I_k}}}\right), \textit{where } k \textit{ is the harmonic number} \qquad (5.1)$$

$V_k e^{j\theta_{V_k}}$ is the phasor of the k^{th} voltage harmonic with magnitude V_k and angle θ_{V_k}.

$I_k e^{j\theta_{I_k}}$ is the phasor of the k^{th} current harmonic with magnitude I_k and angle θ_{I_k}.

$\overline{I_k e^{j\theta_{I_k}}}$ is the complex conjugate of $I_k e^{j\theta_{I_k}}$.

The phasors $V_k e^{j\theta_{V_k}}$ and $I_k e^{j\theta_{I_k}}$ for each phase (A,B and C) are obtained from the voltage and current signals using equation (5.2).

$$\begin{bmatrix} V_{ka}e^{j\theta_{V_{ka}}} \\ V_{kb}e^{j\theta_{V_{kb}}} \\ V_{kc}e^{j\theta_{V_{kc}}} \end{bmatrix} = \frac{2}{T}\int_{t-T}^{t} V(t)\sin(2\pi kf * t)dt + j\frac{2}{T}\int_{t-T}^{t} V(t)\cos(2\pi kf * t)dt \qquad (5.2)$$

T is the period of the input signal ($f = \frac{1}{T}$)

Using the sequence parameter of the block, the active and reactive power of each harmonic sequence (positive, negative and zero sequence) can also be calculated. The total real power and total reactive power are then calculated using the summation of each P_k and Q_k harmonic powers ($P = \sum_{k=0}^{n} P_k \ and \ Q = \sum_{k=1}^{n} Q_k$). The dc component does not contribute to the reactive power calculation. Hence the summation of the harmonic reactive powers starts with the fundamental, $k = 1$.

5.2 IEEE1459 power meter

The IEEE1459 Standard was explained in detail in Section 2.5. In this Section, an IEEE1459 power meter or power measurement block will be developed in MATLAB. The meter was built from simple arithmetic blocks using currents and voltages measured from MATLAB measurement blocks.

The first step is to collect the instantaneous values of currents and voltages across all the phases. These values are then fed through a true RMS block [113]. The neutral current is also measured and converted to its true RMS value. The reason for using the true RMS block is because it computes the RMS value while including all harmonics. If the true RMS block is not used, the RMS value corresponds to the fundamental component of the input signal only.

For a 3-wire system such as at bus 1 and bus 4, there is no neutral and therefore I_n is zero. At bus 2 and 3, the network is a 4-wire system with a neutral wire. Since the neutral wire resistance is 0.2 Ω and the 80 km transmission line phase resistance is 2.208 Ω, ρ is taken as 0.0906 for buses 2 and 3. It is to be noted that the value of ρ does not have much effect on the effective current according to the IEEE1459 standard [83]. Using equation (2.62), the effective current ($I_e = \sqrt{\frac{1}{3}({I_a}^2 + {I_b}^2 + {I_c}^2 + \rho {I_n}^2)}$) can be calculated. Figure 5.1 shows calculations of the effective current, implemented in MATLAB Simulink.

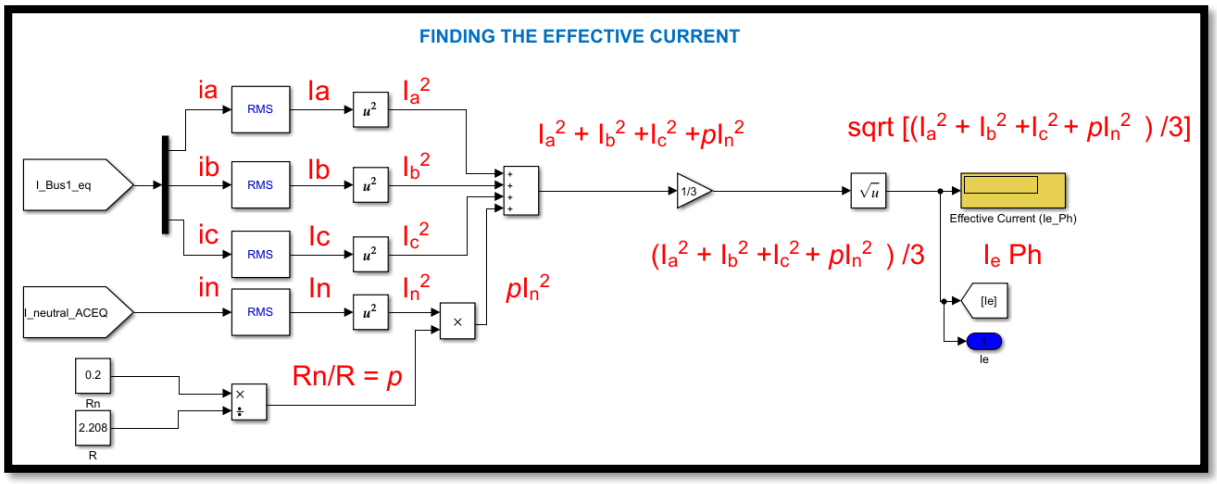

Figure 5.1: IEEE1459 power meter design - Finding the effective current, Ie

Using equation (2.64), effective voltage ($V_e = \sqrt{\frac{3(V_a^2+V_b^2+V_c^2)+(V_{ab}^2+V_{bc}^2+V_{ca}^2)}{18}}$) can also be replicated in MATLAB Simulink as shown in Figure 5.2.

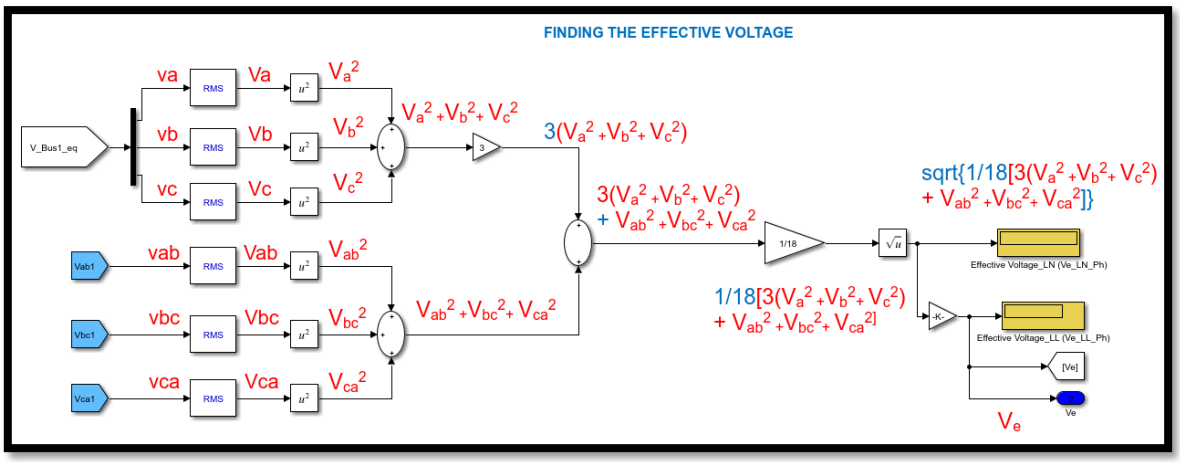

Figure 5.2: IEEE1459 power meter design - Finding the effective voltage, Ve

The product of the effective voltage and current across the three phases gives the apparent power S_e ($S_e = 3V_eI_e$). Calculation of S_e in MATLAB is shown in Figure 5.3.

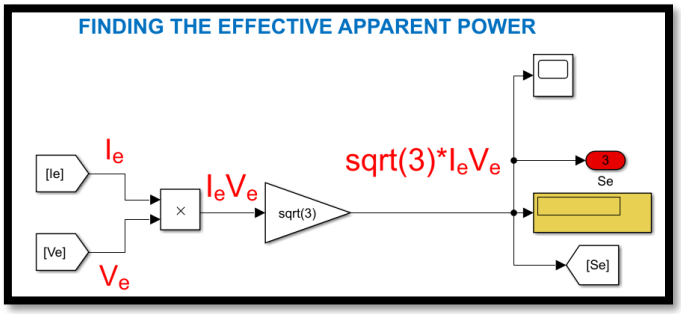

Figure 5.3: IEEE1459 power meter design - Finding the effective apparent power

The active power is calculated using conventional approach that is by the product of instantaneous currents and voltages. Hence, the non-active power can be calculated from Pythagoras theorem using equation 5.3.

$$N = \sqrt{{S_e}^2 - P} \tag{5.3}$$

Calculation of the non-active power was implemented in MATLAB as shown in Figure 5.4

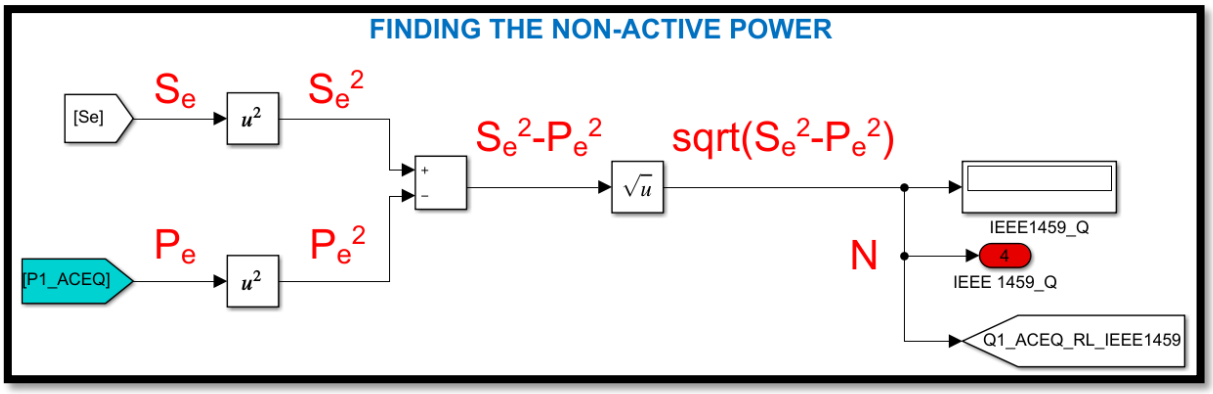

Figure 5.4: IEEE1459 power meter design - Finding the non-active power

5.3 General Power Theory (GPT) meter

A detailed explanation of the General Power Theory (GPT) meter is given in Section 2.5.2. This Section shows the development of the GPT meter using the main equations that govern the GPT.

The first step is to find the instantaneous values of currents and voltages. Using MATLAB measurements blocks, the currents and voltages were recorded. Using simple arithmetic blocks provided by MATLAB Simulink, it is possible to replicate the equations governing GPT into an actual meter that can measure active and non-active powers.

The instantaneous values of the currents in each phase are recorded using MATLAB current measurement blocks. Then, the neutral current is calculated using $\boldsymbol{i_n = -(i_a + i_b + i_c)}$.

If the system is a 3-wire system such as at bus 1 and 4, the neutral current will be zero since there is no neutral wire.

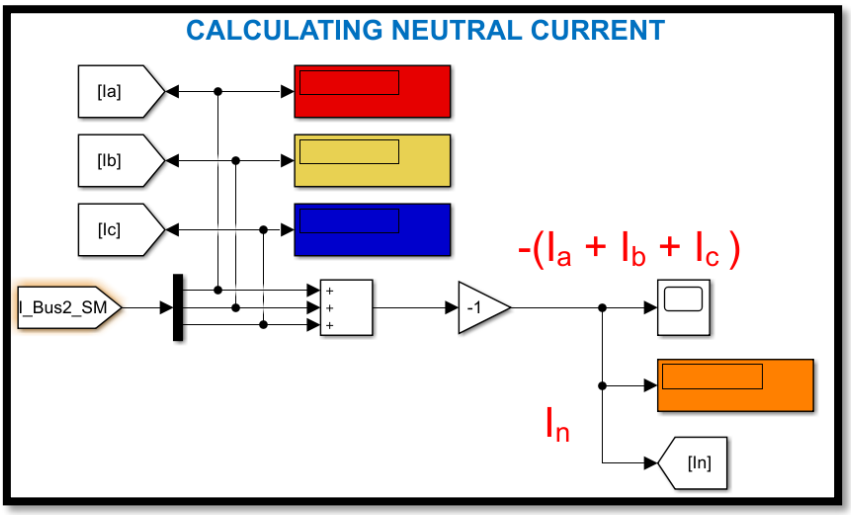

Figure 5.5: GPT power meter design – Calculating neutral current

The resistance-weighed square of the currents ($\|\boldsymbol{i'}\|^2 = (\boldsymbol{i_a}^2 + \boldsymbol{i_b}^2 + \boldsymbol{i_c}^2 + \frac{\boldsymbol{i_n}^2 \boldsymbol{r_4}}{\boldsymbol{r}})\boldsymbol{r}$) is calculated, giving the resistance weighed norm of the current as shown in Figure 5.6.

$\|\boldsymbol{I'}\|^2$ is the average of $\|\boldsymbol{i'}\|^2$ over a whole cycle.

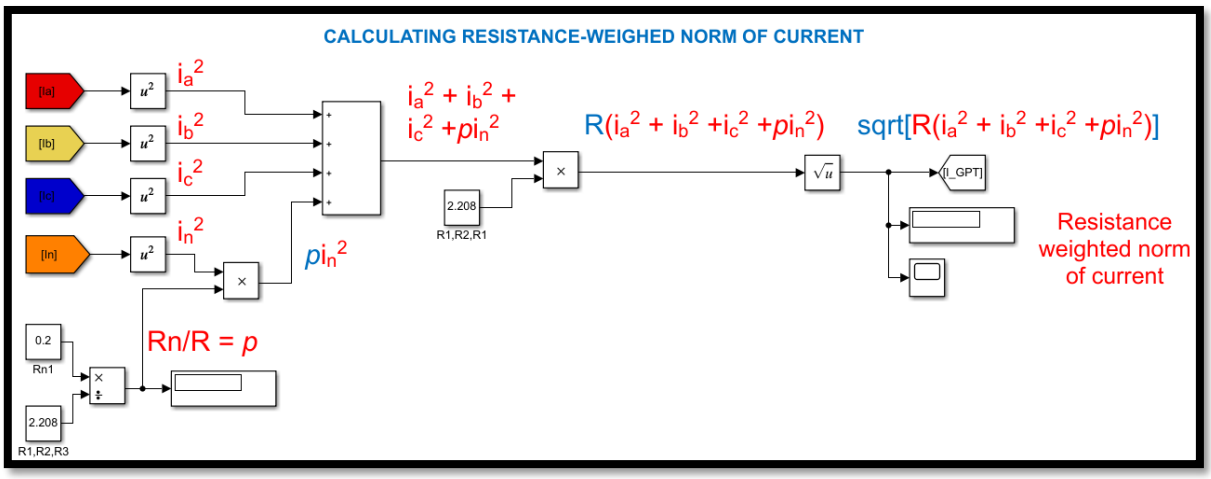

Figure 5.6: GPT power meter design – Calculating $\|\boldsymbol{i'}\|$

Next, for every sample set, a virtual, resistance-weighed reference ($\boldsymbol{e_{ref}} = (\boldsymbol{e_a} + \boldsymbol{e_b} + \boldsymbol{e_c})/(\boldsymbol{3} + \frac{\boldsymbol{r}}{\boldsymbol{r_n}})$) for the voltages is calculated as shown in Figure 5.7.

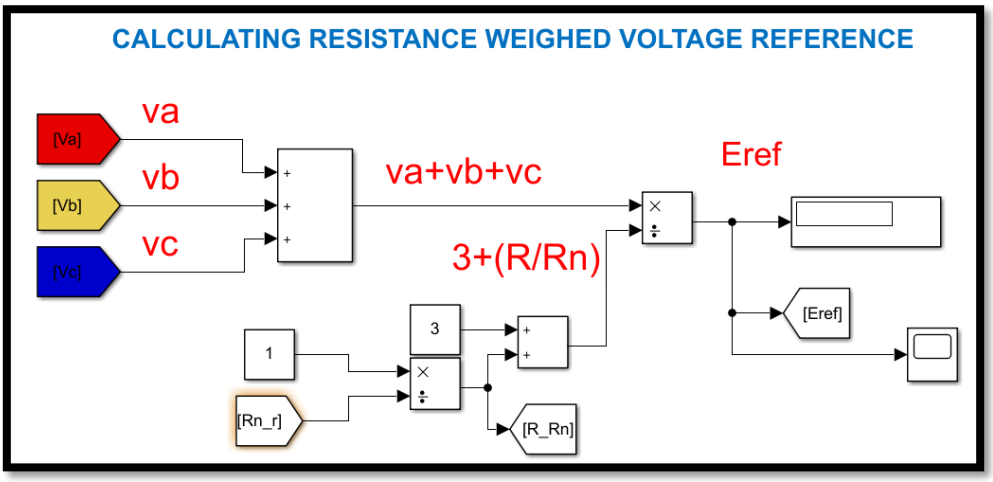

Figure 5.7: GPT power meter design - Calculating resistance weighed voltage reference/null point

Using the value of $\boldsymbol{e_{ref}}$, the meter then calculates the resistance weighed norm of the voltage $\|\boldsymbol{v'}\|$ where $\|\boldsymbol{v'}\|^2 = \left[(\boldsymbol{e_a} - \boldsymbol{e_{ref}})^2 + (\boldsymbol{e_b} - \boldsymbol{e_{ref}})^2 + (\boldsymbol{e_c} - \boldsymbol{e_{ref}})^2 + \frac{(\boldsymbol{0}-\boldsymbol{e_{ref}})^2\boldsymbol{r}}{\boldsymbol{r_4}}\right]\frac{\boldsymbol{1}}{\boldsymbol{r}}$. Implementation of the equation in MATLAB Simulink is shown in Figure 5.8.

$\|\boldsymbol{V'}\|^2$ is the average of $\|\boldsymbol{v'}\|^2$ over a whole cycle.

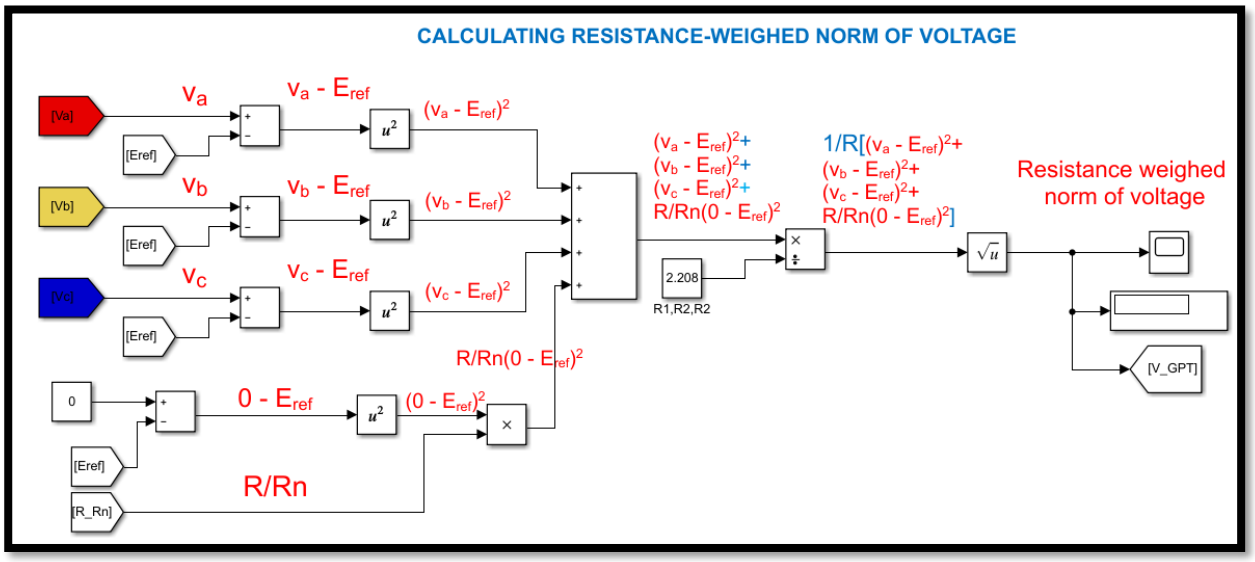

Figure 5.8: GPT power meter design - Calculating resistance weighed norm of the voltage

Finally, the apparent power $\boldsymbol{S} = \|\boldsymbol{V'}\|\|\boldsymbol{I'}\|$ is calculated as shown in Figure 5.9.

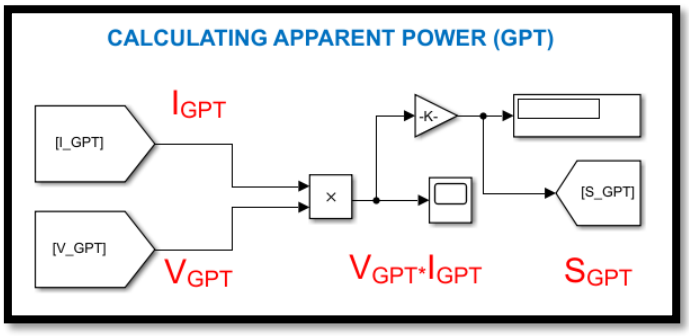

Figure 5.9: GPT power meter design - Calculating apparent power

Since the real power is invariant, it can be computed from the conventional approach or derived from the products of currents and voltages measured from a common virtual reference. Figure 5.10 shows the calculation of active power using the GPT meter with voltages measured from the reference point e_{ref}.

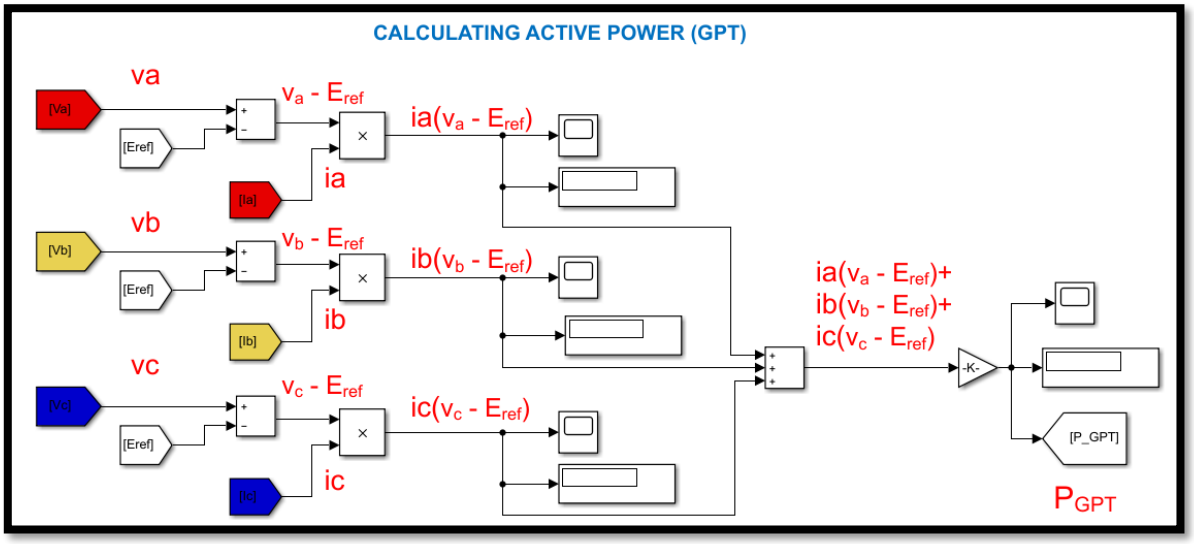

Figure 5.10: GPT power meter design - Calculating active power

The power factor ($\boldsymbol{\lambda = \frac{P}{S}}$) is given by equation (2.95). The total non-active power Q ($\boldsymbol{Q^2 = S^2 - P^2}$) is calculated using equation (2.96). Figure 5.11 shows the blocks used to calculate the non-active power from the apparent power and active power.

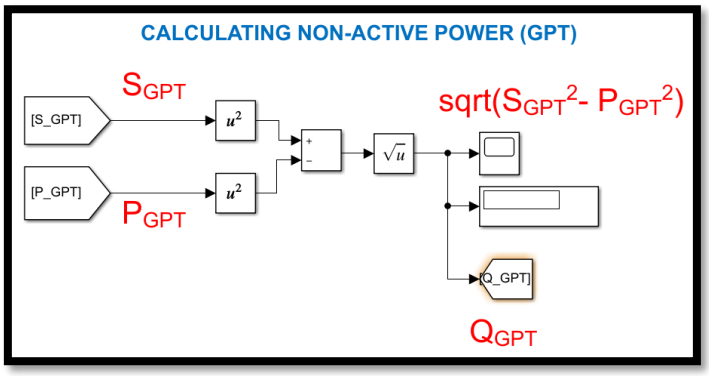

Figure 5.11: GPT power meter design - Calculating non-active power

Section 5 has looked into the development of power meters in MATLAB Simulink. This was an important factor to be considered in the project since an accurate definition of apparent power and non-active power is vital for non-ideal conditions such as during GMDs. It is to be noted, that since the GPT accounts for all the inefficiencies in the power system, the GPT meter will be used to record all power measurements. A comparison between the meters will be shown to highlight the differences in non-active power and apparent power.

5.4 Chapter summary

Chapter 4.3 showed the power measurement blocks available in MATLAB and highlighted that some of these blocks cannot be used for GIC studies. A need for more accurate power measurement blocks were identified. Therefore, two different meters were build within MATLAB Simulink environment. The first meter developed in Section 5.2 was one that agrees to IEEE1459 Standard. Section 5.3 showed the development of a second measurement block which follows the general power theory (GPT). These measurement blocks were designed to compare the differences in power calculated by different methods to understand which method is most suitable for GIC studies.

6 Simulation protocol

6.1 4-bus power system with dc and low frequency ac GIC

The simulation protocol outlines the methods used to address the research questions given in Section 1.1.2. The measurements taken to analyse the results are also identified. It is important to also note that the same 4-bus power system model was simulated using three different source models (see Section 3.2) on the same workspace. The full power system model was built in MATLAB Simulink. The steps used to simulate the 4-bus power system are outlined in Sections 6.1.1 and 6.1.2.

6.1.1 To find the 4-bus system's response to a dcGIC model (dcGIC)

- Using the load flow initialisation tool provided by MATLAB Simulink, the voltages, angles, active, reactive powers consumed or produced at each bus were calculated. The load flow solution was then applied to the model which automatically initializes the synchronous generator and excitation system parameter values.
- The GIC was modelled using a 350 V dc voltage source injected in the neutral. The 4-bus power system was simulated with the GIC injected at t = 25 s. The reason for choosing 25 s was to allow the system to stabilise before any disturbance occurs.
- The simulation was stopped at time t = 200 s, after the power system had reached steady state in a post-GIC equilibrium position.
- The transformer flux, magnetizing currents, bus voltages and currents were captured using the three-phase V/I measurement blocks provided by MATLAB. A ground reference was used to measure the voltages in each phase.
- To find the active power, non-active/reactive power and apparent power at each bus, a comparison of the meters was initially done using the same 4-bus network and the dcGIC. This served to decide which power meter is more accurate under non-ideal conditions.
- For the synchronous generator model, the following measurements were taken;
    - Input mechanical power P_m
    - Field voltage E_{fd}
    - Field current I_{fd}
    - Stator voltage in abc reference frame (V_{as}, V_{bs}, V_{cs})
    - Stator voltage in dq reference frame (V_d, V_q)
    - Stator current in abc reference frame (I_{as}, I_{bs}, I_{cs})
    - Stator current in dq reference frame (I_d, I_q)

- D-axis damper winding current (I_{1d})
- Q-axis damper winding currents (I_{1q}, I_{2q})
- Rotor angle theta (θ)
- Rotor angle deviation ($d\theta$)
- Rotor speed (ω_m)
- Rotor speed deviation ($d\omega_m$)
- Load angle (δ)
- Electromechanical torque (T_e)

- For harmonic analysis, the MATLAB Fast Fourier Transform (FFT) block was used. The input to the block is the 3-phase voltage or current. The block outputs the magnitude and angle of the specified frequency component. All harmonics up to the 15th harmonic were recorded over time and visualized on a scope.

6.1.2 To find the 4-bus system's response to a single frequency acGIC model (SF_ac_GIC)

- The dcGIC model was then replaced by an ac voltage source with a frequency of 20 mHz and peak amplitude 350 Vac.
- The load flow solution was applied and the simulation started.
- A 20 mHz acGIC model was then injected at t = 25 s.
- The simulation was stopped at time t = 200 s when the acGIC has undergone 3.5 cycles.
- Using the measurement blocks provided by MATLAB, the voltages and currents were measured at each bus. For the measurement of power, only the GPT meter was used since the definition of apparent power using GPT is more accurate compared to conventional definitions.
- Under acGIC conditions, similar measurements were taken at three-time instances;
  - when the GIC peaks in the positive half cycle.
  - when the GIC peaks in the negative half cycle.
  - when the GIC crosses the zero-axis.
- For the synchronous generator model, the same measurements as with dcGIC were taken.
- Using an FFT block, the harmonics in voltage and currents were captured under no GIC conditions and at the three-time instances deemed important with the acGIC model.

6.1.2.1 Introducing unbalance to study non-conventional harmonics

The harmonic analysis for the 4-bus system's response to acGIC was extended by introducing unbalance to the system. This followed due to results obtained from the 4-bus system's response to dcGIC which deviated from conventional harmonic sequence theory.

A companion paper has already shown that MATLAB three phase five limb transformers do not model inter-phase magnetic coupling [98]. Therefore, unbalance was intentionally introduced in the system by varying the line resistances and inductances. Two unbalanced scenarios were used; a slightly unbalanced system and an extremely unbalanced system with transmission line impedances (per km) shown in Table 6.1.

Table 6.1: Transmission line impedance for balanced and unbalanced systems with Z_l= 0.0276+jω0.3047, ω=100π

Phase	Balanced	Slight unbalance	Extreme unbalance
A	Z_l	Z_l	Z_l
B	Z_l	0.9 Z_l	0.5 Z_l
C	Z_l	1.1 Z_l	2 Z_l

- Harmonics in the generator bus current were captured using an FFTblock over the full 200 s of simulation time. All harmonics up to the ninth harmonic were extracted as higher order harmonics become increasingly insignificant.
- The sequence of each harmonic was also extracted using the sequence analyser block over the 200 s simulation time. The sequence analyser block applies Fortescue's transformation to calculate the sequence component of each harmonic.
- The percentage voltage unbalance (VUF) was calculated arithmetically using simple blocks in MATLAB as the ratio of negative sequence voltage to positive sequence voltage.

6.2 Multi-machine power system with a dynamic GIC profile

To test the response of the multi-machine system developed, a series of test protocols were used. The base case was called "Test 0". All other tests were compared to "Test 0". Changes to the excitation system of each generator were made to the base case model. These changes were made in tests 1,2 and 3.

6.2.1 Test 0 – Base case and transmission line model comparison

As mentioned in Section 4.1, the multi-machine tie link was modelled as simple RL blocks and full π-equivalent models. These two line models were compared for an 80 km, 400 km and 800 km line

length. The final choice of the line length followed from the results shown in Section 7.6.1 and it was decided that an 80 km line modelled using simple RL blocks would be used for further simulations of test 1,2 and 3. This was because the most important parameters are the resistance and inductance of the line. Any line length can be represented by these parameters. In fact, many GIC studies [105] have used transmission line lengths less than 80 km.

6.2.2 Test 1 - Generator excitation system model

The effect of changing the model of the AC excitation system for different generators was studied. The load bus voltage and var output of the generators were then captured for each test shown in Table 6.2.

Table 6.2: Effect of changing excitation system model at different generators in multi-machine system

Test number	G1	G2	G3	G4
0	AC1A	AC1A	AC1A	AC1A
1a	AC1A	AC1A	AC4A	AC1A
1b	AC1A	AC1A	AC4A	AC4A
1c	AC1A	AC4A	AC4A	AC4A
1d	AC4A	AC4A	AC4A	AC4A

6.2.3 Test 2 - Effect of Kd

Next, the effect of the demagnetising factor was analysed by varying K_D of the excitation system control of different generators. The tests shown in Table 6.3 were carried out sequentially by changing K_D of G3, G4 in area 2, followed by G2 and G1 in area 1. Again, the load bus voltage and var output of the generators were captured.

Table 6.3: Effect of changing Kd of different excitation systems within the multi-machine system

Test number	G1	G2	G3	G4
0	0.38	0.38	0.38	0.38
2a	0.38	0.38	0.19	0.38
2b	0.38	0.38	0.19	0.19
2c	0.38	0.19	0.19	0.19
2d	0.19	0.19	0.19	0.19

6.2.4 Test 3 - Effect of Ke

Test number	G1	G2	G3	G4
0	2.5	2.5	2.5	2.5
3a	2.5	2.5	1.0	2.5
3b	2.5	2.5	1.0	1.0
3c	2.5	1.0	1.0	1.0
3d	1.0	1.0	1.0	1.0

6.3 Chapter summary

Chapter 6 outlined the simulation protocol for both the 4-bus network and multi-machine network. The steps used to test the response of both networks to GIC were highlighted. Methods used to collect the required data for analysis were shown. The next chapter shows the results that were obtained from applying the simulation protocol to the 4-bus and multi-machine systems.

7 Results and Discussion

In this chapter, the results gathered from the MATLAB simulations are presented and discussed. The response of the 4-bus system is considered first, followed by the multi-machine power system's response. With the 4-bus system, the power system's responses to dc GIC and a single frequency acGIC are compared. Differences between the generator models are identified and explained. The ideal source is labelled "ACEQ-IDEAL". The non-ideal source is labelled "ACEQ-RL" whereas the full synchronous generator model is labelled "SM". The effects of excitation system control on reducing the voltage dip from GIC are shown. A comparison of the responses of different IEEE AC excitation systems to GIC is shown. The differences between the power meters developed for this study are identified. Finally, results obtained from simulations of the multi-machine power system model with a dynamic GIC profile are analysed before conclusions drawn in Chapter 8.

7.1 4-bus power system response to dcGIC

Section 7.1 shows the results obtained from simulations of the 4-bus power system subjected to a dcGIC model.

7.1.1 Neutral Current

The dcGIC was injected in the neutral with the positive polarity of the dc voltage source pointing towards T12 (See Figure 3.1). The resulting RMS neutral current is shown in Figure 7.1.

Without GIC, the neutral current was 0.3773 A. In a balanced sinusoidal 3-phase 4-wire system, the neutral current should only contain zero sequence harmonics since they are additive. A harmonic analysis of the neutral current (See Figure 7.13) shows that it consists of the zero-sequence 3^{rd}, 9^{th} and 15^{th} harmonics. However, other harmonics such as the 7^{th}, 11^{th} and 13^{th} are also present. The harmonics drawn by T12 (3^{rd}, 5^{th}, 7^{th}, 11^{th}, 13^{th}; See Figure 7.15) contribute to the neutral current. Unbalance due to core asymmetry in the 3p5L transformer type, although very small, introduces other non-conventional harmonic orders and sequences which add up to the rms value of the neutral current.

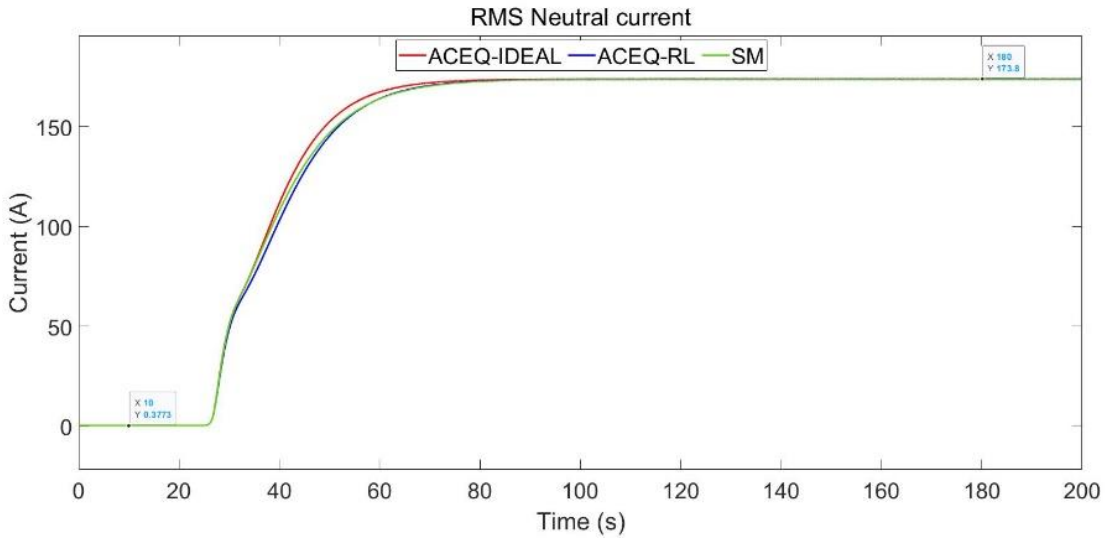

Figure 7.1: RMS Neutral current with dcGIC injected at t = 25s showing increase in neutral current to new steady state value due to dcGIC flux

When the dcGIC was injected, the neutral current increased to a new steady state value of 173.8 A. This is due to increased harmonics resulting from transformer saturation (See Figure 7.14). The GIC flowing in the neutral can be calculated as follows;

$$GIC = 173.8\ A - 0.3773\ A = 173.4\ A$$

The GIC corresponds to 57.8 A per phase, a typically high value of GIC. It takes around 55 s for the neutral current to reach steady state. This transient time depends on the power system inductances [39] . The X/R ratio of network equipment such as transformers causes a time delay in GIC growth as shown in several research [2], [100], [114], [115], [116].

The neutral current settled at the same steady state value irrespective of the model of the source. However, there were differences observed between the sources during the transient phase. The neutral current rose faster with the ideal equivalent source (ACEQ) compared to the synchronous machine (SM) and equivalent source with RL impedance (ACEQ_RL).

The GIC flows from the neutral, into the shunt branch of the step-up transformer T12, and to the transmission lines. Since there is an increased current flowing in the shunt branch of the transformer, the flux increases as shown in Figure 7.2.

7.1.2 T12 and T34 Fluxes

The dcGIC causes an offset in flux as discussed in Section 2.1.1.1. Figure 7.2 shows that T12 and T34 have a flux offset in opposite directions. T12 has a flux offset of 98.6 Vs which means that the transformer goes in deep saturation as per the specified saturation characteristic. The same offset was observed at both positive and negative flux peaks. T34 has a flux offset of 1167 Vs at the positive

peak and 1218.7 Vs at the negative peak. This represents a 4 % difference in offset which can be considered the same within 10 % limit of experimental accuracy.

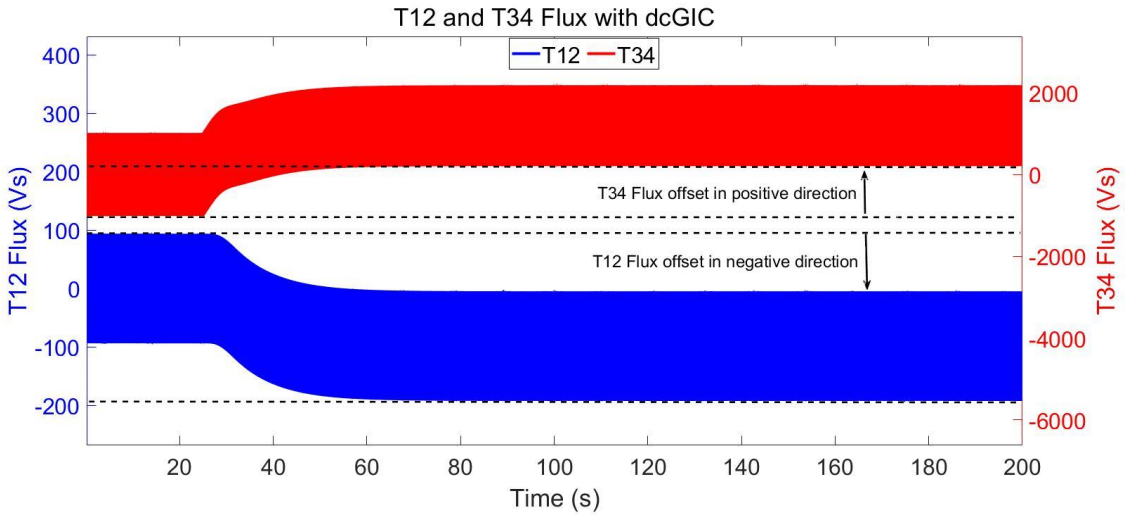

Figure 7.2: T12 and T34 Flux showing offset in the reverse directions

The offset in flux depends on the magnitude of the injected GIC, number of turns in the windings carrying the GIC and the reluctance of the dc flux path [17]. Since the GIC flux opposes T12's normal transformer flux direction, the flux offset is in the negative direction as depicted from Figure 7.3. Hence, on the BH curve or saturation curve of the transformer, this would correspond to a shift in flux in the negative direction until the point of deep saturation. For T34, the GIC flux follows the transformer's magnetising flux direction, causing a flux offset in the positive direction as shown in Figure 7.3. Hence, on the BH curve or saturation curve of the transformer, this would correspond to a shift in flux in the positive direction until the point of deep saturation.

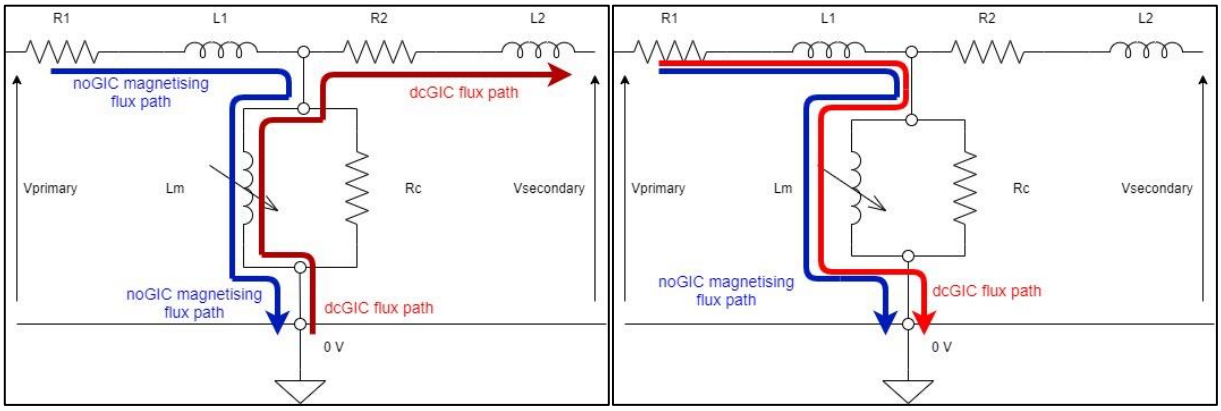

Figure 7.3: dcGIC flux path showing direction of flux offset in saturated T12 (left) and T34 (right)

Within the shunt branch of the transformer, the GIC flows through the magnetising inductance L_m which is lower when operating in saturation [14], [103]. Hence, the magnetising reactance X_m is lowered causing an increase in the magnetising current of the transformer [117]. The increase in the

magnetising current depends on the shape of the saturation curve or BH curve of the transformer core material.

Using Figure 3.3 to derive an equation for T12's saturation curve in the saturation region gives;

$$Flux = 0.0357\ Imag + 111.45 \qquad (7.1)$$

The initial flux is 93.87 Vs with an offset of 98.6 Vs. To represent this flux on the saturation curve, the initial flux is added to the offset yielding 192.47 Vs.

Replacing this flux in equation (7.1) gives;

$$192.47\ Vs = 0.0357\ Imag + 111.45$$

$$Imag = 2269.5\ A$$

Therefore, a magnetising current of 2269.5 A was expected during GIC conditions. The magnetising current observed during the simulation is shown in Figure 7.4.

7.1.3 T12 and T34 Magnetising currents

Figure 7.4 shows the magnetising current of the step-up transformer, T12. The shift in the magnetising current can be observed from the plot. When the GIC is injected at t = 25s, it flows in the shunt magnetising branch causing an increase in current. The magnetising current is no longer symmetrical along the zero-axis due to the presence of even harmonics.

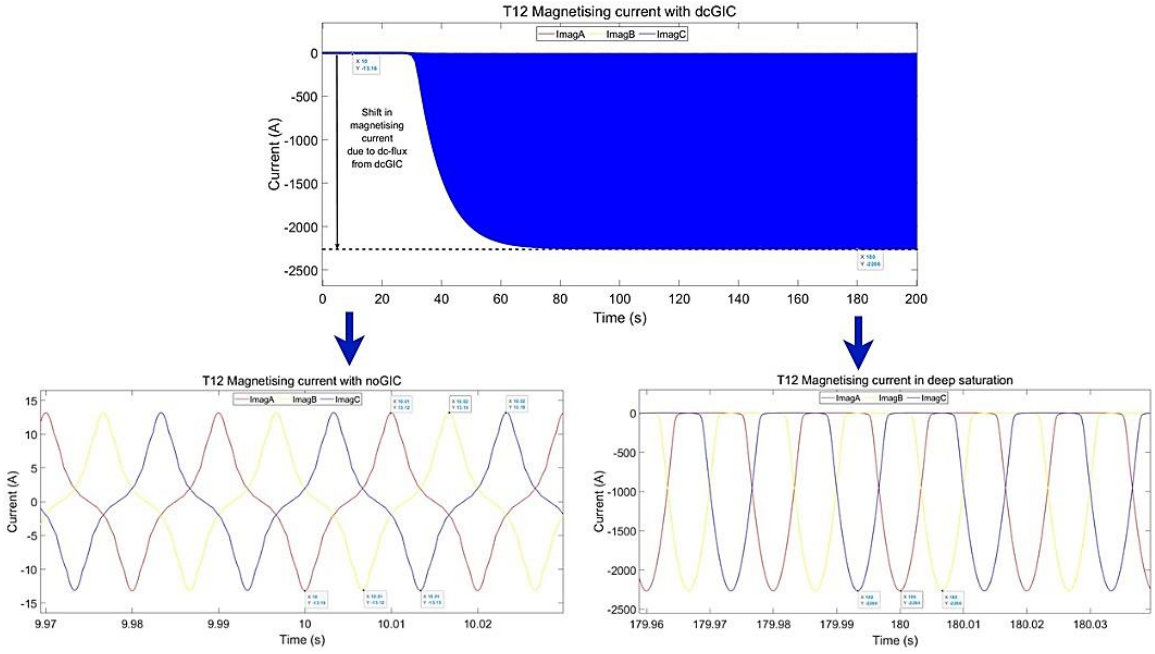

Figure 7.4: T12 Magnetising current with dcGIC injected at t = 25s showing increase and shift according to direction of dc flux from GIC

The lower left plot of Figure 7.4 shows the shape of the magnetising current of T12 under normal operating conditions that is, without any GIC. The shape of the magnetising current without GIC agrees to simulation results and observations reported in literature [8][115][118]. The magnetising current is non-sinusoidal because the generator is overexcited. Hence, the transformer is operating above the knee point of the saturation curve. The magnetising current is not fully symmetrical about the zero-axis showing the presence of low magnitude even harmonics (See harmonic analysis of magnetising current in Figure 7.15). Moreover, it peaks around 13.2 A with slight negligible unbalances across phases due to core asymmetry. For every peak in the flux waveform, the magnetising current has a peaky shape due to the third harmonic component (See Figure 7.15) required to produce the necessary flux. The small magnetising current under no GIC conditions represents 2 % of the full load current, agreeing to literature.

The lower right plot of Figure 7.4 shows the magnetising current of T12 when operating in deep saturation. The magnetising current peaks at -2266 A in all phases. No unbalance was observed although the 3p5L transformer shows significant unbalance in reality. The MATLAB transformer model does not model interphase magnetic coupling. The observed magnetising current is very close to the estimated value of -2269.5 A (See Section 7.1.2) confirming that the transformer model indeed operates based on the saturation curve. The negative sign denotes a shift in the negative half cycle in the magnetising current due to dcGIC flux opposing the normal shunt branch flux direction as previously shown in Figure 7.3. The magnetising current is no longer symmetrical along the zero-axis showing the presence of even harmonics. The harmonic spectrum of T12's magnetising current with GIC, is shown in Figure 7.16.

Transformers under dc-bias or GIC conditions rarely reach deep saturation. Very high levels of dc or GIC are required for long periods of time for the core to fully saturate. However, in simulations, it is good to consider the worse-case scenario, which is shown here, when T12's magnetising inductance drops significantly (deep saturation) leading to very high magnetising currents. Similar high magnetising current peaks have been observed in generator step up transformers with 50 A GIC in the neutral [20].

The GIC flows from T12 into the transmission lines, towards T34. The flux path of this GIC can be observed in Figure 7.3

As calculated for T12, one can estimate the equation of the saturation curve of T34 in the saturation region to calculate the expected magnetising current. Using T34 open circuit test results in Figure 3.3, the equation can be found using equation (7.2).

$$FFlux = 4.7628\, Imag + 1287 \qquad (7.2)$$

The final flux is 2183 Vs. Replacing this flux in the equation above;

$$2183\, Vs = 4.7628\, Imag + 1287$$

$$Imag = 188.1\, A$$

Therefore, a magnetising current of 188.1 A is was expected during GIC conditions. The magnetising current observed during the simulation is shown in Figure 7.5.

The step-down transformer T34 also sees an increase in magnetising current as shown in Figure 7.5. The magnetising current peaks at 0.8234 A when there is no GIC. Introduction of the dcGIC causes the magnetising current to peak at 188 A. This is equal to the expected peak magnetising current calculated. Contrary to T12, the GIC current flows in the same direction as the shunt branch magnetising current as shown in Figure 7.3. Hence, the magnetising current of T34 peaks in the positive half cycle.

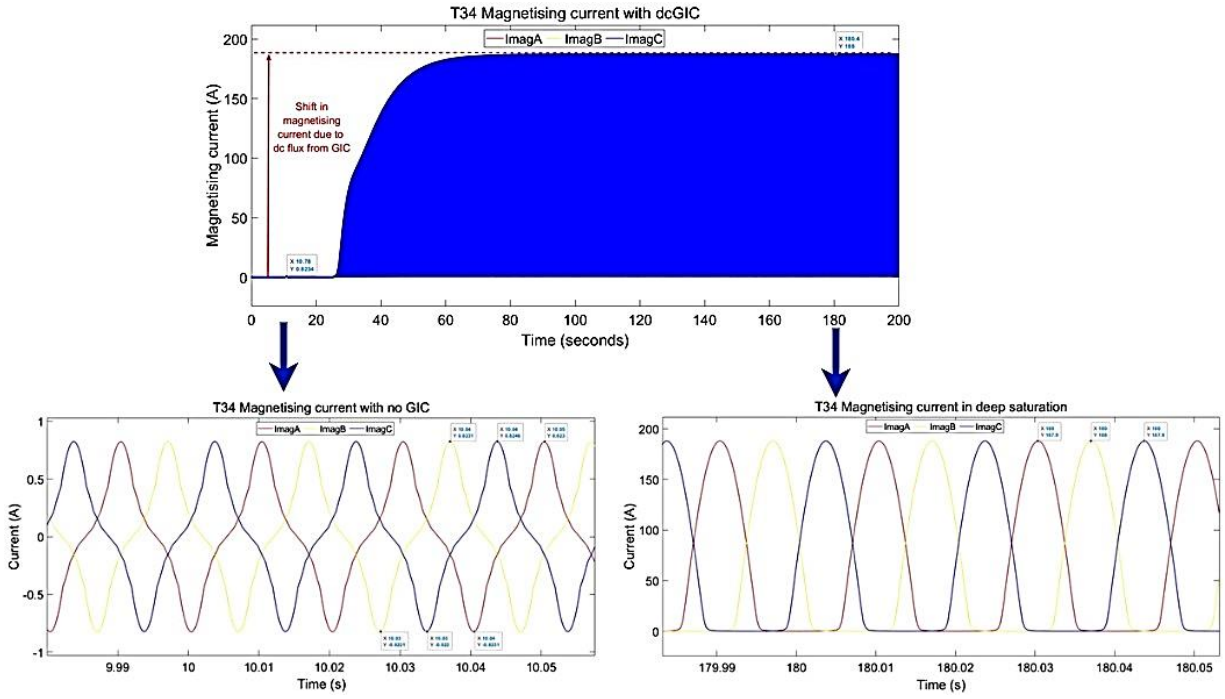

Figure 7.5: T34 Magnetising current with dcGIC injected at t = 25s showing increase and shift according to direction of dc flux from GIC

The lower left plot in Figure 7.5 shows the magnetising current of T34 under normal operating conditions (no GIC). The shape of the magnetising current of T34 is very similar to T12. When the power system reaches a post-GIC steady state condition, the magnetising current of T34 shows high magnitude short duration pulses as shown in the lower right plot of Figure 7.5. The peak magnetising current of T34 has increased from 0.82 A to 188 A. With such high peaks, deep saturation has been

reached. The magnetising current peaks in the positive half cycle and symmetry along the zero-axis is lost. Again, the increased magnetising current leads to increased non-active power consumption of the transformer since it lags the applied primary voltage by 90 degrees.

7.1.4 Bus 1-4 currents (I1 – I4)

Bus 1 and 2 RMS currents (I1, I2) are shown in Figure 7.6 and Figure 7.7 respectively. Bus 3 current (I3) is not shown since it is similar to I2. It is to be noted that only phase A current are shown since the other two phases are balanced. The difference between phase A, B and C RMS currents was less than 0.8 %.

Table 7.1 provides a summary of RMS current at each bus.

Table 7.1: Summary of bus 1-4 RMS currents under noGIC and dcGIC conditions showing comparison different models of the source

Model of source	RMS current without GIC (A)	RMS current at steady state dc GIC condition (A)	% change in RMS current
Bus 1 RMS current			
ACEQ-IDEAL	7517	8718	+15.98
ACEQ-RL	7507	7514	+0.093
SM	7517	7964	+5.61
Bus 2 RMS current			
ACEQ-IDEAL	374.5	397.1	+5.69
ACEQ-RL	374.1	338.5	-9.52
SM	374.5	358.5	-4.27
Bus 4 RMS current			
ACEQ-IDEAL	1132	1104	-2.47
ACEQ-RL	1130	923.6	-18.27
SM	1132	983.9	-13.08

Verifying currents prior to GIC injection

Consider T12 which has a turns ratio, a_{12} where;

$$a_{12} = \frac{V2}{V1} = \frac{I1}{I2} \tag{7.3}$$

Using ACEQ-IDEAL as an example, with $I1 = 7517\ A$, $I2$ can be found.

$$I2 = 7517\ A\ x\ \frac{20\ kV}{400\ kV} = 375.85\ A$$

Similarly,

$$\frac{V3}{V4} = \frac{I4}{I3}$$

With $I3 = 374.5\ A$, $I4$ can be found.

$$I4 = I3\ x\ \frac{V3}{V4} = 374.5\ A\ x\ \frac{400\ kV}{132\ kV} = 1134.8\ A$$

The values given in Table 7.1 are therefore correct considering the losses within the transformer.

The RMS currents at buses 1-4, prior to GIC injection, match closely between the three source models. This current changes to a new steady state value when GIC is injected. The change in RMS current depends on the model of the source as shown in Figure 7.6.

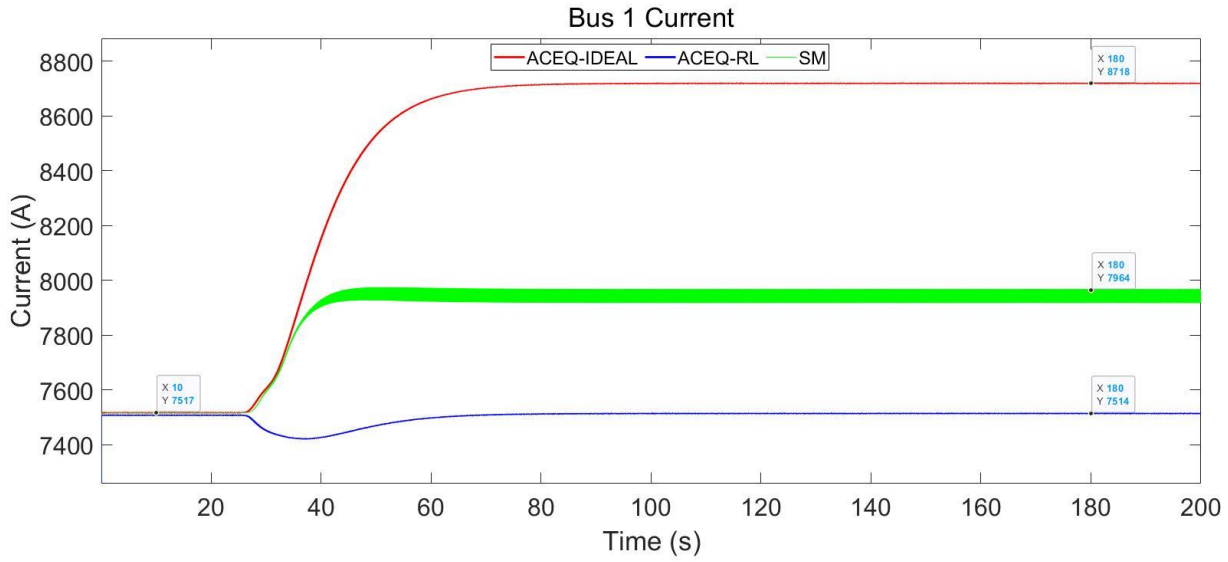

Figure 7.6: Bus 1 RMS current with dcGIC injected at t = 25s

An increase in I1 is the response of the source model to the increased non-active power demand. The sources tend to produce more non-active power (See Figure 7.10) to maintain the bus voltages within limits. The source's inductive reactance X_s appears to have significant effects on the generator's output as discussed in Section 2.3.3.

Bus 2 RMS current varies as shown in Figure 7.7 .

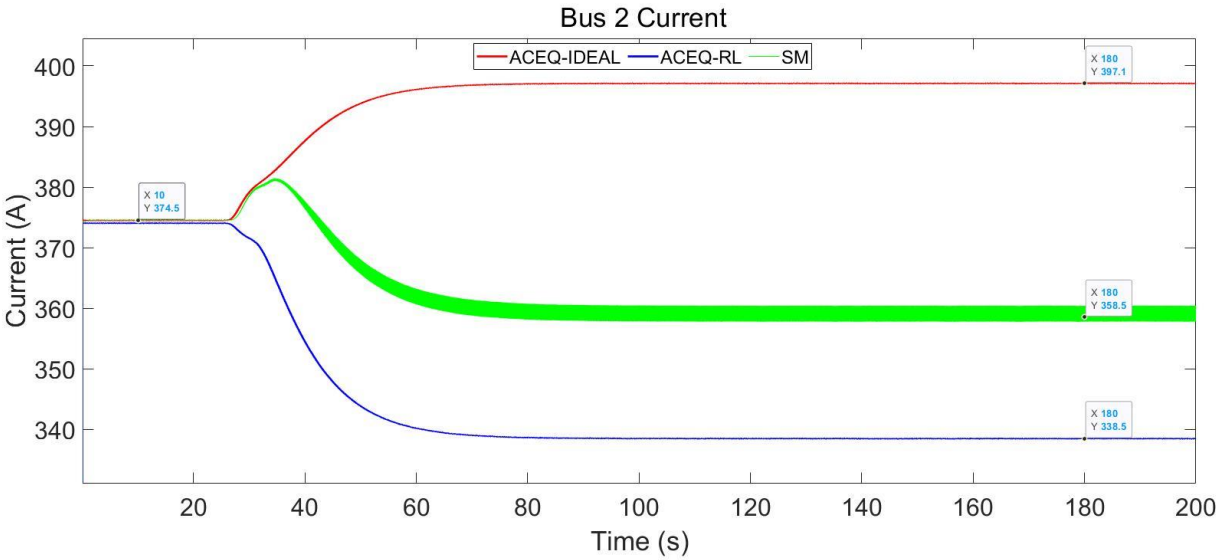

Figure 7.7: Bus 2 RMS current with dcGIC injected at t = 25s

With the ACEQ_IDEAL, I2 increases whereas with the ACEQ_RL and SM, the transmission line current decreases to a new steady state value. A comparison of the ACEQ-IDEAL and ACEQ-RL shows that the ACEQ-IDEAL is able to provide more fundamental frequency current compared to the ACEQ-RL as depicted from Figure 7.8.

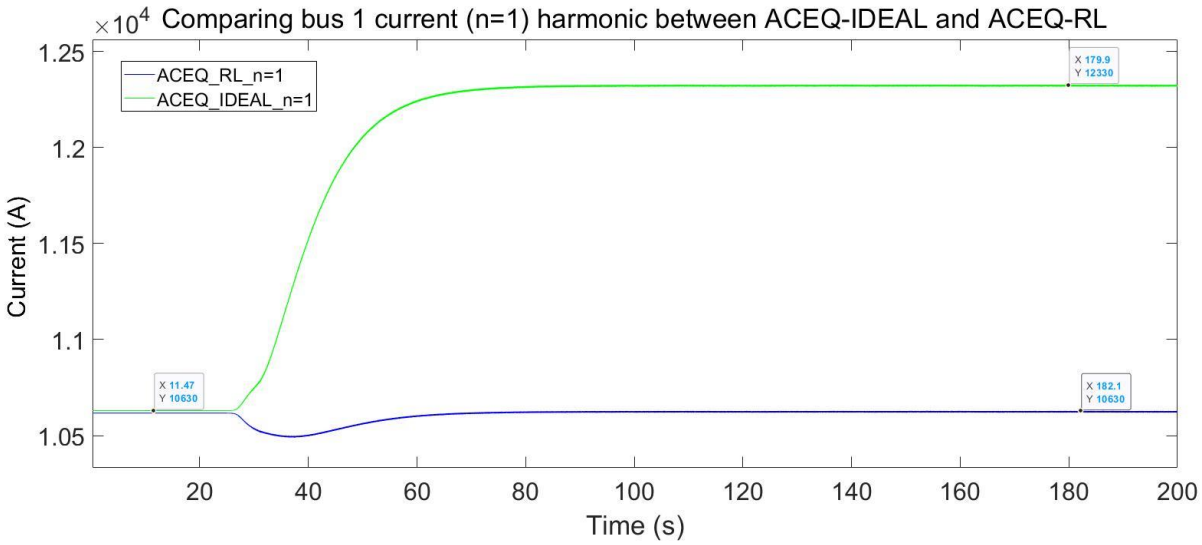

Figure 7.8: Fundamental frequency component of bus 1 instantaneous current

The increase in bus 1 fundamental frequency current for the ACEQ-RL is not enough to support the non-active power demand and therefore a corresponding drop in I2 can be observed.

For all the generator models, I4 drops. However, the drop is more significant for the ACEQ_RL and SM followed by the ACEQ_IDEAL. Since the ideal source can provide more non-active power output (See Figure 7.10), the drop in I4 is smaller.

7.1.5 Bus 1-4 voltages (V1-V4)

Table 7.2 provides a summary of the bus voltages showing how the different responses of the source model reflect on the bus voltages.

Table 7.2: Summary of bus 1-4 voltages under no GIC and steady state dcGIC conditions showing comparison between different source models

Model of source	Voltage without GIC (pu)	Voltage at steady state dc GIC condition (pu)	% change in voltage
Bus 1 voltage			
ACEQ-IDEAL	1.05	1.05	0
ACEQ-RL	1.049	0.8828	-15.84
SM	1.05	0.9453	-9.97
Bus 2 voltage			
ACEQ-IDEAL	1.014	1.004	-0.986
ACEQ-RL	1.012	0.8424	-16.76
SM	1.014	0.8971	-11.53
Bus 3 voltage			
ACEQ-IDEAL	0.9928	0.9761	-1.68
ACEQ-RL	0.9916	0.8181	-17.50
SM	0.9928	0.8743	-11.94
Bus 4 voltage			
ACEQ-IDEAL	0.9659	0.9422	-2.45
ACEQ-RL	0.9648	0.7885	18.27
SM	0.9659	0.8455	12.47

Figure 7.9 shows the voltage at the generator bus for the different sources used.

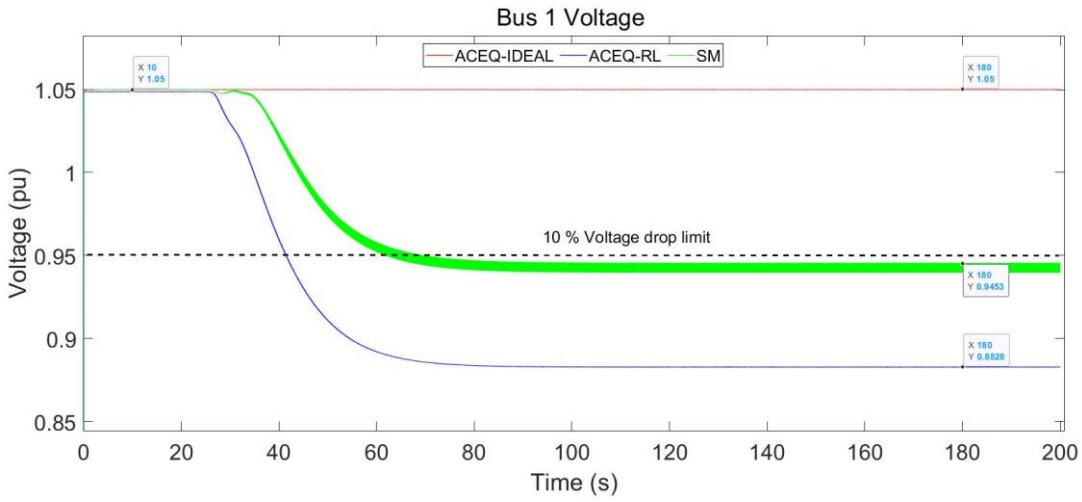

Figure 7.9: Bus 1 voltage with dcGIC injected at t = 25 s

The ACEQ-IDEAL is able to keep the terminal voltage constant at 1.05 pu (21 kV) even under GIC conditions. This is because the ideal source is able to produce enough non-active power to meet the increased demand. Contrarily, with a source impedance included, the generator terminal voltage can no longer be held constant as seen by the response of the ACEQ-RL and SM. Both the SM and ACEQ-RL violate the 10 % voltage drop limit under GIC conditions. Generator undervoltage relays may be triggered causing the source to be disconnected from the power system. With the loss of the generator, the bus voltages may continuously decrease until a voltage collapse occurs.

With the ACEQ-RL and SM, the voltage supplied to the primary windings of the transformer is reduced under steady state dc GIC conditions. Hence, T12 converts a lower primary voltage to its secondary voltage, explaining the lower bus 2 voltages observed. Bus 3 voltages are lower than bus 2 voltages due to the voltage drop across the transmission line impedance. At the load bus, a small voltage drop is observed when the source is modelled as an ACEQ-IDEAL. With the source modelled as a full SM or ACEQ-RL, the voltage drop at the load bus exceeds the 10 % limit. The ACEQ-RL shows the largest voltage drop. Since no load tap changer or dynamic load was modelled, the load bus voltage does not recover from the drop and settles at a steady state value.

The decrease in bus 1-4 voltages can be attributed to the increased non-active power demand due to the saturating transformers. Section 7.1.6 is aimed to show this increased non-active power demand.

7.1.6 Bus 1-4 Non-active power (Q1-Q4)

Since the magnetising currents of the transformers increase under GIC conditions, their non-active power consumption also increases. In response to this increased demand, the generators try to increase their non-active power output to maintain the terminal voltage at 1.05 pu. Figure 7.10 shows the non-active power output of the different source models with 173.4 A GIC in the neutral. The non-active

power has been computed using the GPT meter (See Section 5.3) following group 2 calculations proposed in Table 2 of the initial papers of GPT [85] .

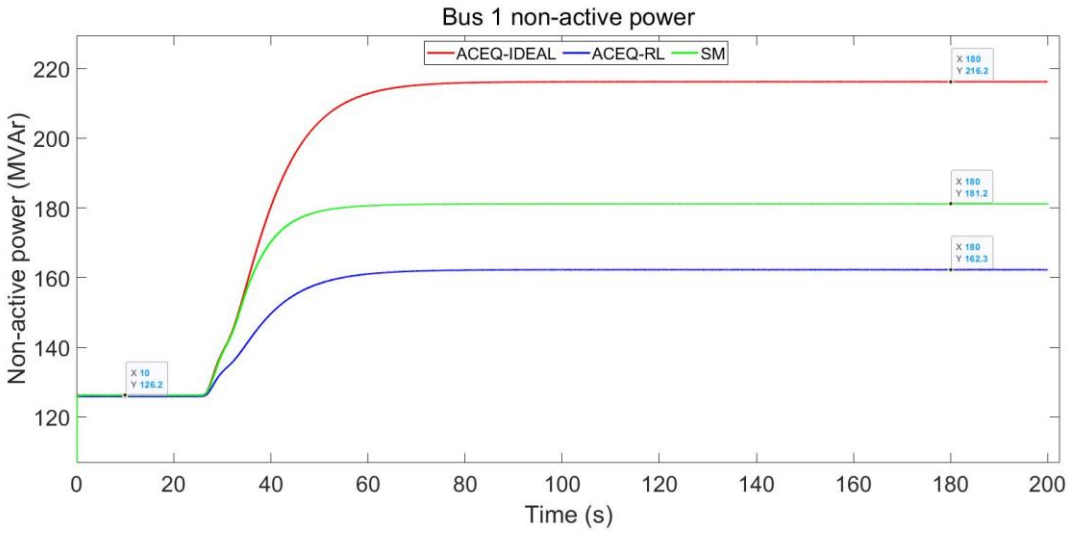

Figure 7.10: Bus 1 Non-active power with dcGIC injected at t = 25 s

Prior to GIC injection, the three source models generate 126.2 MVAr of non-active power, operating at a lagging power factor of 0.8869. The sources produce more non-active power than the specified non-active load since they also supply the transformers T12, T34 and compensate for the non-active power consumed by the transmission line.

The increased non-active power demand on the grid due to the saturated transformers causes the sources to generate more non-active power. The ACEQ-IDEAL produces more non-active power than the SM and ACEQ-RL. This explains why the voltage drops observed with the SM and ACEQ-RL are larger than those observed with the ideal source.

The effects of GIC on non-active power can be traced downstream the system at buses 2,3 and 4. Q2 is less than Q1 since the inductive shunt branch of the step-up transformer T12 lags the system voltage by 90 degrees and hence consumes non-active power. Table 7.3 summarises the non-active power at all buses.

Table 7.3: Summary of non-active power at buses 1 to 4 under no GIC and dc GIC conditions with different models of the source used.

Model of source	Non-active power without GIC (MVAr)	Non-active power at steady state dc GIC (MVAr)	% change in non-active power
Bus 1 non-active power			
ACEQ-IDEAL	126.2	216.2	+71.3
ACEQ-RL	126.0	162.3	+28.8
SM	126.2	181.2	+43.6
Bus 2 non-active power			
ACEQ-IDEAL	109	156.8	+43.9
ACEQ-RL	108.7	117.2	+7.8
SM	109	130.8	+20
Bus 3 non-active power			
ACEQ-IDEAL	97.52	144.5	+48.2
ACEQ-RL	97.29	108.4	+11.4
SM	97.52	120.8	+23.9
Bus 4 non-active power			
ACEQ-IDEAL	78.03	74.05	-5.1
ACEQ-RL	77.85	51.88	-33.4
SM	78.03	59.62	-23.6

The non-active power consumption of T12 can be calculated as the difference between Q1 and Q2. T12's non-active power consumption is shown in Table 7.4. Prior to GIC injection, T12 consumes roughly 17.2 MVAr of non-active power. This represents 4 % of the transformer rating which is valid according to [119]. When the post-GIC steady state equilibrium is reached, T12's non-active power consumption increases depending on the source model used. The increase in non-active power consumed by T12 is comparable to the reactive power consumed by transformers under dc bias reported in literature [5], [8], [117].

Table 7.4: T12 Non-active power consumption with different source models

Source model	Pre-GIC T12 Q – Consumption (MVAr)	Post-GIC T12 Q-Consumption (MVAr)	Increase in T12 Q-Consumption (MVAr)
ACEQ-IDEAL	17.2	59.4	42.2
ACEQ-RL	17.3	45.1	27.8
SM	17.2	50.4	33.2

At the load bus, the non-active power drops leading to a decline in bus voltages as shown in Table 7.2. Since the load used is a constant power load model, the non-active power reaches a steady state condition after the network time response.

7.1.7 Bus 1-4 Active power (P1-P4)

Figure 7.11 shows the active power at bus 1 over the 200 s simulation. Initially, all the sources produce 242.5 MW of active power. The source produces an additional 5 MW of active power to supply the 237.5 MW load. This 5 MW additional power compensates for the active power consumed by T12, T34 and the transmission line active power losses.

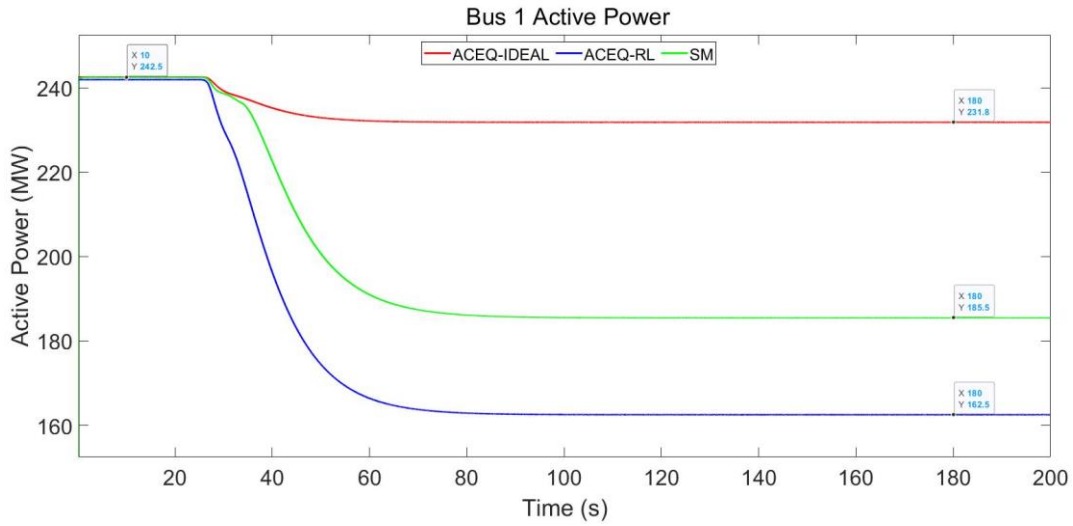

Figure 7.11: Bus 1 active power with dcGIC injected at t = 25 s

When the GIC is injected, P1 drops meaning that the source reduces its active power output. This is because the source operates at a smaller power factor. Since the source tries to maintain the system voltage by supplying more non-active power, the active power drops to remain within the limits of the generator MVA rating. The ACEQ-RL shows the largest drop in active power, followed by the synchronous machine and ideal source.

The active power drop can be traced downstream the system as summarised in Table 7.5

Table 7.5: Summary of active power at buses 1 to 4 under no GIC and dc GIC conditions with different models of the source used.

Model of source	Active power without GIC (MW)	Active power at steady state dc GIC (MW)	% change in active power
Bus 1 active power			
ACEQ-IDEAL	242.5	231.8	-4.41
ACEQ-RL	241.9	162.5	-32.82
SM	242.5	185.5	-23.51
Bus 2 active power			
ACEQ-IDEAL	239.4	227.9	-4.80
ACEQ-RL	238.8	159.6	-33.17
SM	239.4	182.2	-23.89
Bus 3 active power			
ACEQ-IDEAL	238.4	226.9	-4.82
ACEQ-RL	237.8	158.9	-33.18
SM	238.4	181.5	-23.87
Bus 4 active power			
ACEQ-IDEAL	237.5	225.9	-4.88
ACEQ-RL	236.8	158.2	-33.19
SM	237.5	180.6	-23.96

The active power consumption of the transformer T12 can be calculated by the difference between P1 and P2. Consider the ideal equivalent source. Initially, the active power at bus 1 was found to be 242.5 MW. From Table 7.5, the active power at bus 2 prior to GIC was 239.4 MW. Therefore, T12 consumes 3.1 MW of active power under noGIC conditions.

The active power consumed by the transmission line prior to GIC can be calculated from the difference between P2 and P3. The line's active power consumption was calculated as 1 MW.

Figure 7.12 shows the active power at bus 4. Initially, P4 was 237.4 MW. With GIC, P4 decreases since the system operates at a lower power factor. The active power drop depends on the source model.

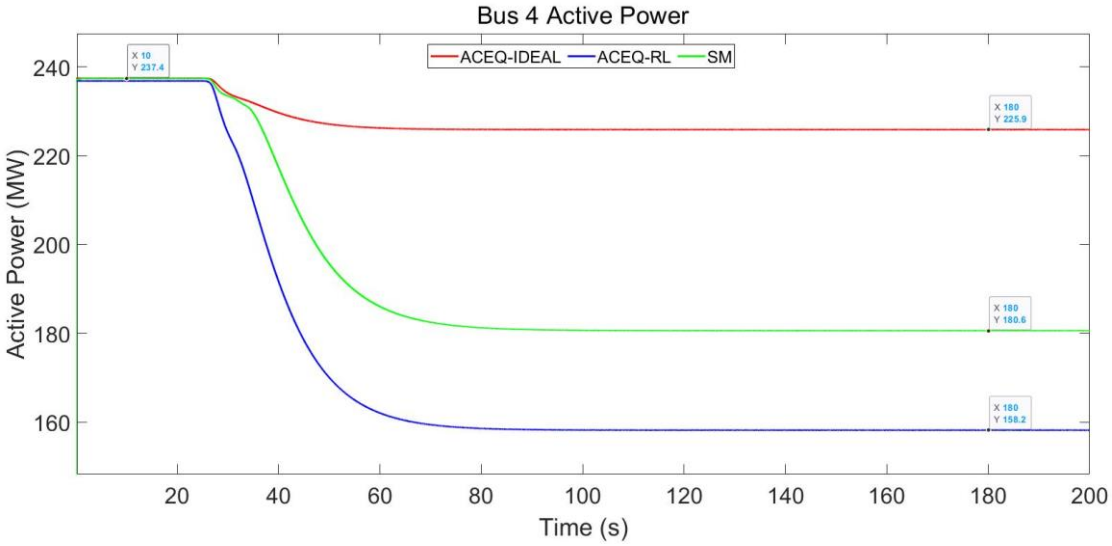

Figure 7.12: Bus 4 active power with dcGIC injected at t = 25 s

The difference between P3 and P4 gives the active power consumption of T34. Hence, T34 consumes 1 MW of power. This value is important since it the sum of the transformer active power consumption and line consumption represents the excess power that the source has to supply. The sum of the line consumption and transformer consumption is as follows;

$$P_{T12} = 3.1\ MW;\ P_{T34} = 1\ MW; P_{line} = 1\ MW$$

$$P_{T12} + P_{T34} + P_{line} = 5.1\ MW$$

This is comparable to the additional 5 MW of active power produced at bus 1 by the source.

7.1.8 Waveshape and harmonic analysis

In this Section, the current harmonics extracted from the MATLAB FFT block will be shown. Firstly, the neutral current harmonics obtained from simulations with the three different source models will be discussed. The effects of GIC on the neutral current harmonics will be shown. Next, the magnetising current harmonics for T12 will be analysed. Then, I1 and I2 harmonics will be discussed. In each case, the phase A harmonics will be compared for the three sources, followed by a comparison of the harmonics across each phase. This will be repeated for both noGIC and dcGIC conditions.

7.1.8.1 Neutral current harmonics

Figure 7.13 shows a comparison of the neutral current harmonics for the three source models used.

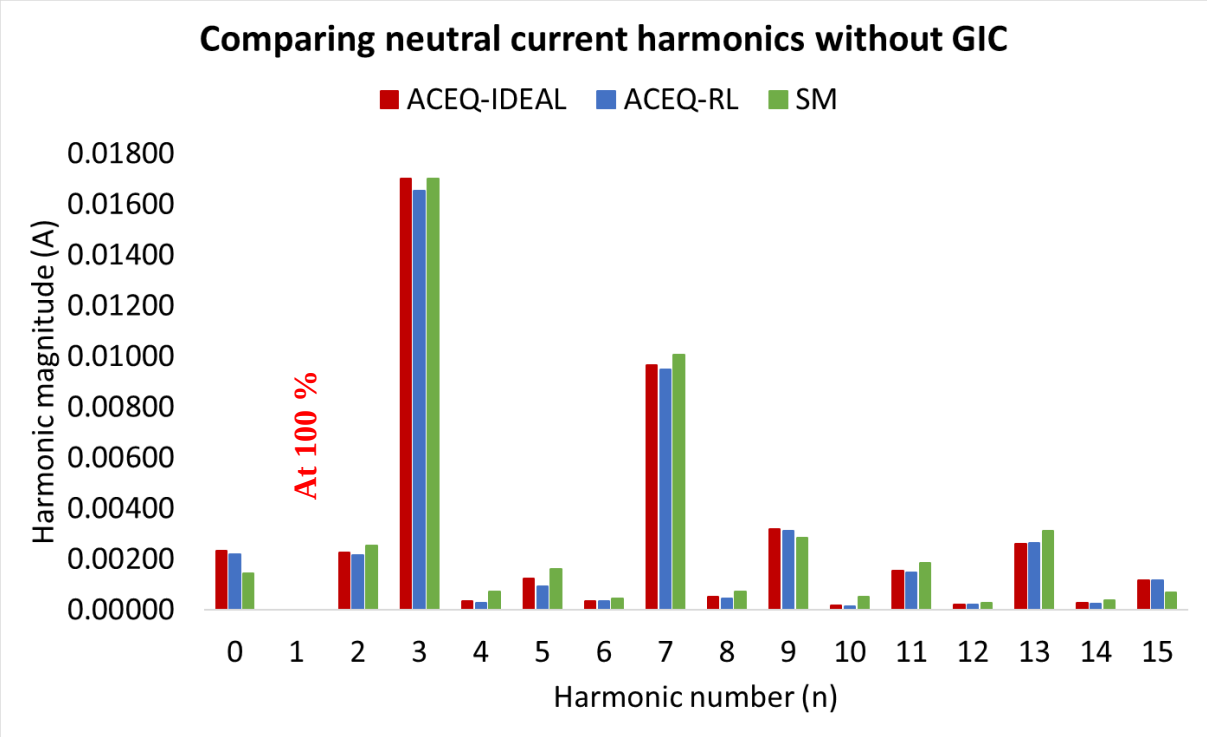

Figure 7.13: Comparing pre-disturbance neutral current harmonics produced with different source models

Without GIC, the neutral current harmonics have a very low magnitude compared to the fundamental. The dominant harmonics are the 3rd, 7th, 9th, 11th, 13th and 15th harmonic. Since the system is balanced, the most significant harmonics in the neutral should be the zero-sequence harmonics, being additive. This explains the 3rd, 9th and 15th harmonics present in the neutral, commonly referred to as triplen harmonics (odd multiples of 3rd harmonic). The third harmonic is drawn by the transformers for producing the required flux, explaining its dominance over other harmonics. The magnetising current harmonics of T12 shows significant levels of 3rd, 5th, 7th, 11th, 13th and 15th harmonics (See Figure 7.15). These harmonics reflect in the neutral current. Due to the over-excitation of the transformers beyond the knee point, a small level of positive and negative sequence harmonics can also be observed in the neutral. The neutral current harmonics differ based on the source used. However, the percentage difference in harmonic magnitudes between the three source models is negligible.

When the dcGIC steady state equilibrium is reached, a significant amount of dc current can be observed, as shown in Figure 7.14. The magnitude of the dc component in the neutral with GIC is 173.4 A. Increased magnitudes of odd and even harmonics were also observed. The difference in harmonic magnitude between the sources increased showing that the response of the source model contributes to determining the level of harmonics in the system.

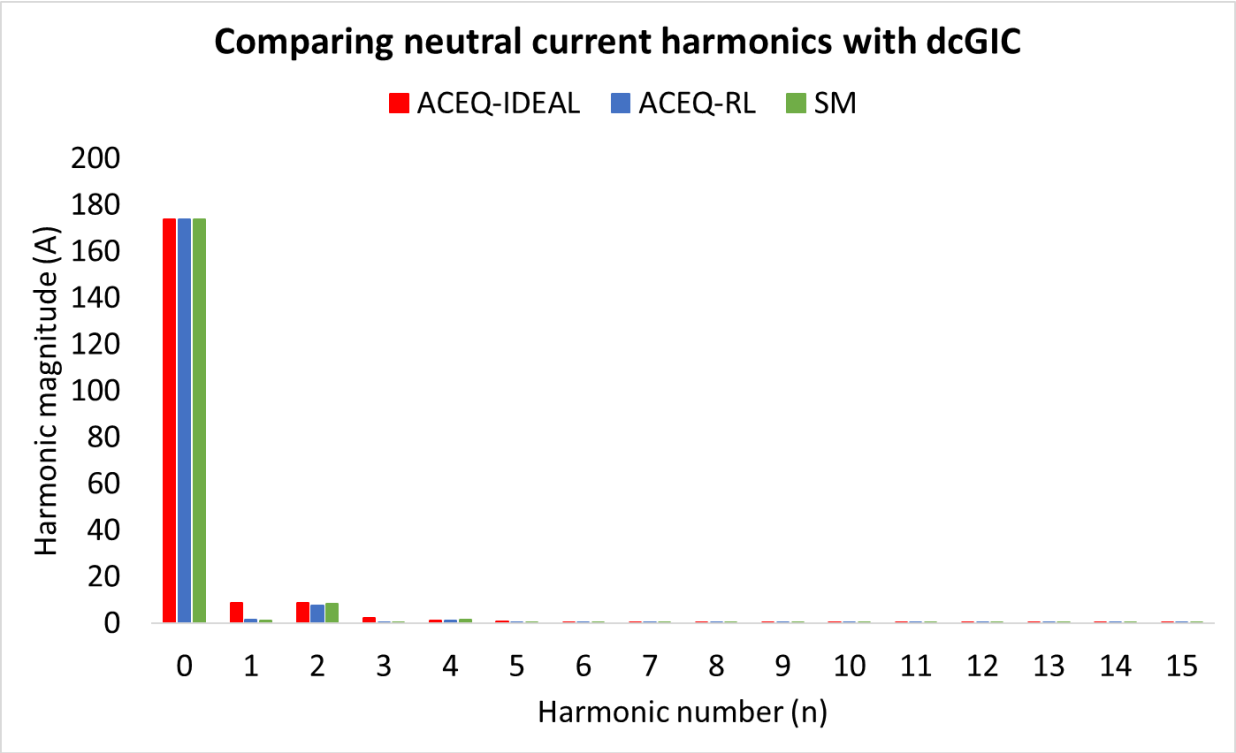

Figure 7.14: Comparing post-disturbance neutral current harmonics produced with different source models

7.1.8.2 T12 Magnetising current harmonics

Figure 7.15 shows T12's magnetising current waveform under no GIC conditions. The harmonic spectrum of the magnetising current is shown in Figure 7.15. The third harmonic component is responsible for the peaky shape of the magnetising current [20]. The third harmonic current drawn by the transformer contributes to the neutral current harmonics which also showed significant third harmonic content.

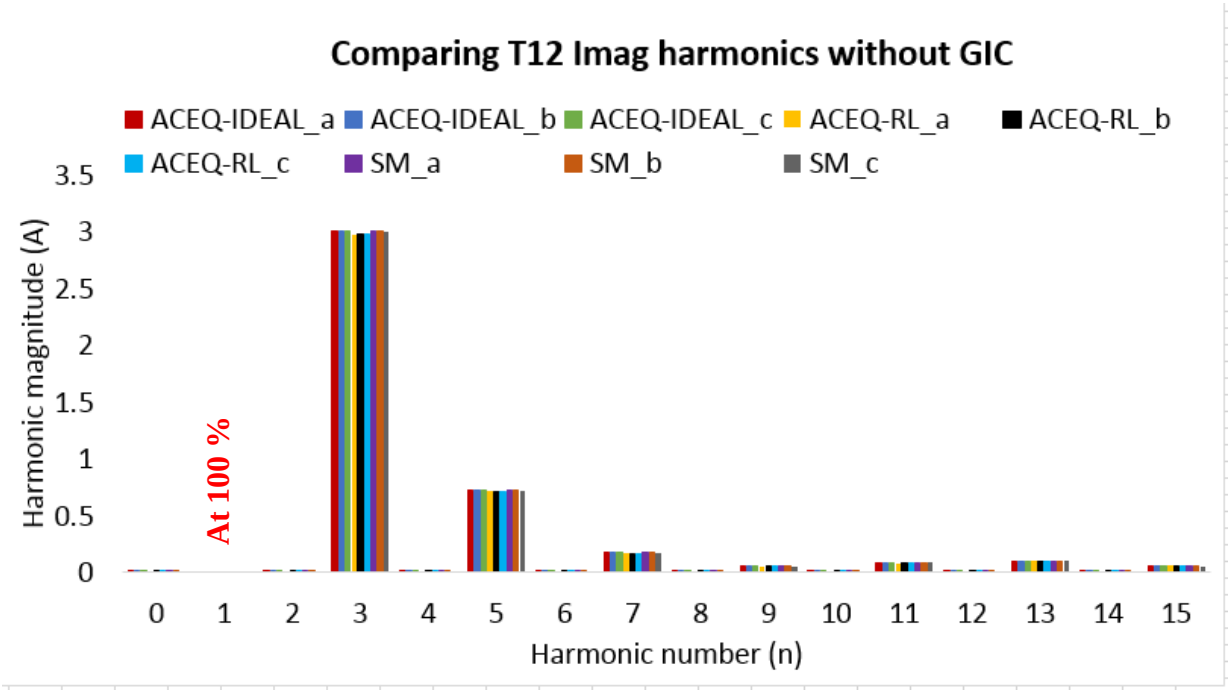

Figure 7.15: T12 Magnetising current harmonics without GIC

Comparing the three phases shows that when using the ac equivalent sources, the magnetising current is balanced in each phase. However, with the full SM model, slight unbalances were observed across the three phases. The magnetising current consists of mainly the 3^{rd}, 5^{th}, 7^{th} , 9^{th}, 11^{th} 13^{th} and 15^{th} harmonics. These are odd harmonics that are drawn by the transformer during normal operating conditions [20].

Figure 7.16 shows the magnetising current under steady state dc GIC conditions. Comparing the three phases shows that with the ACEQ-IDEAL and ACEQ-RL, T12's magnetising current harmonics are balanced. In contrast, with the SM as source, T12's magnetising current shows a small unbalance between the three phases. Comparing the three sources shows that the harmonic magnitudes are largest for the ACEQ-IDEAL and smallest with the ACEQ-RL model

There is an increase in the magnitude of odd harmonics. Moreover, even harmonics of high magnitudes appear indicating transformer asymmetric saturation. The highly non-linear magnetising current that is formed in the saturation region causes generation of even harmonics as reported by many authors [16], [120], [118], [117]

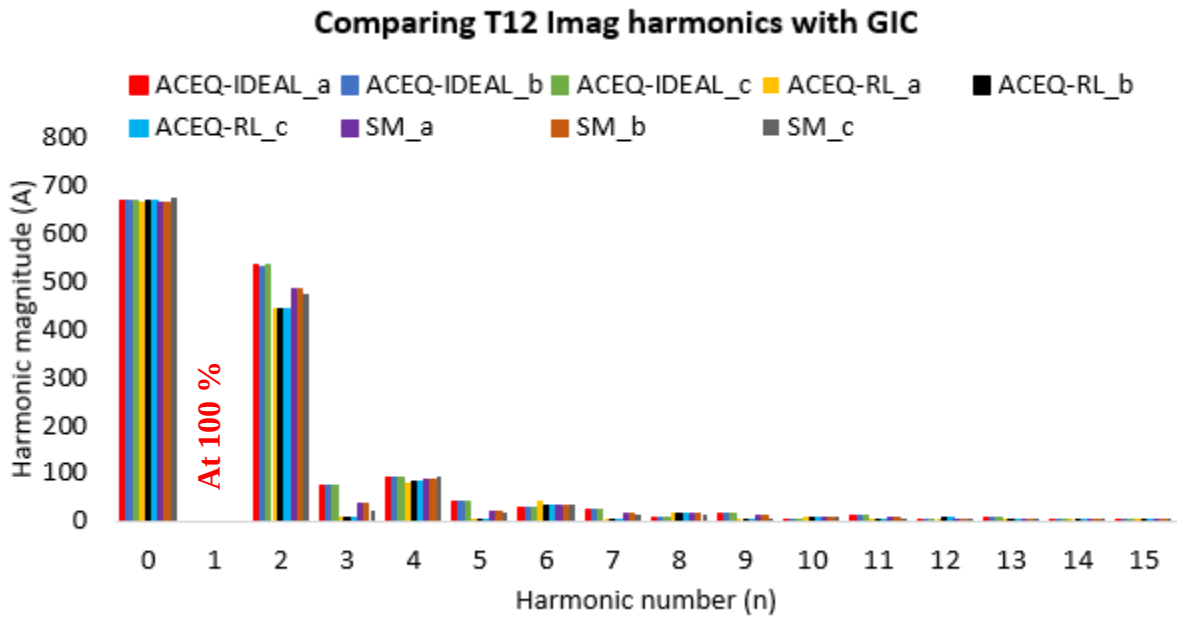

Figure 7.16: T12 Magnetising current harmonics with dc GIC

7.1.8.3 Bus 1 Current harmonics

Figure 7.17 shows a comparison of I1 harmonics across all phases for the ACEQ-IDEAL and SM source model, at the same time interval of t = 10 s. No unbalance was observed in I1 harmonics with the ideal source. However, the full generator model shows slight unbalance in the magnitude of the harmonics.

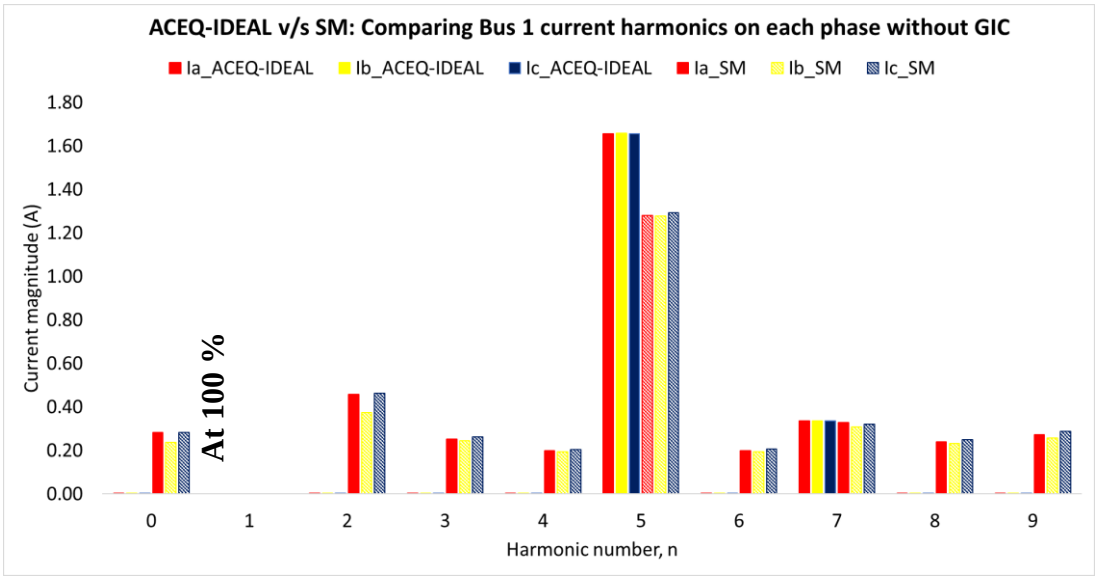

Figure 7.17: Comparing bus 1 current harmonics between the three phases, under noGIC conditions with ACEQ-IDEAL and SM used as the source

With the ACEQ sources, the delta winding of the transformer filters the zero sequence harmonics. However, there were some levels of zero sequence harmonics observed with the full synchronous

machine model. It appears as though the delta winding is not effective in keeping the zero sequence harmonics trapped. This is because the full SM produces slightly unbalanced voltages compared to the ACEQ-IDEAL. When a system is symmetrical and balanced, the phasor components have the same magnitudes and 120-degree phase shift. The sequence component theory can then be applied to each harmonic. An unbalanced system introduces phasors that might not have the same magnitudes and phase shifts. Therefore, the harmonics no longer follow the conventional sequence component theory. Triplen harmonics may exist in the phase current even in a circuit located upstream a delta-connected transformer [121][122]. This deviates from conventional thinking that 3rd, 6th,9th harmonics do not reach the generator bus due to the GSU delta winding.

Figure 7.18 shows a comparison of the phase A current harmonics at under no GIC and steady state dc GIC conditions. The harmonics are shown for all the three source models used.

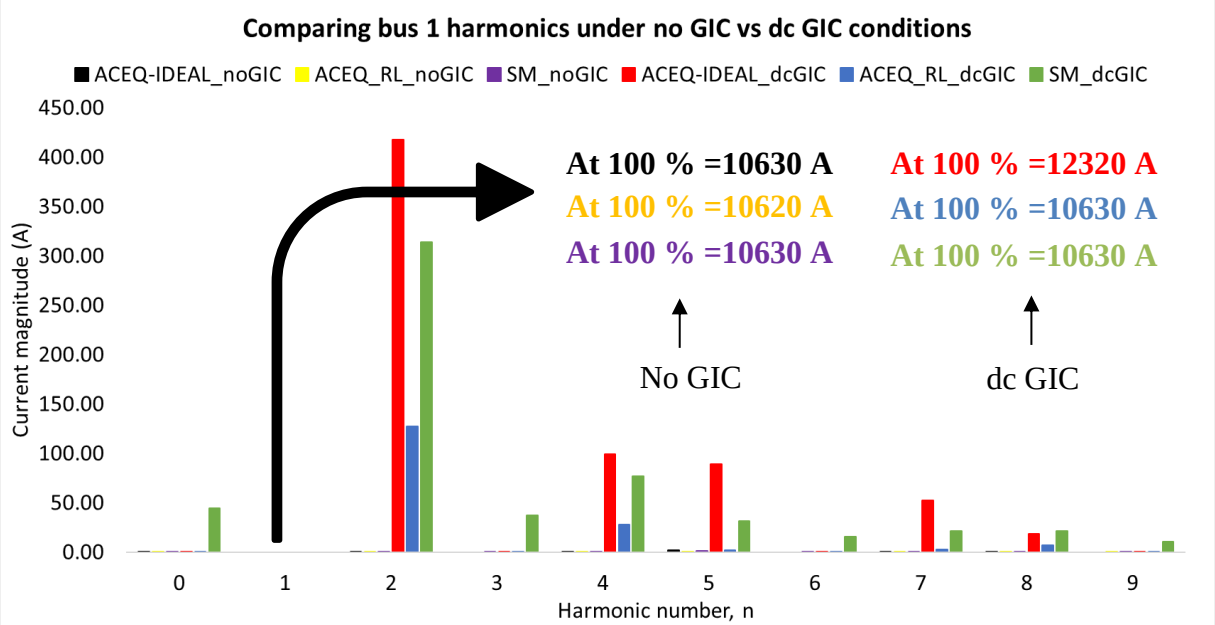

Figure 7.18: Comparing bus 1 phase A current harmonics between the sources under no GIC conditions and steady state dcGIC conditions

Without GIC, I1 harmonics are relatively small compared to the fundamental frequency current which has a magnitude depending on the source model (See Figure 7.17 for a clearer harmonic spectrum). The THD in bus 1 current without GIC is 0.19 % and all harmonics are within limits of IEEE 519 Std [123]. The effect of armature reaction produces a flux that opposes the normal field flux creating a small level of even harmonics. The 5th and 7th harmonics are mainly due to the slot harmonic produced by the generator. However, compared to the fundamental frequency current, these harmonics are negligible although they contribute to power losses. The full synchronous generator model produces higher level of harmonics compared to the ac equivalent sources. There is a decrease in the amplitude of harmonics as the harmonic number increases similar to observations made in [20] and [118].

The introduction of GIC causes an increase in the level of harmonics. The harmonic magnitudes are different for the three sources. The most significant harmonic is the second order harmonic which is a negative sequence harmonic. This harmonic is expected to flow into the generator terminals causing the slowing down of the rotor due to negative sequence flux setup in the rotor windings. The negative sequence harmonics create a flux that opposes the field flux (rotor flux) of the generator. This reduces the resultant air gap flux and hence voltage produced at bus 1.

When the source is modelled with as ACEQ-IDEAL or ACEQ-RL, the delta winding of the generator step up transformer filters the 3^{rd}, 6^{th} and 9^{th} harmonics. However, significant levels of these harmonics were observed when the generator was modelled as SM. This is because of the slightly unbalanced voltages and currents produced by the synchronous machine. When the system is unbalanced, the 3^{rd}, 6^{th} and 9^{th} harmonics no longer have a zero sequence as reported by Chicco *et al.* [121][122]. Hence, the delta winding of T12 does not treat these harmonics as zero sequence. This explains the appearance of 3^{rd}, 6^{th} and 9^{th} harmonics at the generator bus.

In summary, analysis of I1 current harmonics shows the following:

- The level of harmonics depends on the model of the source since the currents generated by the source differ including the magnitude of the fundamental. The ac equivalent source does not produce unbalanced voltages compared to the slight unbalance observed in the full synchronous machine model.
- In an unbalanced system, multiples of the 3^{rd} harmonic (3^{rd}, 6^{th}, 9^{th},…) do not have a zero sequence. Therefore, these harmonics may appear at the generator bus under GIC conditions. Further analysis of the non-conventional harmonics due to unbalance will be shown when studying the response of the 4-bus system to ac GIC in Section 7.2.9.
- Negative sequence harmonics generated due to transformer part wave saturation flow into the generator causing a flux that opposes the direction of the field flux or rotor flux. Hence, the air gap flux is reduced in the synchronous generators causing a decrease in the terminal voltage of the generator for the same field flux. The field flux needs to be increased to cater for the opposing flux generated due to negative sequence harmonics.

7.1.8.4 Bus 2 Current harmonics

Figure 7.19 shows a typical waveshape of bus 2 phase A current. The waveshape follows the same trend when using the different source models and hence only the waveshapes obtained from simulations using the ACEQ-IDEAL are shown.

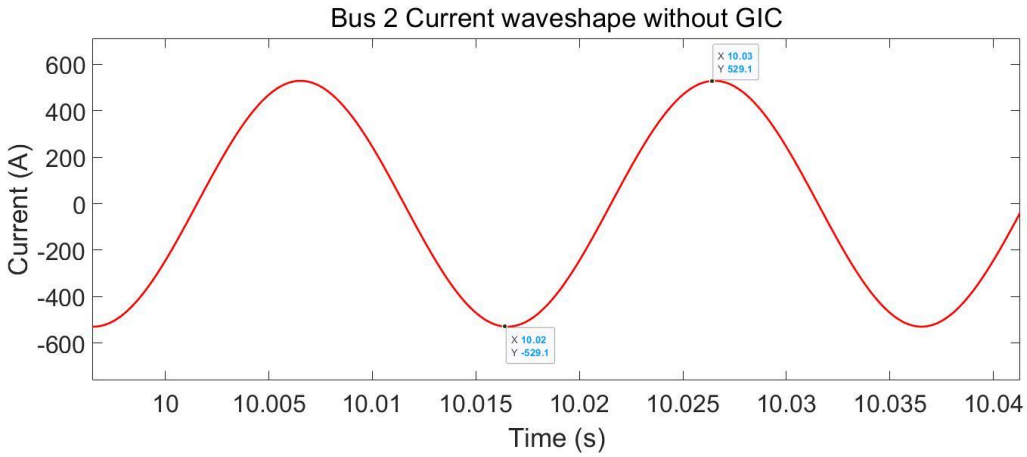

Figure 7.19: Waveshape of bus 2 current without GIC showing a clean waveform without distortion

Without GIC, the bus 2 phase A current waveshape is clean with negligible distortion. Moreover, the waveform is symmetrical about the zero axis, peaking at 529.1 A in both positive and negative half cycles. This means that there are no even harmonics in bus 2 current under no GIC conditions.

Figure 7.20 shows the same bus 2 phase A current waveshape but around t = 180 s when the current has reached the dc GIC steady state condition.

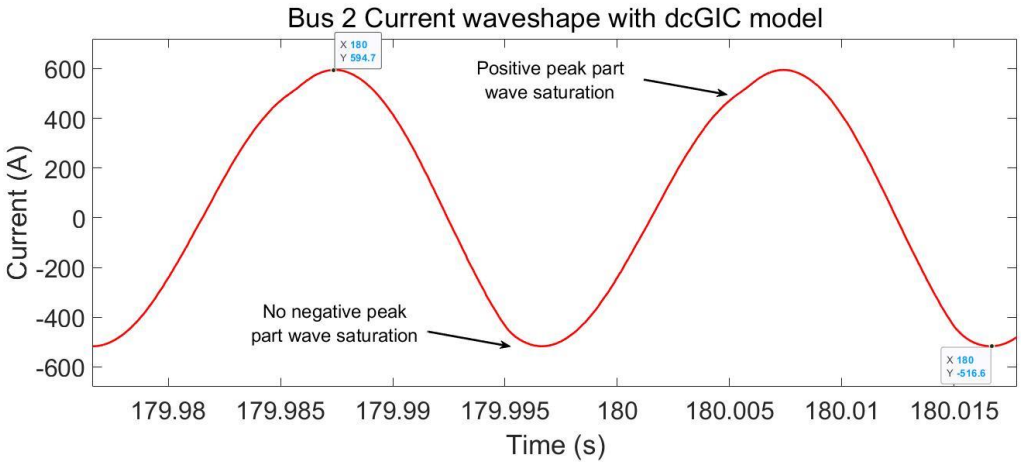

Figure 7.20: Waveshape of bus 2 current with dc GIC showing partial wave saturation in the positive peak only

With GIC, partial wave saturation was observed at the positive peak of bus 2 current. This is due to the polarity of the dcGIC flux as shown in Figure 7.3. No part wave saturation was observed at the negative peak. Moreover, the waveform is no longer symmetrical about the zero axis. Bus 2 phase A current peaks at 594.7 A in the positive half cycle and peaks at – 516.6 A in the negative half cycle. This result proves the dc shift in bus 2 current due to the GIC flux.

Figure 7.21 shows a comparison of bus 2 current harmonics across all phases. The ACEQ-IDEAL and SM have been used to compare the harmonic magnitudes based on the source model.

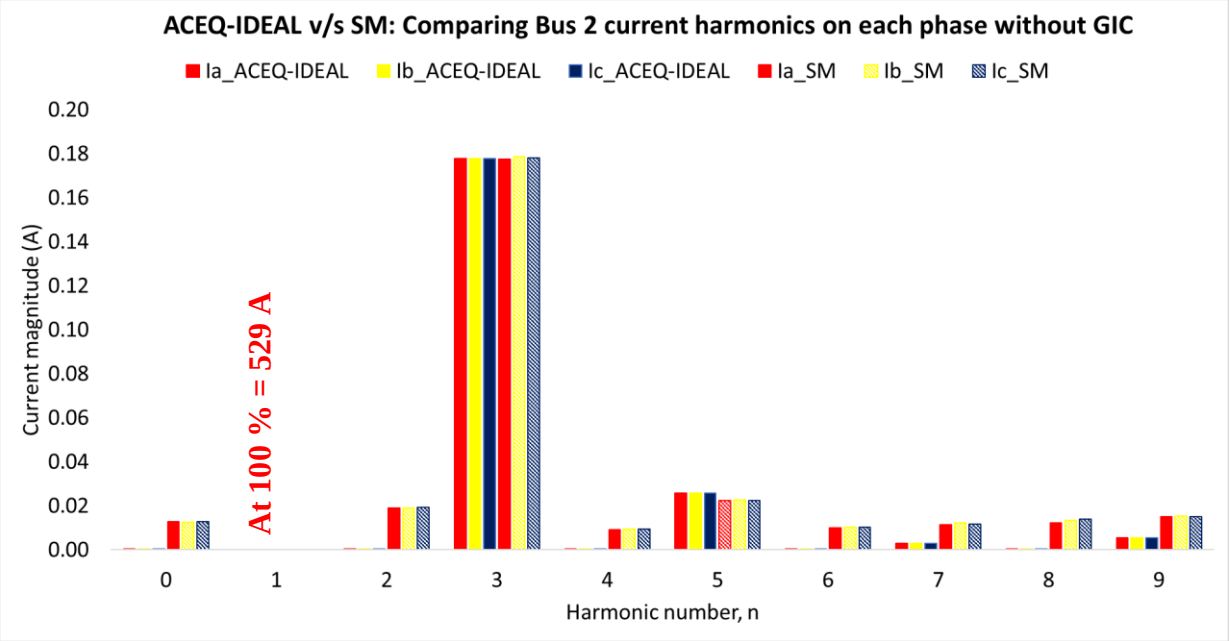

Figure 7.21: Comparing bus 2 current harmonics between the three phases, under noGIC conditions with ACEQ-IDEAL and SM used as the source

When there is no GIC, the harmonic magnitudes are balanced with the ACEQ-IDEAL as the source. A small unbalance was observed with the full SM model. There are differences noted in the harmonic magnitudes with the ACEQ-IDEAL and the SM. Since the system is somewhat stressed with overexcitation of the transformers, a small level of even and odd harmonics appear in bus 2 currents. The harmonic magnitudes decrease as the harmonic order increases. The THD measured in bus 2 current under no GIC conditions is 0.19 % with slight differences depending on the source models used.

Figure 7.22 shows the effect of injecting the GIC and compares the bus 2 harmonics observed when using different models of the source. The harmonics without GIC appear clearer in Figure 7.21.

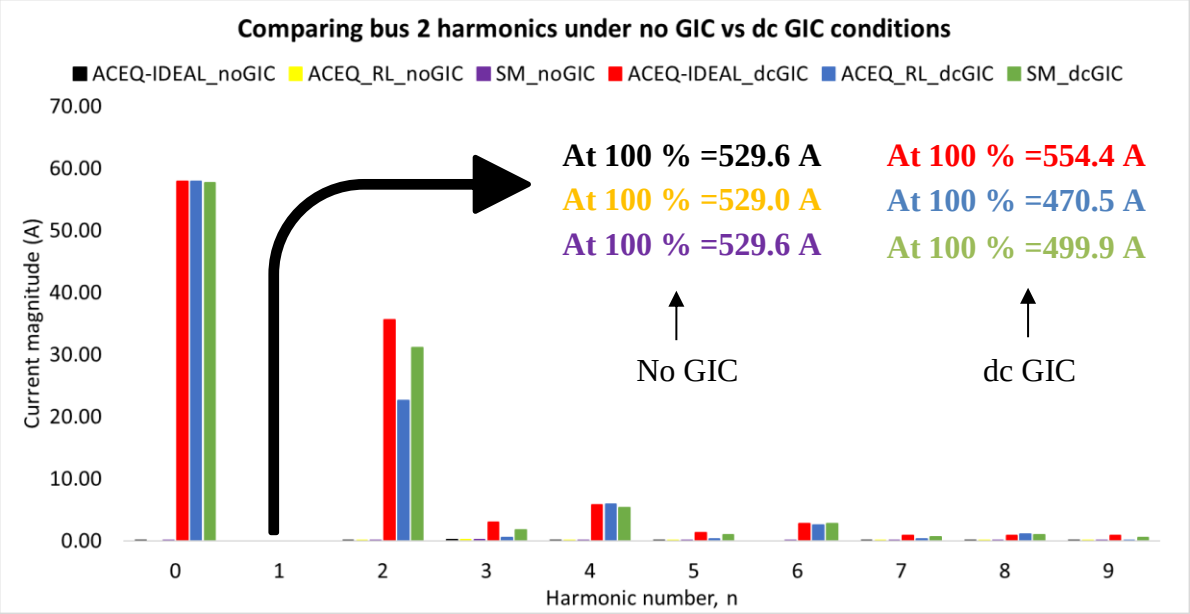

Figure 7.22: Comparing bus 2 phase A current harmonics between the sources under no GIC conditions and steady state dcGIC conditions

The introduction of GIC causes an increase in the dc component. The dc component represents the GIC and is equal to 57.89 A, irrespective of the model of the source. The magnitude of the odd harmonics increased and even harmonics were generated by the transformer. The even and odd harmonics flow in the transmission line causing increased harmonic losses. The magnitude of harmonics due to GIC depends on the source model. With the ACEQ-IDEAL as source, the fundamental component of bus 2 current increases. With the SM and ACEQ-RL, the fundamental frequency component of bus 2 current decreases due to the inability of the source to supply enough fundamental frequency current. Since the fundamental frequency component has a higher magnitude compared to the harmonics, it contributes more to the true rms value of the transmission line current. This deviates from conventional thinking where the transmission line true rms current is believed to increase.

In summary, analysis of bus 2 current harmonics shows the following:

- The level of harmonics depends on the model of the source since the current generated by the source directly affects the harmonic magnitudes.
- The transmission line true rms current is highly dependent on the fundamental frequency current supplied by the source. The source impedance poses a limit to the amount of 50 Hz current output. Hence, the transmission line true rms current does not always increase as per conventional thinking.
- Increased magnitudes of odd harmonics and the generation of even harmonics were noted in the transmission line currents.

7.2 4- bus system response to single frequency acGIC (SF_ac_GIC)

The previous Section showed results obtained from simulations of the 4-bus power system model with a dc GIC model. In this Section, the response of the same 4-bus power system will be studied but with a single frequency (20 mHz) ac GIC model.

7.2.1 Neutral Current

Figure 7.23 shows the instantaneous neutral current when a 20 mHz acGIC model is injected in the neutral at time t = 25 s.

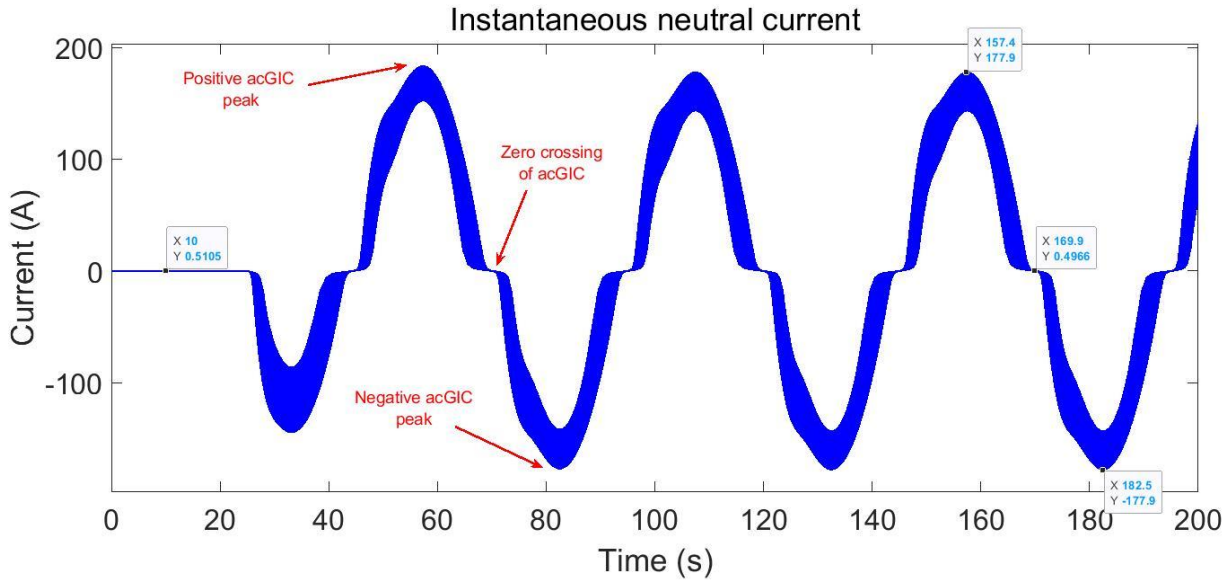

Figure 7.23: Instantaneous Neutral current with acGIC injected at t = 25s showing periodic positive, negative neutral current peaks and zero crossings

The neutral current is different to the one obtained with a dcGIC model. While the instantaneous neutral current increases in only one direction and settles to a steady state value with the dcGIC model, it does not reach such a steady state condition with the acGIC model. Instead, the neutral current peaks in both positive and negative direction depending on the direction of the acGIC flux at a particular time.

Figure 7.24 shows a comparison of the RMS neutral current for the three sources used.

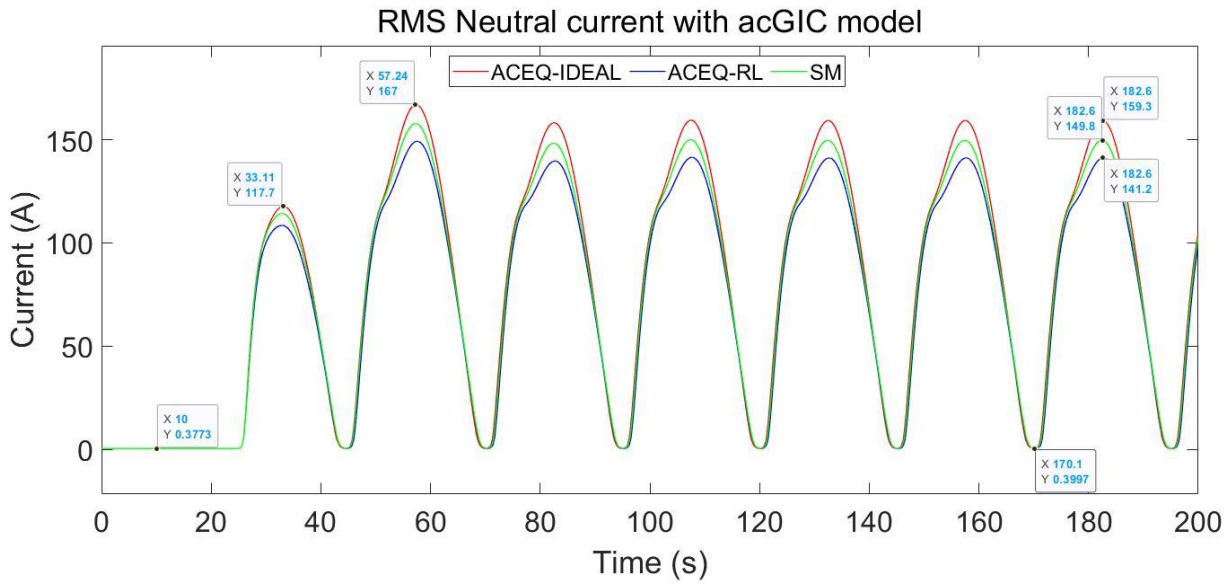

Figure 7.24: RMS Neutral current with acGIC injected at t = 25s showing periodic positive, negative neutral current peaks and zero crossings

The neutral current follows the same trend for all source models. Prior to GIC injection, the neutral current is roughly the same for all sources with a percentage difference less than 3 %. Upon GIC injection, the RMS neutral current increases. The first swing in neutral current shows a smaller peak compared to the other peaks.

Comparing the source models shows that if the source is modelled as an ACEQ-IDEAL, the neutral current peak is the highest, followed by the synchronous machine and ACEQ-RL.

The positive and negative peaks occur periodically based on the acGIC flux direction. Moreover, there are periodic instances where the acGIC model crosses the zero axis. For example, as depicted from Figure 7.23, around t = 170 s, the neutral current shifts from the positive half cycle to the negative half cycle. Hence, this corresponds to the instance similar to the noGIC condition. From Fig 5.35, it is observed that around t = 170 s, the neutral current is slightly higher (0.3997 A) than the no GIC condition (0.3773 A) due to the increased level of harmonics in the neutral current at that instant.

7.2.2 T12 Flux

Figure 7.25 shows the offset in T12's magnetising flux. Unlike with the dcGIC model, the acGIC model shows flux offsets that depend on the amplitude of the acGIC at a particular time instant. When the acGIC peaks in the negative half cycle, T12's flux peaks in the positive half cycle. The reverse direction is due to the fact that the acGIC flux opposes the normal flux direction of T12 as shown in Figure 7.3.

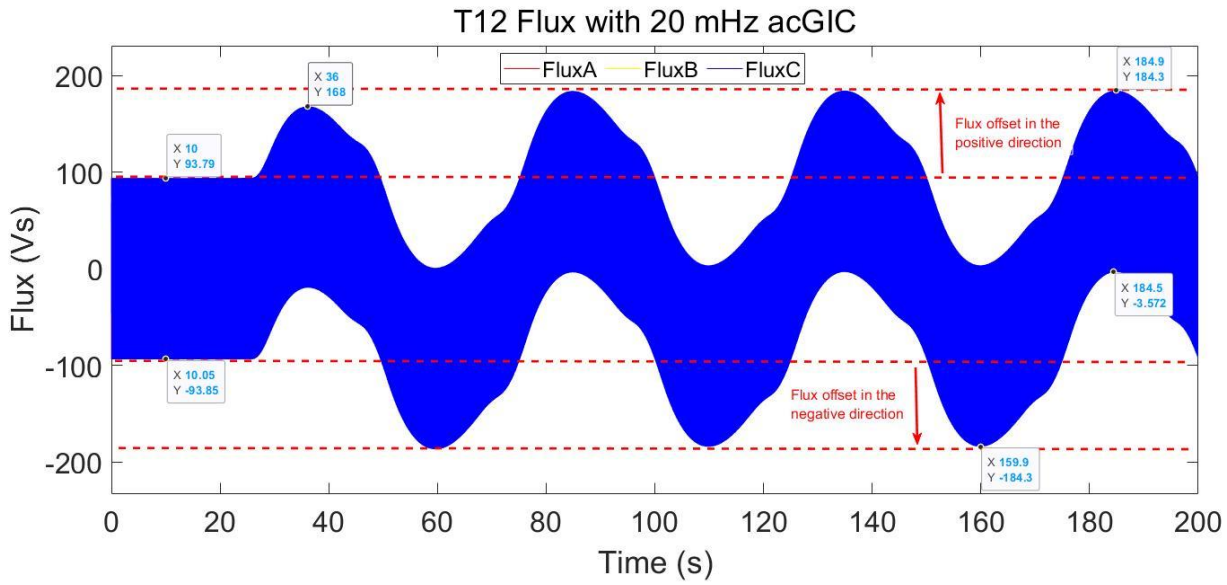

Figure 7.25: T12 Flux showing offset in the both positive and negative directions corresponding to the applied acGIC polarity at different time instances

7.2.3 T12 Magnetising current

Figure 7.26 shows the instantaneous magnetising current of T12 when subject to a 20mHz acGIC injected at t = 25 s. The magnetising current and flux follow the saturation curve. Hence, since the flux of T12 peaks in both positive and negative cycles, and has instances similar to the noGIC operating condition, it's magnetising current follows a similar trend.

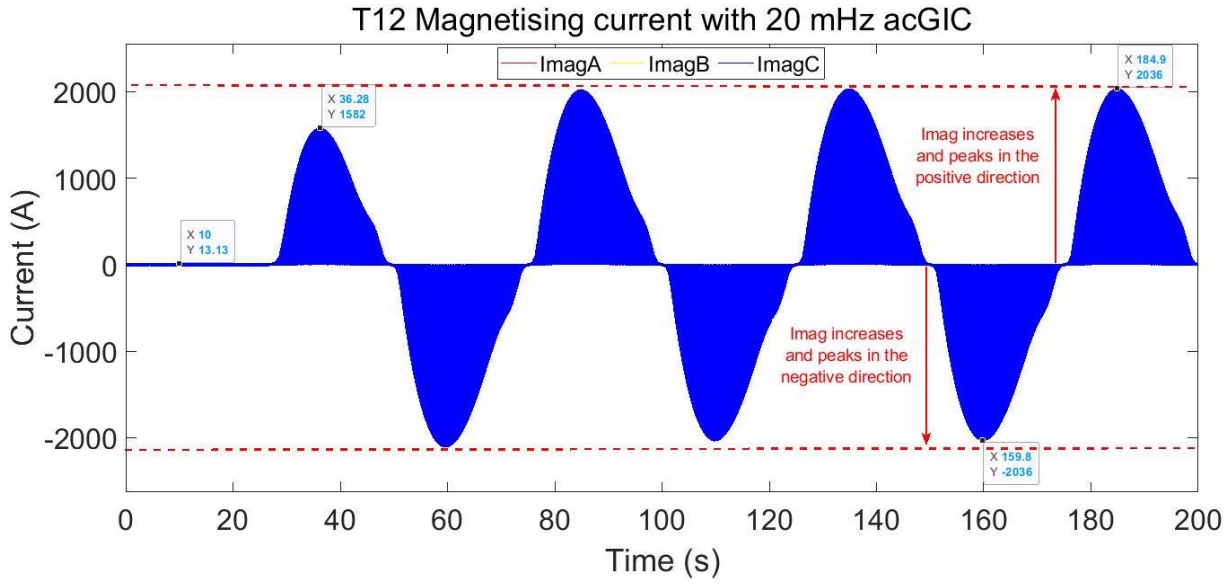

Figure 7.26: T12 Magnetising current with acGIC injected at t = 25s showing shift according to direction of acGIC flux

Prior to GIC injection, the peak magnetising current is 13.13 A. At the acGIC peaks, the magnetising current increases to 2036 A. This is a very high magnetising current, usually not expected in practical

systems. However, since the defined saturation characteristic was designed for deep saturation, the magnetising current is high.

Figure 7.27 shows how the shape of T12's magnetising current varies around the time interval where it moves from positive peak saturation to negative peak saturation. When the flux peaks in the positive direction, the shape of the magnetising current is peaky in the positive cycle. Then, there is a short instance where the shape of magnetising current is similar to the noGIC condition. There are no high magnitude peaks in neither positive cycle nor the negative half cycle. After the short noGIC instance, the magnetising current is peaky in the negative half cycle.

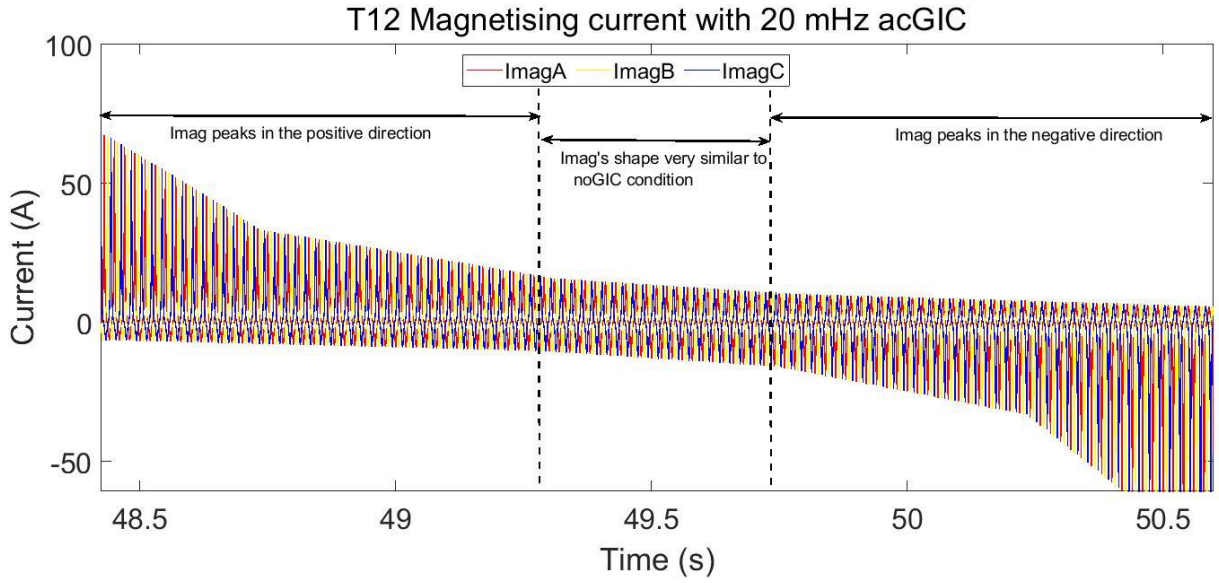

Figure 7.27: T12 magnetising current with 20 mHz acGIC showing the change from positive half part wave saturation to instance of no GIC condition and finally saturating partially in the negative cycle

7.2.4 T34 Flux

Figure 7.28 shows T34's flux during the 200 s of simulation run time. The peak flux is 1015 Vs in both positive and negative half cycles. When the acGIC is injected, T34's flux goes negative, similar to the instantaneous neutral current. This is because of the GIC flux and T34's flux follow the same path as shown in Figure 7.3. As the GIC flux reverses direction and goes positive, T34's flux also goes positive. T34's flux peaks at +2133 Vs at the positive peak and peaks at – 2133 Vs at the negative peak.

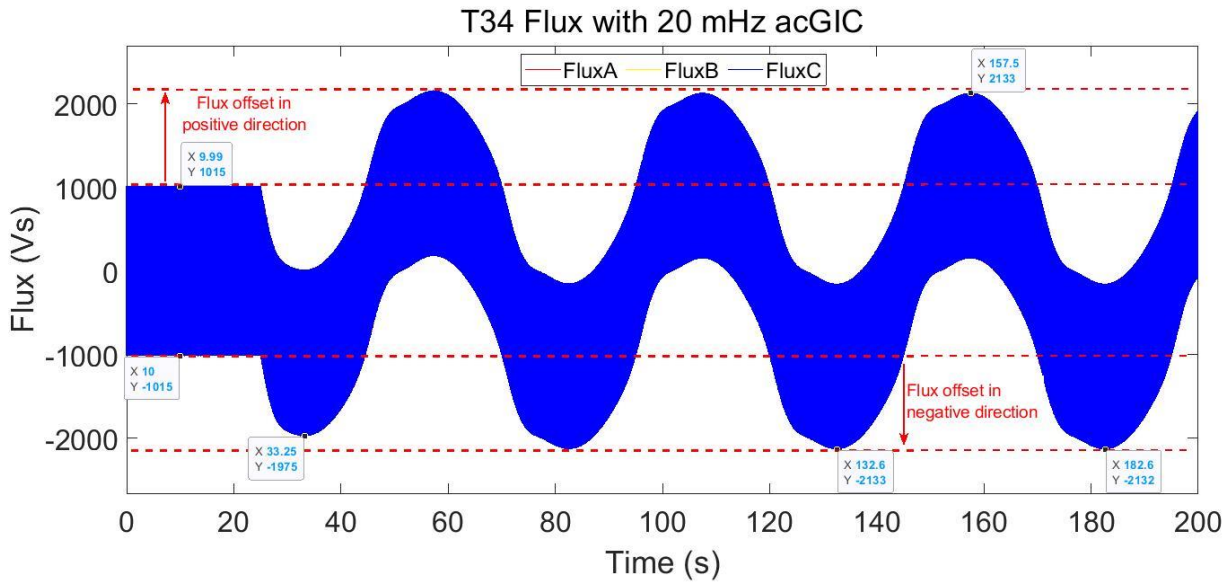

Figure 7.28: T34 Flux showing offset in the both positive and negative directions corresponding to the applied acGIC polarity at different time instances

7.2.5 Generator and load bus currents

The effects of using an acGIC model compared to the conventional dcGIC model can also be traced on the line currents. Figure 7.29 shows the RMS line current at bus 1.

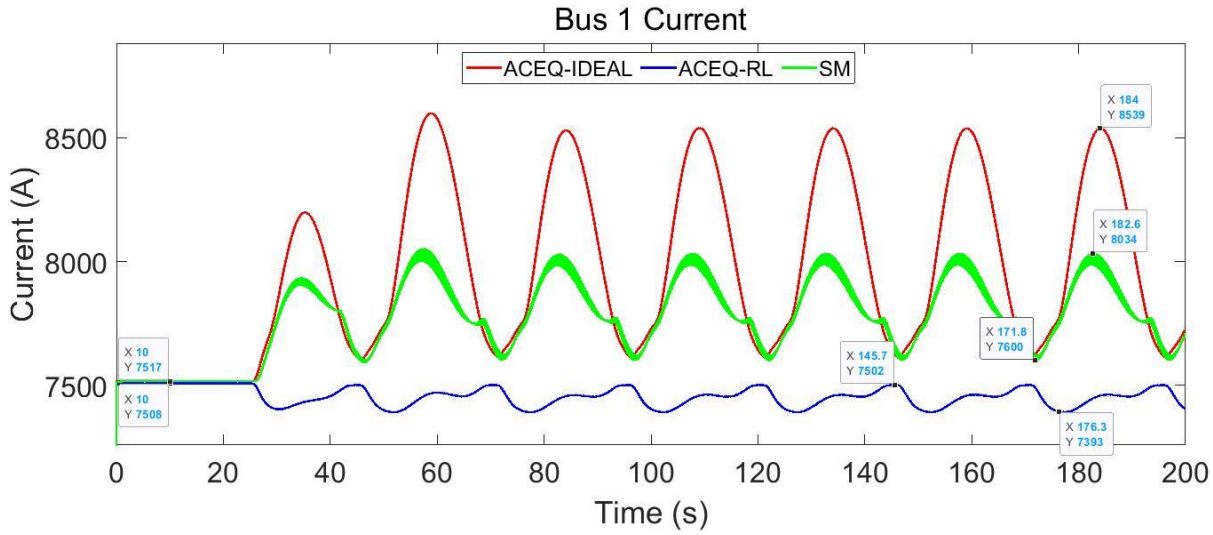

Figure 7.29: Bus 1 RMS current with acGIC injected at t = 25s

It is to be noted that only phase A current are shown since the other two phases behave very similarly. The difference between phase A, B and C currents is less than 10 %.

As shown in Figure 7.29, bus 1 current is nearly the same for all source models under no GIC conditions, with the ACEQ-RL producing 9 A less current than the ACEQ-IDEAL and SM. This RMS current increases upon GIC injection and follows a similar trend to the RMS neutral current.

When the RMS neutral current peaks, the line current also show a peak. When the RMS neutral current returns back to the momentary noGIC instance, bus 1 current does not return to the noGIC condition but shows a slightly higher current (7600 A) compared to noGIC bus 1 current (7517 A).

With the ideal ac equivalent generator used as the source, bus 1 current increases from 7517 A to a maximum of 8539 A representing a 1022 A increase in source current. With the full synchronous generator model as source, bus 1 current only increases by 517 A. With the non-ideal ac equivalent source, bus 1 current actually decreases from 7508 A to 7393 A. The ACEQ-IDEAL and SM source models are able to generate more current output in response to the increased reactive power demand. Since the ACEQ-RL model has been synchronised to the SM model, it was expected that the ACEQ-RL shows a similar increase in bus 1 current to the SM Model. However, it appears that there are differences between the ACEQ-RL and SM despite consistent modelling.

Moving downstream the system towards bus 4, the load bus RMS current decreases since the power transfer capability of the system is reduced as depicted from Figure 7.30. As the acGIC peaks in either positive or negative half cycles, bus 4 current drops. During the momentary noGIC instance, bus 4 current comes back to a slightly higher value (1140 A) than the noGIC condition (1132 A).

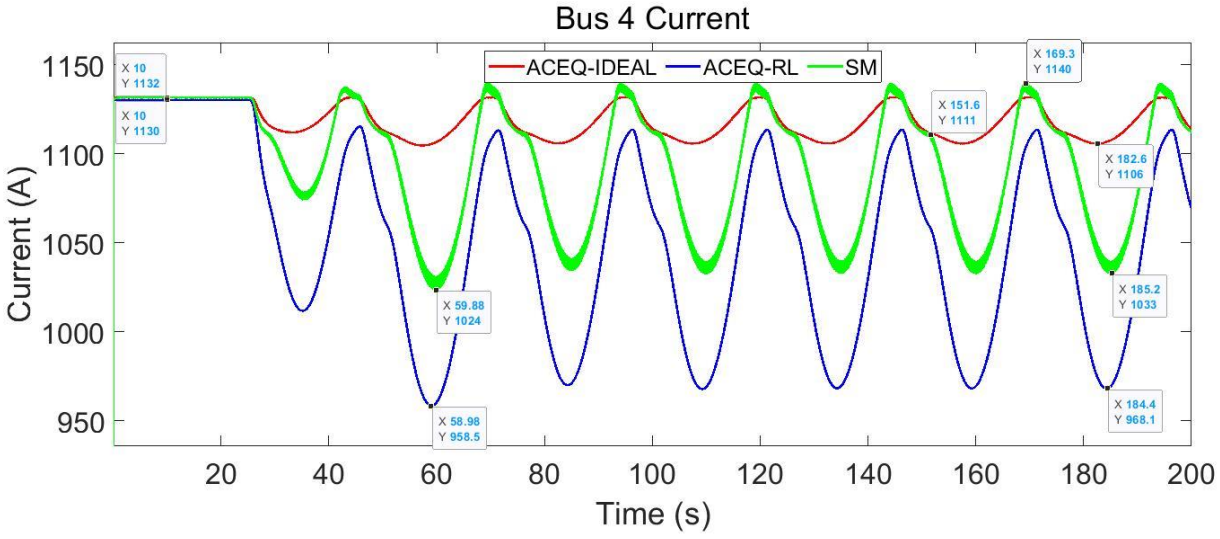

Figure 7.30: Bus 4 RMS current with acGIC injected at t = 25s

7.2.6 Generator and load bus voltages

Figure 7.31 shows a comparison of the terminal voltage of the three sources.

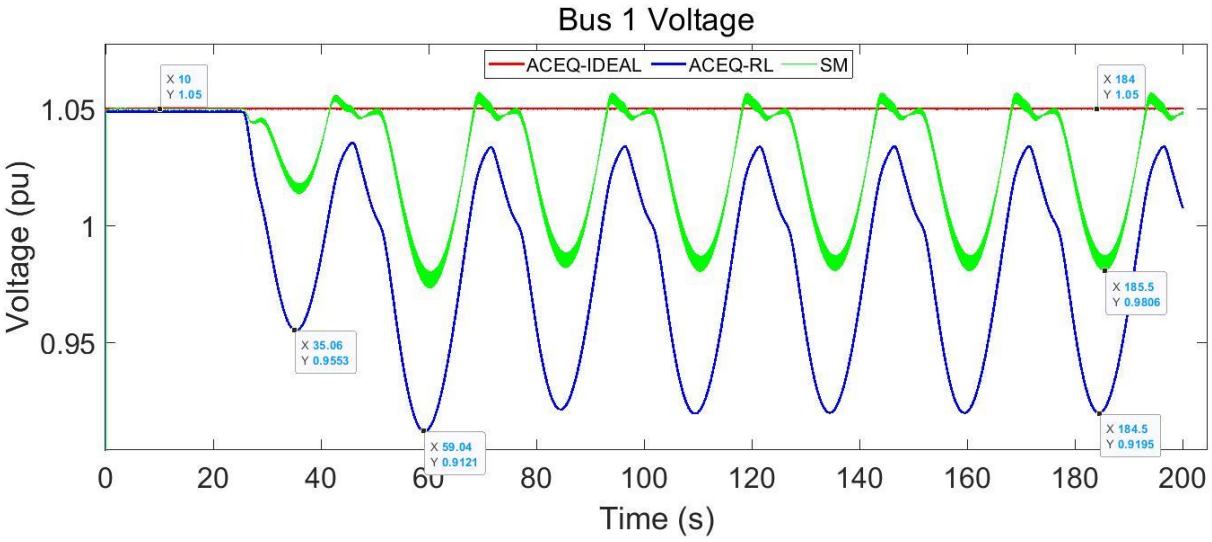

Figure 7.31: Bus 1 voltage with acGIC injected at t = 25 s

Prior to GIC injection, all sources produced 1.05 pu of voltage at bus 1 which corresponds to 21 kV. When the acGIC is injected at time t = 25 s, the bus voltages for the ACEQ-RL and SM drop. Contrarily, the ACEQ-IDEAL appears to be able to maintain its terminal voltage at 1.05 pu throughout the simulation.

Figure 7.31 can also be used to compare the responses of the sources under dcGIC and acGIC conditions. In Figure 7.9, it was observed that the voltage drops to a new steady state value with the ACEQ-RL and SM. However, with an acGIC model, the bus voltages drop periodically with the maximum drops observed at the GIC peaks (positive and negative peaks). At the instance when the amplitude of the acGIC model is momentarily zero or similar to the noGIC condition, the response of the sources is to try to bring the voltage back to 1.05 pu. The synchronous machine manages to bring the voltage to 1.05 pu while the ACEQ-RL terminal voltage is much lower than the 1.05 pu.

The lowest dip in voltage is seen during the second swing, with the SM dropping as low as 0.97 pu and the ACEQ-RL dropping to 0.9121 pu. This represents a maximum voltage drop of 13.8 % for the ACEQ-RL and 8 % for the SM. The ACEQ-RL violates the 10 % voltage drop limit which could lead to generator relay tripping and possibly disconnecting the generator from the power system.

Figure 7.32 shows the load bus voltage under the effects of the 20 mHz acGIC. Prior to GIC injection, the voltage at bus 4 for all sources was 0.9659 pu with very small differences between them. When GIC is injected, the bus voltage varies depending on the magnitude of the acGIC model at any

particular instant. If the GIC peaks in any half cycle, the load bus voltage shows the lowest voltage drops.

This voltage drop depends on how the source has been modelled. With the ACEQ-IDEAL, the percentage voltage drop is only 2.2 %. With the ACEQ-RL, the voltage drops to 0.827 A which represents a 13.9 % voltage drop. With the SM, the percentage voltage drop was 8.4 %. These results show the effect of the source model on the load bus voltage response. It appears that the load bus voltage depends on the source, whether or not, it is able to supply enough reactive power output.

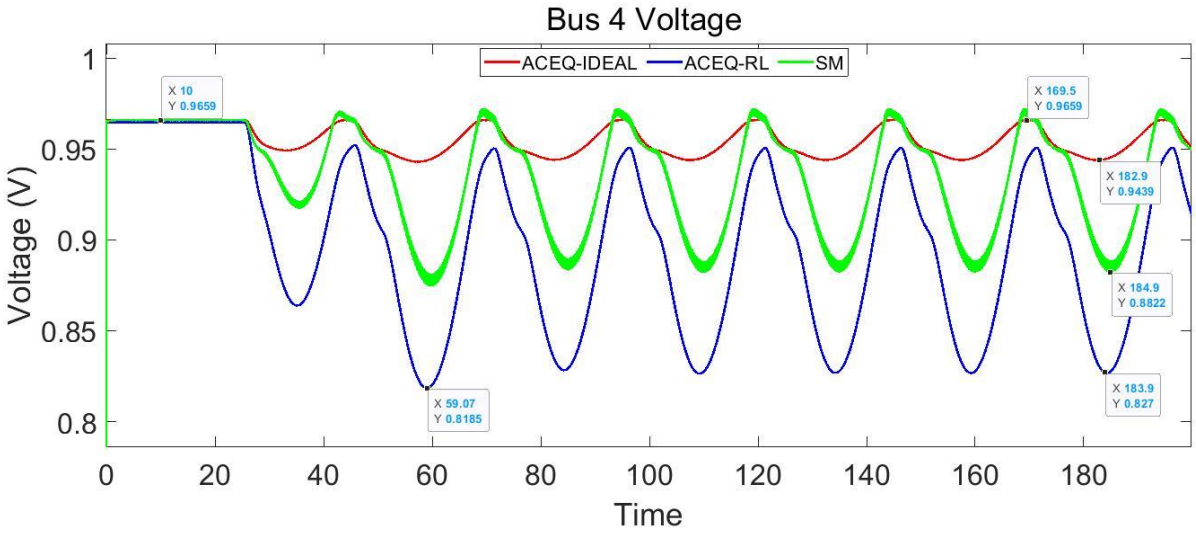

Figure 7.32: Bus 4 voltage with acGIC injected at t = 25 s

7.2.7 Bus 1-4 Non-active power

The non-active power at the generator bus when subject to the 20 mHz acGIC, is shown in Figure 7.33. Prior to GIC injection, the ACEQ-IDEAL and SM both produce 126.2 MVAr of non-active power. When the acGIC is introduced, the non-active power follows a trend similar to the acGIC. When the acGIC peaks, the non-active power also shows a peak. The maximum non-active power produced in response to the increased non-active power demand depends on the source model used. The ACEQ-IDEAL is able to produce the maximum amount of non-active power, followed by the SM and finally the ACEQ-RL. At the zero-crossings of the acGIC model, the non-active power produced by the sources is reduced to a value slightly higher than the noGIC condition. Comparing with Figure 7.10 shows that, with a low frequency acGIC model, the non-active power generated by the source does not reach a steady state as in the case with a dcGIC model. With an acGIC model, the non-active power varies depending on the magnitude of GIC at a particular time instant.

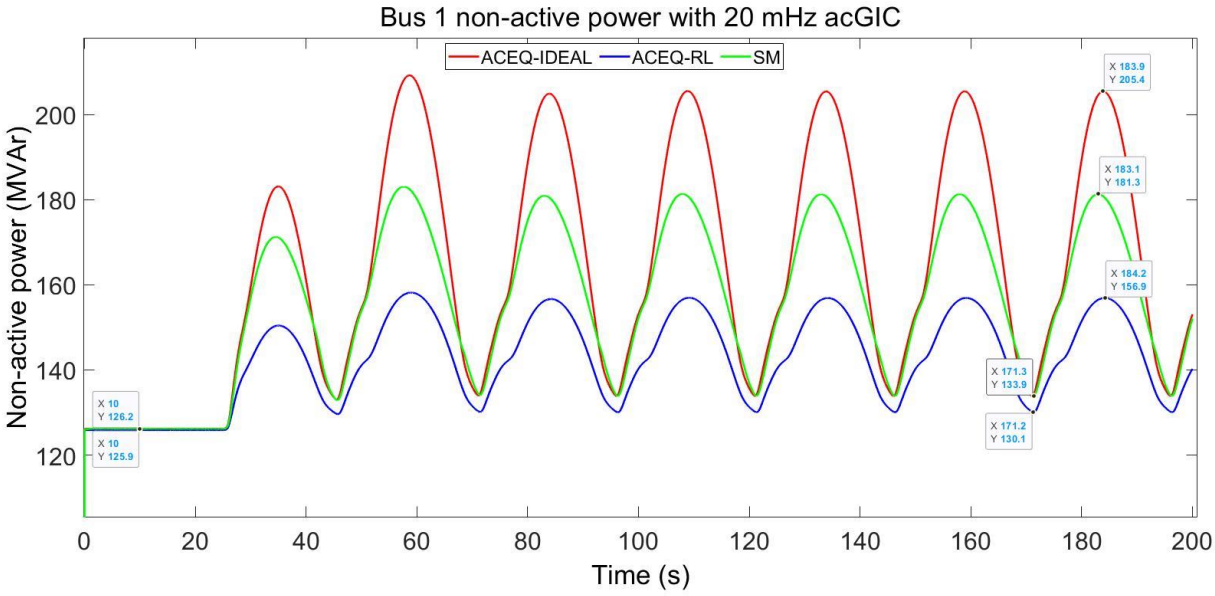

Figure 7.33: Bus 1 non-active power with acGIC injected at t = 25 s

Tracing the effect of the acGIC on the load bus non-active power, Figure 7.34 shows that the non-active power supplied to the load bus varies depending on the acGIC at any particular time. The maximum drops in non-active power are observed at the GIC peaks, whether in the positive half cycle or negative half cycle.

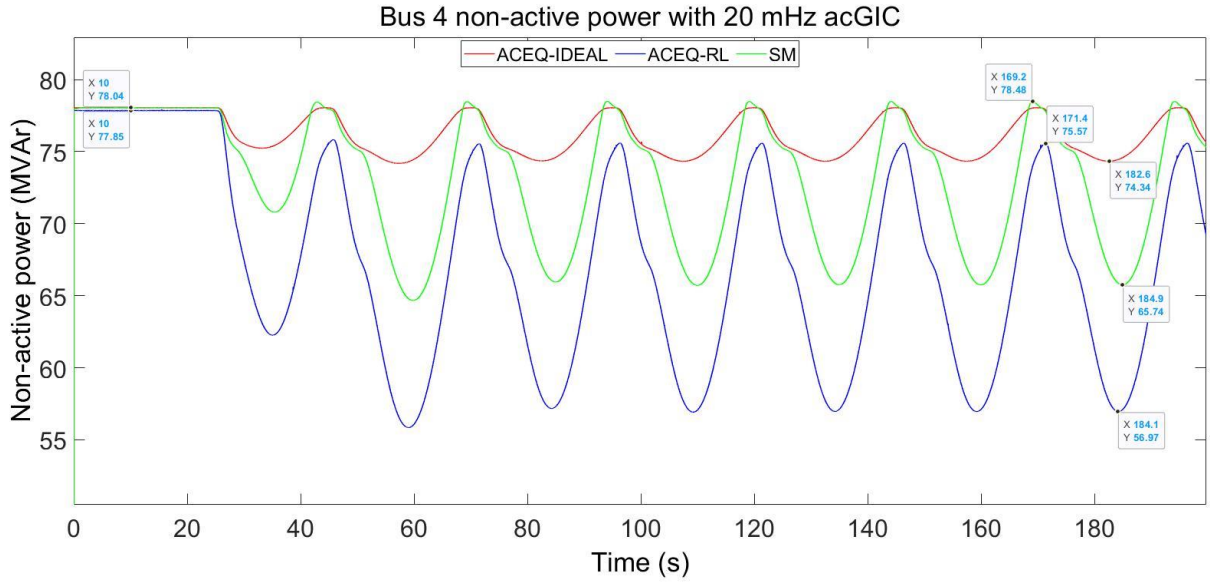

Figure 7.34: Bus 4 non-active power with acGIC injected at t = 25 s

7.2.8 Bus 1-4 Active power

Figure 7.35 shows the active power at bus 1 when the 20 mHz acGIC is injected at t = 25 s. Prior to GIC injection, the ACEQ-IDEAL and SM produce 242.5 MW of active power. This is larger than the load active power requirement since the sources compensate for the active power loss in the transformers and transmission line. The ACEQ-RL produces slightly less active power than the ACEQ-IDEAL and SM.

The bus 1 active power varies based on the acGIC magnitude at any specific time instant. The drop in bus 1 active power supplied is highest for the ACEQ-RL. The lowest drop is observed with the ideal source. Comparing with Figure 7.11 shows that with acGIC, the active power produced by the source never reaches steady state. It always fluctuates depending on the amplitude of the acGIC model used.

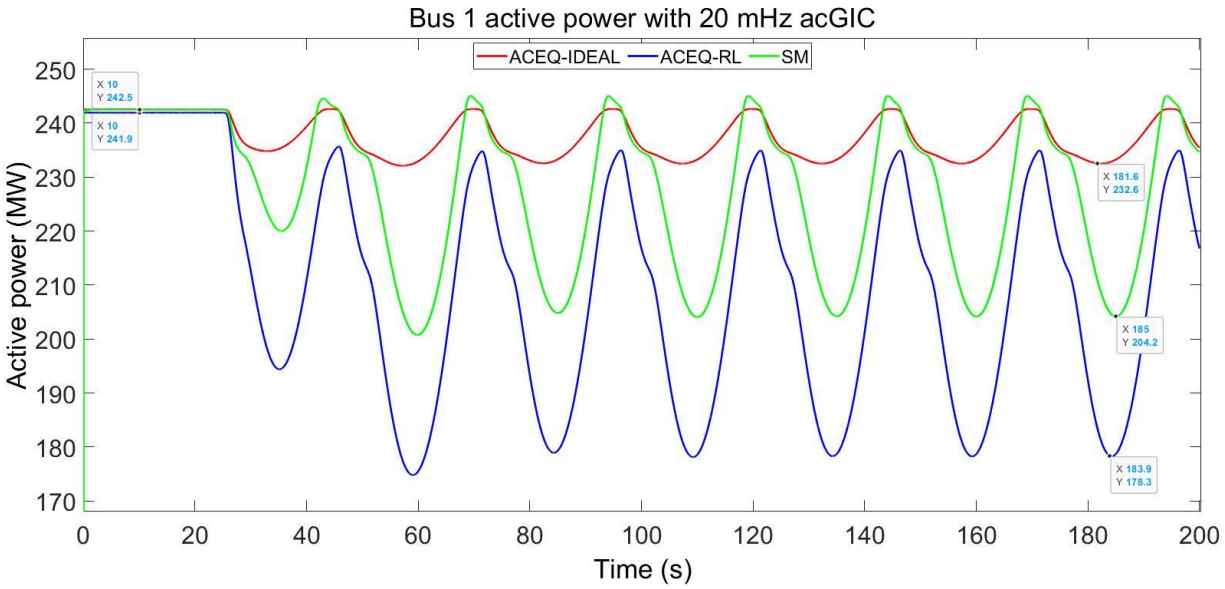

Figure 7.35: Bus 1 active power with acGIC injected at t = 25 s

Again, tracing the effects of the acGIC at the load bus reveals that the acGIC model yields a very different power system response at the load bus compared to a dcGIC model. The effect of the source models on the maximum active power dip is also noted.

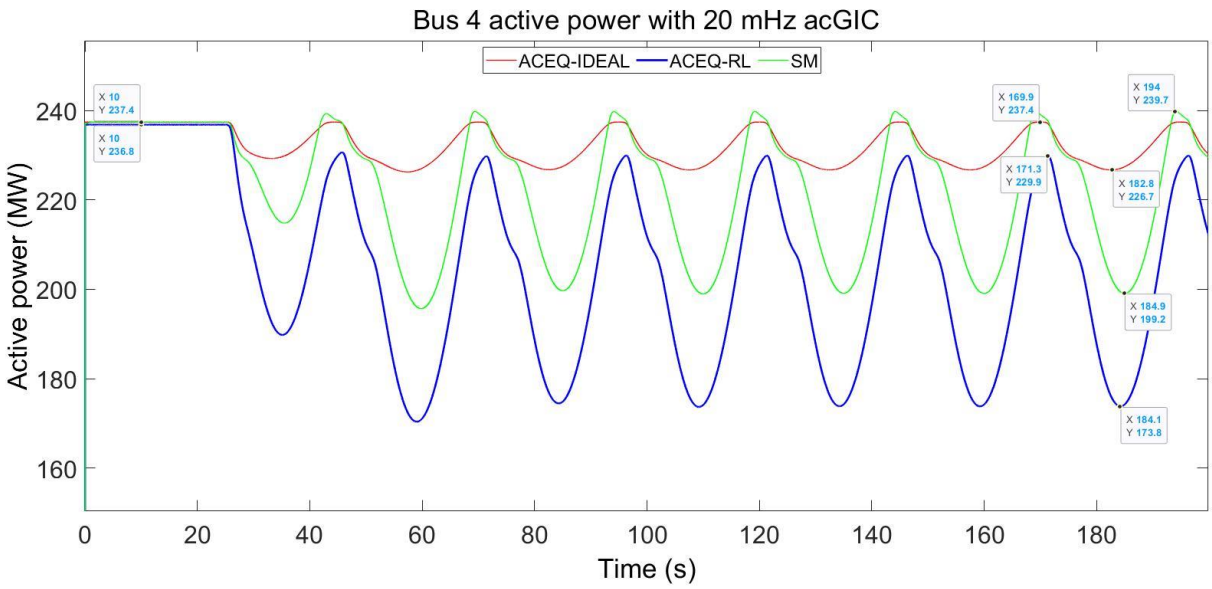

Figure 7.36: Bus 4 active power with acGIC injected at t = 25 s

7.2.9 Waveshape and Harmonic analysis

In this Section, the current harmonics at buses 1 and 2 will be discussed. In the case of bus 1 harmonic analysis, the effect of unbalance introduced in the system (See Table 6.1) on the observed harmonics will be shown. Bus 2 harmonics will only be considered for the balanced system scenario.

Prior to GIC, the percentage voltage unbalance (ratio of negative sequence to positive sequence fundamental frequency voltage) for the balanced system was 0.005 %. Slight unbalance appeared due to the 3p5L transformer core asymmetry but will be regarded as negligible and referred to as the "balanced system". In fact, the MATLAB transformer does not model interphase-coupling as discussed in a companion paper [98]. With the unbalanced system, the average value of VUF was 0.262 %. As GIC was injected, VUF increased for both balanced and unbalanced systems. Since an acGIC model was used, VUF does not reach steady state. VUF reached a maximum of 1 % with the unbalanced system compared to a maximum of 0.359 % with the balanced case. The unbalance falls within the maximum limit of 1% or 3 % imposed by NEMA and ANSI C84.1 respectively [124][125].

The stator winding instantaneous current harmonics (Bus 1) for the extremely unbalanced system are shown in Figure 7.37. The fundamental frequency component is not shown but has both a positive and negative sequence.

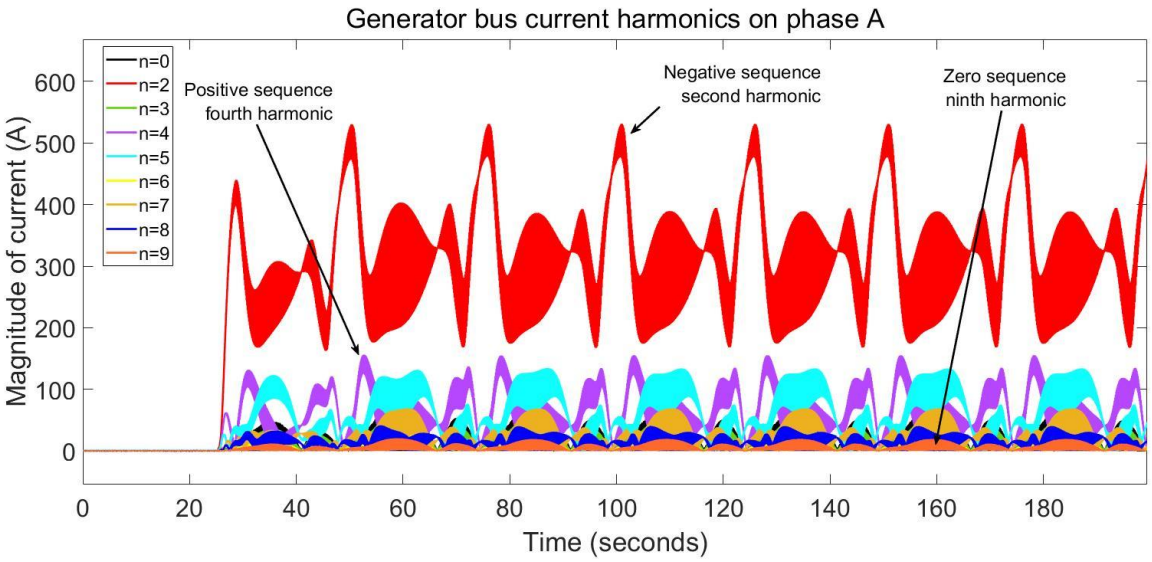

Figure 7.37: Generator bus instantaneous current harmonics' magnitude excluding the fundamental component, showing increase in positive, negative and zero sequence harmonics due to acGIC

Prior to GIC injection, the stator winding harmonics were less than 2 A in magnitude and can be considered negligible. There were no zero sequence harmonics such as the balanced third, sixth and ninth harmonics. When GIC was injected, all harmonic magnitudes increased including the conventionally assumed zero sequence harmonics. The magnitude of the harmonics did not reach steady state as with conventional dcGIC models. Instead, the magnitudes varied depending on the GIC magnitude at any specific time instant.

The second harmonic was the highest reaching a maximum of 527 A. Third, sixth and ninth harmonics appeared at the generator bus. These are conventionally assumed zero sequence harmonics. The third, sixth and ninth harmonics were not 'trapped' in the delta winding of the GSU as commonly assumed. Analysis of the sequence components of the second and third harmonics are shown in Figure 7.38 and Figure 7.39 respectively. If harmonics are unbalanced in the three phases, they no longer follow the conventional sequence and therefore, zero sequence harmonics may appear at the utility side.

Figure 7.38 shows the sequence component of the second harmonic in the generator bus current.

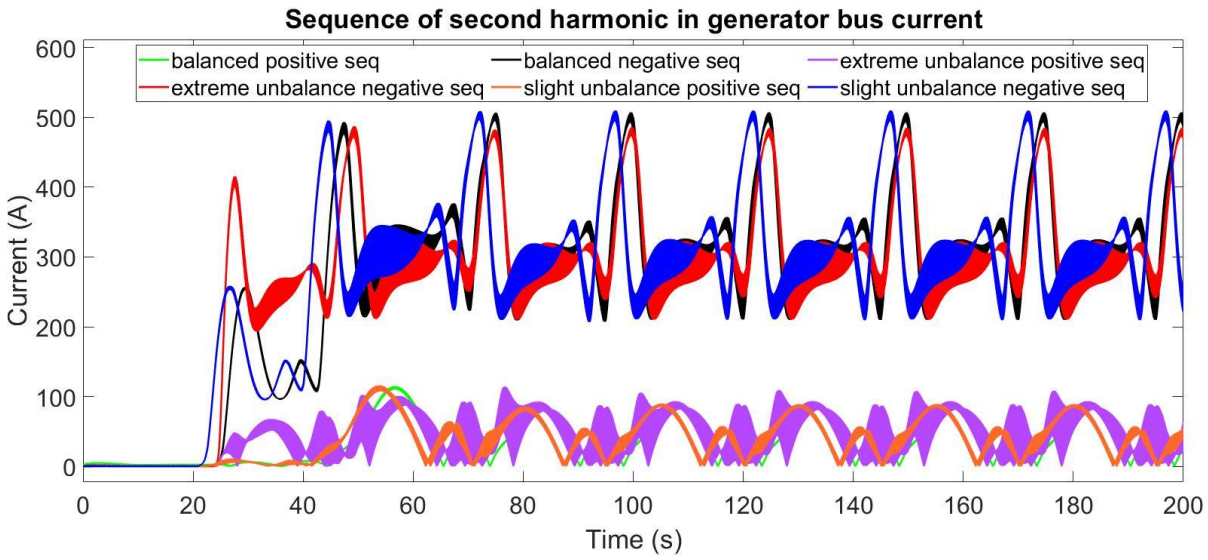

Figure 7.38: Sequence components of second harmonic current under balanced and unbalanced system condition showing both conventional negative sequence and non-conventional positive sequence

Prior to GIC injection, there are no second harmonics observed at the generator bus. Hence, the sequences are zero. When GIC was injected, the GSU now operates in the saturation region of its B-H characteristics and therefore generates even harmonics. The balanced second harmonic current has both a negative and positive sequence. The negative sequence component is higher than the positive sequence component. Appearance of non-conventional harmonics in the balanced system scenario is due to the small unbalanced supply voltages and currents but will be referred to as the balanced case. The unbalanced system's response appears similar to the balanced case. From the results, it is clear that the second harmonic does not strictly have a negative sequence. Also, under unbalanced conditions, positive sequence components can be observed within the second harmonic current consistent with earlier reports in the literature [29].

Figure 7.39 shows the third harmonic sequences. Prior to GIC injection, the third harmonic current was small and within limits of the IEEE 519 Std [123]. When T12 saturates due to GIC, there is an increase in the magnitude of the odd harmonics drawn by the shunt magnetizing branch of the transformer. It appears that the third harmonic current does not only have a zero sequence but includes positive and negative sequence components. The magnitudes of these sequences are higher in an unbalanced system compared to the balanced case. Moreover, the magnitudes of the positive sequence third harmonic are always larger than those of the negative sequence third harmonic, irrespective of whether the system is balanced or unbalanced.

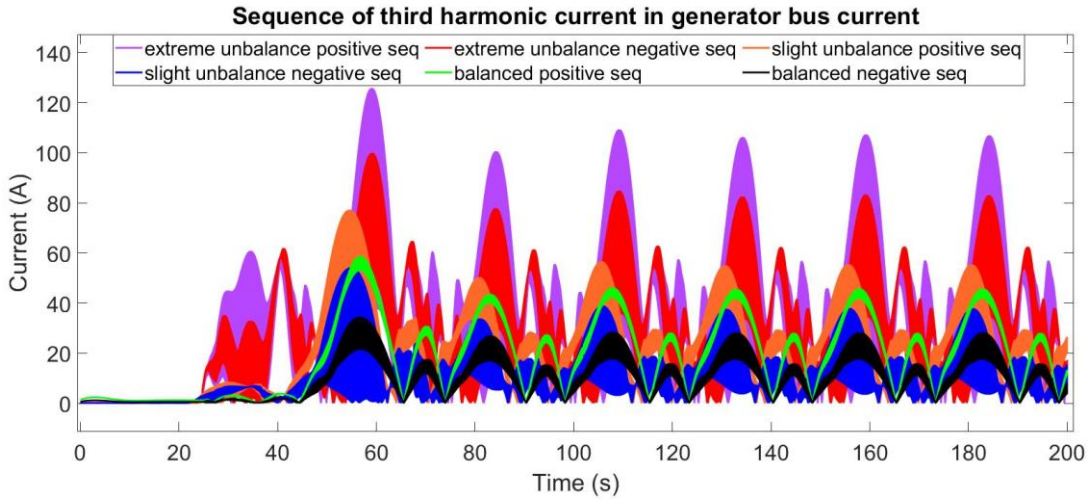

Figure 7.39: Sequence components of third harmonic current under balanced and unbalanced system condition showing a non-conventional positive and negative sequence nature

Figure 7.40 shows the waveshape of bus 2 current during a short time interval around t = 10 s. Bus 2 current will only be analysed for the balanced case. In the case of unbalance, similar non-conventional harmonic sequences to bus 1 current were observed for each of bus 2 current harmonics.

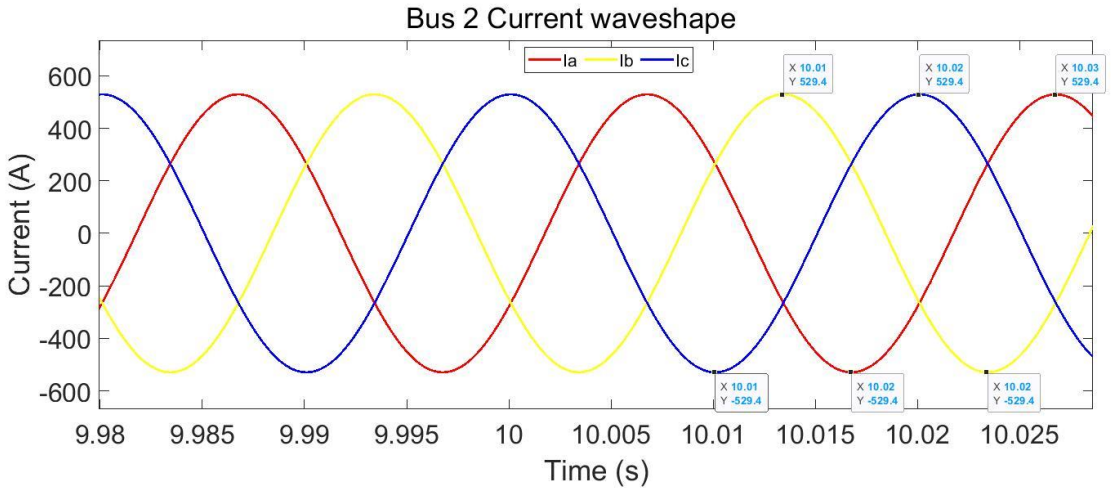

Figure 7.40: Bus 2 current waveshape at t = 10 s showing no distortion and symmetrical waveform

As shown in Figure 7.40, when there is no GIC flowing in the network, there is no distortion in the transmission line current.

Figure 7.41 shows bus 2 current waveshape during a short time interval at the positive acGIC peak. Clearly, the waveshape appears distorted at the positive peak due to part wave saturation caused by acGIC in the positive half cycle. Moreover, the presence of even harmonics can be depicted due to the fact that the current is not symmetrical about the zero axis.

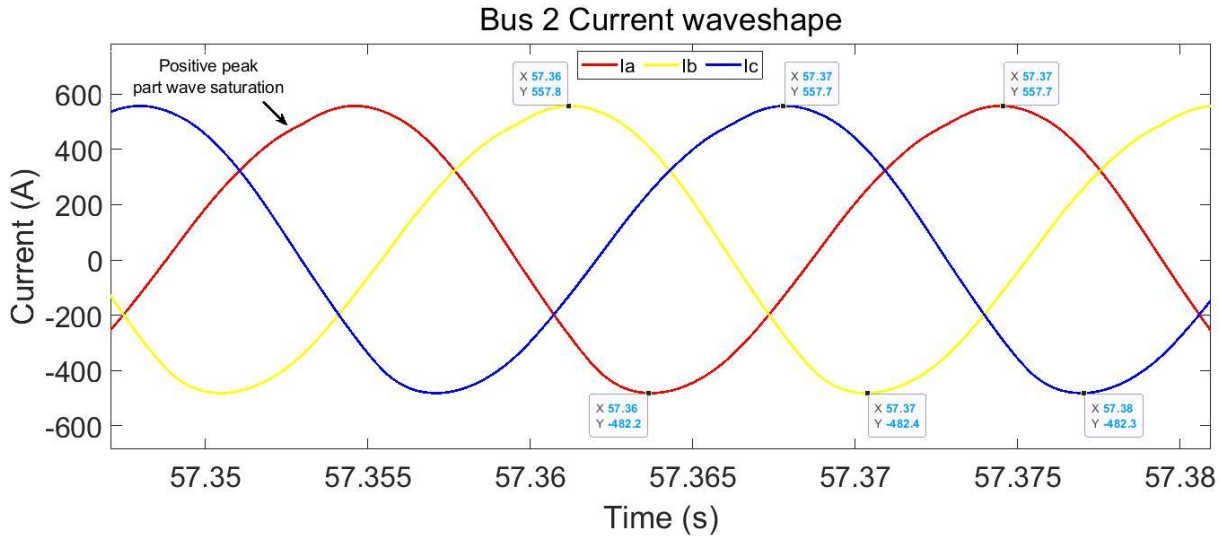

Figure 7.41: Bus 2 current waveshape at positive ac GIC peak showing part wave saturation in positive half cycle

Figure 7.42 shows the bus 2 current waveshape during a short time interval at the negative acGIC peak. Clearly, the waveshape appears distorted, but at the negative peak due to part wave saturation caused by acGIC in the negative half cycle. Again, the presence of even harmonics can be depicted due to the fact that the current is not symmetrical about the zero axis.

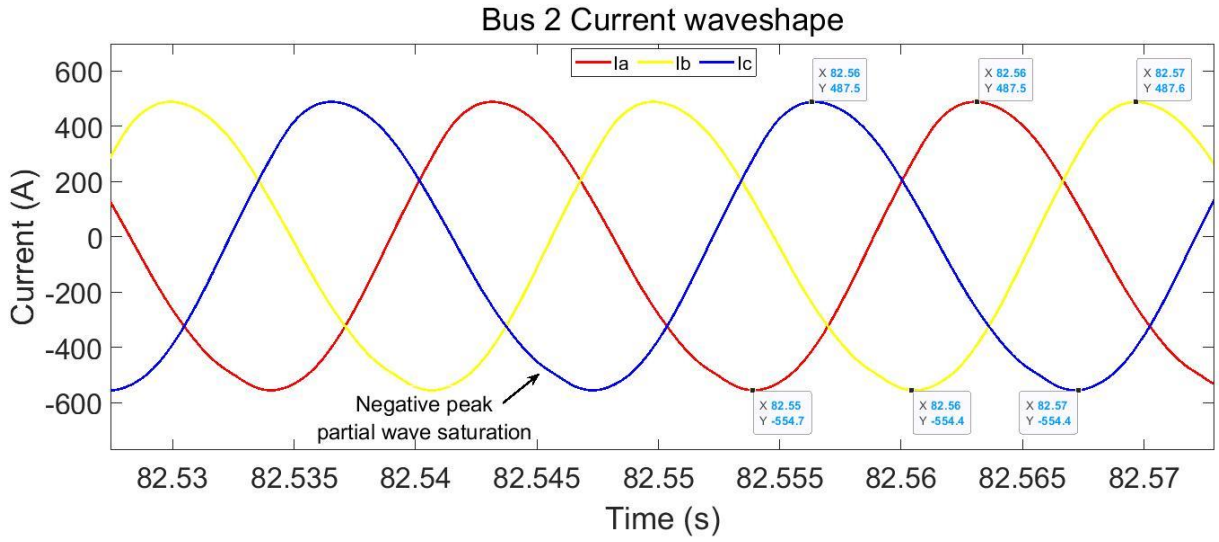

Figure 7.42: Bus 2 current waveshape at negative ac GIC peak showing part wave saturation in negative half cycle

Analysis of bus 2 current shows that part wave saturation in the transmission line current occurs at both the positive and negative peaks. This is due to the model of the GIC used. While part wave saturation with a dcGIC model only occurs in the half cycle corresponding to the polarity of the applied dcGIC, it is shown that with an acGIC model, part wave saturation depends on the polarity of the GIC peak. This means that the total harmonic distortion under realistic geomagnetic disturbances varies depending on the magnitude of the GIC at any particular time. The same applies to bus 4 currents.

7.3 Differences between dcGIC and acGIC models

Figure 7.43 shows a summary of the waveshape variation with acGIC models. It is to be noted that the diagrams are not to scale and are only for illustration.

The 20 mHz acGIC waveform acts as an envelope to 50/60 Hz fundamental current. Part wave saturation with acGIC models occurs at both positive and negative peaks. At the instance where the GIC crosses the time axis, there is no part wave saturation and therefore current or voltage distortion.

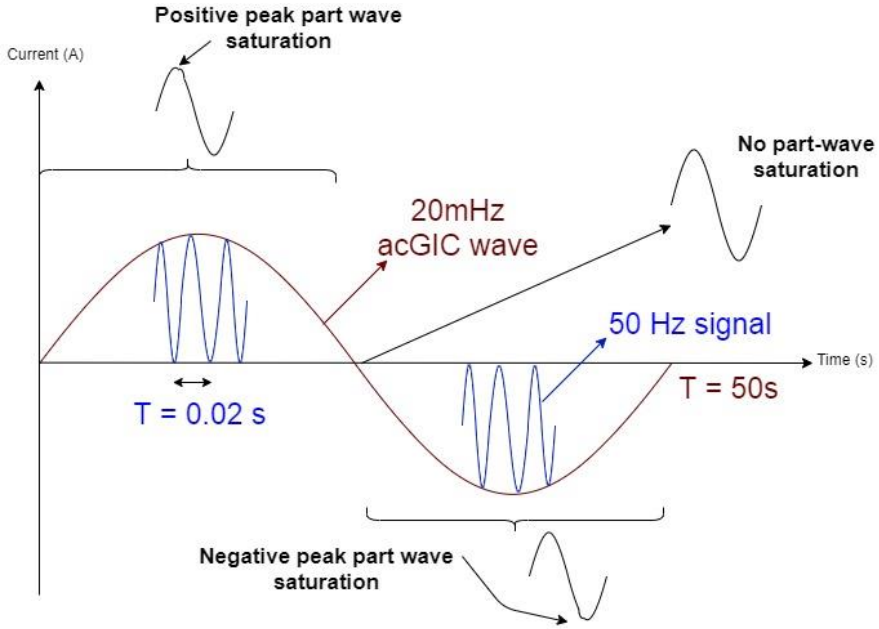

Figure 7.43: Superimposition of 50 Hz power frequency waveform and 20mHz acGIC showing periodic part wave saturation in both positive and negative peaks

Figure 7.44 is a novel illustration of the conventionally used image showing the dc bias and saturation phenomena due to GIC. The novel idea stems from the model of the GIC. If an acGIC is used, saturation occurs both at the positive and negative peaks of voltages and currents. This will be explained using Figure 7.44. Please note that the diagram is only for illustration and is not to scale. This means that the number of cycles of fundamental frequency magnetising flux waveform within acGIC envelope is only for illustration. In reality, the number of cycles within the GIC envelope will depend on GIC frequency. For example, with a 20 mHz GIC and 50 Hz fundamental frequency flux, there will be 1250 cycles of fundamental frequency flux within the positive half cycle of the the 20 mHz acGIC model and 1250 other cycles in the negative half.

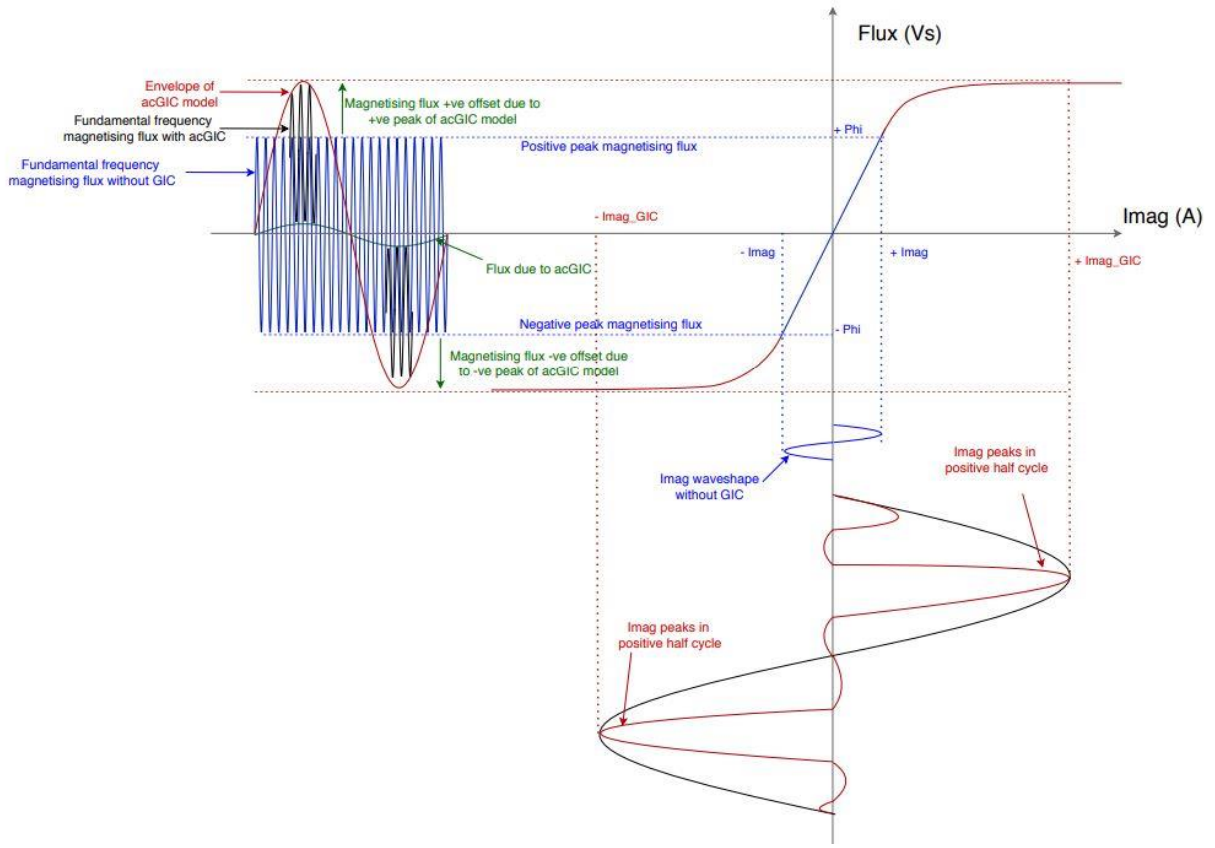

Figure 7.44: Illustration of a more realistic saturation phenomena due to ac GIC

Without GIC, the transformer operates in the linear region (blue on flux v/s Imag plot), usually close to the nose point. The magnetising flux and shape of the magnetising current of the transformer is shown in blue.

With GIC, the transformer operates in the non-linear region (red on flux v/s Imag plot). As seen from Figure 7.43, the acGIC model acts as an envelope over the 50 Hz fundamental frequency waveforms. The flux due to the GIC is shown in green. The GIC flux depends on the transformer design but it usually small compared to the fundamental frequency flux. With the acGIC model, the flux due to GIC is always changing with time. Hence, the offset in the magnetising flux of the transformer also changes with time following the trend of the acGIC envelope. When the GIC peaks in the positive half cycle, the flux increases beyond the knee point of the saturation curve (BH curve) causing a positive peak in the magnetising current. When the GIC peaks in the negative half cycle, the flux increases beyond the knee point of the saturation curve, but in the opposite direction causing the magnetising current to peak in the negative half cycle. At the instance when the acGIC crosses the zero-axis, the only flux in the transformer is its magnetising flux and hence, it operates again in the linear region. This finding shows that saturation in a transformer due to acGIC occurs periodically and depends on the GIC properties (magnitude and frequency) at a particular time. The shape of the magnetising current also varies periodically. Therefore, the harmonics generated due to transformer

saturation depends on the GIC model used. With a dcGIC model, harmonic currents reach a steady state value whereas with an acGIC model, the harmonic currents at any time instant, depends on the magnitude of the GIC.

7.4 Differences between power measurements

In this chapter, the differences between the 4 power meters described in Section 5 are shown by calculating the active power and reactive or non-active power at bus 2. Bus 2 was chosen since the transmission line currents are the richest in harmonics compared to buses 1 and 4. Moreover, to simplify the comparison, a dcGIC model has been used.

Figure 7.45 shows the active power at bus 2 when a dcGIC is injected at time t = 25 s.

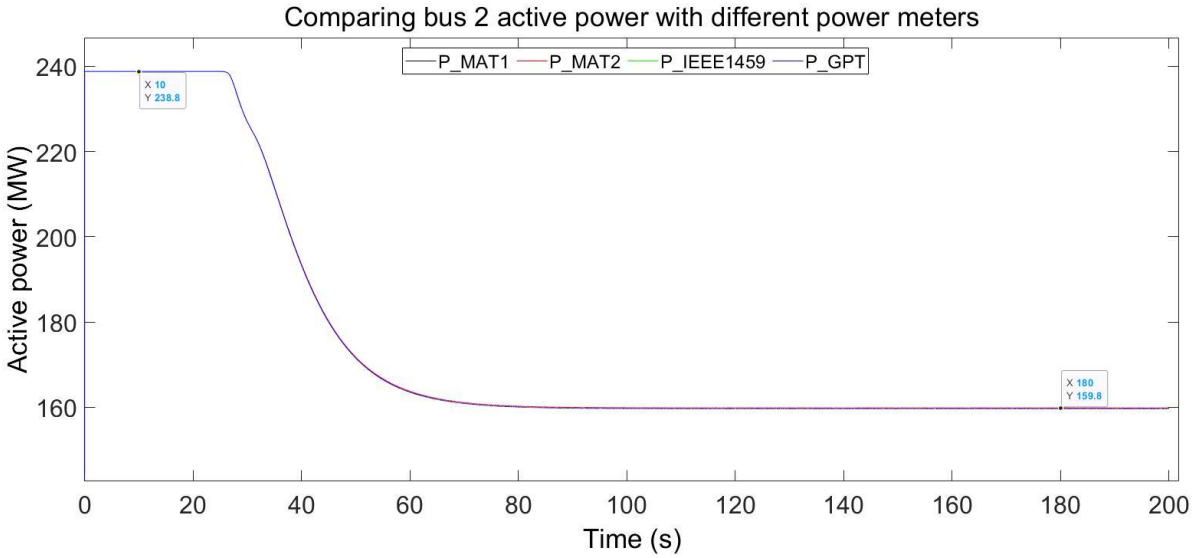

Figure 7.45: Comparing bus 2 active power using different power meters

The active power calculated by the four meters is the same. This is expected because the IEEE1459 standard and the General Power Theory only differ in their definitions of apparent power. The active power is calculated in the same way as the product of the instantaneous voltages and currents.

Figure 7.46 shows the non-active power at bus 2, calculated by the four meters.

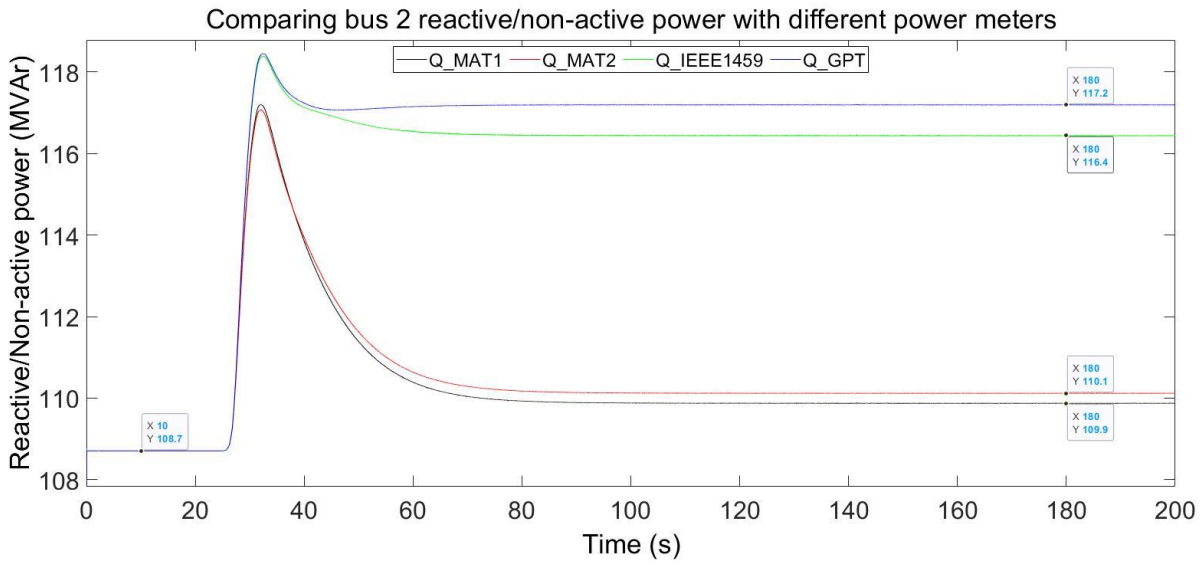

Figure 7.46: Comparison of bus 2 reactive/non-active power computed using different power meters

Prior to GIC injection, the harmonics present in bus 2 are small and therefore, the four meters calculate the same reactive or non-active power. At steady state conditions with dcGIC, the 3ph instantaneous power measurement block (Q_MAT1) gives the smallest rise in reactive power since it does not include the harmonics present in the signal when calculating reactive power (See Section 5.1). The 3ph continuous power measurement block (Q_MAT2) gives higher reactive power than Q_MAT1 since it includes the harmonics in the calculation of reactive power. However, only the harmonics belonging to a specific sequence are used in the reactive power calculation. It becomes a tedious task and to add the harmonics from each sequence to calculate the reactive power. Moreover, this increases the simulation time.

Contrary to the MATLAB meters, the IEEE1459 power meter and the GPT meter show significant increases in non-active power with dcGIC. This is because the meters take into account the resistance of the neutral and the power losses in the neutral when defining and calculating the apparent power. The GPT meter shows the highest increase in non-active power since it includes all the system losses; the neutral losses, losses due to dc components and harmonics. This finding agrees to those reported in [54][26][3].

Currently, synchronous generators are designed using conventional power theories to calculate reactive power. Comparison of the var defined by different power theories has shown that during non-ideal system conditions such as GIC, the increased reactive power demand calculated by synchronous generators' var controllers is less than non-active power calculated using IEEE1459 Std. Therefore, synchronous generators respond by producing less var output than actually required under such GIC conditions which further aggravates the voltage stability of power systems.

7.5 Synchronous machine and excitation system response to GIC

This Section will focus on the response of the excitation system and synchronous machine to both dcGIC and acGIC.

7.5.1 Steady state analysis

Using the mathematical model of the synchronous generator given in [92], one can easily carry out a steady state analysis to find the initial conditions for the generator parameters. Note that the steady state analysis can only be used to study the effects of a dc GIC on the generator's response. This is because, steady state is not reached with an ac GIC model as shown by Jankee *et al* [98]. .

MATLAB machine implements one d-axis winding and two q-axis windings. Hence k = 1 and q = 1,2 from MATLAB synchronous machine mathematical equations given in [92]. At steady state, all time derivative terms equal to zero. The damper winding currents are also zero at steady state since $R_{1d}i_{1d} = R_{1q}i_{1q} = R_{2q}i_{2q} = 0$. Re-writing the synchronous machine equations at steady state yields;

$$V_d = -i_d R_s - \omega\psi_q \tag{7.4}$$

$$V_q = -i_q R_s + \omega\psi_d \tag{7.5}$$

$$FV_{fd} = i_{fd}R_{fd} \tag{7.6}$$

$$\psi_d = -(L_{md} + L_l)\, i_d + L_{md}i_{fd}, where\ L_{md} + L_L = L_d \tag{7.7}$$

$$\psi_q = -(L_{mq} + L_l)\, i_q, where\ L_{mq} + L_l = L_q \tag{7.8}$$

$$\psi_{fd} = -L_{md}i_d + \left(L_{md} + L_{lfd} + L_{fld}\right)i_{fd}, where\ L_{md} + L_{lfd} + L_{fld} \tag{7.9}$$

$$\psi_{1d} = -L_{md}i_d + (L_{md} + L_{fld})i_{fd} \tag{7.10}$$

$$\psi_{1q} = \psi_{2q} = -L_{mq}i_q \tag{7.11}$$

To find the field current at steady state

From (7.7),

$$i_{fd} = \frac{\psi_d + L_d\, i_d}{L_{md}}, here\ L_{md} + L_L = L_d \tag{7.12}$$

From (7.5), $\psi_d = -\frac{(V_q + i_q R_s)}{\omega}$

Replacing the expression for ψ_d in (7.12) gives;

$$i_{fd} = \frac{V_q + i_q R_s + \omega L_d\, i_d}{\omega L_{md}} \tag{7.13}$$

In pu, the d-axis reactance and inductance have the same value since the same base frequency is used in the pu to SI conversion. Hence, one can replace L_d in equation (7.13) to X_d if both are expressed in pu.

$$i_{fd} = \frac{V_q + i_q R_s + X_d\, i_d}{(X_d - X_l)} \tag{7.14}$$

To find the d-axis voltage V_d at steady state

To find the d-axis voltage in terms of the machine reactances, equation (7.8) is substituted in equation (7.4).

$$V_d = -i_d R_s + \omega L_q i_q = -i_d R_s + \omega X_q i_q \tag{7.15}$$

To find the q-axis voltage V_d at steady state

To find the q-axis voltage in terms of the machine reactances, equation (7.7) is substituted in equation (7.5).

$$V_q = -i_q R_s + \omega\left(L_d i_d + L_{md} i_{fd}\right) = -i_q R_s + X_d i_d + (X_d - X_l) i_{fd} \tag{7.16}$$

To find the active power output P_t at steady state

$$P_t = V_d i_d + V_q i_q \tag{7.17}$$

To find the reactive power output Q_t at steady state

$$Q_t = V_q i_d - V_d i_q \tag{7.18}$$

Using the steady state equivalent circuit of the synchronous machine given below;

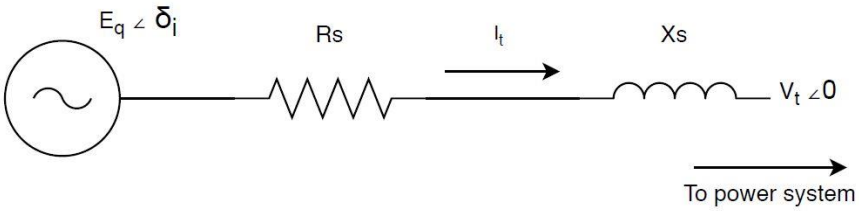

$$E_q = V_q = V_t + (R_s + jX_s)I_t \tag{7.19}$$

Using (7.16) and realising that damper winding currents are zero,

$$|V_q| = X_{md} i_{fd} \tag{7.20}$$

V_q represents the effective internal voltage of the synchronous generator. It is also known as the excitation voltage due to field current.

Using the phasor diagram of the above circuit (See Figure 2.10) and equating the parallel and perpendicular components of V_t gives;

$$P_t = V_t I_t \cos\varphi = V_t \frac{X_{md} i_{fd} \sin\delta_i}{X_s} \tag{7.21}$$

$$Q_t = V_t I_t \sin\varphi = V_t (\frac{X_{md} i_{fd} \cos\delta_i - V_t}{X_s}) \tag{7.22}$$

The equations that govern the steady state analysis of the synchronous generator were used to ensure that the values obtained from the simulations agree with theory.

Synchronous generator parameters,

$$S_{machine} = 450\ MVA$$

$$R_s = 0.0025\ ; X_d = 1.8\ ; X_l = 0.2; X_q = 1.7$$

Initial conditions

$$V_t = 1\ pu$$

$$P_t = \frac{242.5}{450}\ MW = 0.5389\ pu$$

$$Q_t = \frac{126.2}{450}\ MVAr = 0.2804\ pu$$

Using the steady state synchronous generator equations and the initial specified conditions, all the generator quantities can be calculated.

$$I_t = \frac{\sqrt{{P_t}^2 + {Q_t}^2}}{V_t} = 0.6075\ pu$$

$$\vartheta = \arccos(\frac{P_t}{V_t I_t}) = 27.48882444\ ^\circ$$

$\vartheta = power\ factor\ angle$

$\delta = load\ angle$

$$\delta = \arctan\frac{X_q I_t \cos\vartheta - R_s I_t \sin\vartheta}{V_t + R_a I_t \cos\vartheta + X_q I_t \sin\vartheta} = 31.77^\circ$$

$$V_d = V_t \sin\delta = 0.5265\ pu$$

$$V_q = V_t \cos\delta = 0.8502\ pu$$

$$i_d = I_t \sin(\delta + \vartheta) = 0.5222\ pu$$

$$i_q = I_t \cos(\delta + \vartheta) = 0.3104\ pu$$

$$\psi_d = V_q + i_q R_s = 0.8510\ pu$$

$$\psi_q = -V_d - i_d R_s = -0.528\ pu$$

$$X_{md} = X_d - X_l = 1.6\ pu$$

$$i_{fd} = \frac{V_q + i_q R_s + X_d\, i_d}{(X_d - X_l)} = \frac{1.791}{1.8 - 0.2} = 1.1193\ pu$$

Table 7.6 shows a comparison of the calculated values and measured values in MATLAB. All measured values are exactly similar to the calculated values except for V_{fd} which appears as $|V_q|$ in MATLAB. The calculations show that the field current is 1.1195 pu. Only after multiplying by the denominator $X_d - X_l = X_{md}$, one gets the value of 1.791 pu measured in the simulations.

Table 7.6: Comparison of synchronous generator calculated quantities from steady state analysis and measured values from MATLAB simulations

Synchronous generator parameters	Calculated/specified values using steady state analysis	Measured values from MATLAB simulations
P_e	0.5389	0.5389
Q_e	0.2804	0.2804
V_t	1	1
I_t	0.6075	0.6075
δ	31.77	31.77°
V_d	0.5265	0.5265
V_q	0.8502	0.8501
i_d	0.5222	0.5222
i_q	0.3104	0.3105
$i_{fd} = V_{fd}$	1.1193	1.791

7.5.2 Field voltage of excitation system

Figure 7.47 shows the field voltage input to the synchronous machine during the 200 s of simulation run time with a dc GIC injected at t = 25 s.

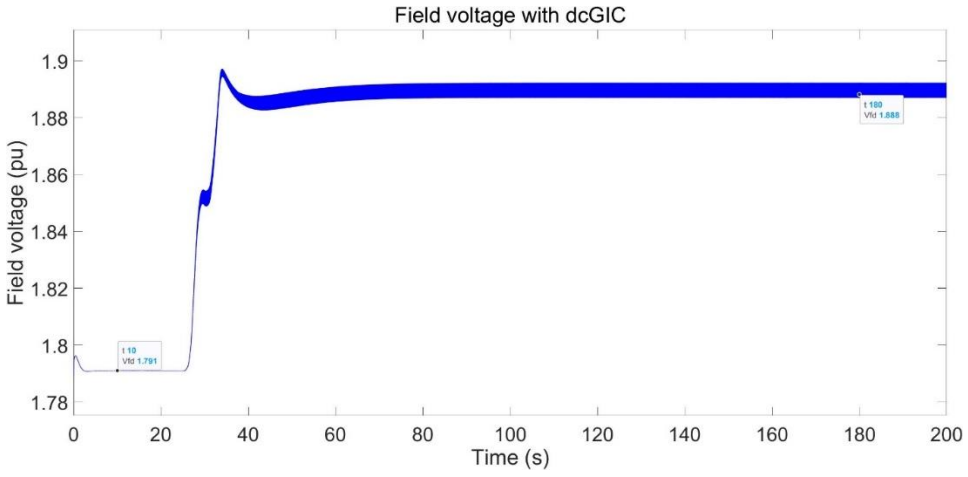

Figure 7.47: Field voltage supplied by AC1A excitation system to full synchronous generator model

The initial measured field voltage prior to GIC injection was 1.791 pu. Using equation (7.14), the calculated field current was:

$$i_{fd} = \frac{V_q + i_q R_s + X_d\, i_d}{(X_d - X_l)} = \frac{1.791}{1.8 - 0.2} = 1.1193\ pu$$

Note the 1.791 pu value appearing in the numerator. This is the field current and field voltage that was observed in MATLAB (See Figure 7.47). The field current and field voltage have the same pu values because they are only linked by the field resistance. Hence $i_{fd} = V_{fd}$

However, the calculations show that the field current is 1.1195 pu. Only after multiplying by the denominator $X_d - X_l = X_{md}$, one can get the value of 1.791 pu.

Using the steady state equivalent circuit of the synchronous machine and equation (7.19), the excitation voltage was calculated;

$$E_q = V_q = V_t + (R_s + jX_s)I_t$$

Kundur specifies that V_q is the excitation voltage due to the field current. Neglecting saliency and realising that damper winding currents are zero,

$$|V_q| = X_{md} i_{fd} = 1.6 * 1.1193 = 1.791\ pu$$

It appears that the field voltage observed in MATLAB is $|V_q|$ and not V_{fd}.

7.5.3 Load angle

Using the steady state analysis, the load angle was calculated as follows:

$$\delta = \arctan \frac{X_q I_t \cos\vartheta - R_s I_t \sin\vartheta}{V_t + R_a I_t \cos\vartheta + X_q I_t \sin\vartheta} = 31.77°$$

The measured load angle is shown in Figure 7.48.

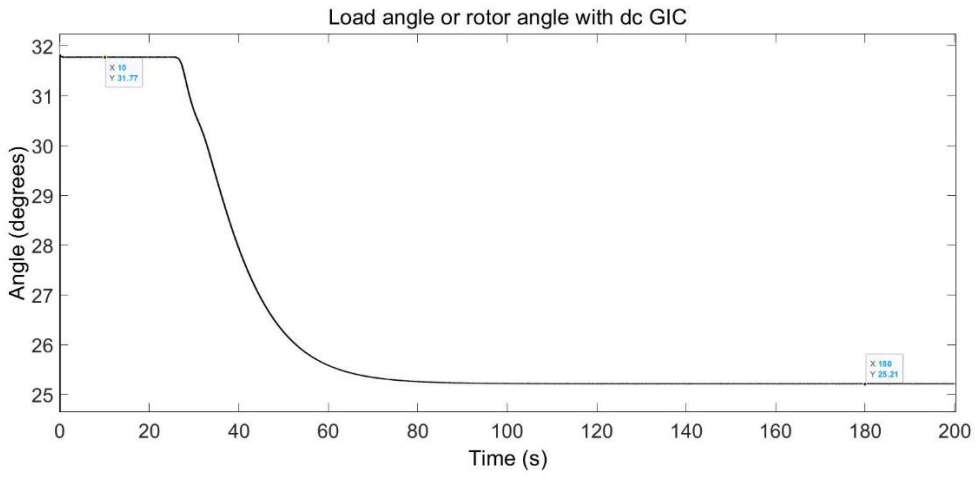

Figure 7.48:Load angle or rotor angle of synchronous generator

Prior to GIC injection, the load angle (average) was 31.77 °. When the system reaches the dc GIC steady state condition, the load angle reduced to 25.21. Thus, the active power transfer to the load has been reduced.

7.5.4 d,q axis voltages

The d-axis voltage was calculated using the steady state analysis as follows:

$$V_d = V_t \sin\delta = 0.5265\ pu$$

Similarly, the q-axis voltage was calculated using steady state analysis as follows:

$$V_q = V_t \cos\delta = 0.8502\ pu$$

Figure 7.49 shows the terminal voltage of the generator expressed in terms of d-axis and q-axis voltage. Prior to GIC, the d-axis voltage was 0.5265 pu, exactly similar to the calculated value. The q-axis voltage was 0.8501 pu, very similar to the calculated value. At the post GIC steady state condition, there is a drop in terminal voltage of the generator. Therefore, the d and q axis voltages show a decrease to a new steady state average value.

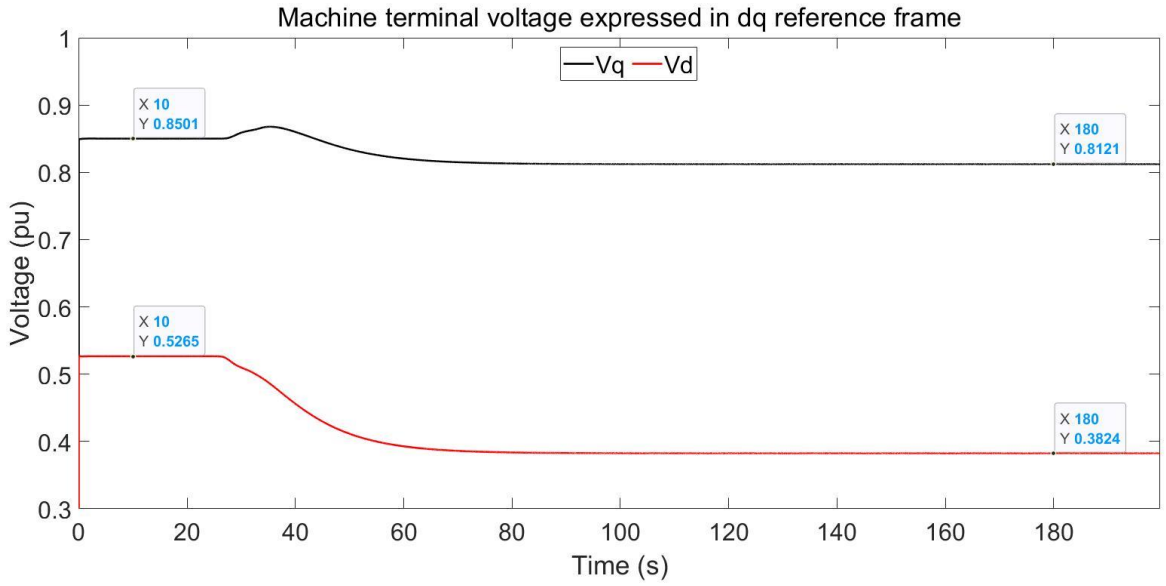

Figure 7.49: Terminal voltage of synchronous generator, expressed in dq reference frame

7.5.5 Damper winding currents

The damper winding currents carry no current under steady state conditions. Hence prior to GIC, the damper winding currents are very small and can be considered as zero as shown in Figure 7.50. When GIC flows in the network, there is an increase in the damper winding currents, with the q-axis damper winding 1 being the highest followed by the d-axis damper winding and q-axis damper winding 2. The rise in damper winding currents is due to the increase in harmonics induced on the damper bars coming from the saturating generator step up transformer. This causes heating of the damper windings and potential damage to the rotor bars as discussed in [29] [31].

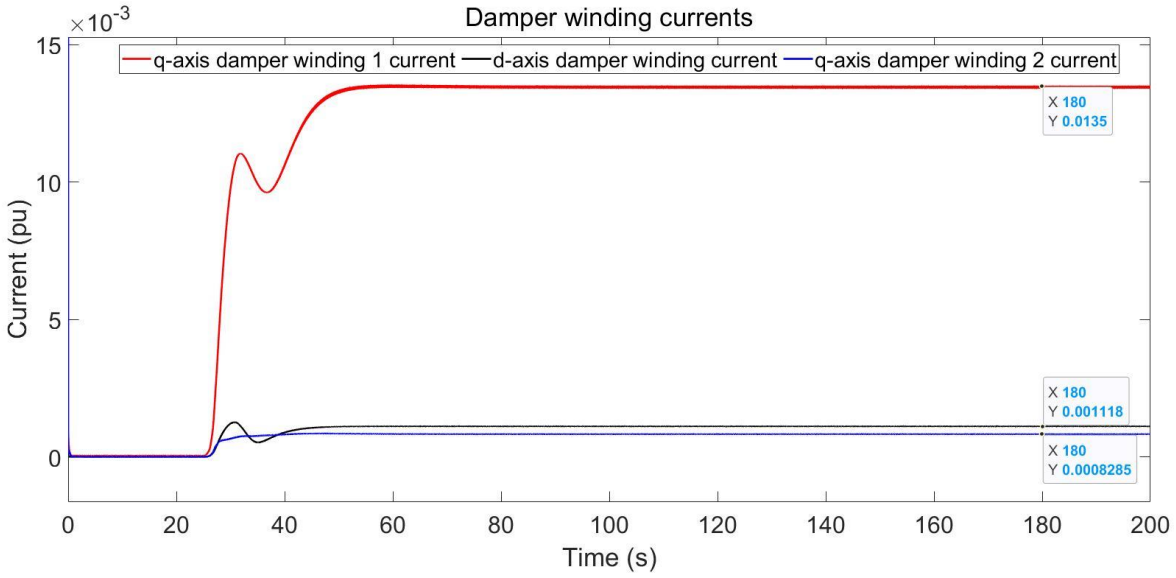

Figure 7.50: Damper winding currents during dc GIC conditions

Neglecting saturation and using the IEEE 1110 - 2002 d-q equivalent circuit of the synchronous generator [70][50], the rotor damper winding flux linkage can be expressed using equations (7.23 to 7.25).

$$\psi_{1d} = L_{f1d} i_{fd} + L_{11d} i_{1d} - L_{md} i_d \qquad (7.23)$$

$$\psi_{1q} = L_{11q} i_{1q} + L_{mq} i_{2q} - L_{mq} i_q \qquad (7.24)$$

$$\psi_{2q} = L_{22q} i_{2q} + L_{mq} i_{1q} - L_{mq} i_q \qquad (7.25)$$

It is also important to note that i_{1d} is a function of the field current i_{fd}. L_{f1d} is the mutual inductance between field and d-axis damper winding. L_{11d} is the self-inductance of the d-axis damper winding. L_{11q} is the self-inductance of the q-axis damper winding 1 and L_{22q} is the self-inductance of the q-axis damper winding 2. L_{md} and L_{mq} represent the mutual inductance between stator and field winding along the d-axis and q-axis respectively.

The corresponding damper winding currents i_{1d}, i_{1q} and i_{2q} can then be calculated by replacing the expression for i_d and i_q in (7.23 to 7.25). Using I_{pd} to represent the peak d-axis winding current and n to represent the harmonic order, i_d can be calculated using equation (7.26).

$i_d = I_p \sin(n\omega_s t + \vartheta - \varphi)$, where $\varphi = \omega_r t$ and ω_r is the rotor angular velocity (7.26)

Similarly, the q-axis current can be calculated using equation (7.27).

$$i_q = -I_{pq}\cos(n\omega_s t + \vartheta - \varphi) \tag{7.27}$$

Replacing the expressions for i_d and i_q from (7.26) and (7.27) into (7.23), (7.24) and (7.25) gives the relationship between the damper winding flux and stator induced harmonic currents expressed in dq0 components.

$$\psi_{1d} = L_{f1d}i_{fd} + L_{11d}i_{1d} - L_{md}(I_p \sin(n\omega_s t + \vartheta - \varphi)) \tag{7.28}$$

$$\psi_{1q} = L_{11q}i_{1q} + L_{mq}i_{2q} - L_{mq}(-I_p \cos(n\omega_s t + \vartheta - \varphi)) \tag{7.29}$$

$$\psi_{2q} = L_{22q}i_{2q} + L_{mq}i_{1q} - L_{mq}\big(-I_p \cos(n\omega_s t + \vartheta - \varphi)\big) \tag{7.30}$$

At steady state the damper winding currents are zero and hence the flux on both d and q axes simplify to (7.31) and (7.32) respectively.

$$\psi_{1d} = -L_{md}i_d + (L_{md} + L_{fld})i_{fd} \tag{7.31}$$

$$\psi_{1q} = \psi_{2q} = -L_{mq}i_q \tag{7.32}$$

Under harmonic conditions, the flux linking the damper windings (ψ_{1d}, ψ_{1q} and ψ_{2q}) are no longer zero. Hence according to equations 7.28, 7.29 and 7.30, GIC-induced harmonic currents are induced on the rotor damper bars as reported in literature [36][29][31]. The increase in i_{1d}, i_{1q} and i_{2q} leads to heating of the rotor damper bars as the flux reaches the end-rings shown in Figure 2.2. In general, for any rotor coil on the d-axis, the angle between the rotor coil and stator phase A axis is φ. Suppose that the phase angle relative to the axis of phase A stator winding for a positive sequence harmonic is expressed as φ_p, that of a negative sequence harmonic is expressed as φ_n, the magnitude of the positive sequence air gap harmonic is P_n and that of the negative sequence harmonic is N_n, then one can easily calculate i_{1d} using resolution of vectors.

$$i_{1d} = -P_n \cos\big((n_{stator} - 1)\omega t + \varphi_p - \varphi\big) - N_n \cos(-(n_{stator} + 1)\omega t + \varphi_n - \varphi) \tag{7.33}$$

Since the d-axis is orthogonal to the q-axis, the general expression for the q-axis damper winding current where $k = 1$ or 2.

$$i_{kq} = -P_n \cos\Big((n_{stator} - 1)\omega t + \varphi_p - \varphi - 90\Big) - N_n \cos(-(n_{stator} + 1)\omega t + \varphi_n - \varphi - 90) \quad (7.34)$$

Figure 7.51 shows the harmonics present in one of the rotor windings of the synchronous generator, more specifically the d-axis damper winding for a simulation run using a 20 mHz acGIC model. Applying an FFT analysis showed that the d and q axis damper winding had very low second and fourth harmonics. However, the stator positive sequence stator fourth harmonic and negative sequence second harmonic were significant. In fact, positive sequence stator harmonics appear as one harmonic less than the fundamental frequency and negative sequence stator harmonics appear as one harmonic plus the fundamental frequency [29][36]. Therefore, the positive sequence stator fourth harmonic and negative sequence stator second harmonic appear as a third order harmonic on the rotor.

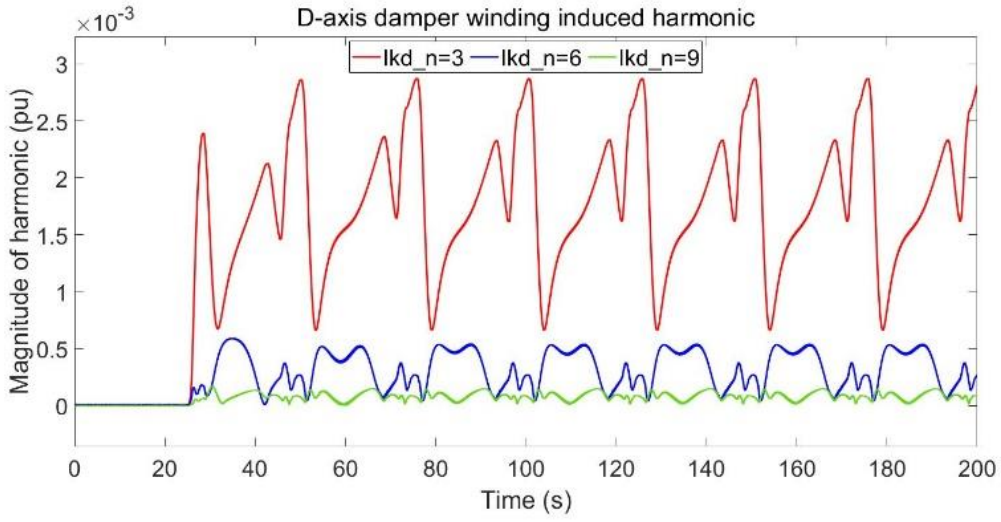

Figure 7.51: Stator second and fourth harmonic inducing the third harmonic on the d-axis damper winding; rotor winding second and fourth harmonics are relatively much lower in magnitude.

7.5.6 Effect of excitation system control on field current, reactive power and voltage dip due to GIC

In this Section, the effects of varying some of the AC1A excitation system control parameters will be investigated to see the power system's dynamic response under 20 mHz acGIC conditions. The findings show how the excitation system control can help to reduce some of the effects of GIC such as the voltage dip at the buses.

7.5.6.1 Effect of exciter gain (Ke)

Figure 7.52 shows the effect of using different exciter gains on the field current supplied to the synchronous generator

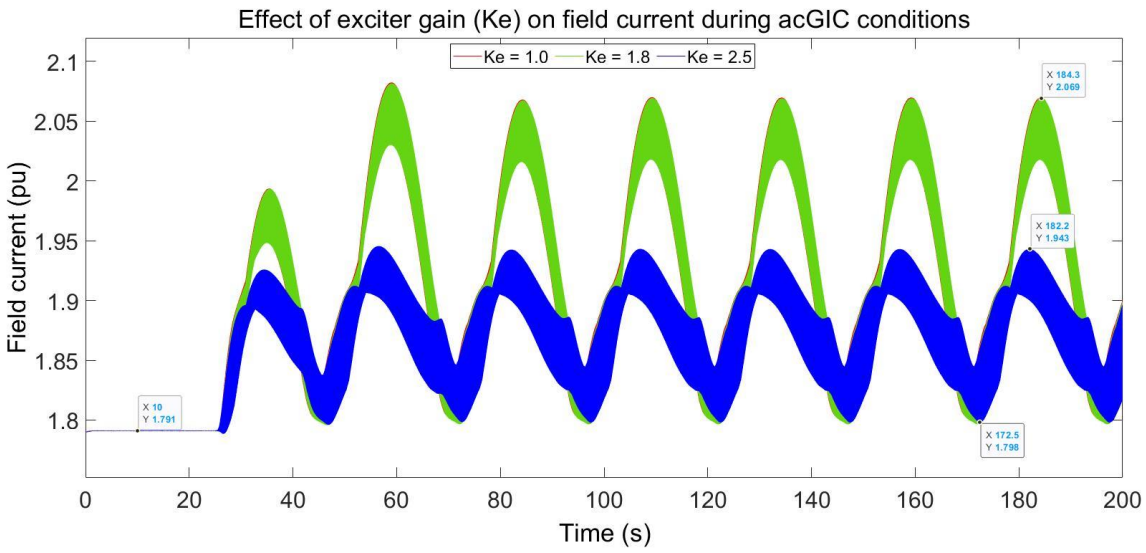

Figure 7.52: Effect of exciter gain (Ke) on field current during GIC conditions

During the first 25 s, the field current is 1.791 pu for all the three AC1A excitation systems used. When the acGIC peaks, the field current peaks for the three different excitation systems. However, the peak in field current depends on the value of the exciter gain. With $K_e = 1.0$ and $K_e = 1.8$, the field current reaches a maximum of 2.069 pu. With $K_e = 2.5$, the field current can only reach a maximum of 1.943 pu. Clearly, a smaller exciter gain appears to produce higher field currents during GIC conditions.

From Chapter 2, the field voltage of the AC1A excitation system was found to be related to the exciter gain by the following equation:

$$E_{fd} = \frac{(V_{ref} - V_C - \left(\frac{sK_F}{1+sT_F}\right)V_{FE} + V_S)(\frac{1+sT_C}{1+sT_B})\frac{K_A}{1+sT_A} - K_D I_{FD} - K_E V_E + S_E(V_E)V_E}{sT_E} F_{EX}$$

This means that the maximum reactive power output of the synchronous machine during GIC conditions is dependent on the value of K_e since the field current controls the generator's reactive power output. The reactive power output seen at the machine terminals can be expressed in terms of the field current expression as follows;

$$Q_t = V_t\left(\frac{X_{md}\left(\frac{(V_{ref} - V_C - \left(\frac{sK_F}{1+sT_F}\right)V_{FE} + V_S)(\frac{1+sT_C}{1+sT_B})\frac{K_A}{1+sT_A} - K_D I_{FD} - K_E V_E + S_E(V_E)V_E}{R_{fd}sT_E} F_{EX}\right)\cos\delta_i - V_t}{X_s}\right) \quad (7.35)$$

Figure 7.53 shows the generator's reactive power output.

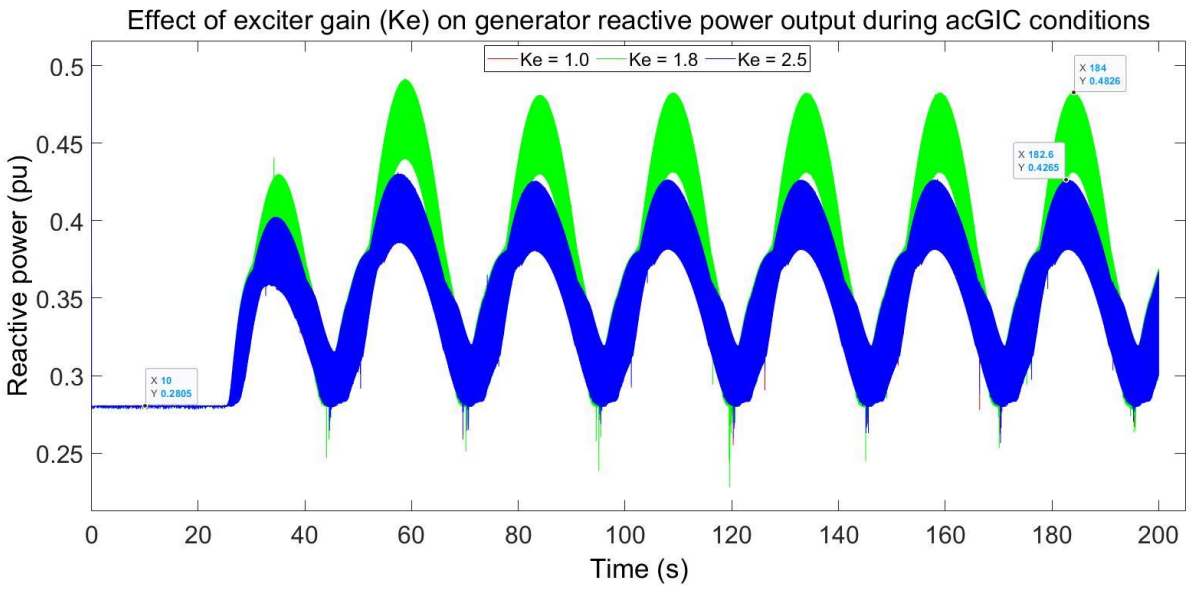

Figure 7.53: Effect of exciter gain (Ke) on generator reactive power output during GIC conditions

The reactive power output of the generator follows a similar trend to the field current. It is clear from Figure 7.53 that a smaller value of exciter gain produces more reactive power. Contrarily, with $K_e = 2.5$, the reactive power output of the generator reaches a smaller peak than with a value of $K_e = 1.8$ or $K_e = 1.0$. The higher reactive power output with smaller values of K_e implies that the exciter gain can be controlled to provide more reactive power support under GIC conditions. With more reactive power support, the dip in bus voltages is expected to be less.

The effect of the exciter gain on the field current reflects on the terminal voltage of the synchronous generator as shown in Figure 7.54.

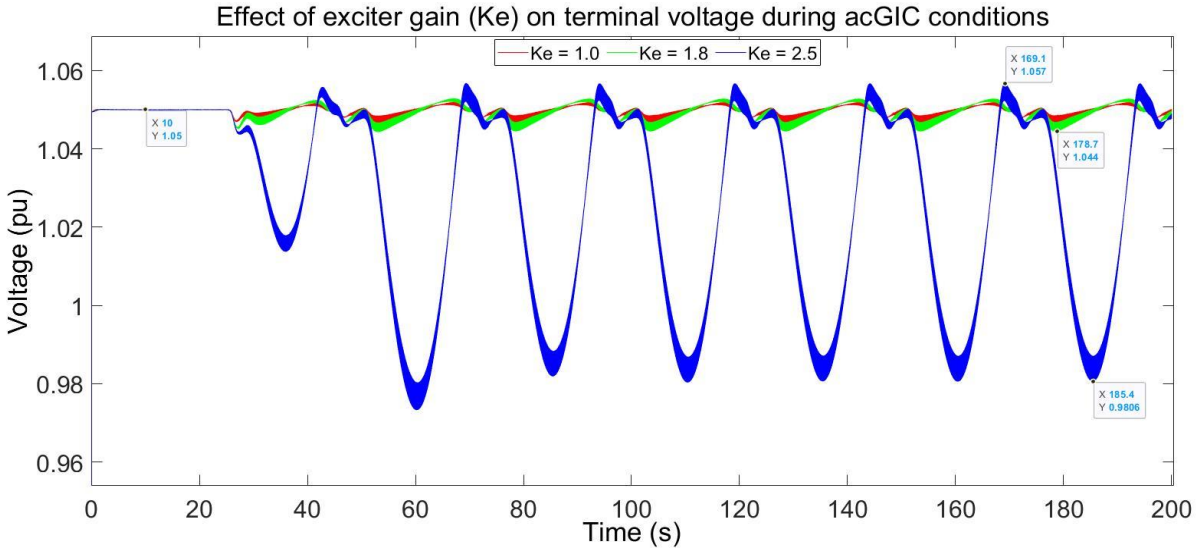

Figure 7.54: Effect of exciter gain (Ke) on synchronous machine terminal voltage during GIC conditions

Prior to GIC, the terminal voltages of the synchronous generators are similar and equal to 1.05 pu (21 kV). When GIC is injected, the drop in terminal voltage depends on the value of the exciter gain. A small exciter gain causes smaller voltage dip at the generator bus. The maximum voltage dip observed with $K_e = 1.0$ was 0.8 %. With $K_e = 2.5$, the dip in terminal voltage was more significant and represents a 6.94 % voltage dip. This is because the peak in field current is smaller with a higher value of K_e causing less reactive power output from the synchronous generator. With less reactive power at bus 1, the bus voltage decreases more.

The effect of the exciter gain on bus voltages can be traced downstream the system at the load bus as shown in Figure 7.55.

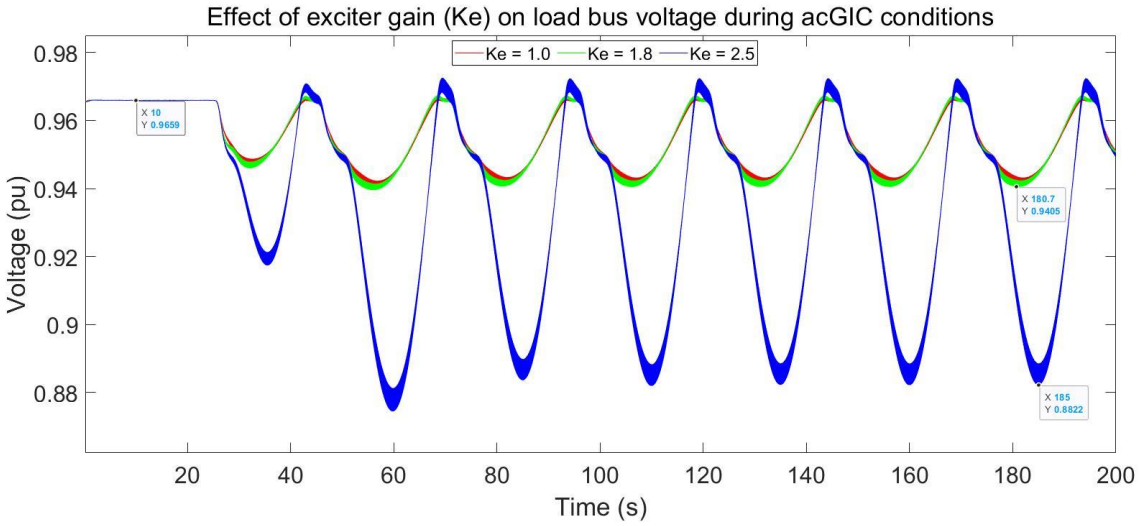

Figure 7.55: Effect of exciter gain (Ke) on load bus voltage during GIC conditions

Prior to GIC, the load bus voltage was 0.9659 pu for the three different excitation systems. Since the terminal voltage of the synchronous generator decreases with GIC, the load bus voltage also decreases. Moreover, we have seen that the terminal voltage is dependent on the exciter gain. Hence, the voltage dip at the load bus is also a function of the exciter gain. With $K_e = 2.5$, the load bus voltage drops from 0.9659 pu to a minimum of 0.8822 pu. This represents a maximum of 8.37 % decrease in the load bus voltage compared to a 2.54 % decrease with $K_e = 1$.

A static analysis of the voltage stability of the 4-bus network reveals that the value of exciter gain affects the power transfer under both noGIC and dcGIC conditions as shown in Figure 7.56.

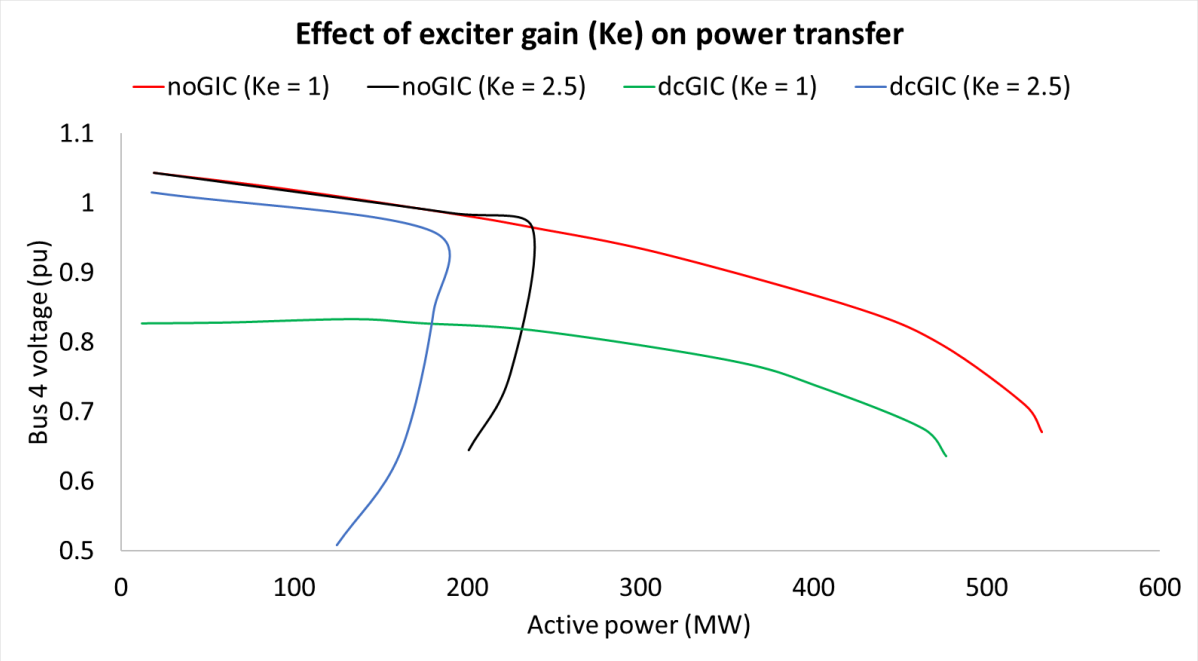

Figure 7.56: Effect of exciter gain (Ke) on power transfer - PV curve with dcGIC

With $K_e = 1.0$, the nose point of the load bus PV curve sits at 540 MW under noGIC conditions. With $K_e = 2.5$, the nose point of the load bus PV curve is reduced to 243 MW under noGIC conditions showing less power transfer capability of the system. This is because, with a value of $K_e = 2.5$, the steady state stability limit of the generator is reached at a loading level of 242.4 MW. Any increase in load beyond 242.4 MW causes a drop in the terminal voltage of the generator. With $K_e = 1.0$, as the loading increases, the generator's terminal voltage is maintained at 1.05 pu (21 kV). Active power transfer is dependent on the voltage between the generator bus and load bus, the load angle, and the reactance of the transmission system. Since the load angle and reactance of the initialized systems with $K_e = 1.0$ and $K_e = 2.5$ are the same, the difference in active power transfer without GIC is due to the voltage between the sending end and receiving end. With a reduced sending end voltage due to a larger value of K_e, the receiving end voltage and hence active power transfer is reduced. With dcGIC, there is a drop in the load bus voltage and active power. The loadability of the network is less with $K_e = 2.5$ compared to $K_e = 1.0$.

7.5.6.2 Effect of demagnetising factor (Kd)

In this Section, the effects of the demagnetising factor on the field current, reactive power output of generator and the load bus voltage will be shown. Figure 7.57 shows the field current supplied by three different AC1A excitation systems. The three exciters differ in their demagnetizing factors K_D.

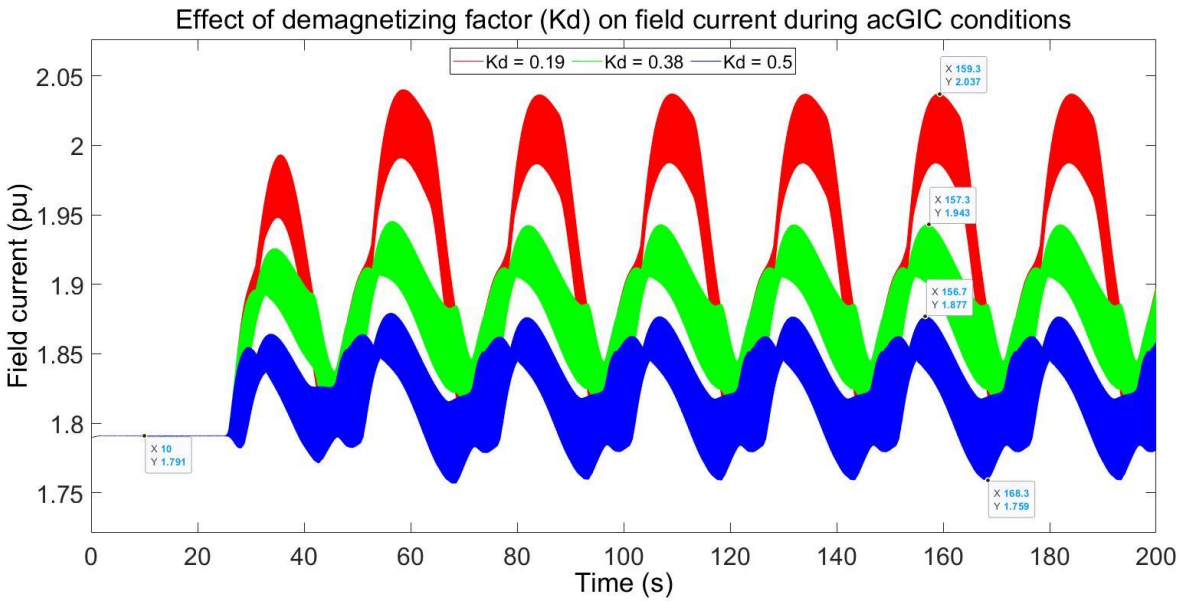

Figure 7.57: Effect of demagnetising factor (Kd) on field current during acGIC conditions

Prior to GIC injection, the field current supplied by all three AC1A excitation systems was 1.791 pu. Upon injection of GIC, the field current rises following a similar trend to the GIC. When the GIC peaks, the field current also peaks and when the GIC crosses the zero axis, the field current tries to return to its initial value of 1.791 pu. The highest peaks in field current can be observed with $K_d = 0.19$ pu, reaching a maximum of 2.037 pu. With $K_d = 0.38$ pu, the field current peaks at 1.943 pu. Finally, with $K_d = 0.5$ pu, exciter produces a maximum field current of 1.877 pu. Clearly, the demagnetizing factor appears to have significant effects on the maximum field current that can be supplied by the excitation system.

The demagnetising factor accounts for the effect of armature reaction which is demagnetising for lagging power factor loads. With a higher demagnetising factor K_d, the effect of armature reaction is more pronounced leading to a decrease in the resultant flux in the air gap. Hence, the flux required to produce the terminal voltage is reduced causing a further drop in the terminal voltage. With a smaller value of K_d, the effect of armature reaction is less demagnetising and therefore the resultant flux in the air gap reduces by a smaller amount.

These differences can also be observed in the reactive power output of the generator as shown in Figure 7.58.

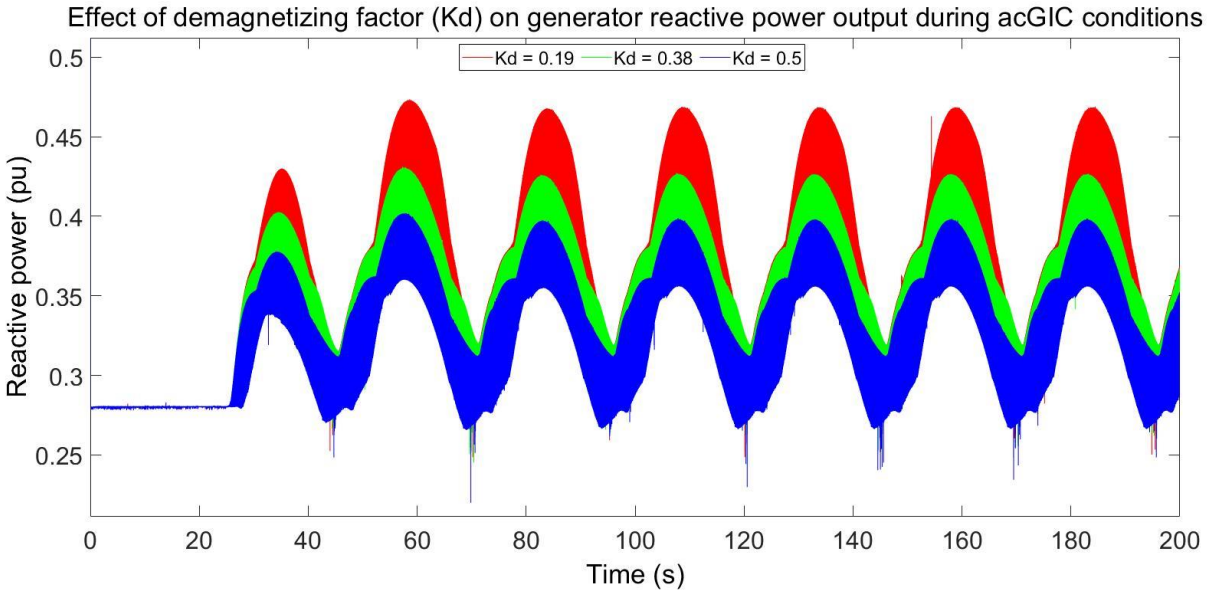

Figure 7.58: Effect of demagnetising factor (Kd) on generator's reactive power output during acGIC conditions

With a smaller value of K_d, the excitation system is able to produce more reactive power. This is because the field current supplied by the excitation system is greater with a smaller value of K_d. With more reactive power support, the bus voltages drop to a lesser extent as shown in Figure 7.59.

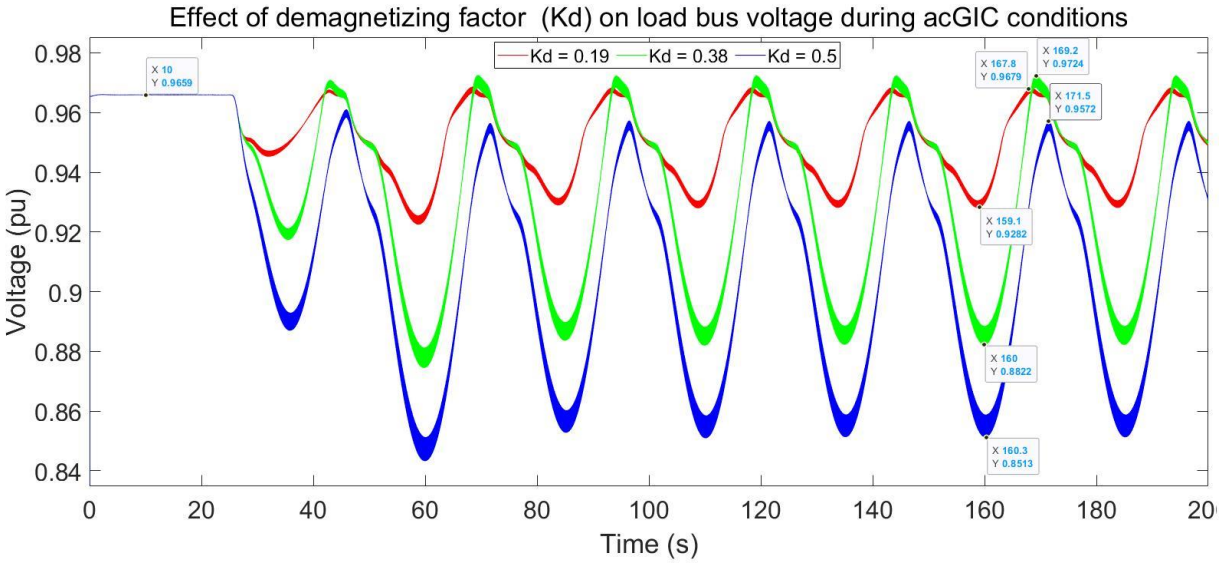

Figure 7.59: Effect of demagnetising factor (Kd) on load bus voltage during acGIC conditions

During the pre-disturbance 25 s interval, the load bus voltage was 0.9659 pu as calculated by the initial load flow. When acGIC is injected, the bus voltage drops depending on the magnitude of GIC at a particular time. With $K_d = 0.19$ pu, the load bus voltage drops to a minimum of 0.9282 pu. With $K_d = 0.38$ pu, the load bus voltage drops to a minimum of 0.8822 pu. With $K_d = 0.5$ pu, the load bus voltage violates the 10 % voltage drop limit and reaches a minimum of 0.8513 pu.

The results clearly show that the excitation system demagnetising factor K_d has a direct effect on the field flux and therefore, the field current supplied to the generator. Reducing the demagnetising effect of armature reaction appears to have positive effects during GIC conditions since the generator is able to supply more non-active power. As a result, the bus voltages will drop to a lesser extent, avoiding violations of the 10 % voltage drop limit. This can help to reduce unnecessary tripping of undervoltage relays.

7.5.7 Comparison of AC1A, AC4A and AC5A excitation systems' response to GIC

In this chapter, three excitation systems namely the AC1A, AC4A and AC5A are compared to see how they behave under acGIC conditions. Figure 7.60 shows the field current of the different excitation systems under noGIC and acGIC conditions.

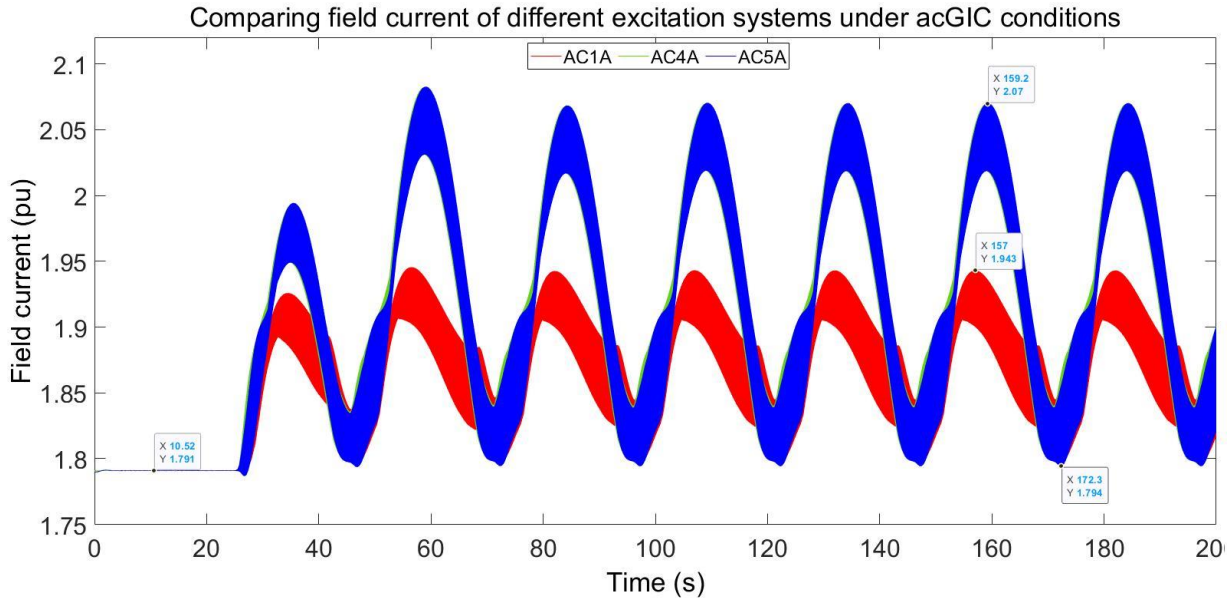

Figure 7.60: Comparing the field current generated by different excitation systems under acGIC conditions

Prior to GIC injection, all the three excitation systems are able to supply 1.791 pu of field current. At the GIC peaks, the maximum field current produced by the excitation system is very much dependent on the excitation system model. The AC4A and AC5A excitation systems are able to provide more field current than the AC1A excitation system. It is to be noted that the AC4A and AC5A behave very similarly despite the latter being more oscillatory than the AC4A.

The reactive power output of the generators depends on the field current supplied by the excitation system as shown in Figure 7.61.

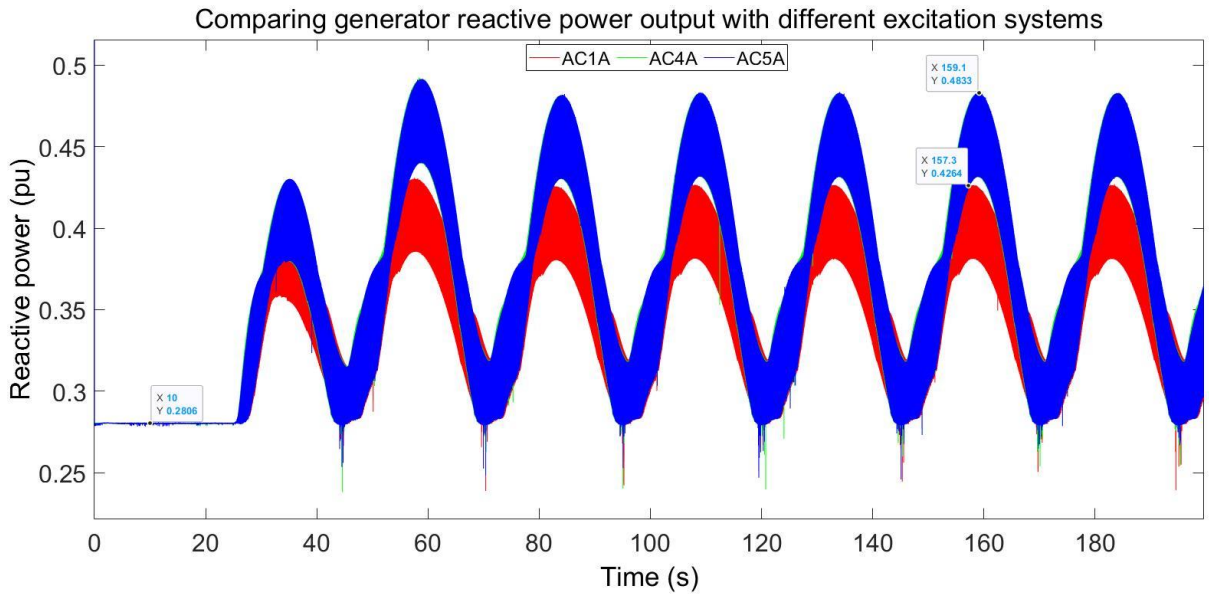

Figure 7.61: Comparing the reactive power output of the synchronous generator supplied by different excitation systems under acGIC conditions

Figure 7.61 shows a very important finding. The reactive power output of the generator depends on the excitation system used. Since the AC4A and AC5A excitation systems produce more field current, the synchronous generator is able to generate more reactive power output than a synchronous generator supplied by the AC1A excitation system.

Speaking of reactive power supplied into the network, the effect on the load bus voltage can be observed from Figure 7.62.

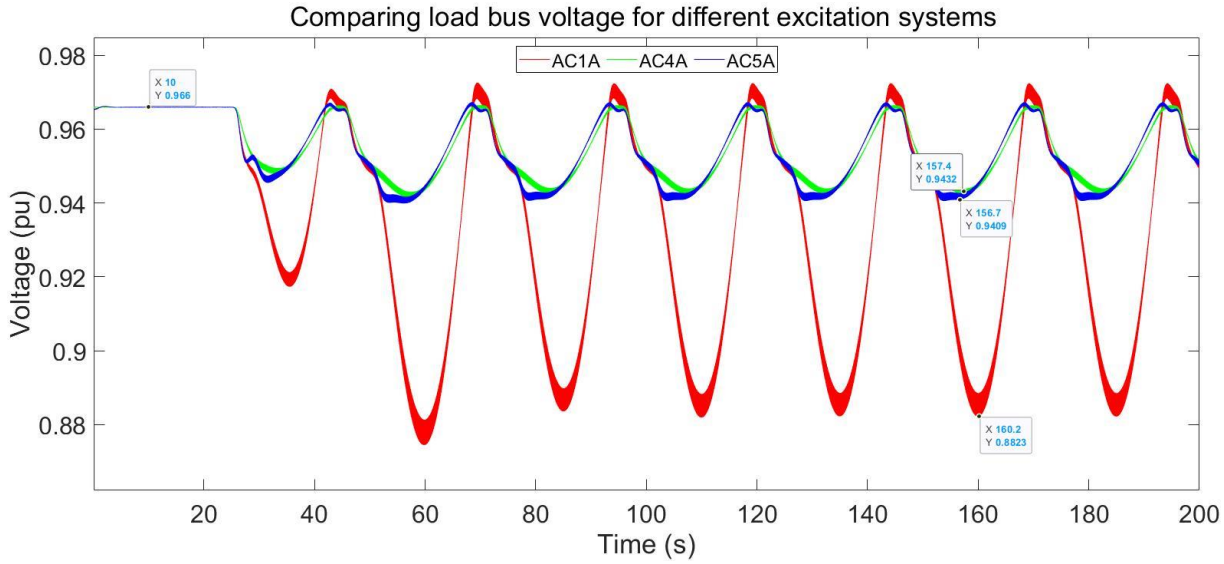

Figure 7.62: Comparing the load bus voltage when using different excitation systems to supply the synchronous generator under acGIC conditions

As expected, the AC1A excitation system produces the lowest voltages at the GIC peaks compared to the AC4A and AC5A excitation system. The findings agree to those of Oyedokun and Scheit [74] where the authors found out that the AC4A produces smaller voltage dips compared to other excitation systems.

7.6 Multi-machine power system response to GIC

While the 4-bus network provided useful insights on the response of generators and excitation systems to GIC, a realistic power system is made up of multiple generators supplying loads that can be located in different areas. In this Section, the response to GIC of the 2-area multi-machine system will be shown. The simulation protocol for Tests 0,1,2 and 3 were given in Section 6.2.

7.6.1 Test 0 results

In test 0, the effect of the transmission line was studied first before deciding on the final length and model to be used for tests 1,2 and 3. The effect of line length for 80 km, 400 km and 800 km are shown in Figure 7.63, Figure 7.64 and Figure 7.65 respectively.

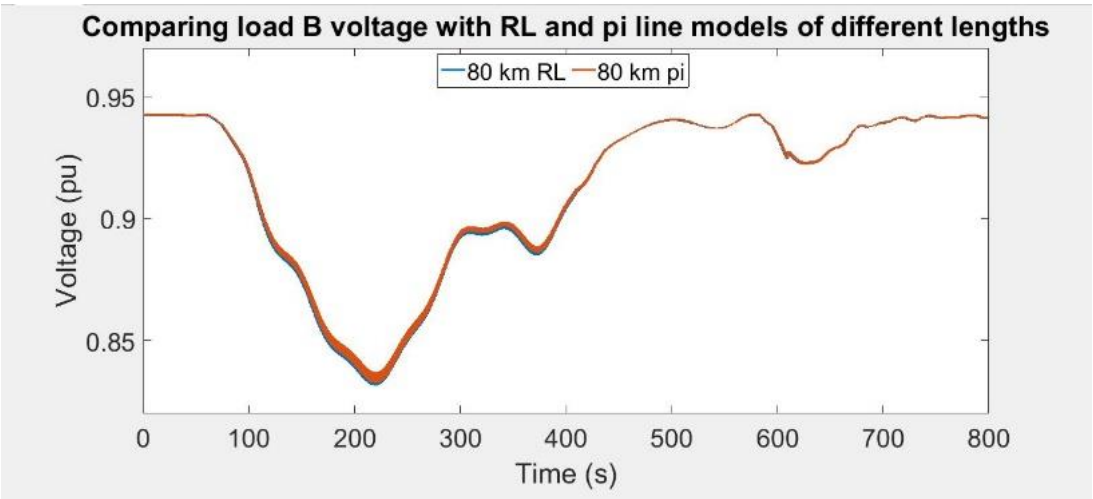

Figure 7.63: Comparing effect of line model - Load bus voltage with 80 km RL line model and 80 km pi line model

For an 80 km line, the RL line model and the pi line model produce very similar voltages at the load buses. This is because the 80 km line is a short line and therefore the capacitive effects of the line are negligible.

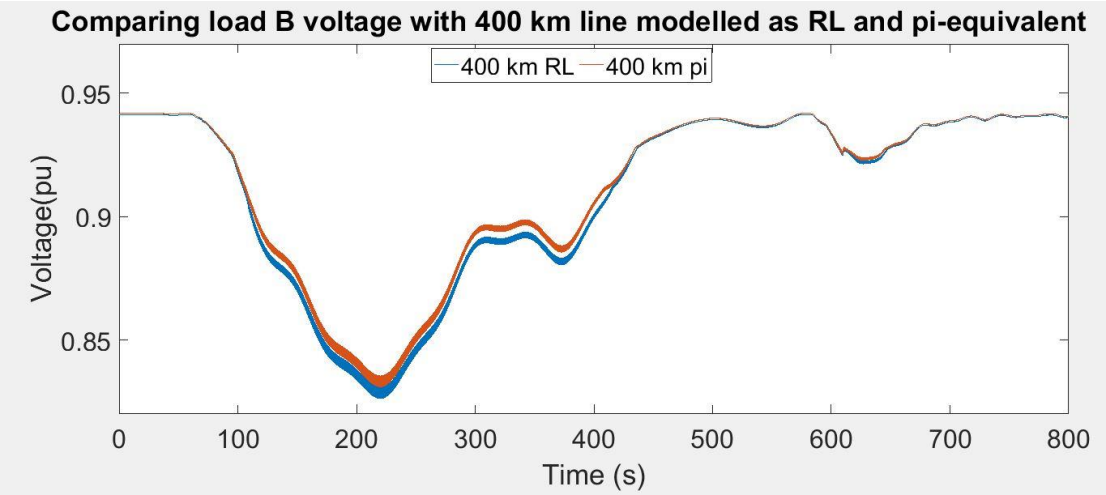

Figure 7.64: Comparing effect of line model - Load bus voltage with 400 km RL line model and 400 km pi line model

If a 400 km line is used, there is more voltage drop at the load bus with the RL line model than the pi line model. The RL line model does not include the line capacitance whereas the pi-line model includes a shunt capacitance. The latter tends to improve the voltage profile at the receiving end of the line causing a smaller voltage drop at the load bus despite having specified the same line resistance and inductance for both models.

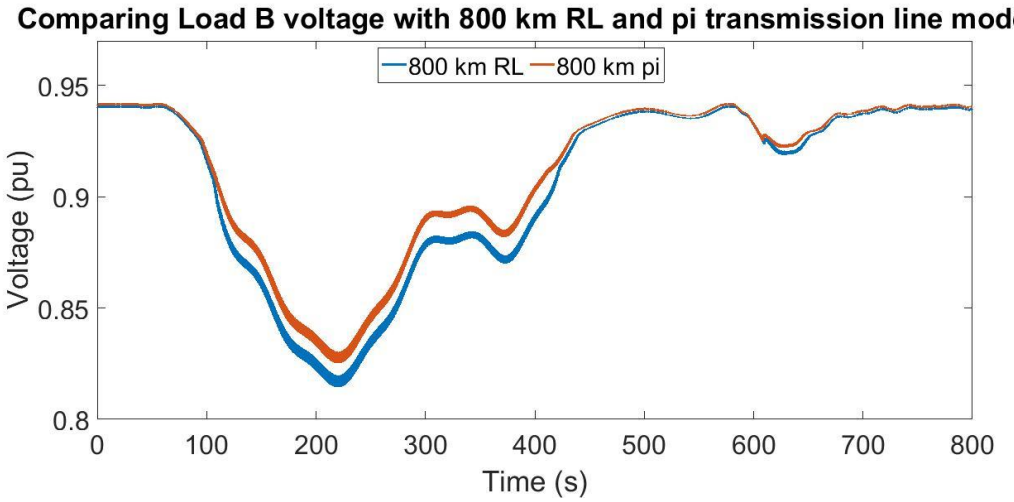

Figure 7.65: Comparing effect of line model - Load bus voltage with 800 km RL line model and 800 km pi line model

As the line length is increased, the differences between the RL line model and pi line model increased. Moreover, irrespective of the line model, as the line length is increased, the voltage drop at the load bus increased for both models.

Therefore, the final line model chosen for the tie link in the multi-machine system was an 80 km RL line. The results of test 1,2 and 3 are still valid for longer line lengths producing higher voltage drops compared to the 80 km line.

Test 0 is the base case scenario with all generators supplied with field current by the AC1A excitation system. The dynamic GIC profile developed for the multi-machine system and the corresponding variation in load bus voltages are shown in Figure 7.66.

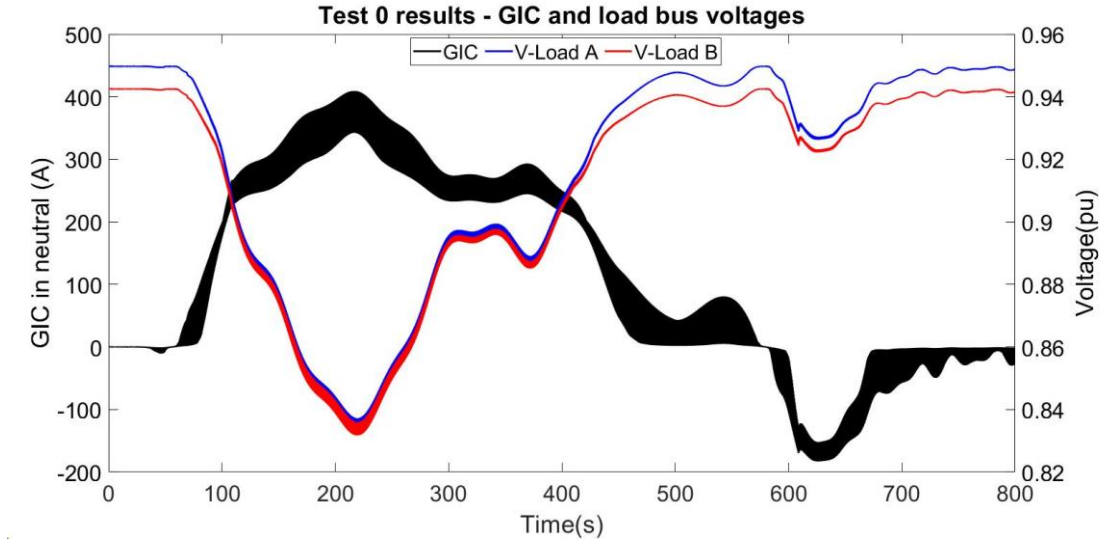

Figure 7.66: Load bus voltage and dynamic GIC profile

Prior to GIC injection that is before t = 25 s, the load bus voltages are at steady state. Since load B is larger than load A, the voltage observed at load B bus is always smaller than that at load A. When GIC was injected, it was observed that the GIC drives the response of the power system. When the GIC peaks in either positive or negative peaks, the load bus voltage drops the lowest. The maximum GIC was 409 A which is a relatively high value of GIC. However, as mentioned in Section 4.2, this value of GIC caters for worst system conditions such as extreme storms or superstorms with Dst index up to 6000 nT/min. At the instance when the GIC is zero, the load bus voltage regains its initial value to when there is no GIC. The load voltages drop below the 10 % voltage dip limit for longer than 80 s. This causes undervoltage relays to be trip network equipment.

There appears to be a time lag between the GIC peaks and the voltage minima. This time delay is due to the network time response which includes the time constants associated with the transformers GSU4, T_L2 and the 10 km transmission line. The X/R ratio of such transformers and transmission lines provide a good approximation of their time response to GIC.

Figure 7.67 shows the reactive power output of all generators and their relationship with the load A bus voltage.

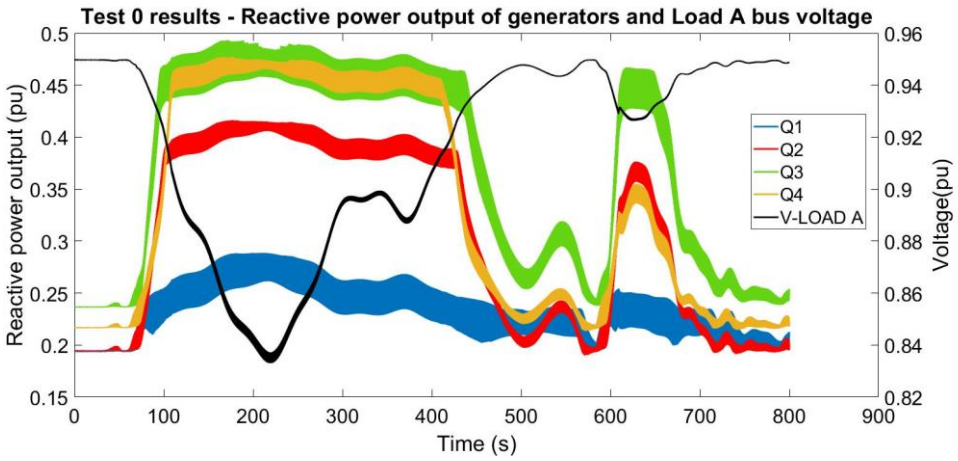

Figure 7.67: Reactive power output of all generators and corresponding load A voltage

It can be observed that, during peak GIC conditions, there is a huge increase in reactive power output of the generators. This rise in var output is not sufficient to maintain the voltage at the load A bus within limits. Hence, the load A bus voltage drops when the reactive power output increases. Again, the drop in load voltage and increase in reactive power output of the generators does not happen at exactly the same time. There are observable delays between the reactive power output and the corresponding voltage drop. Moreover, studying both Figure 7.66 and Figure 7.67, it appears that the injected GIC leads the var output of G1 which in turn, leads the load bus voltage change.

7.6.2 Test 1 results

In test 1, the excitation system model of each generator, initially supplied with an AC1A exciter, were changed one by one until all generators were equipped with the AC4A excitation system. Figure 7.68 shows the results of test 0 and test 1 on load A bus voltage.

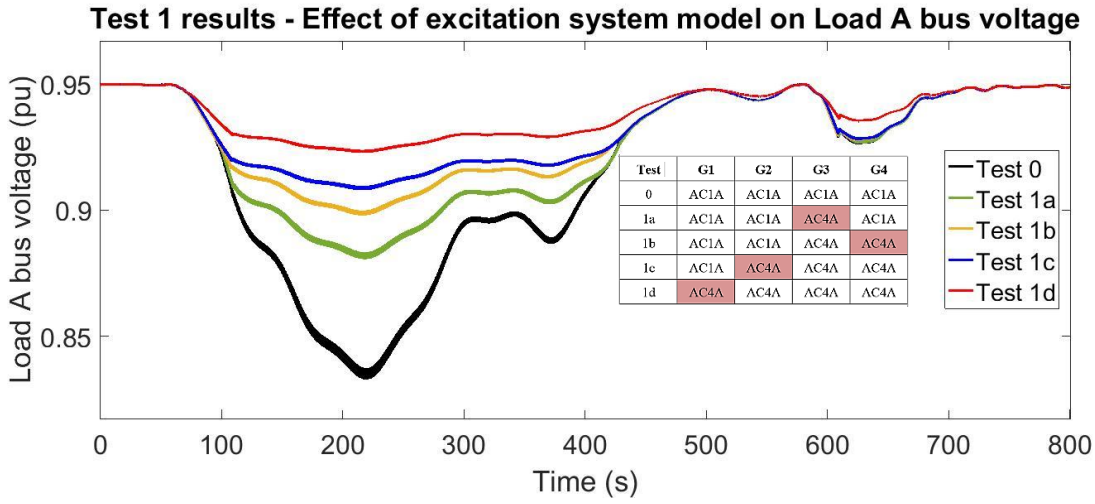

Figure 7.68: Test 1 results showing effect of changing excitation system model from AC1A to AC4A

Figure 7.69 shows the effect of changing the excitation system model and quantitatively shows the reduction in voltage dip at the load A bus.

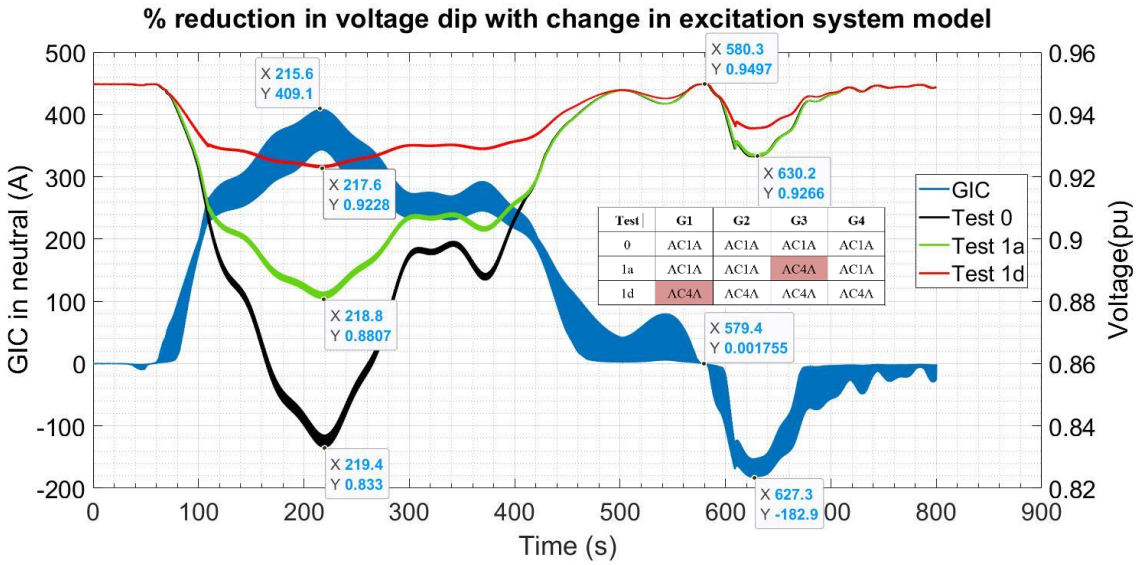

Figure 7.69: % reduction in load A bus voltage with change in excitation system model

When all generators are fed with field current from the AC1A excitation system (test 0), the GIC causes a violation of the 10 %v voltage drop limit. If G3's excitation system model is changed from AC1A to AC4A, there is a 4.7 % reduction of the voltage drop observed at the load bus as depicted from Figure 7.69. When the GIC peaks at 400 A, the system with all generators equipped with AC4A excitation systems is able to reduce by voltage dip by 8.95 %. This is the difference between the pu voltages at the troughs in the red and black curve. The results imply that power systems with generators equipped with the AC4A excitation system model can accommodate higher magnitude GICs, before violating the 10 % voltage dip limit. The reduction in voltage drop observed at the load bus can be explained by studying the var output of the generators.

The var output from test 1a is shown in Figure 7.70. When G3's excitation system model is changed from AC1A to AC4A, G3 provides more var output under strong GIC conditions. The AC4A has field forcing capabilities producing higher field currents during GIC conditions. Therefore, the var output of G3 is greater than the other 3 generators. The increased var output due to G3 causes a reduced voltage drop.

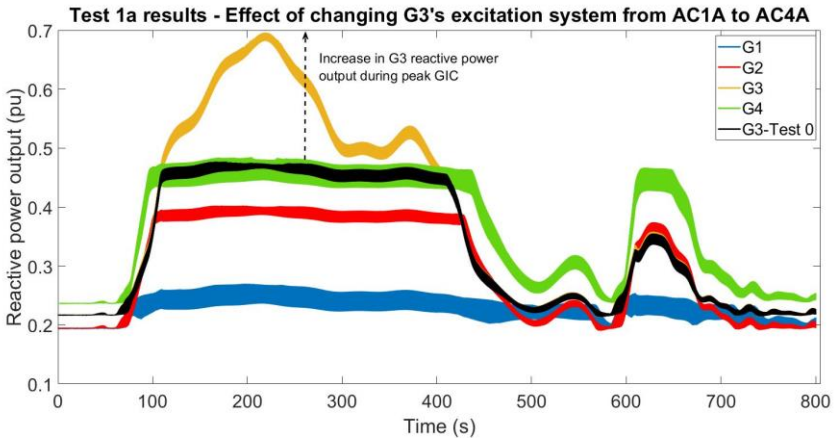

Figure 7.70: : Test 1a results showing effect of changing the excitation system model from AC1A to AC4A for G3 only

As more generators' exciter model is changed to AC4A, the total var output from all generators is higher as depicted from Figure 7.71. G1 and G4 seem to produce the highest var output compared to Q2 and Q3. This is because, the GSU transformers supplying G1 and G4 are subject to GIC flowing through them. Therefore, G1 and G4 must increase their var output to supply the increased demand for reactive power from the saturating GSUs transformers.

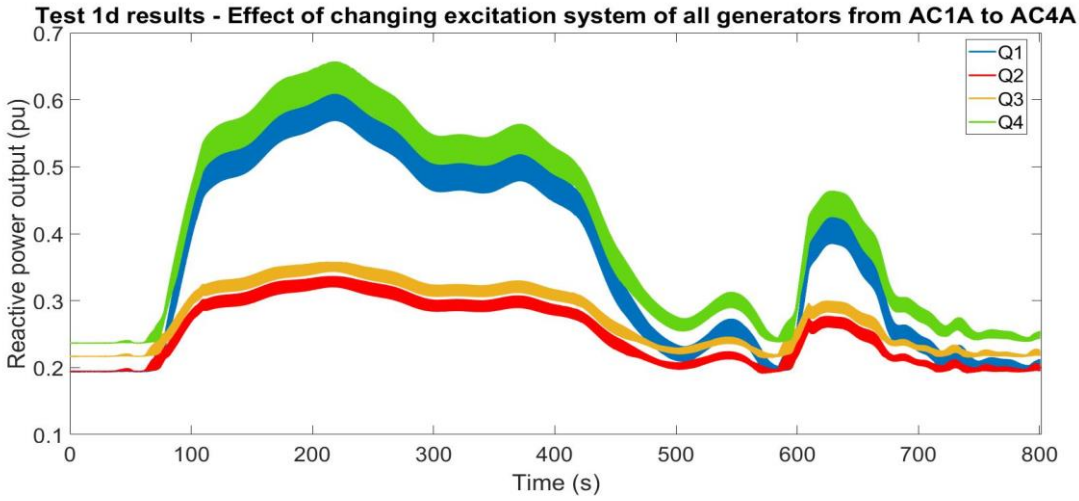

Figure 7.71: Test 1d results showing effect of changing the excitation system model from AC1A to AC4A for all generators

7.6.3 Test 2 results

In test 2, all generators were supplied with field current by the AC1A excitation system. However, the demagnetising factor was changed from 0.38 to 0.19 for each generator one by one until all generators had a demagnetising factor of 0.19. Figure 7.72 shows the results of test 0 and test 2 on load A bus voltage.

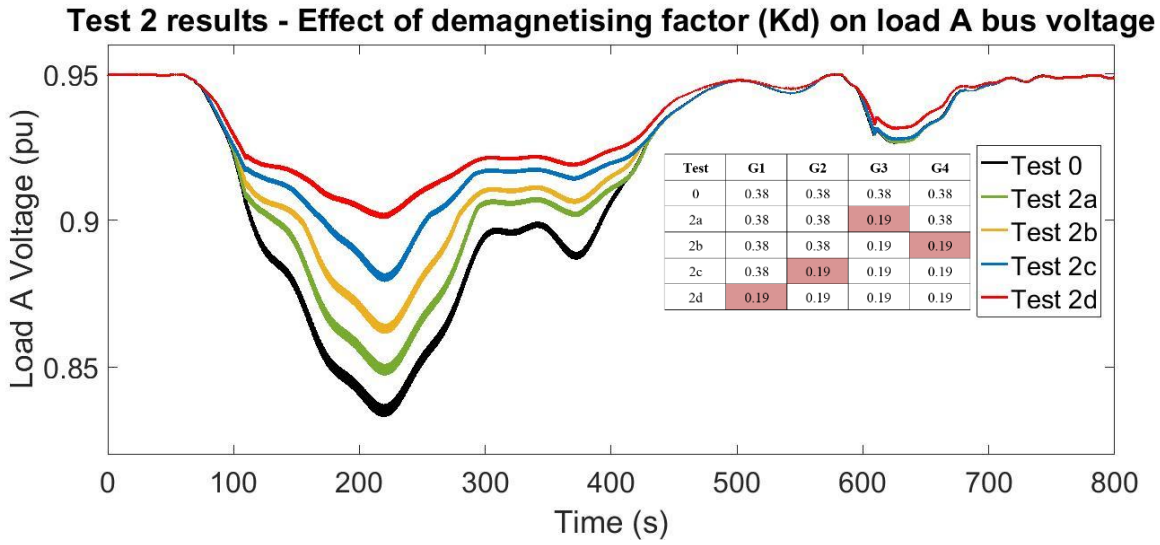

Test	G1	G2	G3	G4
0	0.38	0.38	0.38	0.38
2a	0.38	0.38	0.19	0.38
2b	0.38	0.38	0.19	0.19
2c	0.38	0.19	0.19	0.19
2d	0.19	0.19	0.19	0.19

Figure 7.72: Test 2 results showing the effect of changing the demagnetizing factor (Kd) for one or multiple generators

Test 0 had all generators' excitation system modelled with a demagnetizing factor of 0.38. As this factor is halved for one generator (Test 2a) or multiple generators (Tests 2b, 2c and 2d), there is a reduction in the voltage drop observed. It is interesting to note that the voltage drop limit is violated for tests 0 and 2a. However, if at least 2 generators have a demagnetizing factor of 0.19, then the voltage drop limit is not violated. While with one generator, the system might not be able to maintain the load bus voltage within limits, a group of generators may respond to the increased var demand by producing more total var output, just enough to maintain the voltage stability of the system.

Figure 7.73 shows the var output of all generators for test 2a. Test 2a had only G3's excitation system demagnetizing factor reduced from 0.38 to 0.19.

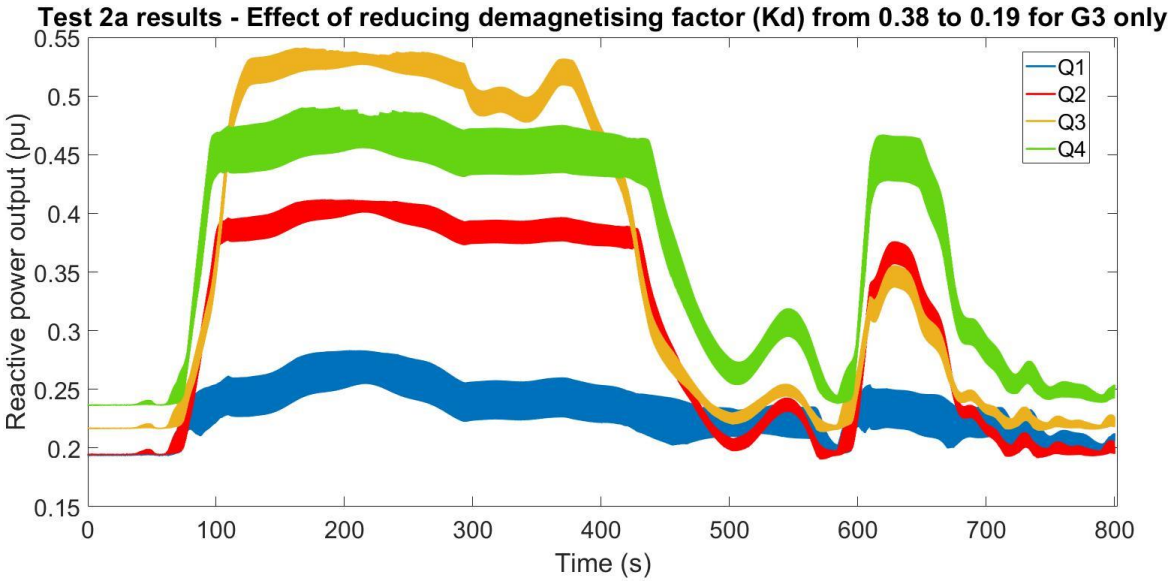

Figure 7.73: Test 2a results showing the effect of changing the demagnetizing factor (Kd) of G3's excitation system only

A reduction in K_D causes G3 to produce more var output compared to the other generators. With more var flowing to the load bus, the load bus voltage drops to a lesser extent compared to the base case (test 0). Figure 7.74 shows the var output of all generators for test 2d, whereby all generators have a demagnetizing factor of 0.19.

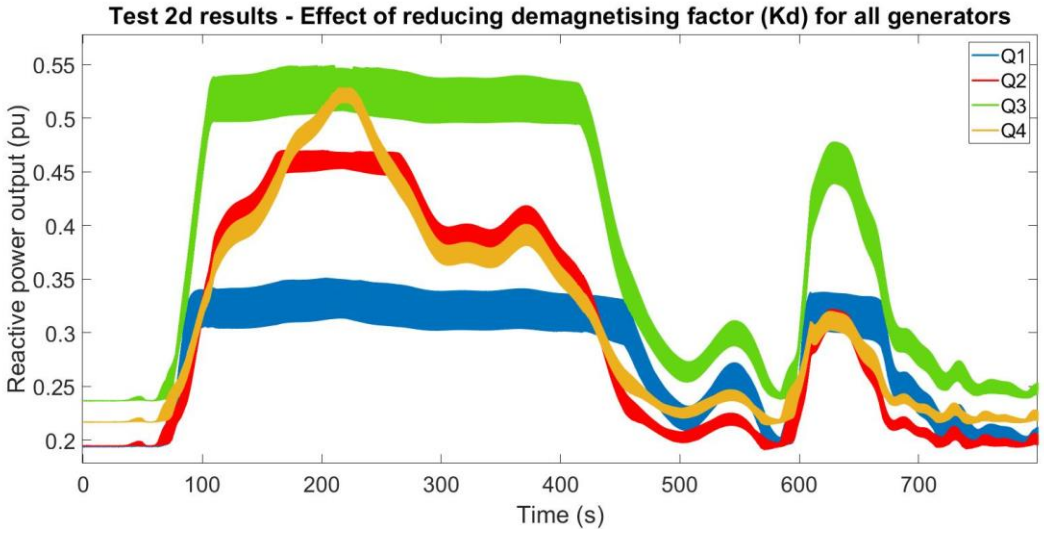

Figure 7.74: Test 2d results showing the effect of changing the demagnetizing factor (Kd) of all generators' excitation systems

Comparing Figure 7.73 and Figure 7.74 shows that the var output of G1, G2 and G4 have also increased. Therefore, the total var supplied to the load bus is higher causing less reduction in the load bus voltage compared to test 2a.

7.6.4 Test 3 results

Figure 7.75 shows the results of test 3 on the load bus voltage.

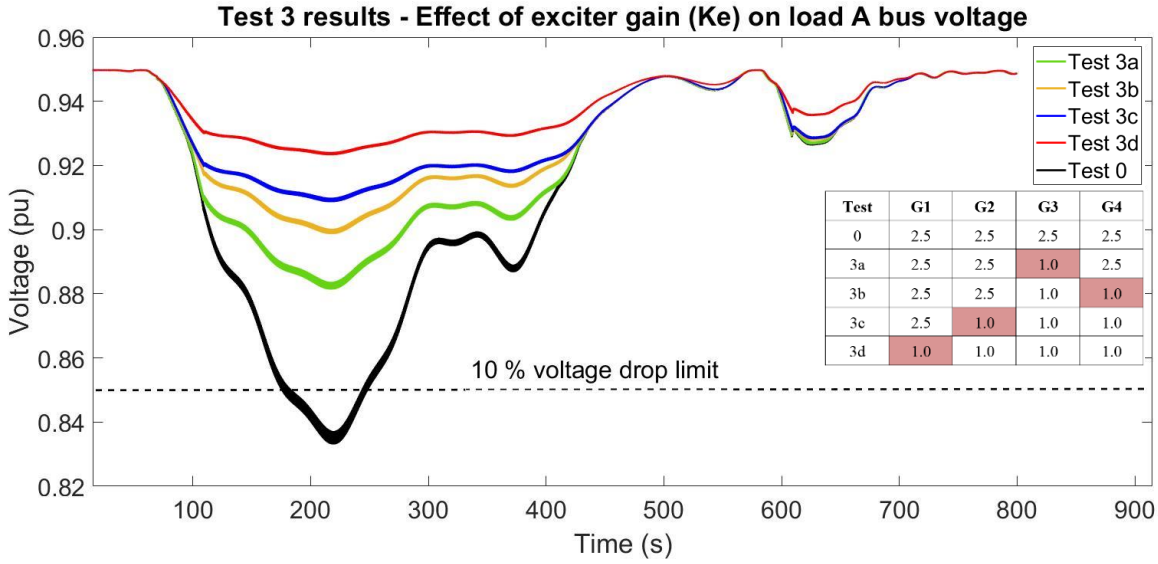

Figure 7.75: Test 3 results showing the effect of changing the exciter gain (Ke) for one or multiple generators

Test 0 had all generators' excitation system modelled with an exciter gain of 2.5. As this gain is reduced to 1.0 for one generator (Test 3a) or multiple generators (Tests 3b, 3c and 3d), there is a reduction in the voltage drop observed. It is interesting to note that the voltage drop limit is violated for test 0. However, if one of the generators' exciter gain is reduced to 1.0, then the voltage drop limit is not violated. Reducing K_E to 1.0 for a group of generators causes a further reduction in the voltage drop due to the increased var output as shown in Figure 7.76 and Figure 7.77.

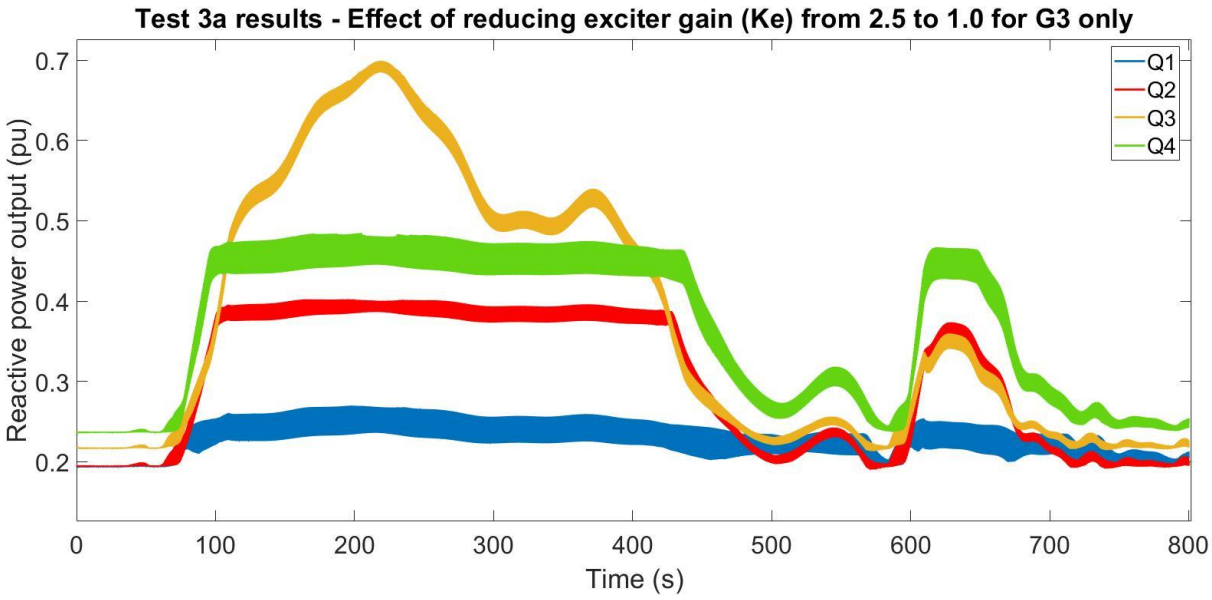

Figure 7.76: Test 3a results showing the effect of changing the exciter gain (Ke) of G3's excitation system only

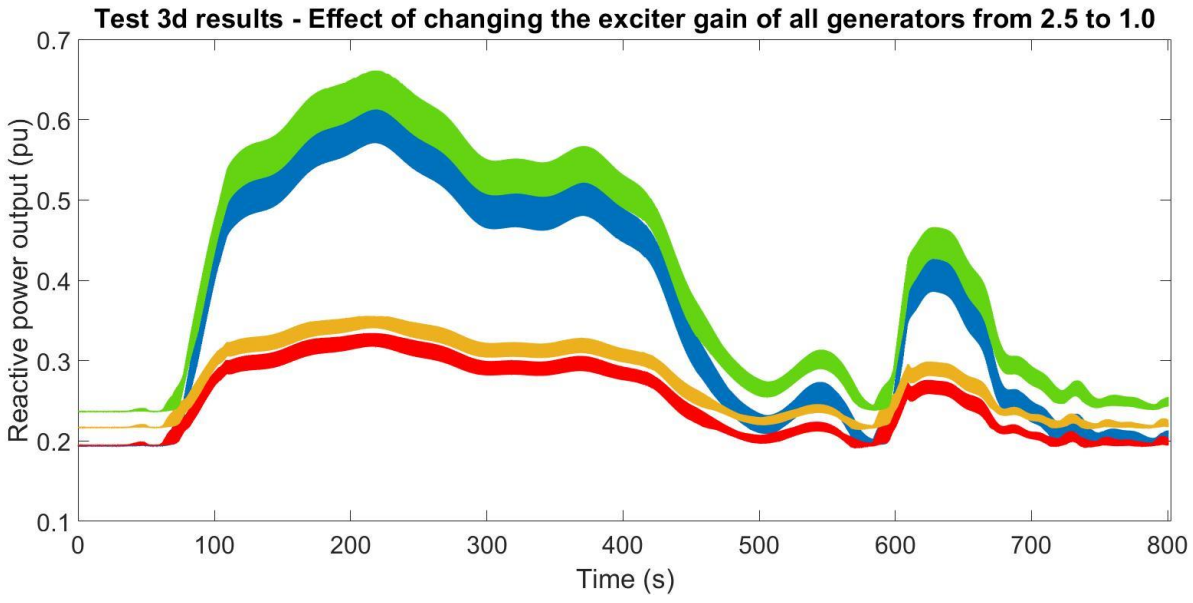

Figure 7.77: Test 3d results showing the effect of changing the exciter gain (Ke) of all generators' excitation systems

7.7 Chapter summary

In Section 7.1, the response of the 4-bus power system to GIC modelled as dc, was discussed. It has been shown that, with a dc GIC model the part wave saturation occurs in only one half cycle which depends on the GIC flux path and the transformer magnetising flux path within its shunt branch. An important finding in Section 7.1 was that the power system's response to GIC is very much dependent on the model of the source. The differences between an ideal equivalent ac voltage source, non-ideal equivalent ac voltage source and a full synchronous machine model were discussed based on their responses to GIC. Moreover, the effect of the source reactance was shown to have significant effect on power system's response. The finite limits of the full synchronous machine model with the excitation system and governor, appear more representative of practical systems' responses to GIC compared to ac equivalent sources.

In Section 7.2, the response of the 4-bus system to a GIC modelled as a 20 mHz single frequency wave, was discussed. An important take-away from this chapter is that the power system's response depends highly on the model of the GIC used. The response of the power system to the acGIC is very different to the conventional dcGIC model. With an acGIC, the transformer peak flux gets offset in both the positive and negative direction leading to periodic part wave saturation in both positive and negative peaks. Since the magnetising current depends on the flux, peaks are observed in both the positive half cycle and negative half cycle. When the acGIC peaks in either half cycle, the bus voltage drops are the highest. At the short instance when the acGIC crosses the time axis, the magnitude of GIC is zero and hence the power system tries to return to the pre-disturbance equilibrium state. Hence, the model of the GIC drives the system's response which identifies a need to drop the dc assumption and use more representative acGIC models.

Section 7.3 summarised the differences between the dc and ac GIC models including differences in power system response to both GIC models. Also shown was how a single frequency 20 mHz acGIC wave with period 50 s, acts as an envelope to the 50 Hz fundamental frequency component which has a much smaller period of 0.02 s. A new illustration of periodic part wave saturation causing both positive and negative peaks in the magnetising current drawn by transformers was given. The dynamic nature of GIC including events such as geomagnetic pulsations implies that one should now relax the dc assumption and model GIC exactly as they are; low frequency ac currents with different magnitudes at different times.

As highlighted in the literature review, studies on GIC and voltage stability need to include reactive or non-active power measurements. As debate on the definition of non-active power continues, Section 7.4 showed that indeed, there are differences observed when calculating non-active power

using the IEEE 1459 Standard and the general power theory. The GPT shows higher non-active power demand on the grid during GIC conditions compared to conventional power theories. Hence, there seems to be a higher voltage stability threat to power systems, commonly ignored with inaccurate definitions of power.

While the previous Sections helped to gain an understanding of the differences between the source models, Section 7.5 provided an in-depth analysis of the response of full synchronous generator models to GIC. Different electrical quantities such as the field voltage, load angle, dq axis voltages and damper winding currents were investigated. Changes in such quantities due to GIC were discussed. More importantly, the effect of excitation system control on mitigating some of the effects of GIC were shown by varying the exciter gain, demagnetising factor and the model of the excitation system itself. The results showed that a decrease in exciter gain and demagnetising factor reduced the voltage dip at the buses. Moreover, it was shown that the AC4A performs better than the AC1A and AC5A excitation systems during peak GIC conditions. This is due to the field forcing capabilities of the AC4A exciter.

Finally, section 7.6 showed the response of a more realistic power system consisting of several generators working in a synchronised manner to supply the loads. The multi-machine system's response confirmed the findings from the 4-bus network revealing that excitation system control parameters have a range of stable and unstable operating points. Operating further from the unstable operating point causes less voltage dips from GIC since the excitation system provides more field current output in an attempt to meet the var demand. While excitation system control of only one generator might not produce enough var output to meet the increased var demand due to GIC, a group of generators increasing their var output may help to maintain the voltage stability of the grid. The findings suggest that geomagnetic disturbances can be used for excitation control parameter determination.

8 Conclusions

This dissertation began with the objective of understanding the response of power systems including synchronous generators and excitation systems, to GIC, modelled as conventional dc and low frequency ac. Conclusions are drawn in this chapter, representing significant contributions to GIC research.

In Chapter 1, four research questions were posed to guide this research and understand the power system's response to GIC. The results of this project are applied to each research question addressed in the following paragraphs.

1. ***How does the power system's response to GIC differ when the GIC is modelled as conventional dc compared to low frequency ac?***

In the literature review, the need for more representative GIC models for power system studies, was highlighted following recent GIC or magnetic field measurements using small data cadence. Wavelet analysis revealed that GIC have properties of amplitude and frequency that vary over time. Incorporating these GIC properties in power system studies allows for a more accurate dynamic analysis. GIC are known to be low frequency currents and it may be beneficial to model them having multi-frequency and magnitudes that vary with time.

This research is one of the first attempts showing the differences in power systems' response to dcGIC and low frequency acGIC. Usually, when using the conventional dcGIC model, static voltage stability analysis techniques such as PV/QV curves are used. While these approaches might have given some indication of the proximity to voltage instability and collapse, they fail to capture the dynamics associated with the decline in bus voltages due to realistic GIC. Consequently, using the dc GIC model, it is not possible to show the actual dynamic power system's response to geomagnetic disturbances. There is a need to focus on dynamic power system studies looking into the vulnerability of network equipment to more representative GIC and the mechanism of voltage collapse. In this regard, real time-domain simulations with accurate representation of power system equipment dynamics deem more appropriate. This study has provided a better understanding of the dynamic power system response to GIC modelled with practical magnitudes and frequencies over time. Worse system conditions have been observed with acGIC models compared to dcGIC models regarding voltage stability. Moreover, voltages and currents are always in a transient phase with an acGIC. Harmonics vary depending on the model of the GIC. With a dcGIC model, harmonic currents or voltages reach a steady state value when the GIC has settled whereas with an acGIC model, the harmonics depend on the GIC magnitude and frequency at any time instant. This implies that control

and decisive actions taken by protective relays and excitation control systems are not definite. As a result, network equipment are continuous tripped and switched back online unless on manual control. The results from this research show that power systems may be affected to a larger extent than we originally believed when dc is assumed for GIC and highlight the need to model GIC as multi-frequency currents with time varying amplitudes.

2. ***How do synchronous generators and excitation systems respond to GIC?***

Section 2.3 of the literature review was aimed at understanding the hypothesized role of synchronous machines and excitation systems in providing non-active power support during GIC conditions. Synchronous generators are the main source of power, the non-active power being controlled by the field current. The field windings are instead supplied with field current by an excitation system. The excitation system is made up of the main exciter, automatic voltage regulator, compensators, protective and control circuits. The synchronous generator usually operates within its capability curve whose limits are defined by some protective and control circuits of the excitation system. The literature review compared different types of excitation systems and components making up the excitation system were discussed. Standard IEEE models were shown including derivations of the relationship between excitation system parameters and synchronous generator parameters.

This research has proved that synchronous generators are affected by GIC due to the induced harmonics flowing into their stator windings. Such harmonics are always fluctuating, with their magnitudes, depending on the GIC magnitude and frequency at any particular time instance. The most dangerous harmonics are of negative sequence inducing an air gap flux opposite to the direction of the positive sequence fundamental frequency field flux. GIC induced negative sequence harmonics cause rotor heating, a reduction in air gap useful flux, and reduced fundamental frequency current output. Rotor heating occurs due to GIC-induced harmonics which cause damper winding currents to flow. Moreover, leakage harmonic fluxes and the demagnetising effect of armature reaction limit the non-active power output of synchronous generators under GIC conditions.

Under unbalanced system conditions, non-traditional and complicated harmonic sequence patterns such as negative sequence fundamental are also generated. These non-conventional harmonic sequences are not only generated by transformers with unbalanced magnetics, but also arise from any system unbalance such as load unbalance or transmission line unbalance. While zero sequence harmonics will never reach a generator with delta connected primary winding, non-conventional triplen harmonics having a positive and negative sequence do appear at generator terminals. Currently, there is no standard that describes generator limits to such non-conventional harmonics. Moreover, generator protection relays are currently designed to operate based on conventional

harmonic levels. As such, these relays might trip the generator due to higher magnitude harmonics flowing into the generator terminal, causing further voltage stability complications. This research raises concern on the vulnerability of synchronous generators to such non-conventional harmonics even if the primary winding of the generator is delta connected.

3. ***To what extent can excitation system control be used to reduce the effects of GIC?***

In terms of the source's modelling for GIC studies, this research has shown that, in the absence of generator excitation models, care should be taken with ac equivalent sources. The source reactance needs to be accounted for GIC studies since the generator's power capability curve is limited by its reactance. Modelling of an ideal source is not realistic. Full synchronous generator models appear to offer better flexibility in terms of the field current control using the excitation system. With control of the field current, one has control of the var output from the generator. Generator excitation models appear to be of more utility in GIC studies. Excitation system control therefore leads to the possibility of mitigating a voltage collapse under GMD conditions. As shown in Figure 7.75 significant reduction in voltage dips can be achieved without violating the 10 % voltage drop limit, preventing under-voltage relay tripping. This allows for more SVCs to stay online and provide non-active power support. With multiple generators the system can therefore withstand higher GIC before violating the 10 % voltage drop limit.

In practice, excitation system control parameters such as K_E and K_D are determined by voluntarily running different contingencies on the power system. Such contingencies include three-phase bolted short circuit faults, line to ground faults amongst others. Usually, the worse-case scenario is imposed on the system to determine a range of stable and unstable operating points as shown in Figure 8.1. Tuning of the excitation system is carried out using frequency domain and time domain analysis to decide on optimal control parameters for power system stability. This research proposes that the GIC problem be added as one additional contingency used in determining such parameters since they have a huge impact on voltage and non-active power.

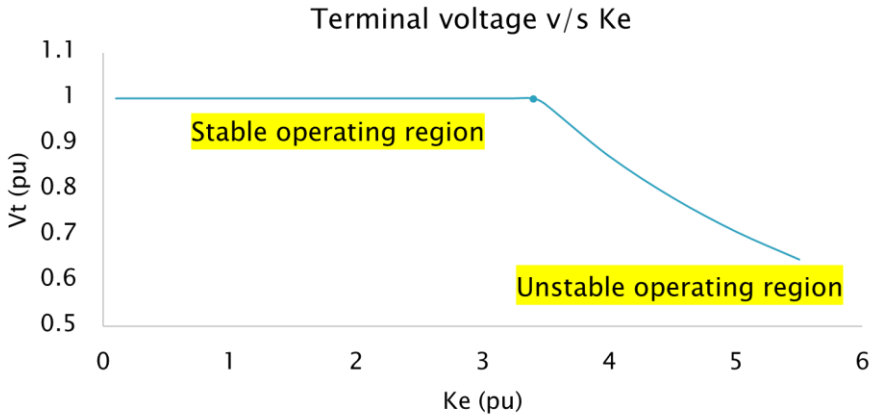

Figure 8.1: Stable and unstable operating region for excitation system control parameters

4. What is the correct definition of apparent power and non-active power applicable to GIC studies?

At present, no holistic definition of apparent power or non-active power exists that is applicable for GIC studies, agreeing with Kirkham and White [80]. When currents and voltages are not pure sinusoids due to GIC-induced harmonics, non-active power measurement results, depend on the calculations used to evaluate the value. While there are many proposed approaches to estimating non-active power, they may underestimate the increased non-active power demand due to GIC. Currently, synchronous generators are designed using conventional power theories to calculate reactive power. This research has shown that during non-ideal system conditions such as GIC, the increased reactive power demand calculated by synchronous generators' var controllers is less than non-active power calculated using IEEE1459 Std. Therefore, synchronous generators respond by producing less var output than actually required under such GIC conditions which further aggravates the voltage stability of power systems. A correct power theory applicable to GIC studies should cater for all system inefficiencies such as unbalance, conventional and non-conventional harmonic sequences, dc components amongst others. Moreover, the theory should be suited for both static and dynamic power system studies. At present, the best approximation of the increased non-active power demand due to GIC can be achieved using the IEEE1459 standard. The point of measurement of currents and voltages is also a major factor to be considered to accurately calculate power taking into account all system inefficiencies such as neutral wires losses, imbalance, harmonics and dc components as highlighted by the GPT. More accurate power measurements and meters need to be modelled to calculate the actual increase in var demand during GMDs.

Future work

Rigorous analysis on power theory for delivery systems addresses the ambiguities in interpreting power components, specifically reactive/non-active power, resulting in the application of a general

power theory not limited by any system state assumptions [42]. Future work incorporates this rigorous approach in the context of excitation system control and GIC. Moreover, the GPT approach can also be used for optimal current injection under GIC conditions to minimise transmission losses and extended to the design of compensators. Furthermore, this dissertation focussed on ac transmission lines with no HVDC lines modelled. GIC affect the inverter controls and extinction angle. This is caused by increased non-characteristic harmonics in the ac-side currents and voltages. Moreover, under light loading conditions, parallel resonance affect filter operation. Due to a global transition of power systems from synchronous generation to converter-interfaced generation, the effect of GIC on HVDC lines including power converters and filters offers possibilities for future studies. Lastly, no PSS were included in the excitation system model. The role of the PSS in providing additional damping and improving small signal stability is reserved for future research avenues.

9 List of References

[1] T. R. Hutchins and T. J. Overbye, “The effect of geomagnetic disturbances on the electric grid and appropriate mitigation strategies,” *NAPS 2011 - 43rd North Am. Power Symp.*, pp. 1–5, 2011.

[2] A. Haddadi, R. Hassani, J. Mahseredjian, G.-L. Luc, and A. Rezaei-Zare, “Evaluation of Simulation Methods for Analysis of Geomagnetic Disturbance System Impacts,” *IEEE Trans. Power Deliv.*, no. July, pp. 1–1, 2020.

[3] S. Mkhonta, T. T. Murwira, D. T. O. Oyedokun, K. A. Folly, and C. T. Gaunt, “Investigation of Transformer Reactive Power and Temperature Increases under DC,” in *2018 IEEE PES/IAS PowerAfrica, PowerAfrica 2018*, 2018, pp. 595–600.

[4] NERC, “Effects of Geomagnetic Disturbances on The Bulk Power System,” 2012.

[5] Y. Zhang, K. S. Shetye, R. H. Lee, and T. J. Overbye, “Impact of Geomagnetic Disturbances on Power System Transient Stability,” in *2018 North American Power Symposium, NAPS 2018*, 2019, pp. 1–6.

[6] D. Oyedokun, M. Heyns, P. Cilliers, and C. T. Gaunt, “Frequency Components of Geomagnetically Induced Currents for Power System Modelling,” in *South African Universities Power Engineering Conference 2020*, 2020.

[7] E. H. Bernhardi, P. J. Cilliers, and C. T. Gaunt, “Improvement in the modelling of geomagnetically induced currents in southern Africa,” *S. Afr. J. Sci.*, vol. 104, no. 7–8, pp. 265–272, 2008.

[8] J. G. Kappenman and D. Albertson, “Bracing for the geomagnetic storms,” *IEEE Spectr.*, vol. 27, no. 3, pp. 27–33, 1990.

[9] C. T. Gaunt and G. Coetzee, “Transformer failures in regions incorrectly considered to have low GIC-risk,” *2007 IEEE Lausanne POWERTECH, Proc.*, pp. 807–812, 2007.

[10] T. R. Hutchins and T. J. Overbye, “Power system dynamic performance during the late-time (E3) high-altitude electromagnetic pulse,” in *19th Power Systems Computation Conference, PSCC 2016*, 2016, no. 3, pp. 1–6.

[11] T. J. Overbye, K. S. Shetye, Y. Z. Hughes, and J. D. Weber, “Preliminary consideration of voltage stability impacts of geomagnetically induced currents,” *IEEE Power Energy Soc. Gen. Meet.*, 2013.

[12] H.K.Chisepo, “The response of Transformers to Geomagnetically-Induced Currents,” M.S. thesis, Department of Electrical Engineering, University of Cape Town, Cape Town, South Africa, 2014.

[13] T. J. Overbye, K. S. Shetye, T. R. Hutchins, Q. Qiu, and J. D. Weber, “Power grid sensitivity analysis of geomagnetically induced currents,” *IEEE Trans. Power Syst.*, vol. 28, no. 4, pp. 4821–4828, 2013.

[14] H. Chisepo, “Measurements and finite element modelling of transformer flux with dc and power frequency current,” Ph.D dissertation, Department of Electrical Engineering, University of Cape Town, Cape Town, South Africa, 2019.

[15] J. Koen, “Geomagnetically Induced Currents and its Presence in the Eskom Transmission Network,” M.S. thesis, Department of Electrical Engineering, University of Cape Town, Cape Town, South Africa, 2000.

[16] P. R. Price, “Geomagneticaily Induced Current Effects on Transformers,” *IEEE Power Eng. Rev.*, vol. 22, no. 6, p. 62, 2002.

[17] R. Girgis and K. Vedante, “Effects of GIC on power transformers and power systems,” *Proc. IEEE Power Eng. Soc. Transm. Distrib. Conf.*, pp. 1–8, 2012.

[18] H. L. Weng, L. Liu, Y. Wan, X. N. Lin, Z. X. Li, and J. G. Huang, “Studies on the Variation of Transformer Reactive Power Caused by DC Bias and Its Impacts on System Voltage,” in *ICHVE 2018 - 2018 IEEE International Conference on High Voltage Engineering and Application*, 2019, pp. 13–16.

[19] A. Jakoet, D. T. O. Oyedokun, C. T. Gaunt, and P. J. Cilliers, “Preliminary modeling of geomagnetically induced currents in South Africa using PowerWorld Simulator,” *IEEE PES PowerAfrica Conf. PowerAfrica 2016*, pp. 234–238, 2016.

[20] M. Subudhi, D. P. Carroll, and S. Kasturi, “The Effects of Solar geomagnetically Induced Currents on Electrical Systems in Nuclear Power Stations,” 1994.

[21] X. Dong, Z. Liu, and B. Liu, “Simulating analysis of magnetization characteristic curve and exciting current of transformer on DC bias,” *DRPT 2011 - 2011 4th Int. Conf. Electr. Util. Deregul. Restruct. Power Technol.*, pp. 1848–1851, 2011.

[22] Xuzhu Dong, Yilu Liu, and J. G. Kappenman, “Comparative analysis of exciting current harmonics and reactive power consumption from GIC saturated transformers,” 2002, no. C, pp. 318–322.

[23] H. Weng, G. Yang, X. Li, and X. Lin, “The impact of GIC on system voltage and generator

output," *Proc. 5th IEEE Int. Conf. Electr. Util. Deregulation, Restruct. Power Technol. DRPT 2015*, pp. 1736–1739, 2016.

[24] G. Gnetically-induced and V. D. Albertson, "Load Flow Studies in the presence of Geomagnetically Induced Currents," no. 2, 1981.

[25] B. R. Fehr and E. Consultant, "Harmonics Made Simple," no. x, 2004.

[26] C. T. Gaunt and M. Malengret, "Why we use the term non-active power, and how it can be measured under non-ideal power supply conditions," *IEEE Power Energy Soc. Conf. Expo. Africa Intell. Grid Integr. Renew. Energy Resour. PowerAfrica 2012*, no. July, 2012.

[27] S. Meliopoulos, J. Xie, and G. Cokkinides, "Power system harmonic analysis under geomagnetic disturbances," *Proc. Int. Conf. Harmon. Qual. Power, ICHQP*, vol. 2018-May, pp. 1–6, 2018.

[28] D. M. Oyedokun and C. T. Gaunt, "Laboratory Test for GIC Effects on Power Transformers," no. October 2015, pp. 1–7, 2011.

[29] W. B. Gish, W. E. Feero, and G. D. Rockefeller, "Rotor heating effects from geomagnetic induced currents," *IEEE Trans. Power Deliv.*, 1994.

[30] J. Q. Wang, P. C. Song, C. H. Cui, J. K. Li, and T. Yang, "Analysis of operation of synchronous generator under the distortion of harmonic current," *Asia-Pacific Power Energy Eng. Conf. APPEEC*, pp. 0–3, 2012.

[31] A. Rezaei-Zare and L. Marti, "Generator thermal stress during a Geomagnetic Disturbance," *IEEE Power Energy Soc. Gen. Meet.*, 2013.

[32] J. Melorose, R. Perroy, and S. Careas, *IEEE Std C50.13 - IEEE Standard for Cylindrical-Rotor 50 Hz and 60 Hz Synchronous Generators Rated 10 MVA and Above*. 2014.

[33] R. A. Walling and A. H. Khan, "Characteristics of transformer exciting-current during geomagnetic disturbances," *IEEE Trans. Power Deliv.*, 1991.

[34] Y. Li and C. Zhang, "Simulation of harmonic armature reaction in synchronous brushless excitation," *2011 2nd Int. Conf. Artif. Intell. Manag. Sci. Electron. Commer. AIMSEC 2011 - Proc.*, pp. 4304–4306, 2011.

[35] W. Fan and Y. Liao, "Impacts of flickers, harmonics and faults on synchronous generator operations," *Proc. Annu. Southeast. Symp. Syst. Theory*, pp. 220–225, 2012.

[36] V. D. Albertson *et al.*, "Geomagnetic disturbance effects on power systems," *IEEE Trans. Power Deliv.*, 1993.

[37] A. Abuhussein, "Impact of Geomagnetically Induced Current on Distributed Generators,"

Proc. IEEE Power Eng. Soc. Transm. Distrib. Conf., vol. 2018-April, pp. 1–5, 2018.

[38] M. Lehtinen and R. Pirjola, "Currents produced in earthed conductor networks by geomagnetically-induced electric fields.," *Ann. Geophys.*, 1985.

[39] D. H. Boteler and R. J. Pirjola, "Modeling geomagnetically induced currents," *Sp. Weather*, 2017.

[40] D. H. Boteler and R. J. Pirjola, "Modelling geomagnetically induced currents produced by realistic and uniform electric fields," *IEEE Trans. Power Deliv.*, 1998.

[41] O. Nayak, G. Irwin, and A. Neufeld, "GUI enhances electromagnetic transients simulation tools," *IEEE Comput. Appl. Power*, 1995.

[42] R. Horton, D. Boteler, T. J. Overbye, R. Pirjola, and R. C. Dugan, "A test case for the calculation of geomagnetically induced currents," *IEEE Trans. Power Deliv.*, 2012.

[43] T. J. Overbye, K. S. Shetye, Y. Z. Hughes, and J. D. Weber, "Preliminary consideration of voltage stability impacts of geomagnetically induced currents," in *IEEE Power and Energy Society General Meeting*, 2013.

[44] J. Kappenman, "Geomagnetic Storms and Their Impacts on the U.S. Power Grid," Tennessee, 2010.

[45] I. P. and E. Society, *IEEE Guide for Establishing Power Transformer Capability while under Geomagnetic Disturbances IEEE Guide for Establishing Power Transformer Capability while under Geomagnetic Disturbances Corrigendum 1*, vol. 2016. 2016.

[46] M. Heyns, S. Lotz, and C. Gaunt, "Geomagnetic Pulsations Driving Geomagnetically Induced Currents," *Sp. Weather*, 2020.

[47] E. O. Falayi, O. Ogunmodimu, O. S. Bolaji, J. D. Ayanda, and O. S. Ojoniyi, "Investigation of geomagnetic induced current at high latitude during the storm-time variation," *NRIAG J. Astron. Geophys.*, 2017.

[48] M. Maminimini, "Frequency Domain Characterisation of Geomagnetic Fields and Geomagnetically Induced Currents (GICs) using Wavelets," University of Cape Town, 2020.

[49] K. Prabha *et al.*, "Definition and Classification of Power System Stability IEEE/CIGRE," *Proc. R. Soc. Med.*, vol. 19, no. 2, pp. 1387–1401, 2004.

[50] P. Kundur, *Power System Stability And Control by Prabha Kundur.pdf*. 1994.

[51] Power System Dynamic Performance Committee, T. F. on S. definitions and characterization of Dynamic, behavior in systems with high penetration of power electronic Interfaced, and Technologies, "Stability definitions and characterization of dynamic behavior in systems with

high penetration of power electronic interfaced technologies," 2020.

[52] M. Hasani and M. Parniani, "Method of combined static and dynamic analysis of voltage collapse in voltage stability assessment," in *Proceedings of the IEEE Power Engineering Society Transmission and Distribution Conference*, 2005.

[53] G. B. Morison Gao, M. P. IEEE Kundur, and F. Ieee, "Voltage Stability Analysis Using Static and Dynamic Approaches," *IEEE Trans. Power Syst.*, vol. 8, no. 3, pp. 1159–1171, 1993.

[54] S. Tigere, L. Phaphathisa, K. A. Folly, D. T. O. Oyedokun, and C. T. Gaunt, "Power System Voltage Stability in the Presence of GIC-Like Currents," in *2018 IEEE PES/IAS PowerAfrica, PowerAfrica 2018*, 2018.

[55] C. C. Liu and K. T. Vu, "Analysis of Tap-Changer Dynamics and Construction of Voltage Stability Regions," *IEEE Trans. Circuits Syst.*, vol. 36, no. 4, pp. 575–590, 1989.

[56] B. H. Chowdhury and C. W. Taylor, "Voltage stability analysis: v-q power flow simulation versus dynamic simulation," *IEEE Trans. Power Syst.*, vol. 15, no. 4, pp. 1354–1359, 2000.

[57] M. L. Crow and J. Ayyagari, "The Effect of Excitation Limits on Voltage Stability," *IEEE Trans. Circuits Syst. I Fundam. Theory Appl.*, vol. 42, no. 12, pp. 1022–1026, 1995.

[58] V. Balamourougan, T. S. Sidhu, and M. S. Sachdev, "Technique for online prediction of voltage collapse," pp. 453–460.

[59] A. T. M. M. Rahman and A. H. Chowdhury, "Reactive power reserve management to prevent voltage collapse in Bangladesh power system," in *Proceedings of 9th International Conference on Electrical and Computer Engineering, ICECE 2016*, 2017, pp. 423–426.

[60] J. Heydeman, S. C. Tripathy, G. C. Paap, and L. Van Der Sluis, "Digital and experimental study of voltage collapse and instability in power system," *Int. J. Electr. Power Energy Syst.*, vol. 22, no. 4, pp. 303–311, 2000.

[61] C. F. Yang, G. G. Lai, C. H. Lee, C. T. Su, and G. W. Chang, "Optimal setting of reactive compensation devices with an improved voltage stability index for voltage stability enhancement," *Int. J. Electr. Power Energy Syst.*, 2012.

[62] G. M. Huang, S. Member, N. C. Nair, and S. Member, "Detection of Dynamic Voltage Collapse," pp. 1–6.

[63] D. E. Julian, R. P. Schulz, K. T. Vu, W. H. Quaintance, N. B. Bhatt, and D. Novosel, "Quantifying proximity to voltage collapse using the voltage instability predictor (VIP)," in *Proceedings of the IEEE Power Engineering Society Transmission and Distribution Conference*, 2000, vol. 2, no. c, pp. 931–936.

[64] A. Chaithra and S. Modi, “Evaluation of Power System Stability using Voltage Proximity Index,” in *2018 International Conference on Recent Innovations in Electrical, Electronics and Communication Engineering, ICRIEECE 2018*, 2018.

[65] A. Chaithra and S. Modi, “Power system vulnerability assessment using voltage collapse proximity index,” in *2018 2nd IEEE International Conference on Power Electronics, Intelligent Control and Energy Systems, ICPEICES 2018*, 2018.

[66] M. Nizam, A. Mohamed, and A. Hussain, “Performance evaluation of voltage stability indices for dynamic voltage collapse prediction,” *J. Appl. Sci.*, vol. 6, no. 5, pp. 1104–1113, 2006.

[67] M. S. S. Danish, T. Senjyu, S. M. S. Danish, N. R. Sabory, K. Narayanan, and P. Mandal, “A recap of voltage stability indices in the past three decades,” *Energies*, vol. 12, no. 8, pp. 1–18, 2019.

[68] I. The Institute of Electrical and Electronics Engineers, *IEEE recommended practice for excitation system models for power system stability studies (IEEE Std 421.5-1992)*, vol. 2016. 2016.

[69] IEEE Power Engineering Society, *IEEE Recommended Practice for Excitation System Models for Power System Stability Studies (IEEE 421.5)*. 2005.

[70] I. P. and E. Society, *IEEE Guide for Synchronous Generator Modeling Practices and Applications in Power System Stability Analyses*, vol. 2, no. November. 2002.

[71] IEEEStd115, “IEEE Guide: Test Procedures for Synchronous Machines Part I– Acceptance and Performance Testing Part II-Test Procedures and Parameter Determination for Dynamic Analysis,” *IEEE Std 115*, 2010.

[72] MathWorks, “Implements IEEE type AC1A excitation system model - Simulink - MathWorks United Kingdom.” [Online]. Available: https://www.mathworks.com/help/physmod/sps/powersys/ref/ac5aexcitationsystem.html. [Accessed: 23-May-2019].

[73] B. Zaker, G. B. Gharehpetian, M. Karrari, and N. Moaddabi, “Simultaneous Parameter Identification of Synchronous Generator and Excitation System Using Online Measurements,” *IEEE Trans. Smart Grid*, vol. 7, no. 3, pp. 1230–1238, 2016.

[74] D. T. O. Oyedokun and F. Scheit, “Grid impact analysis of excitation control in mitigating the effects of geomagnetically induced currents,” in *IEEE AFRICON Conference*, 2019, vol. 2019-Septe.

[75] C. D. Vournas, A. V. Machias, and J. L. Souflis, “Determination of excitation parameter limits for generator dynamic stability,” 1989.

[76] B. Zhou, W. Yao, T. Xu, Y. Dong, and X. Xie, “Investigating the influence of types and parameters of excitation systems on the dynamic reactive power reserve of synchronous generators,” in *2015 12th International Conference on Fuzzy Systems and Knowledge Discovery, FSKD 2015*, 2016, pp. 2432–2436.

[77] R. C. Schaefer and K. Con; Kim, “Excitation Control of Synchronous Generators,” *IEEE Industry Applications*, no. April, pp. 37–43, 2001.

[78] IEEE. task Force, “Load representation for dynamic performance analysis,” *IEEE Trans. Power Syst.*, vol. 8, no. 2, pp. 472–482, 1993.

[79] G. J. R. C, W. Taylor; W. W. Price, M. K. P. K. C. K. Srinivasan; C. Concordia, and E. V. J. and B. K. Bess; P. Kundur; B. L. Agrawal; J. F. Luini, “Standard Load Models for Power Flow and Dynamic performance simulation,” *IEEE Trans. Power Syst.*, vol. 10, no. 3, pp. 1302–1313, 1995.

[80] H. Kirkham and D. R. White, “Reactive Power and GIC: The Problems of an Unrecognized Operationalist Measurement,” *9th IEEE Int. Work. Appl. Meas. Power Syst. AMPS 2018 - Proc.*, pp. 1–6, 2018.

[81] A. E. Emanuel, “Summary of IEEE Standard 1459: Definitions for the Measurement of Electric Power Quantities Under Sinusoidal, Nonsinusoidal, Balanced, or Unbalanced Conditions,” *IEEE Trans. Ind. Appl.*, vol. 40, no. 3, pp. 869–876, 2004.

[82] S. Edition, *The Authoritative Dictionary of IEEE Standards Terms*. 2000.

[83] *IEEE Standard Definitions for the Measurement of Electric Power Quantities Under Sinusoidal, Nonsinusoidal, Balanced, or Unbalanced Conditions*. IEEE, 2010.

[84] “IEEE Standard Definitions for the Measurement of Electric Power Quantities Under Sinusoidal, Nonsinusoidal, Balanced, or Unbalanced Conditions,” IEEE, 2010.

[85] M. Malengret and C. T. Gaunt, “General theory of instantaneous power for multi-phase systems with distortion, unbalance and direct current components,” *Electr. Power Syst. Res.*, vol. 84, no. 1, pp. 224–230, 2012.

[86] M. Malengret and C. T. Gaunt, “General theory of average power for multi-phase systems with distortion, unbalance and direct current components,” *Electr. Power Syst. Res.*, vol. 84, no. 1, pp. 224–230, 2012.

[87] M. Kazerooni and T. J. Overbye, “Incorporating the geomagnetic disturbance models into the existing power system test cases,” in *2017 IEEE Power and Energy Conference at Illinois, PECI 2017*, 2017.

[88] C. M. Liu, L. G. Liu, and R. Pirjola, “Geomagnetically induced currents in the high-voltage power grid in China,” *IEEE Trans. Power Deliv.*, 2009.

[89] C. M. Liu, L. G. Liu, and Y. Yang, “Monitoring and modeling geomagnetically induced currents in power grids of China,” in *Asia-Pacific Power and Energy Engineering Conference, APPEEC*, 2009.

[90] R. Pirjola, “Properties of matrices included in the calculation of geomagnetically induced currents (GICs) in power systems and introduction of a test model for GIC computation algorithms,” *Earth, Planets Sp.*, 2009.

[91] T. T. Murwira, S. Mkhonta, D. T. O. Oyedokun, K. A. Folly, and C. T. Gaunt, “Three-Phase Five-Limb Transformer Harmonic Analysis under DC-bias,” in *Proceedings - 2019 Southern African Universities Power Engineering Conference/Robotics and Mechatronics/Pattern Recognition Association of South Africa, SAUPEC/RobMech/PRASA 2019*, 2019, pp. 420–424.

[92] “Model the dynamics of three-phase round-rotor or salient-pole synchronous machine - Simulink.” [Online]. Available: https://www.mathworks.com/help/physmod/sps/powersys/ref/synchronousmachine.html. [Accessed: 13-Dec-2020].

[93] A. Moeini, I. Kamwa, P. Brunelle, and G. Sybille, “Synchronous Machine Stability Model, an Update to IEEE Std 1110-2002 Data Translation Technique,” in *IEEE Power and Energy Society General Meeting*, 2018.

[94] L. Salvatore and M. Savino, “Experimental determination of synchronous machine parameters,” *IEE Proc. B Electr. Power Appl.*, vol. 128, no. 4, pp. 212–218, 1981.

[95] B. R. Prentice, “Fundamental Concepts of Synchronous Machine Reactances,” *Trans. Am. Inst. Electr. Eng.*, vol. 56, no. 12, pp. 1–21, 2009.

[96] J. C. Peqqueña Suni, E. Ruppert, and F. Fajoni, “A guide for synchronous generator parameters determination using dynamic simulations based on IEEE standards,” *19th Int. Conf. Electr. Mach. ICEM 2010*, no. 1, 2010.

[97] Mathworks, “Simscape Electrical User ’s Guide (Specialized Power Systems) Version 7.1,” 2019.

[98] P. Jankee, H. Chisepo, V. Adebayo, D. Oyedokun, and C. T. Gaunt, “Transformer models and meters in MATLAB and PSCAD for GIC and leakage dc studies,” in *South African Universities Power Engineering Conference 2020*, 2020.

[99] C. Liu, Y. S. Ganebo, H. Wang, and X. Li, “Geomagnetically induced currents in Ethiopia power

grid: Calculation and analysis," *IEEE Access*, vol. 6, pp. 64649–64658, 2018.

[100] D. T. O. Oyedokun, "Geomagnetically Induced Currents (GIC) in Large Power Systems Including Transformer Time Response," Ph.D dissertation, Department of Electrical Engineering, University of Cape Town, Cape Town, South AfricaUniversity of Cape Town, 2015.

[101] J. E. Berge, "Impact of Geomagnetically Induced Currents on Power Transformers," Ph.D dissertation, Electrical and Computer Engineering department, University of Western Ontario, London, Ontario, Canada, 2011.

[102] "Implement two- or three-winding saturable transformer - Simulink." [Online]. Available: https://www.mathworks.com/help/physmod/sps/powersys/ref/saturabletransformer.html. [Accessed: 27-May-2020].

[103] L. D. Borrill, H. K. Chisepo, and C. T. Gaunt, "Importance of core joints in GIC/dc studies with scaled down laboratory transformers," *Int. J. Electr. Power Energy Syst.*, 2020.

[104] K. Zheng *et al.*, "Effects of system characteristics on geomagnetically induced currents," *IEEE Trans. Power Deliv.*, vol. 29, no. 2, pp. 890–898, 2014.

[105] A. Haddadi, A. Rezaei-Zare, L. Gerin-Lajoie, R. Hassani, and J. Mahseredjian, "A Modified IEEE 118-Bus Test Case for Geomagnetic Disturbance Studies-Part I: Model Data," *IEEE Trans. Electromagn. Compat.*, vol. 62, no. 3, pp. 955–965, 2020.

[106] M. Klein, G. J. Rogers, and P. Kundur, "A fundamental study of inter-area oscillations in power systems," vol. 6, no. 3, 1991.

[107] I. Kamwa, "Performance of Three PSS for Interarea Oscillations - MATLAB & Simulink." [Online]. Available: https://www.mathworks.com/help/physmod/sps/examples/performance-of-three-pss-for-interarea-oscillations.html. [Accessed: 31-Aug-2020].

[108] D. H. Boteler and R. J. Pirjola, "Modeling geomagnetically induced currents," *Sp. Weather*, vol. 15, no. 1, pp. 258–276, Jan. 2017.

[109] C. J. Rodger *et al.*, "Long-Term Geomagnetically Induced Current Observations From New Zealand: Peak Current Estimates for Extreme Geomagnetic Storms," *Sp. Weather*, vol. 15, no. 11, pp. 1447–1460, 2017.

[110] R. Kataoka and C. Ngwira, "Extreme geomagnetically induced currents," *Prog. Earth Planet. Sci.*, vol. 3, no. 1, 2016.

[111] Mathworks, "Compute three-phase instantaneous active and reactive powers - Simulink."

[Online]. Available: https://www.mathworks.com/help/physmod/sps/powersys/ref/power3phinstantaneous.html. [Accessed: 04-Nov-2019].

[112] "Calculate three-phase real and reactive power - Simulink." [Online]. Available: https://www.mathworks.com/help/physmod/sps/ref/powermeasurementthreephase.html. [Accessed: 11-Aug-2020].

[113] "Compute true root mean square (RMS) value of signal - Simulink." [Online]. Available: https://www.mathworks.com/help/physmod/sps/powersys/ref/rms.html. [Accessed: 29-Aug-2020].

[114] C. McGlade, "Uncertainties in the outlook for oil and gas," *Dr. thesis, UCL (University Coll. London).*, no. November, p. 329, 2013.

[115] L. Bolduc, A. Gaudreau, and A. Dutil, "Saturation time of transformers under dc excitation," *Electr. Power Syst. Res.*, vol. 56, no. 2, pp. 95–102, 2000.

[116] A. Haddadi, L. Gerin-Lajoie, A. Rezaei-Zare, R. Hassani, and J. Mahseredjian, "A Modified IEEE 118-Bus Test Case for Geomagnetic Disturbance Studies - Part II: Simulation Results," *IEEE Trans. Electromagn. Compat.*, vol. 62, no. 3, pp. 966–975, 2020.

[117] J. Ramírez-Niño, C. Haro-Hernández, J. H. Rodriguez-Rodriguez, and R. Mijarez, "Core saturation effects of geomagnetic induced currents in power transformers," *J. Appl. Res. Technol.*, vol. 14, no. 2, pp. 87–92, 2016.

[118] W. Hanli *et al.*, "Saturation characteristics of a transformer under DC bias and their influence on the distribution of DC current in an AC power grid," *IEEJ Trans. Electr. Electron. Eng.*, vol. 14, no. 2, pp. 231–237, 2019.

[119] "How to calculate reactive power of a transformer? – Voltage Disturbance." [Online]. Available: http://voltage-disturbance.com/power-engineering/how-to-calculate-reactive-power-of-a-transformer/. [Accessed: 03-Aug-2020].

[120] I. T. and D. Committee *et al.*, "GEOMAGNETIC DISTURBANCE EFFECTS ON POWER SYSTEMS," 1993.

[121] G. Chicco and A. Mazza, "100 Years of Symmetrical Components," *Energies*, vol. 12, no. 3, p. 450, 2019.

[122] G. Chicco, P. Postolache, and C. Toader, "Triplen harmonics: Myths and reality," *Electr. Power Syst. Res.*, vol. 81, no. 7, pp. 1541–1549, 2011.

[123] IEEE Power and Energy Society, "IEEE Recommended Practice and Requirements for

Harmonic Control in Electric Power Systems," *IEEE Std. 519-2014*, 2014.

[124] E. P. Systems and V. Ratings, "ANSI C84.1-2006 American National Standard," *Power*, 2006.

[125] National Electrical Manufacturers Association, "American National Standard for Electric power systems and equipment—Voltage ratings (60 Hertz)," *Am. Natl. Stand. Inst.*, 2016.

10 Appendix

10.1 Appendix A: Mind-Map for Literature Review